STRUCTURAL AND CHEMICAL DERIVATIZATION OF GRAPHENE FOR ELECTRONICS AND SENSING

by

NIHAR RANJAN MOHANTY

B.Tech, Indian Institute of Technology, Kharagpur, 2007

AN ABSTRACT OF A DISSERTATION

Submitted in partial fulfillment of the requirements for the degree

DOCTOR OF PHILOSOPHY

Department of Chemical Engineering
College of Engineering

KANSAS STATE UNIVERSITY
Manhattan, Kansas

2011

Abstract

Graphene - *a single atom thick two dimensional sheet of sp^2 bonded carbon atoms arranged in a honeycomb lattice* - has shown great promise for both fundamental research & applications because of its unique electrical, optical, thermal, mechanical and chemical properties. Derivatization of graphene unlocks a plethora of novel properties unavailable to their pristine parent "graphene". In this dissertation we have synthesized various structural and chemical derivatives of graphene; characterized them in detail; and leveraged their exotic properties for diverse applications. We have synthesized protein/DNA/ethylenediamine functionalized derivatives of graphene via a HATU catalyzed amide reaction of primary-amine-containing moieties with graphene oxide (GO) – *an oxyfunctional graphene derivative*. In contrast to non-specificity of graphene, this functionalization of GO has enabled highly specific interactions with analytes. Devices fabricated from the protein (concanavalin – A) and DNA functionalized graphene derivatives were demonstrated to enable label-free, specific detection of bacteria and DNA molecules, respectively, with single quanta sensitivity. Room temperature electrical characterization of the sensors showed a generation of ~ 1400 charge carriers for single bacterium attachment and an increase of 5.6 X 10^{12} charge carriers / cm^2 for attachment of a single complementary strand of DNA. This work has shown for the first time the viability of graphene for bio-electronics and sensing at single quanta level.

Taking the bio-interfacing of graphene to the next level, we demonstrate the instantaneous swaddling of a single live bacterium (*Bacillus subtilis*) with several hundred sq. micron (~ 600 μm^2) areal protein-functionalized graphene sheets. The atomic impermeability and high yield strength of graphene resulted in hermetic compartmentalization of bacteria. This enabled preservation of the dimensional and topological characteristics of the bacterium against the degrading effects of harsh environments such as the ultrahigh vacuum (~ 10^{-5} Torr) and high intensity electron beam (~ 150 A/cm^2) in a transmission electron microscope (TEM) column. While an unwrapped bacterium shrank by ~ 76 % and displayed significant charge buildup in the TEM column; a wrapped bacterium remained uncontracted and undamaged owing to the graphenic wraps. This work has shown for the first time an impermeable graphenic encasement

of bacteria and its application in high vacuum TEM imaging without using any lengthy traditional biological TEM sample preparation techniques.

In an inch-scale, we fabricated robust free-standing paper composed of TWEEN/Graphene composite which exhibited excellent chemical stability and mechanical strength. This paper displayed excellent biocompatibility towards three mammalian cell lines while inhibiting the non-specific binding of bacteria (*Bacillus cereus*). We predict this composite and its derivatives to have excellent applications in biomedical engineering for transplant devices, invasive instrument coatings and implants. We also demonstrate a novel, ultra-fast and high yield process for reducing GO to reduced graphene oxide (RGO) using a facile hydride-based chemistry. The RGO sheets thus-produced exhibited high carrier mobilities (~ 100-600 $cm^2/V{\cdot}s$) and reinstatement of the ambipolar characteristic of graphene. Raman spectra and UV-Vis spectroscopy on the RGO sheets displayed a high degree of restoration of the crystalline sp^2 lattice with relatively low defects.

We fabricated graphene nanoribbons (GNRs) – *1D structural derivatives of graphene* – using a nano-scale cutting process from highly oriented pyrolytic graphite (HOPG) blocks, with widths pre-determinable between 5 nm to 600 nm. The as-produced GNRs had very high aspect ratio in the longitudinal direction (~ 0.01); exhibited predominantly mono-layered structure (< 10 % bilayer); and smooth edges (Raman $I_{D/G}$ ~ 0.25 -0.28). Low temperature electrical transport measurements on back-gated thin film GNR devices were performed and a carrier mobility of ~ 20 ± 4 $cm^2/V{\cdot}s$ with sheet resistances of 2.2-5.1 MΩ / □ was extracted. Despite the ~ 50 nm thicknesses of the films, a clear bandgap scaling was observed with transport via variable range hopping (VRH) in 2 and 3 dimensions. This work demonstrates the first fully functional narrow pristine GNR thin-film field effect transistors (FETs).

In addition we fabricated graphene quantum dots (GQDs) – *0D derivatives of graphene* with dimensions < 100 nm – using a slight variation of our nano-scale cutting strategy, where the cleavage process is carried out in two dimensions. A high degree of control on the dimensions (Std. Dev. of ~ 5 nm for 50 X 50 nm square GQDs) and shape (pre-determinable between square, rectangle, triangle and trapezoid) of the as-synthesized GQDs is demonstrated. The optical properties of the GQDs such as the UV-Vis absorbance and photoluminescence were studied and their facile tunability was demonstrated depending on their dimensions. This work demonstrates for the first time the high throughput fabrication of GQDs with tunable dimensions and shape.

STRUCTURAL AND CHEMICAL DERIVATIZATION OF GRAPHENE FOR ELECTRONICS AND SENSING

by

NIHAR RANJAN MOHANTY

B.Tech, Indian Institute of Technology, Kharagpur, 2007

A DISSERTATION

Submitted in partial fulfillment of the requirements for the degree

DOCTOR OF PHILOSOPHY

Department of Chemical Engineering
College of Engineering

KANSAS STATE UNIVERSITY
Manhattan, Kansas

2011

Approved by:

Major Professor
Dr. Vikas Berry

Copyright

Abstract

Graphene - *a single atom thick two dimensional sheet of sp^2 bonded carbon atoms arranged in a honeycomb lattice* - has shown great promise for both fundamental research & applications because of its unique electrical, optical, thermal, mechanical and chemical properties. Derivatization of graphene unlocks a plethora of novel properties unavailable to their pristine parent "graphene". In this dissertation we have synthesized various structural and chemical derivatives of graphene; characterized them in detail; and leveraged their exotic properties for diverse applications. We have synthesized protein/DNA/ethylenediamine functionalized derivatives of graphene via a HATU catalyzed amide reaction of primary-amine-containing moieties with graphene oxide (GO) – *an oxyfunctional graphene derivative*. In contrast to non-specificity of graphene, this functionalization of GO has enabled highly specific interactions with analytes. Devices fabricated from the protein (concanavalin – A) and DNA functionalized graphene derivatives were demonstrated to enable label-free, specific detection of bacteria and DNA molecules, respectively, with single quanta sensitivity. Room temperature electrical characterization of the sensors showed a generation of ~ 1400 charge carriers for single bacterium attachment and an increase of 5.6 X 10^{12} charge carriers / cm^2 for attachment of a single complementary strand of DNA. This work has shown for the first time the viability of graphene for bio-electronics and sensing at single quanta level.

Taking the bio-interfacing of graphene to the next level, we demonstrate the instantaneous swaddling of a single live bacterium (*Bacillus subtilis*) with several hundred sq. micron (~ 600 μm^2) areal protein-functionalized graphene sheets. The atomic impermeability and high yield strength of graphene resulted in hermetic compartmentalization of bacteria. This enabled preservation of the dimensional and topological characteristics of the bacterium against the degrading effects of harsh environments such as the ultrahigh vacuum (~ 10^{-5} Torr) and high intensity electron beam (~ 150 A/cm^2) in a transmission electron microscope (TEM) column. While an unwrapped bacterium shrank by ~ 76 % and displayed significant charge buildup in the TEM column; a wrapped bacterium remained uncontracted and undamaged owing to the graphenic wraps. This work has shown for the first time an impermeable graphenic encasement

of bacteria and its application in high vacuum TEM imaging without using any lengthy traditional biological TEM sample preparation techniques.

In an inch-scale, we fabricated robust free-standing paper composed of TWEEN/Graphene composite which exhibited excellent chemical stability and mechanical strength. This paper displayed excellent biocompatibility towards three mammalian cell lines while inhibiting the non-specific binding of bacteria (*Bacillus cereus*). We predict this composite and its derivatives to have excellent applications in biomedical engineering for transplant devices, invasive instrument coatings and implants. We also demonstrate a novel, ultra-fast and high yield process for reducing GO to reduced graphene oxide (RGO) using a facile hydride-based chemistry. The RGO sheets thus-produced exhibited high carrier mobilities (~ 100-600 $cm^2/V{\cdot}s$) and reinstatement of the ambipolar characteristic of graphene. Raman spectra and UV-Vis spectroscopy on the RGO sheets displayed a high degree of restoration of the crystalline sp^2 lattice with relatively low defects.

We fabricated graphene nanoribbons (GNRs) – *1D structural derivatives of graphene* – using a nano-scale cutting process from highly oriented pyrolytic graphite (HOPG) blocks, with widths pre-determinable between 5 nm to 600 nm. The as-produced GNRs had very high aspect ratio in the longitudinal direction (~ 0.01); exhibited predominantly mono-layered structure (< 10 % bilayer); and smooth edges (Raman $I_{D/G}$ ~ 0.25 -0.28). Low temperature electrical transport measurements on back-gated thin film GNR devices were performed and a carrier mobility of ~ 20 ± 4 $cm^2/V{\cdot}s$ with sheet resistances of 2.2-5.1 MΩ /□ was extracted. Despite the ~ 50 nm thicknesses of the films, a clear bandgap scaling was observed with transport via variable range hopping (VRH) in 2 and 3 dimensions. This work demonstrates the first fully functional narrow pristine GNR thin-film field effect transistors (FETs).

In addition we fabricated graphene quantum dots (GQDs) – *0D derivatives of graphene* with dimensions < 100 nm – using a slight variation of our nano-scale cutting strategy, where the cleavage process is carried out in two dimensions. A high degree of control on the dimensions (Std. Dev. of ~ 5 nm for 50 X 50 nm square GQDs) and shape (pre-determinable between square, rectangle, triangle and trapezoid) of the as-synthesized GQDs is demonstrated. The optical properties of the GQDs such as the UV-Vis absorbance and photoluminescence were studied and their facile tunability was demonstrated depending on their dimensions. This work demonstrates for the first time the high throughput fabrication of GQDs with tunable dimensions and shape.

Table of Contents

List of Figures

List of Tables

List of Supplemental Files

3SV1 Three dimensional reconstruction of the tilt-series TEM tomographs of a 90 nm section of fully wrapped bacterium shown in 3SV2

3SV2 Collection of tilt-series (-30° to +30° in steps of 2°) TEM tomographs of a 90 nm thick section of fully wrapped bacterium

3SV3 Time-lapse images of the fully wrapped bacteria shown in Figure 3.6 - b and c exposed to the high vacuum (~ 10^{-5} Torr) and high intensity electron beam current (~ 150 A/cm^2) in the TEM column: a clear preservation of the dimensional and topological characteristics is achieved up to 40 minutes of exposure due to graphenic encasements

3SV4 Time-lapse images of unwrapped bacteria exposed to the high vacuum (~ 10^{-5} Torr) and high intensity electron beam current (~ 150 A/cm^2) in the TEM column: severe bubbling of the bacterial samples was observed attributed to boiling up and efflux of the volatile intracellular components

3SV5 Time-lapse images of unwrapped bacteria exposed to the TEM column showing extensive bubbling and delamination

3SV6 First time-lapse images of unwrapped bacteria exposed to the TEM column showing TEM beam + UHV induced compromization of the bacterial membrane integrity resulting in out-diffusion of plumes of intracellular volatile matter

3SV7 Second time-lapse images of unwrapped bacteria exposed to the TEM column showing TEM beam + UHV induced compromization of the bacterial membrane integrity resulting in out-diffusion of plumes of intracellular volatile matter

6SV1 Low frame rate, annotated time-lapse video showing the nanotomy process for producing graphene nanoblocks (GNBs)

6SV2 High frame rate video showing the nanotomy of HOPG to produce GNBs

Acknowledgements

When I joined Dr. Vikas Berry's lab in January 2008, I joined as a Master's candidate in Chemical Engineering. Working for a year with Dr. Berry changed my whole attitude towards research. His excitement for research brushed off on me to such a degree that I went forward to get my PhD degree. I consider myself lucky to have had an opportunity to learn from Dr. Berry. The support, encouragement and guidance that I received from Dr. Berry were instrumental in shaping my intellect and carving my career path: I would like to thank Dr. Berry for all of that. It has been a wonderful experience working with him and being a part of his effort in advancing graphene science.

I would like to thank the members of my thesis committee, Dr. Gurpreet Singh, Dr. James H Edgar, Dr. Jun Li and Dr. Keith Hohn for their constructive inputs during the course of my PhD, which was crucial in making this dissertation a reality. I would like to extend my special thanks to Dr. Singh for the countless times when I popped into his office to discuss about my career plans. I would also like to thank Dr. Z J Pei for always helping me out in figuring my career path.

I had the unique fortune of having excellent co-workers in the Berry lab, graduate students and undergraduates alike, including Kabeer, Ashvin, Steven, Jose, Josh, Monica and Phong. I would like to extend special thanks to Ashvin for all the help I received during my research including drawing cartoons and animations in addition to experimental support. He is one of the smartest people I have ever come across and I would like to wish him success in his career. I would like to thank Jose and Monica for their help during several of the projects. I would like to thank Kabeer for his help during my ramp-up at initial stages. I would also like to thank Phong for his assistance in the later stages of my PhD. Outside our group, I would like to thank Myles for all the countless hours he spent in running my XPS samples. I would also like to thank all the members of the chemical engineering department for their support and in making the 3.5 years one of the best periods in my life.

Outside the department I would like to thank Dr. Dan Boyle for the help with TEM, confocal and the FESEM. I would also like to thank Dr. Joe Nabity for the training on E-Beam and FESEM. I would like to thank Mr. Kent Hampton for giving me unfettered access to the

sputtering system for metal PVD for electrodes. I would also like to thank Dr. John Tomich for providing me access to his fluorometer.

I would like to thank my good friends Mandeep, Neha and Hussain who have made my stay in Manhattan a pleasant experience. I would always cherish our last minute trips / picnics / PS-3 sessions / game days that formed an exciting part of my graduate life. I would like to extend special thanks to my fiancée Angela for her continued support throughout my graduate school and her patience while proof-reading the > 200 pages of my dissertation.

Graduate school has been the best time of my life until now. Being all set to join the semiconductor industry in a few weeks, I would miss this phase of life the most. Every new step in life brings with itself the excitement of delving into the unknown and the quest to achieve tangible results, I hope I would be able to maintain the same pace of innovations in the industry as I have until now in the academics.

Dedication

I would like to dedicate this thesis to my parents Mr. Rabi Narayan Mohanty and Ms. Nirupama Mohanty, I owe it to them for what I am today and who have supported me in every aspect of my life even though they are thousands of miles away; to my kid brother Mr. Tusar Mohanty, who has always looked up to me for inspiration which in turn has made me work twice as hard at everything; to my fiancée (and soon to be wife) Ms. Angela Adams, who has been a constant source of inspiration to me and believed in my abilities when I didn't; to my friend since 8th grade Mr. (to be Dr. soon) Kaniska Mohanty, who has always been there whenever I needed support; to my friends in Kansas State University, who made my stay in Manhattan as pleasant as it could possibly be; and finally to the **Indian Institute of Technology system**, which shaped my way of thinking and made me the person I am today.

Chapter 1 - Graphene

Graphene: *the 2 dimensional carbon crystal*

Rarely in the history of science does the discovery of a new material usher such profound advancements in fundamental research and applications in a short time (~ 6 years) and result in one of the fastest Nobel prizes: such was the effect of the discovery of *Graphene* by A. K. Geim and K. S. Novoselov, a material long termed as an "academic material" and theorized not to exist [1-8]. Graphene, a two dimensional atomic thick sheet of sp^2 bonded carbon atoms arranged in a honeycomb lattice, is considered as the precursor of the other known carbon nanomaterials viz. 3D graphite (stacked up graphene sheets with weak van der Waals forces between layers), 1D carbon nanotubes (rolled up graphene with reconnected edge lines) and 0D fullerenes (spherical wraps obtained via introduction of pentagons to create positive curvature defects) (Figure 1.1) [4, 5].

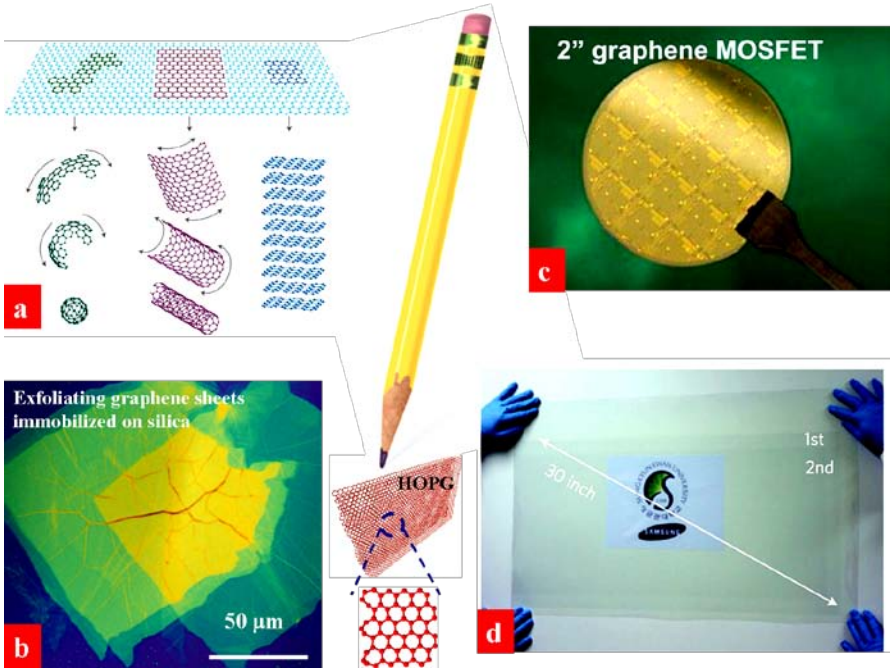

Figure 1-1 (a) Schematic diagram of the wonder material graphene which forms the precursor for many of the known carbon nanomaterials such as 0D fullerenes, 1D nanotubes and 3D graphite [adapted from Geim, A.K., Novoselov, K.S. "*The rise of graphene.", Nat. Mater.* 6, 183-191 (2007)], (b) Optical image of exfoliating graphene sheets deposited on a 300 nm thick silicon dioxide substrate, Center picture shows a pencil [adapted from http://spiritually-true.blogspot.com/2010/09/pencilparable-of-pencil.html]

and the schematic diagram of a highly oriented pyrolytic graphite (HOPG) block, an excellent source of graphene, with the bottom panel showing a close up figure of the hexagonal lattice of carbon atoms in graphene. (c) Optical image of wafer scale graphene devices [adapted from First, P.N. *et al* "*Epitaxial graphenes on silicon carbide.*", *MRS Bulletin*, 35, 296-305 (2010)], (d) Optical image of 30 inch graphene grown on copper [adapted from Bae, S. *et al*, "*Roll-to-roll production of 30-inch graphene films for transparent electrodes.*", *Nat. Nano.*, 5, 574-578 (2010)]. Starting with micro-mechanical exfoliation of graphene via the duct tapes, the field has advanced into large scale production onto inch scale.

In the short time since its isolation in 2004 (some 440 years after its invention), graphene has been shown to possess a plethora of exceptional properties which until now had been confined to the realm of condensed matter theorists, starting a gold rush among researchers all around the world and thus making it the scientific equivalent of a "*global equalizer*" (Figure 1.1) [2-6, 9]. This is evident from the sea of graphene-based articles appearing every year from around the world and more predicted to in future [10]. The list of exceptional electrical, mechanical, chemical, thermal and optical properties includes ambipolar field effect, quantum Hall effect at room temperature, dispersion-free ballistic charge carrier mobility (~ 200, 000 $cm^2/V{\cdot}s$ [11, 12]), high thermal conductivity (~ 5000 W/mK [13]), extraordinary mechanical strength (~ 1 TPa Young's modulus [14]), atomic impermeability (even to helium [15]), high optical transparency (~ 97 % [16]) and many others [4-7]. Structurally the hybridization of s, p_x and p_y atomic orbitals of graphene forms a trigonal planar hexagonal arrangement of sp^2 carbons (σ bonds between carbon atoms with a bond length of ~ 0.142 nm) providing the exceptional chemical and mechanical stability; the p_z orbitals (perpendicular to the planar surface) covalently bind to those of the neighboring carbon atoms forming the shared π-electron cloud (half-filled π-band) which is responsible for the exceptional electrical, optical and thermal properties [1-3, 5, 17-19]. This has led to potential applications of graphene in meta-material / composite fabrication, super-capacitors, batteries, high speed interconnects, transparent conducting electrodes, organic photovoltaics, catalysis, bio/chemical sensors, impermeable casings for electron microscopy, RF applications, thermal management in ICs, nanoelectromechanical systems (NEMS) and many others (Figure 1.1) [4, 5, 13, 20-33].

Synthesis of Graphene

As with any new material, the initial major research effort goes into the invention of synthesis strategies that fulfill the key attributes of reproducibility and repeatability. Some of the major reported methods for producing graphene are as follows:

1. Micromechanical cleavage: This is the method that led to the first isolation of graphene in 2004 and is currently the only one that produces the best quality of single crystal graphene up to 100 μm in size [3]. The basic steps involve repeated peeling of a graphite block (or highly oriented pyrolytic graphite (HOPG)) using an adhesive tape until a single layer of graphene is produced (Figure 1.2). One of the keys to the successful discovery of graphene has been the successful optical visualization of transparent monolayers of graphene on ~ 300 nm thick silicon dioxide substrate, a crucial invention by *Novoselov et al* [34]. This method however is tedious (taking several hours to produce a single sheet of graphene), has extremely low throughput and produces graphene of micro-scale dimensions [35], which demand precision handling (large areal graphene such as inch scale would enable easier handling and processing).

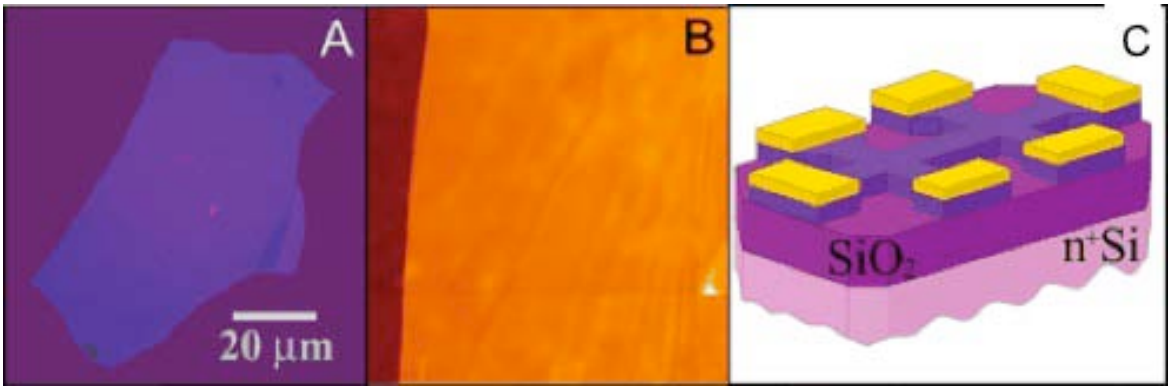

Figure 1-2 (A, B) Optical image and AFM scan of a multi-layered graphene sheet with thickness ~ 3 nm; (C) Schematic diagram of a graphene device [Figure adapted from Novoselov, K. S. *et al*, "*Electric field effect in atomically thin carbon films.*", *Science*, 22, 666-669 (2004)]

2. Chemical <u>top down</u> methods: These methods exfoliate the individual graphene sheets from source graphite and stabilize them in solution via a plethora of reported routes [36]. The most common route is the graphene oxide (GO) route which involves the exfoliation of graphene from

graphite via harsh oxidation reactions in presence of strong acids / oxidizing agents [37] and the subsequent reduction of the GO sheets into a form of graphene known as reduced graphene oxide (RGO) [22, 38, 39]. The GO sheets produced in the first step of the GO route contain several oxy-functional groups (carboxyl, carbonyl, hydroxyl, epoxy, quinone, etc) bound to sp^3 islands on the sp^2 graphenic structure, ensuing a overall negative charge on the sheets which aids in exfoliation and subsequent stabilization in solution (typical zeta potentials at pH 7.0 ~

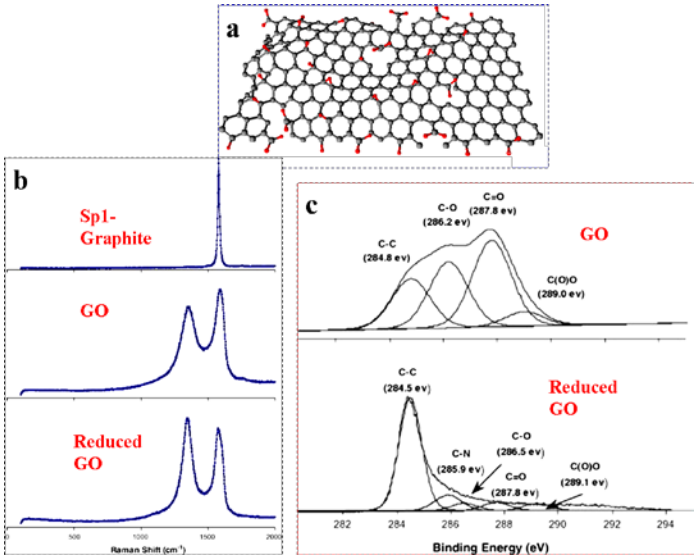

Figure 1-3 (a) Schematic diagram showing a GO sheet (carbon atoms – grey; oxygen atoms – red) with the various oxy-functional groups. (b) Panel showing the Raman spectra for GO and reduced RGO taken from Stankovich, S. *et al*, "*Stable aqueous dispersions of graphitic nanoplatelets via the reduction of exfoliated graphite oxide in the presence of poly(sodium 4-styrenesulfonate).*", *J Mater. Chem.* 16, 155-158 (2006). The continued presence of the Raman bands corresponding to defects demonstrates incomplete reduction of GO. (c) Panel showing the XPS spectra for GO and the reduced GO adapted from Stankovich, S. *et al*, "*Stable aqueous dispersions of graphitic nanoplatelets via the reduction of exfoliated graphite oxide in the presence of poly(sodium 4-styrenesulfonate).*", *J Mater. Chem.* 16, 155-158 (2006), demonstrating the incomplete reduction of GO.

negative 60-70 mV) (Figure 1.3a, c) [40]. GO can be reduced into RGO via a number of reagents such as hydrazine hydrate [22, 41], hydroquinone [42], sodium borohydride [40, 43], ascorbic acid [44], thermal treatment [45, 46] and hydrogen plasma [47, 48]. Recently the use of high-

intensity light flash (xenon flash) [49] and the use of microbes for reduction have been reported [47, 50]. Even though very high typical efficiencies (> 60 %) have been achieved via these methods [22, 30], the quality of RGO produced is orders of magnitude lower than that of micro-mechanically exfoliated graphene [51]. This can be attributed partly to the resilient oxy-functional groups in graphene oxide such as the carbonyl groups, which are difficult to remove upon reduction [52, 53]; and to the significant defect sites generated as a result of the harsh reaction conditions (Figure 1.3b, c). These sp^3 bonded islands / defect sites in the crystalline graphenic sp^2 framework of RGO result in severe degradation in electrical properties (such as carrier mobilities: ~ 100 - 200 $cm^2/V{\cdot}s$ compared to 100,000 $cm^2/V{\cdot}s$ in suspended micromechanically exfoliated graphene [11, 12, 36]), thermal and mechanical properties [4, 36, 52, 54]. In this thesis an alternate high efficiency, instantaneous (< 5 min) strategy for reducing GO in solution using sodium hydride (Chapter 5) is presented. In addition to being significantly less toxic than most reducing agents reported this far, this method produced RGO with a high degree of restoration of the crystalline sp^2 lattice with fewer defects, as deduced from the low Raman $I_{D/G}$ ratios and high electrical conductivity, comparable to or surpassing most reported methods.

The other chemical top-down route involves a class of compounds known as the graphite intercalation compounds (GICs) for stable dispersion of graphite in solution [55-58]. As the name suggests, the GICs intercalate between the individual graphene sheets and result in production of stably dispersed pristine graphene in solution [36] (Figure 1.4). In spite of several such compounds being described in the literature (Eg: $K(THF)_xC_{24}$; PmPV and TCNQ) [56, 57, 59], the efficiencies of graphene production have been extremely low (1 – 12 wt %), raising their cost of synthesis and thus preventing wide spread adoption.

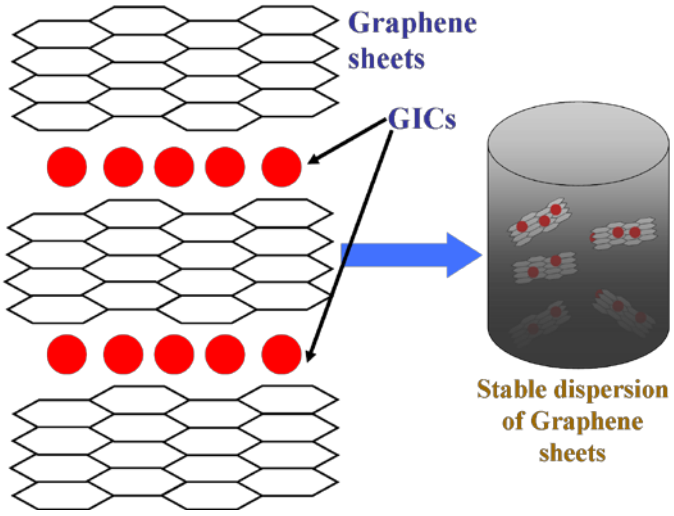

Figure 1-4 Schematic diagram showing the application of GICs in producing a stable dispersion of pristine graphene

Several solvent based approaches for sonication based exfoliation and stabilization of graphene in organic solvents such as NMP or DMEU have been reported [55]. Notwithstanding the high quality of graphene produced (sheet conductivity of ~ 6500 S/m), the yields have been too low (< 0.15 mg/ml [56]) to result in wide spread adoption. Further, the employment of sonication produces harsh mechanical forces, which limits the size of the graphene sheets produced. Recently, a new superacid based exfoliation of graphite has been reported which has shown very promising yields (~ 2 mg/ml) and quality (80,000 - 95,000 S/m) [60]. Using chlorosulfonic acid, a commodity chemical, *Behabtu et al* [60] showed the synthesis of a high concentration (~ 2 mg/ml) stable dispersion of graphene without the employment of any harsh mechanical agitation strategies (Figure1.5). Owing to the exfoliation of graphene via repulsion between protonated individual graphene layers, this method produces pristine graphene without any damage [60, 61]. In this thesis, this method was extensively employed owing to the afore-mentioned advantages for exfoliation of the graphene nanoribbons (GNRs) and graphene quantum dots (GQDs), 1D and 0D structural derivatives of graphene, respectively.

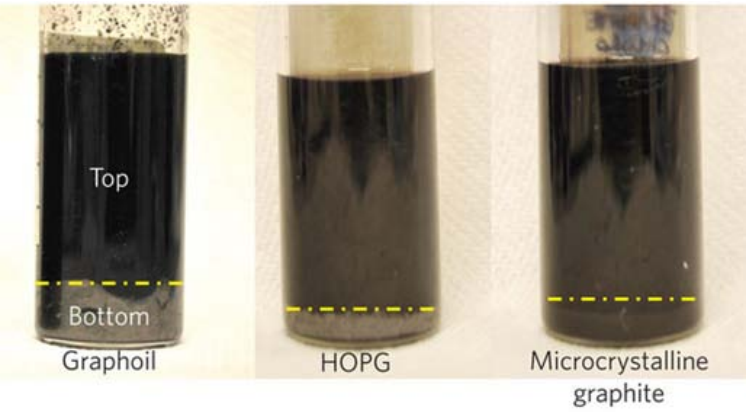

Figure 1-5 Chlorosulfonic acid dispersions of graphene obtained from different sources [figure adapted from Behabtu, N. *et al*, "*Spontaneous high-concentration dispersions and liquid crystals of graphene.*", *Nat. Nano.* 5, 406-411 (2010)

3. Chemical Vapor Deposition on transition metals: High quality graphene films have been grown on Ni (and other transition metals such as Pt, Ir, Ru) with potential for large-scale production and integration with existing CMOS unit processes for deposition / film growth [62-65] (Figure 1.6). This method comprises of two steps: (1) carbon-saturation of transition metals from a hydrocarbon gas (such as CH_4) at a high temperature, and (2) precipitation of the dissolved carbon upon cooling forming a thin film of graphene. In-spite of good electrical properties (~ 3700 $cm^2/V{\cdot}s$) of as-produced graphene and large scale, there are several major issues that need to be addressed such as controlling the thickness of graphene sheets and their grain boundaries or efficient transfer procedures [35, 63, 65].

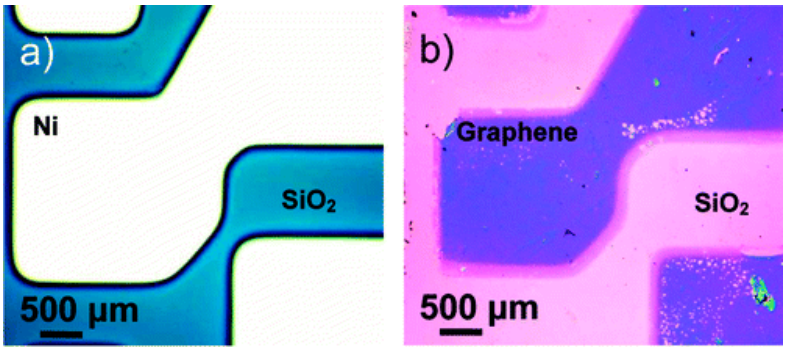

Figure 1-6 Optical image of Ni on SiO_2/Si and CVD growth of graphene on the deposited nickel [Figure adapted from Reina, A. *et al, "Large area, few layer graphene films on arbitrary substrates by chemical vapor deposition.", Nano Lett.* 9, 30-35 (2009)]

Another graphene growth technique that has been recently reported and has shown a lot of promise is the CVD growth of graphene on Cu films pioneered by the *Ruoff* group [66] (Figure 1.7). Owing to the low solubility of carbon in copper, in contrast to the Ni-growth, a time-independent nucleation based growth of graphene (as large as 30 inch sheets) was observed which is self-limiting (> 95 % of area mono-layered) [66, 67]. However, several critical issues need to be resolved before wide spread adoption of this method for graphene synthesis including the transfer methods and the reduction of the grain boundaries.

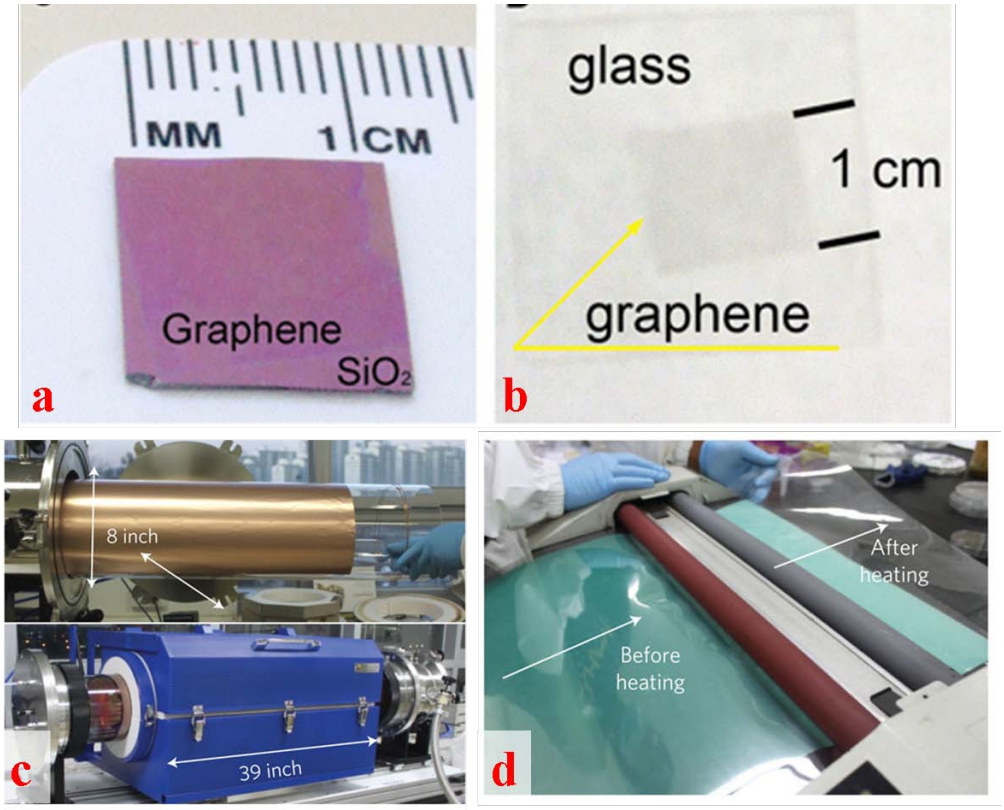

Figure 1-7 (a, b) Optical images of graphene grown on copper foils and subsequently transferred onto silica and glass substrates [Image adapted from Li, X. *et al*, "*Large-area synthesis of high-quality and uniform graphene films on copper foils.*", *Science* 324, 1312-1314 (2009)] (c) Optical images of the setup employed to fabricate 30 inch graphene films on copper foils (d) Optical image of the roll-to-roll fabrication of graphene films on PET polymer [images c and d adapted from Bae, S. *et al*, "*Roll –to-roll production of 30-inch graphene films for transparent electrodes.", Nat. Nano.* 5, 574-578 (2010)]

4. Sublimation of Si from SiC: This epitaxial growth of graphene, pioneered by the *de Heer* group [68-72], involves the high temperature sublimation of Si from silicon carbide (Si-terminated and C-terminated 4H and 6H SiC crystals) resulting in graphene islands [69] (Figure 1.8). While the growth on Si face is slow and self-limiting, producing single or double layers; the growth on C-face produces thick layers (~ 5- 100 layers), both being two completely different types of graphene. The physical properties of the epitaxial graphene grown from C-face, known as turbostatic graphene, differ in several ways from those of the micro-mechanically exfoliated graphene owing to the interfacial effects, which are still unclear at this time [4]. The interaction with the substrate induces strong doping levels (~ 10^{13} / cm^2) and spectral disorder at low energies. The epitaxial graphene grown on the Si-face shows the most promise with excellent crystal quality and large coverage. However, similar to the CVD techniques, more work still needs to be done on obtaining further control of the graphene film thickness, grain boundaries and on facile transfer methods.

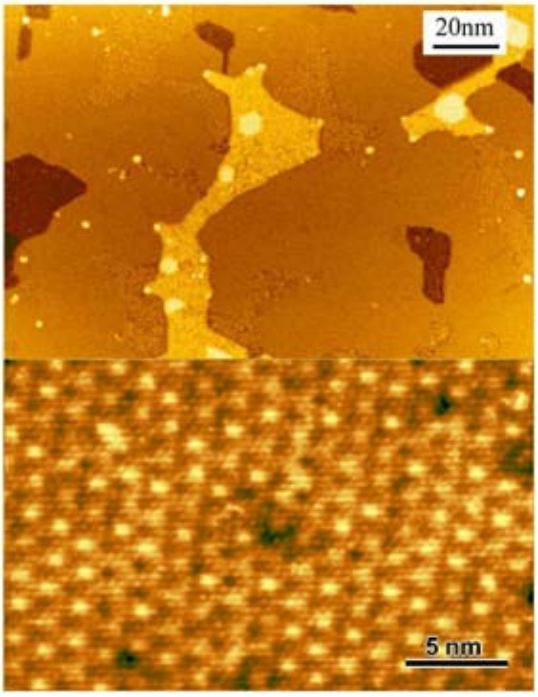

Figure 1-8 STM topographs of a monolayer of epitaxial graphene on the (0001) face of SiC. Top image shows large flat regions of partially formed monolayers of graphene. Bottom image shows the reconstructed image through a graphene layer on the SiC face. [Image

taken from de Heer, W. A. *et al*, "*Epitaxial graphene.*", *Solid State Comm.* 143, 92-110 (2007)]

Properties of Graphene

Chemical properties

Graphene is a unique chemical platform: its sp^2 bonded hexagonal carbon lattice alloyed with the ultimate 2D surface - *two faces of the bulk-less monolayer*. This provides graphene with extraordinary sensing abilities owing to (a) the carriers being easily modulated in absence of any dilution from the bulk, and (b) a potentially defect free crystal lattice which leads to low intrinsic noise (low thermal noise and low 1/f noise) thereby showing potential for single quanta detection [4, 5, 19]. This has been shown experimentally by *Schedin et al* [73] in the employment of graphene for detection of individual gas molecules adsorbed on graphene, the ultimate limit to sensing (Figue 1.9). Successful detection of various gas molecules has been achieved on pristine graphene which leads to step-by-step modulation of local carrier concentration resulting in step-like changes in electrical resistance (Figure 1.9).

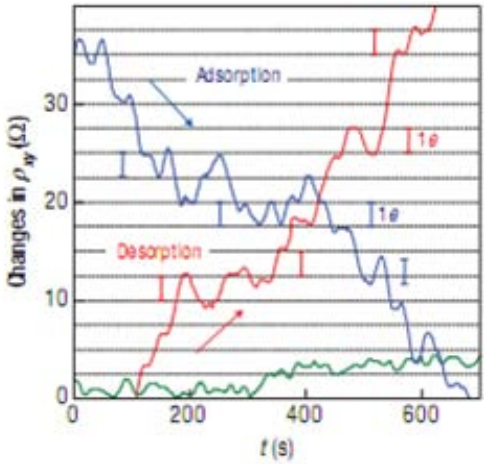

Figure 1-9 Image showing the step-by-step decrease (blue curve) in the Hall resistivity upon adsorption of strongly diluted NO_2 and a step-by-step increase (red curve) upon desorption. The green curve is the control, which is exposed to pure He. [adapted from Schedin, F. *et al*, "*Detection of individual gas molecules adsorbed on graphene.*", *Nat. Mater.* 6, 652-655 (2007)]

Notwithstanding the excellent propensity of pristine graphene for ultra-sensitive detection, the specificity is an issue [35, 74, 75]. Chemically functionalized graphene, which forms a new class of graphene with starkly different properties, offers an excellent route for highly specific chemistries [30]. The most common derivative of graphene is GO - the oxy-functional derivative of graphene. Comprising of an amalgam of sp^2 bonded crystalline islands separated by sp^3 bonded oxy-functionalized carbon (typical functional groups being hydroxyl, epoxy, carbonyl, quinone and others, see Figure 1.3a, c) structure, GO is a new variety of graphene [38, 47, 52]. The most common synthesis strategy is the Hummer's acid oxidation method involving sulfuric acid and potassium permanganate based oxidation [37]. As expected, owing to the loss of the highly mobile π electrons due to sp^3 bonds, GO is electrically insulating (or semiconducting) depending on the degree of oxidation [54]. However, the most important advantage offered by GO is the easy availability of basal oxy-functional groups, which has been employed for further functionalization to confer high specificity (Figure 1.10). In chapter 2, a novel functionalization route for attaching peptides and DNA molecules onto GO is presented and subsequently employed in fabricating ultra-sensitive sensors with single quanta sensitivity [30].

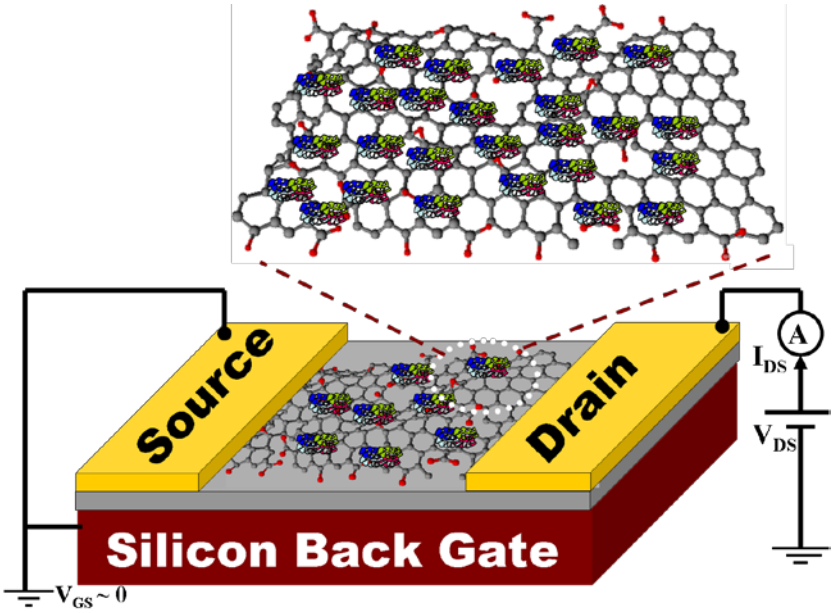

Figure 1-10 A schematic diagram of a sample peptide-functionalized GO device: GO was functionalized with chemical moieties including peptides and DNA for fabricating ultrasensitive bacteria and DNA sensors

Electronic properties

First demonstrated by P. R. Wallace in 1947 [76], graphene displays an unusual semi-metallic behavior arising from the π and π^* bands touching at the corners of the hexagonal Brillouin zone denoted by K and K' momentum vectors, shown in Equation 1.1 (Figure 1.11)

$$K = \left(\frac{2\pi}{3a_{C-C}}, \frac{2\pi}{3\sqrt{3}a_{C-C}} \right); K' = \left(\frac{2\pi}{3a_{C-C}}, -\frac{2\pi}{3\sqrt{3}a_{C-C}} \right) \ldots (1.1),$$

where $a_{C\text{-}C}$ ~ 0.142 nm is the C-C bond length [3, 5, 17, 19]. Unlike traditional semiconductors, the π and π^* bands are quasi-linear close to the Fermi energy whose surface is now reduced to 6 points at the corners of 2D hexagonal Brillouin zone (Figure 1.11). Further, this linear energy-momentum relation leads to the electronic group velocity at the Dirac points to be $1/300^{th}$ the velocity of light in vacuum (1 X 10^6 m/s) with the properties of the charge carriers being explained by the relativistic Dirac equation for zero effective mass particles instead of the non-relativistic Schrodinger equation for non-zero effective mass, given by Equation 1.2,

$$E^{\pm}(k) = \pm t \sqrt{1 + 4\cos\frac{\sqrt{3}k_x a}{2}\cos\frac{k_y a}{2} + 4\cos^2\frac{k_y a}{2}} \ldots (1.2)$$

where, a = $\sqrt{3}a_{C-C}$, t (the transfer integral) is the nearest neighbor hopping energy with a magnitude of 2.8 eV [19]. Expansion of the equation 1.2 near the Dirac points leads to Equation 1.3,

$$E^{\pm}(\kappa) = \pm \hbar v_F |\kappa| \ldots (1.3)$$

where, κ = k – K is the momentum momentum measured relative to the Dirac point; and v_F is the electronic group velocity for graphene ~ 1 X 10^6 m/s. This band structure is for the Dirac spectrum for massless fermions, with the effective Hamiltonian given by Equation 1.4 [19],

$$\hat{H} = \hbar \begin{pmatrix} 0 & k_x - ik_y \\ k_x + ik_y & 0 \end{pmatrix} \ldots(1.4)$$

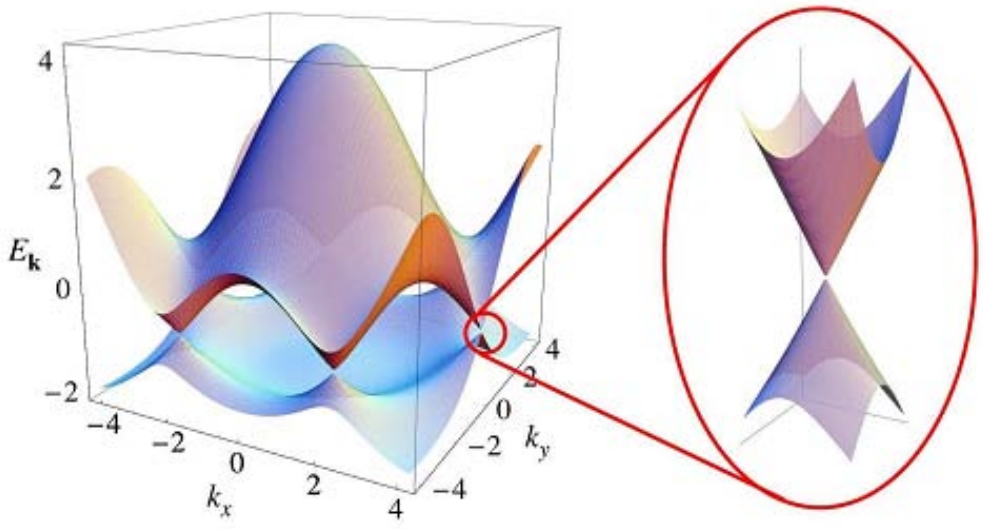

Figure 1-11 Energy spectrum of graphene in the Brillouin zone. Right panel shows a zoomed-in picture of the energy bands close to the Fermi energy at the Dirac point [Figure taken from Castro Neto, A. H. *et al, "The electronic properties of graphene."*, *Rev. Mod. Phys.* 81, 110-155 (2009)]

An interesting property of graphene is its ambipolar nature with unusually high carrier mobility [19]. The symmetric transfer characteristics around the Dirac point demonstrate equal electron and hole mobilities i.e. ambipolarity (Figure 1.12) given in Equation 1.5,

$$\mu_h \sim \mu_e \quad \ldots(1.5)$$

that have been found to be carrier-density and temperature independent. For suspended micro-mechanically exfoliated graphene sheets, the highest mobilities reported have been ~ 250,000 $cm^2/V{\cdot}s$ [12], significantly higher than most electronic materials. For the substrate deposited samples, the mobilities reported range from 2000 – 20,000 $cm^2/V{\cdot}s$ owing to carrier scattering by impurities, adsorbents and defects [47]. These high values of carrier mobility (for comparison,

typical mobility in bulk Si ~ 1400 $cm^2/V{\cdot}s$ for electrons and much less for current industry standard strained Si or Si on insulator) [77] have the potential for ultra-fast electronics and logic applications.

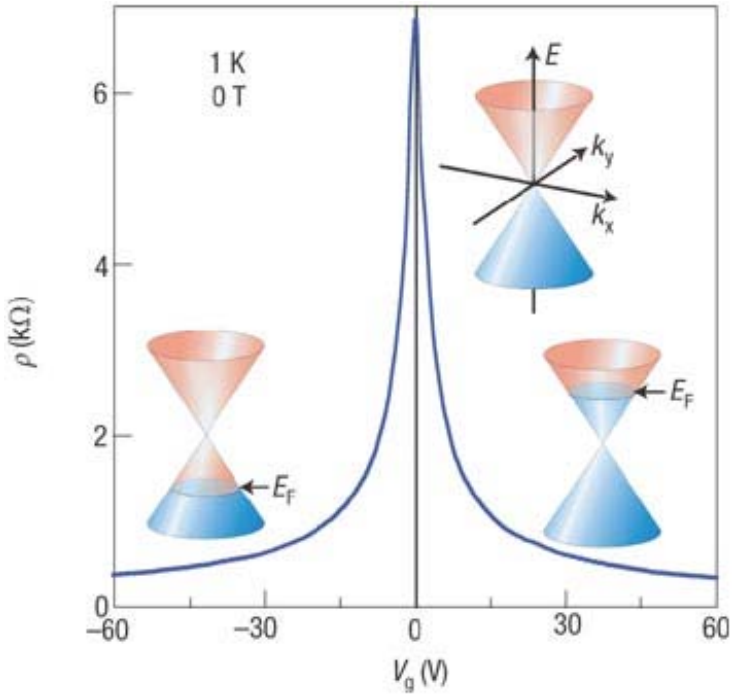

Figure 1-12 Transfer characteristics of graphene demonstrating its ambipolar nature. Insets show the change in the low-energy spectrum (E(k)) of graphene vs. the V_g in the FET device. The mobility, μ of the carriers is ~ 5000 $cm^2/V{\cdot}s$ displays extremely weak dependence on the temperature. [Figure taken from Geim, A. K. and Novoselov, K. S. "*The rise of graphene.*", *Nat. Mater.* 6, 183-191 (2007)]

Another interesting property of graphene is its finite minimum conductivity (σ_{xx}) at the Dirac point equaling $4e^2/h$ arising either from the linear excitation spectrum of Dirac fermions or the chiral nature of quasi-particles or a combination of both [5, 19]. However, for practical devices the origin of this conductance relation is not clear owing to the concomitant substrate effects or graphene sheet rippling induced formation of local puddles of charge carriers, which could lead to finite conductance. Further, in contrast to the conventional semiconductors, in the presence of a vertical magnetic field the linear excitation spectrum of Dirac fermions in graphene evolves into discrete landau levels given by Equation 1.6,

$$E_n = \pm v_F \sqrt{2e\hbar |n| B} \quad \ldots(1.6)$$

This splitting in graphene in the presence of large magnetic fields is responsible for the observation of the "half integer" quantum Hall effect at room temperature [19, 78, 79] (Figure 1.13). This effect at high temperatures has been attributed in part to the large cyclotron gaps, $\hbar\omega_C$ of the relativistic mass-less Dirac fermions in graphene, the high intrinsic carrier concentrations (10^{13} /cm^2) with only a single 2D subband occupation, and the temperature independent mobility of charge carriers in graphene [78, 79].

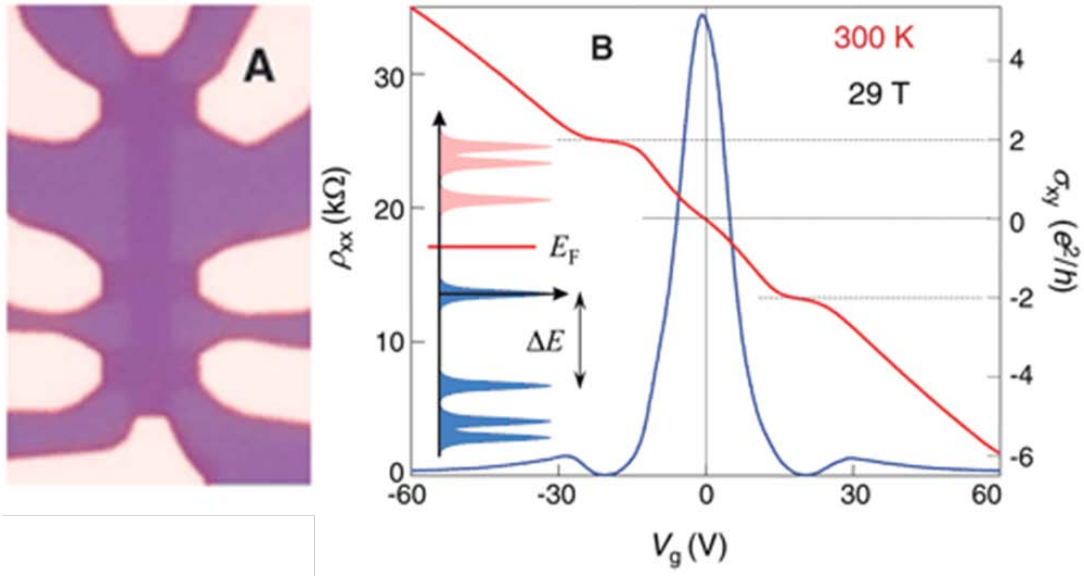

Figure 1-13 (a) Optical micrograph of the graphene device used for hall measurements, (b) σ_{xy} (Red curve) and ρ_{xx} (Blue curve) as a function of gate voltages (V_g) in a magnetic field of 29 T demonstrating the quantum hall effect in graphene. [Figure adapted from Novoselov, K. S. *et al*, "*Room-temperature quantum hall effect in graphene.*", *Science* 315, 5817-5818 (2007)]

Further, graphene offers the avenue for bandgap generation via breaking of symmetry states in electrically gated bilayer graphene or via quantum confinement (lateral / 2D) in nanoribbons of graphene [80-82]. In-line with the theoretical predictions, *Zhang et al* [80] have unambiguously shown the successful generation of a widely tunable bandgap in AB

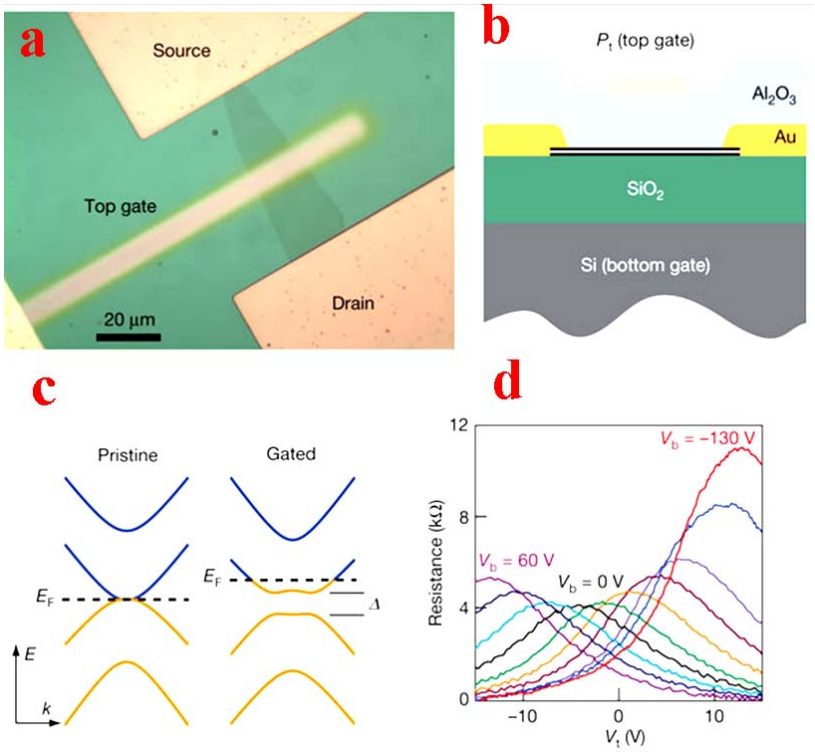

Figure 1-14 (a, b) Optical image and schematic diagram of the bilayer graphene device with the dual gate stacks, (c) Schematic diagram of generation of the electrical displacement fields generated upon gating, (d) Shift in the Fermi energies and the generation of the non-zero band-gaps in the device via the displacement fields [images adapted from Zhang, Y. *et al,* "*Direct observation of a widely tunable bandgap in bilayer graphene.*", *Nature* 459, 820-823 (2009)]

stacked bilayer graphene as high as ~ 250 meV (Figure 1.14). In the electronic structure of bilayer graphene, where the lowest conduction band of the two nearly parallel conduction bands touches the highest valence band of the two nearly parallel valence bands, application of electrical gating produces a shift in Fermi energy depending on $\delta D = D_b - D_t$, where D_b is the bottom displacement field and D_t is the top displacement field. The average displacement field, $\bar{D} = \frac{D_t + D_b}{2}$, breaks the inversion symmetry resulting in the generation of a non-zero bandgap depending on $\bar{D}$ when δD is zero for charge neutrality conditions [80].

Graphene nanoribbons (GNRs), on the other hand, display a measurable bandgap owing to lateral quantum confinement of charge carriers or due to the staggered sub-lattice potential from spin-ordered states at the edges (Figure 1.15) [59, 83-94]. While the former is the cause of

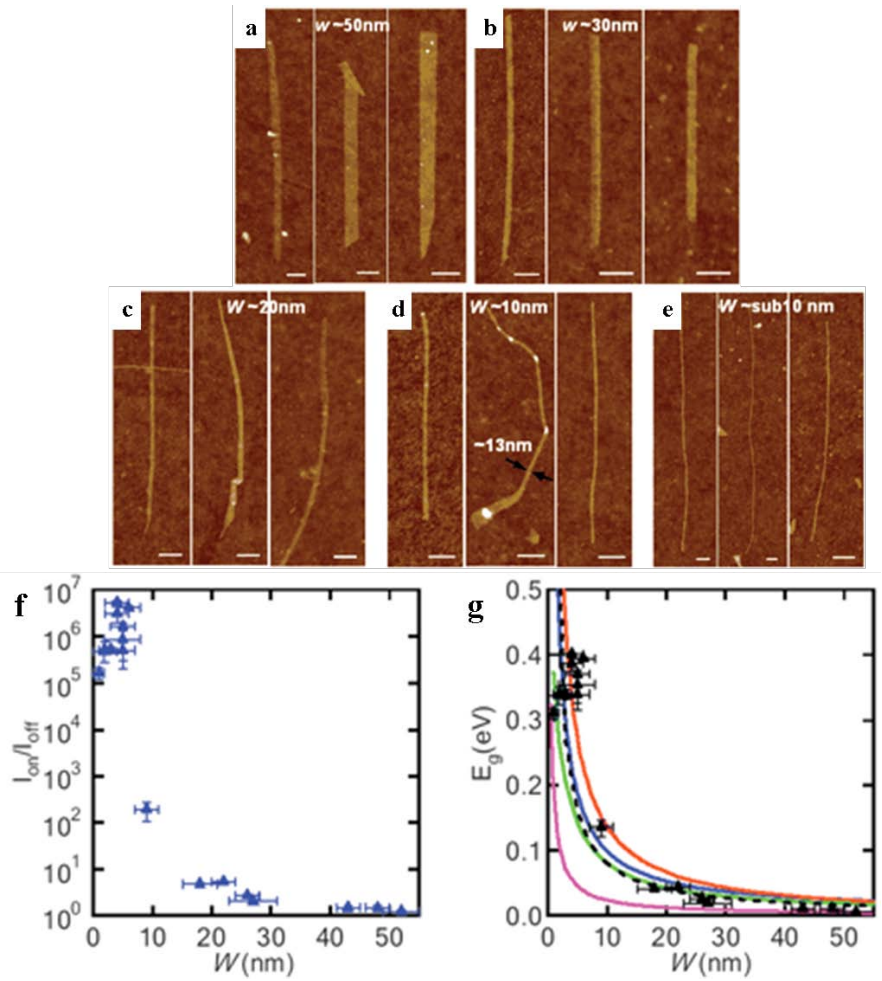

Figure 1-15 (a-e) AFM images of Graphene nanoribbons (GNRs) deposited on 300 nm thick silicon dioxide substrates, (f, g) Typical On-F ratios and bandgaps for the GNR-FETs for various ribbon widths demonstrating the excellent applicability of GNRs for applications demanding a measurable bandgap such as Logic [images adapted from *Li, X. et al,* "*Chemically derived, ultrasmooth graphene nanoribbon semiconductors.*", *Science* 319, 1229-1232 (2008)]

bandgap generation in the ideal *arm-chair* edged GNRs, the latter is the cause in ideal *zig-zag* GNRs. For the practical GNRs with mixed edges, a combination of the both effects results in the

generation of the bandgap with one more dominant than the other [47, 90]. Even though the symmetry breaking strategy also produces a measurable bandgap, the challenges associated with forming an exact bilayer and the high voltages involved for symmetry breaking (~ 100 V) make GNRs an attractive route to generate a bandgap. The potential applicability of the GNRs in the traditional CMOS circuits has in fact been recognized by the International Technology Roadmap for Semiconductors (ITRS) in its emerging electronic materials roadmap [95]. Several strategies have been reported for the synthesis of the GNRs such as chemical top-down methods [59], lithographic methods [83, 90, 96-98], CVD synthesis [99], CNT unzipping strategies [93, 94, 100, 101], chemical bottom-up methods [102] and the recent sublimation of Si on SiC steps [103]. However, in most methods it is difficult to control the width and the edge crystallography hence enabling a low degree of control on the GNR bandgap. In this thesis, a novel high throughput strategy for synthesizing GNRs with controlled width and smooth edges is presented via nanotomy (nanoscale cutting) of commercially available highly oriented pyrolytic graphite (HOPG) blocks using a ultra-sharp diamond knife (Chapter 6). The as-produced GNRs were characterized in detail for elucidating their structural, chemical, electrical and optical properties.

Mechanical properties

Graphene has been shown to be one of the strongest materials found in the universe with a Young's modulus of E ~ 1 TPa for a defect free sheet (Table 1.1 shows the typical values of Young's modulus for various materials.) [14].

Table 1-1 Young's moduli for various materials [taken from Wikipedia page on Young's modulus]

Sl. No.	Material	Young's modulus (in GPa)
1	Rubber	0.01-0.1
2	Teflon	0.5
3	Polystyrene	3-3.5
4	Aluminum	69
5	Glass	50-90
6	Kevlar	70.5-112.4
7	Titanium alloys	105-120
8	Silicon	185
9	Steel	200
10	Silicon carbide	450
11	CNTs	1000
12	Diamond	1220
13	**Graphene**	**1000**

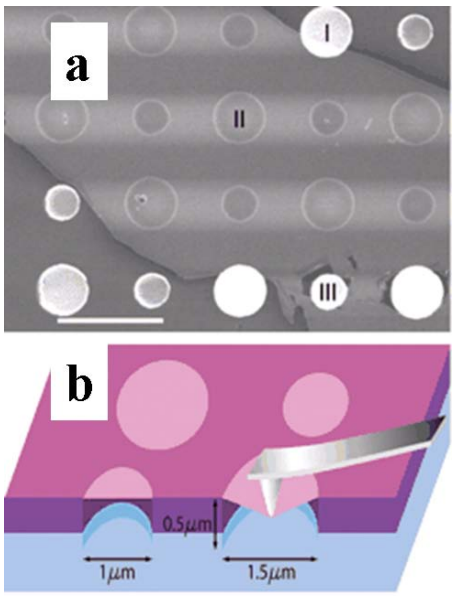

Figure 1-16 (a) SEM image of graphene spanning an array of circular holes for nano-mechanical indentation experiments (scale bar is 3 μm), (b) Schematic diagram showing the nano-indentation experiments using an AFM cantilever on the graphene membranes shown in (a) for determination of the mechanical properties. [both images adapted from Lee, C. *et al*, "*Measurement of the elastic properties and intrinsic strength of monolayer graphene.*", *Science* 321, 385-388 (2008)]

Nano-indentation studies on suspended defect-free graphene sheets (produced via micro-mechanical exfoliation) have used the model given by equation 1.7,

$$\sigma_m^{2D} = \left(\frac{FE^{2D}}{4\pi R} \right)^{\frac{1}{2}} \quad \ldots(1.7),$$

where σ_m^{2D} is the maximum stress at the central point of graphene; R is the indenter tip radii; $F = \sigma_0^{2D}(\pi a)\left(\frac{\delta}{a}\right) + E^{2D}(q^3 a)\left(\frac{\delta}{a}\right)^3$; E is the Young's modulus ; a is radius of graphene membrane; δ is the deflection at center point; σ_0^{2D} is membrane pre-tension; q is given by q = 1/(1.049-0.15γ-0.16 γ^2) with the Poisson's ratio γ being 0.165 [14]. They demonstrated that the intrinsic breaking strength of graphene is ~ 125 GPa (compared to 1.86 GPa for steel and 2.8 GPa for diamond) [14] (Figure 1.16). In spite of these high values of the elastic constants, for

macroscale graphene, the mechanical strength is expected to be severely limited by the presence of a multitude of defects and grain boundaries [14, 47, 104-107].

Another interesting mechanical property of graphene is its atomic impermeability to standard gases including helium [15]. The closely packed honeycomb lattice of carbon atoms in graphene leaves extremely small interstitial space making it an ultimate membrane (1 atom thick). In addition to experimentally demonstrating the impermeability of graphene, *Bunch et al* have shown that graphene membranes can sustain pressure differences of > 1 atm [15]. For a graphene-sealed-microchamber as shown in Figure 1.17, in presence of a pressure difference of ~ 0.92 atm, the surface tension of the graphene membrane as determined from the Young – Laplace equation, $S_{Graphene} = \left(\frac{\Delta P \times R_X \times R_Y}{R_X + R_Y} \right)$, where R_X and R_Y are the radii of curvature in the X or Y direction respectively, was found to be 1 N/m, which is 14 times that of water [15].

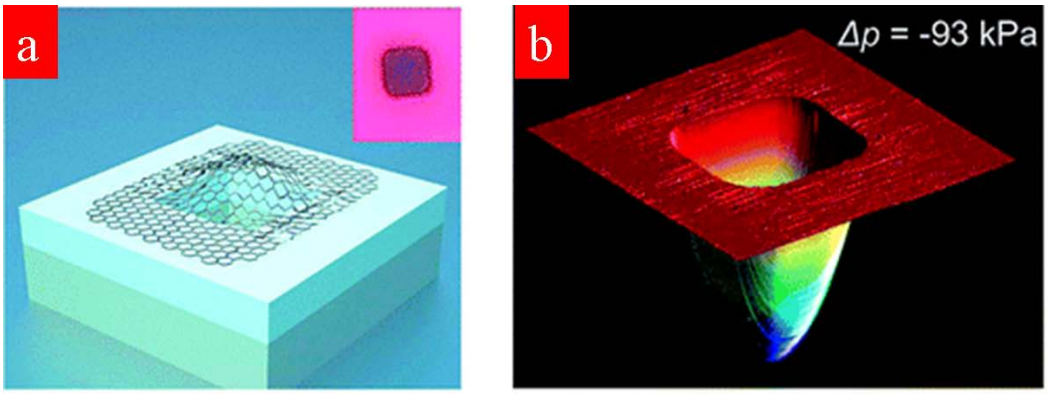

Figure 1-17 (a) Schematic diagram of the device structure used by *Bunch et al* to study the impermeability of graphene membranes, (b) AFM image of the membrane under 0.92 atm pressure difference showing the graphene nano-balloon. [image adapted from Bunch, J. S. *et al*, "*Impermeable atomic membranes from graphene sheets.*", *Nano Lett.* 8, 2458-2462 (2008)]

However, this corresponds to ~ 0.26 % strain on graphene which suggests the potential of graphene to withstand much higher pressure gradients [15]. In this thesis, this facet of graphene has been employed and impermeable encasements for wet bacterial cells have been fabricated to facilitate facile native state TEM and FESEM imaging in UHV (Chapter 3).

Optical properties

The high-frequency conductivity G for Dirac fermions in graphene is an universal constant, G = $\frac{e^2}{4\hbar}$, [16, 108-110], leading to very interesting optical properties. The optical transmittance and the reflectance of graphene are universal constants for normal incidence,

$$\text{Transmittance, } T = \frac{1}{\left(1+\frac{2\pi G}{c}\right)^2} \text{ ;}$$

$$\text{Reflectance, } R = \frac{1}{4}\pi^2\alpha^2 T \text{ , where } \alpha = \frac{e^2}{\hbar c} \text{ ;}$$

$$\text{Opacity, O = 1-T…(1.8),}$$

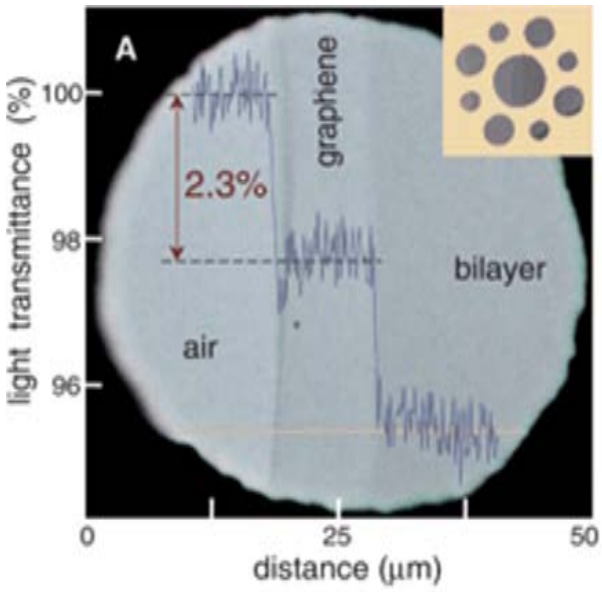

Figure 1-18 Optical micrographs showing a 50 micron aperture covered by graphene and its bilayer. Line scan profiles show the intensity of transmitted light along the yellow line embedded in the figure: Single layer graphene displays ~ 97 % transmittance and the bilayer ~ 95 % transmittance. [Image adapted from Nair, R. R. *et al,* "*Fine structure constant defines visual transparency of graphene*.", *Science* 320, 1308-1309 (2008)]

As can be observed from the equation 1.8, the expressions do not involve any material parameters and hence are a consequence of the intrinsic properties of graphene. Figure 1.18 shows the transmittance profile on a monolayer and bilayer graphene placed on a 50 micron aperture. Very high transmittance for visible light has been observed (~ 97 % for monolayer and

~ 95 % for bilayer graphene), whose magnitude linearly decreases upon increase in the number of layers [16]. This high transparency coupled with the excellent electrical conductivity of graphene, makes it an excellent candidate for transparent electrodes [67, 111-123]. Further, the transmittance in graphene can be tuned via the gate potential mediated Fermi level shifts resulting in significant shifts in the charge density [91, 124, 125]. Ultrafast (~ 40 GHz) and highly efficient (6-16 % internal quantum efficiency) photo-response times have been observed in graphene FETs, attributed to the ballistic carrier mobilities [124]. This has applications for high speed optoelectronic devices.

Another interesting optical property of graphene is the quantum confinement and edge effect mediated emergence of photoluminescence [126-134]. Unlike their 2D graphene counterpart, 1 dimensional graphene quantum dots (GQDs), *nano-sheets of graphene with dimensions less than 100 nm*, display strong luminescence owing to the prominent effects of the quantum confinement and the edge terminations [134]. Both theoretical and experimental studies have demonstrated the emergence of unique UV-Vis absorption bands and photoluminescence emission spectra for the GQDs depending on their dimensions and edge crystallographic structure [126-142]. Figure 1.19 shows the photoluminescence emission from the GQDs dispersed in water.

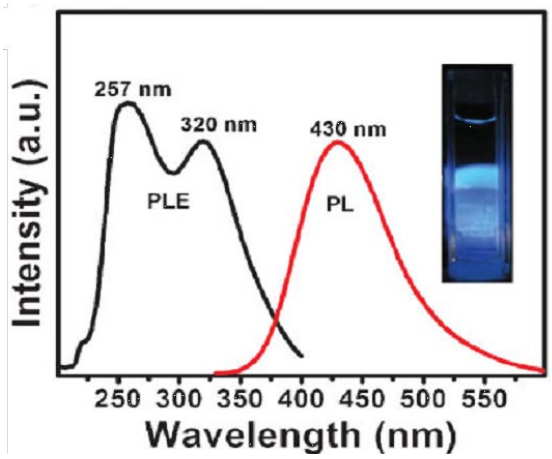

Figure 1-19 Photoluminescence spectra for the GQDs dispersed in water showing the excitation spectra (black curve) for emission at 430 nm and the emission spectra (red curve) for excitation at 257 nm. Inset shows the optical image of the vial under UV light showing blue luminescence. [Image adapted from Pan, D. *et al,* "*Hydrothermal route for cutting graphene sheets into blue-luminescent graphene quantum dots*.", *Adv. Mater.* 22, 734-738 (2010)]

Several strategies have been proposed for synthesizing GQDs such as sonochemical methods[133, 143], lithographic methods[132], chemical bottom-up strategies[126, 127] and the recent opening of fullerene molecules[138]. However, it is still challenging to control the dimensions and edge terminations while producing GQDs at large scale. In this thesis a novel high throughput strategy for synthesizing GQDs has been presented via two step nano-scale cutting of HOPG using an ultrasharp diamond knife mounted on an ultramicrotome (Chapter 7). In addition to sensitive dimensional control, the successful production of various shapes of GQDs (squares, rectangles, triangles and trapezoids) with smooth edge lattice terminations has been demonstrated.

Chapter 2 - Chemically modified graphene for bio/chemo-interfacing in bio-devices and DNA-sensors

Abstract

Establishing "*large-contact-area*" interfaces of sensitive nanostructures with microbes and mammalian cells will lead to the development of valuable tools and devices for biodiagnostics and biomedicine. Chemically modified graphene (CMG) nanostructures with their micro-scale area, sensitive electrical properties, and modifiable chemical functionality are excellent candidates for such bio-devices at both bio-cellular and bio-molecular scale. Here, we report on the fabrication and functioning of a novel CMG-based (i) single-bacterium bio-device, (ii) label-free DNA sensor, and (iii) bacterial DNA/protein and polyelectrolyte chemical transistor. The bacteria bio-device was highly sensitive with a single-bacterium attachment generating 1400 charge carriers in a p-type CMG. Similarly, single-stranded DNA tethered on graphene hybridizes with its complementary DNA strand to reversibly increase the hole density by 5.61×10^{12} cm^{-2}. We further demonstrate (a) a control on the device sensitivity by manipulating surface groups, (b) switching of polarity specificity by changing surface polarity, and (c) a preferential attachment of DNA on thicker CMG surfaces and sharp CMG wrinkles.

Published as

Mohanty, N., Berry, V., "Graphene-based single-bacterium resolution biodevice and DNA transistor: Interfacing graphene derivatives with nanoscale and microscale biocomponents." *Nano Letters* **8** 4469-4476 (2008)

Introduction

In the past decade, there have been a plethora of studies on building nano/bio interfaces with electrically, optically and thermally active nanoscale materials, which have tremendously advanced the fields of biomedicine, [1] bioactuated devices, [2, 3] biodetection, [4-6] and diagnostics [7, 8]. The current generation of electrically active nano/bio devices built using zero-dimensional (0D) nanoparticles, [8, 9] one-dimensional (1D) nanowires, [4, 10, 11] and two-dimensional networks [12] have shown excellent detection and interfacing ability for both molecular (DNA, ATP, proteins, etc.) and nanoscale (viruses etc.) biocomponents. However, the incompatibility in areal dimensions makes it challenging to apply individual 0D and 1D nanostructures for building strong interfaces with larger-sized microorganisms or for retaining them on their networks [12]. Chemically modified graphenes (CMGs), with their two-dimensional nanostructures and adjustable surface chemistry, can interface strongly with the biological systems without geometric restrictions and without compromising the integrity of the microbial attachment.

Recently, chemical [13-17] and geometric [15, 18-20] manipulation of graphene has shown great potential to control its band gap between semimetallic and semiconducting. Furthermore, with its low electrical noise (and low charge-scattering) [21-23] and ballistic transport, [22, 24] graphene nanostructures have been incorporated into various electronic and optoelectronic applications [25] such as gas sensor, [26] transistors, [27, 28] solar cells, [29-32] and liquid-crystal elements [33]. However, there has been no report on application of graphene in biological devices. Here, we demonstrate the interfacing of CMGs with biological systems to build a novel live-bacterial-hybrid device and a DNA-hybridization device with excellent sensitivity. We illustrate two crucial characteristics of the CMGs which make them promising building blocks for biodevices. First, via chemical modification and subsequent integration of CMGs with corresponding biocomponents, various functional biohybrids can be developed. Further, with their relatively large area, CMGs can be strongly interfaced with microscale biocomponents. This versatile bonding compatibility of the CMGs is demonstrated here by their ability to (a) attach with microscale bacterial cells, (b) tether and hybridize DNA molecules on their surface, and (c) bind with polyelectrolytes and proteins. Second, the CMGs are semiconducting nanosheets and thus undergo a highly sensitive charge-carrier modulation upon their interaction with various biological species. This is attributed to CMGs' p-type

characteristics and their subnanoscale thickness, where external interactions from tiny entities can produce an extraordinary response. Furthermore, CMG devices are polarity-specific with a high resolution. This is shown here for (i) attachment of a single bacterium on graphene-amine (GA), which generated 1400 conducting holes and (ii) generation of (on an average) a single quantum of hole by hybridization of approximately six complementary DNA (*cDNA*) strands on a graphene−DNA (*G-DNA*) device. Also, attachment of approximately four monomers (average) of positively charged polyallylamine hydrochloride (PAH) on the p-type graphene oxide (GO) reduced the number of holes by one quanta; while a further attachment of negatively charged polystyrene sulfonate (PSS) monolayer increased the hole density by 1.42×10^{13} cm^{-2}. We also show that the DNA tethering process on the CMGs was preferential (a) on thicker than on thinner CMGs and (b) on wrinkles than on flat surfaces of CMGs. These results show that with their modifiable chemistry and sensitive electronics, CMGs can be custom-designed and integrated with various biochemical systems to develop next-generation applications and tools such as (i) biobatteries, where electrically conducting graphene could be interfaced with Geobacter, a bacteria known to produce electrons on the cell wall, (ii) bioprocess analysis tools, where the cell's selective metabolism of nutrient molecules (like lysine) can be studied by measuring the H^+-potential produced on the cell wall during the ATP cycle, (iii) graphene genetic devices for pathogen identification, (iii) CMG-CMG ultrathin pn-junction solar cells, (iv) bioelectronic devices, (v) smart circuits, and (vi) molecular transistors.

Experimental Methods

In this study, the CMGs and their bio-hybrids were synthesized using GO or plasma-modified GA (PGA) or Graphene amine (GA) immobilized on silica substrate.

Preparation of Graphene Oxide (GO)

GO sheets dispersed in aqueous media were synthesized from graphite flakes (mesh 7) by the modified Hummers method [13, 25, 34]. About 7 grams of mesh 7 graphite flakes (Cat # 332461, Sigma Aldrich Inc.) were suspended in a mixture of 200 ml of 96 % sulfuric acid and 33 ml of 68 % nitric acid in a 4 °C water bath and stirred for about 30-45 minutes. Then 30 g of potassium permanganate was added slowly onto the mixture while maintaining the temperature of the mixture at 4 °C with constant agitation. Subsequently the temperature of the mixture was raised to 40 °C (with a ramp of 1 °C per minute) and held constant for 6 hours. The mixture was

then cooled down to 4 °C in an ice bath and 30 % H_2O_2 (in DI water) was added slowly drop-by-drop with adequate mixing to neutralize the excess potassium permanganate. Upon cessation of the reaction, the resulting GO solution was left undisturbed overnight, after which the GO sheets were spun down (11,000g, 60 min, 300 K), washed with DI water followed by HCl and then again by water. The washing step was repeated at least 2 more times after which the aqueous suspension of GO was dialyzed in copious amounts of DI water for a week.

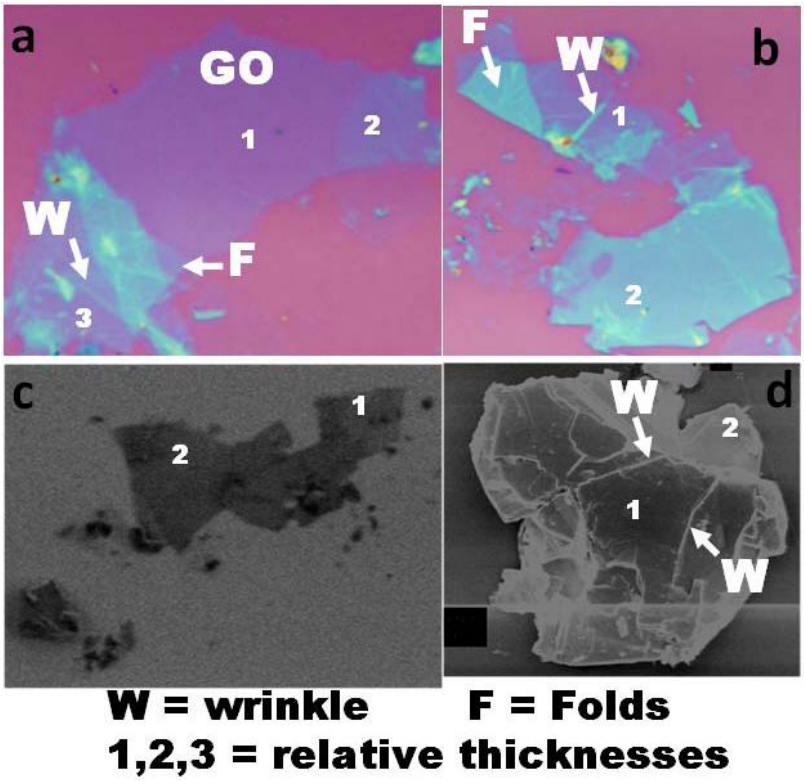

Figure 2-1 (a,b) Optical images of graphene-oxide (GO) deposited on 300 nm thick Silica substrate. On 300 nm thick silica, the graphene nanostructures appear clearly. (c,d) FE-SEM images of GO deposited on 300nm thick silica substrate. Here 1, 2 and 3 represent the relative thickness of GO sheets, F represents the folds and W represents the wrinkles.

This process functionalizes the surface of the GO sheets with epoxy, hydroxyl, and negatively charged carboxylic acid groups [17]. Energy dispersive X-ray spectroscopy of the samples detected the presence of oxygen. The GO was immobilized on heavily doped n-type silicon substrate with a 300 nm [35] or 1 μm thick thermally grown silica layer, patterned with predeposited or postdeposited gold electrodes (300 nm thick and 5 μm apart). The patterned

substrate was first exposed to oxygen plasma (100 W, 2 mbar, 2 min) and subsequently functionalized with a monolayer of (3-aminopropyl)triethoxysilane to make the silica surface positively charged with tethered amine groups. This substrate was then immersed in the GO solution for 10 min to electrostatically deposit GO sheets on silica (Figure 2.1). The deposited GO sheets remained intact after thorough washing with deionized (DI) water, indicating their strong and multipoint electrostatic attachment with the substrate.

Preparation of Plasma Graphene Amine (PGA)

In order to introduce primary amine groups onto the graphene surface, 1 gram of the graphite flakes were treated with nitrogen plasma (4:1 mixture of He and N_2 , 100 W, 2 mbar, 100 min) or ammonia (100 W, 2 mbar, 100 min) and subsequently suspended in DI water. The plasma modified graphene sheets were cleaved and separated via ultrasonication in DI water for 5 minutes. The aqueous suspension was then stored at room temperature. Thus produced graphene derivative was called plasma graphene amine (PGA). The successful conjugation of the fluorescein isothiocyanate (FITC) dye with the PGA deposited on a gold chip validated the presence of primary amine groups on graphene (Figure 2.2). Plasma graphene amine was also prepared from the GO sheets by initially reducing them with a hydrogen plasma (100 W, 2 mbar, 6 seconds) and then treating them with a nitrogen plasma (4:1 mixture of He and N_2 , 100 W, 2 mbar, 5 min) or an ammonia plasma (100 W, 2 mbar, 5 min).

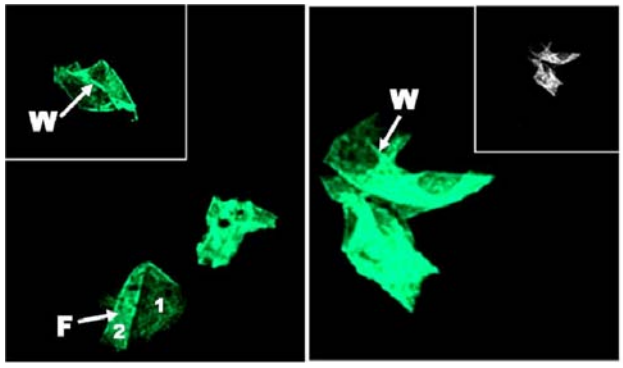

Figure 2-2 Confocal microscope images of PGA-FITC conjugate showing the folds on PGA. This also shows the efficacy of the PGA preparation method. Here 1, 2 and 3 represent the relative thickness of PGA sheets, F represents the folds and W represents the wrinkles.

Preparation of Graphene Amine (GA)

The previously prepared graphene oxide coated chip was treated with a mixture of 20 ml of 99% valeric acid, mixed with 5 milligrams of HATU for 8 hours, and then washed for 30 minutes with methanol. This led to capping of the positively charged aminated silica with a 5 carbon-long valeric acid chain thus making the silica surface hydrophobic. Subsequently, the chip was incubated with 20 ml ethylenediamine with 5 mg 2-(7-aza-1H-benzotriazole-1-yl)-1,1,3,3-tetramethyluronium hexafluorophosphate (HATU) (in an incubator-shaker), at room temperature for 8 hours. The chip was then washed with methanol for 30 minutes, followed by washing with DI water and finally drying with nitrogen. This produced positively charged graphene amine (GA) with hydrophobic and neutral silica substrate around it.

Preparation of Bacteria

25 ml of LB media was inoculated with *Bacillus cereus* cells and cultured for 14 hours. The *Bacillus cereus* cells were then pelleted by centrifugation at 2000 rpm (400 g) in a microcentrifuge for 5 minutes, followed by repeated (5 times) washing by re-suspending the cells in DI water and centrifuging. Finally, the negatively charged bacterial cells were suspended in 500 µl of DI water.

Preparation of GA-bacteria ensemble

The previously prepared GA chips were immediately immersed in this suspension for 10 minutes and then washed gently with DI water for 10 seconds and dried. This produced selective deposition of bacterial cells on the surface of the positively charged GA.

Live-Dead test on bacteria

LIVE/DEAD-confocal-test was conducted to determine if the bacteria were dead or alive. In this process, the bacteria were stained with Syto-9 + PI and observed under a confocal microscope. The live bacteria appear green in color due to Syto-9 staining and the dead bacteria appear red in color due to PI staining. The bacteria were found to remain alive after their electrostatic deposition onto GA, as has been previously reported in the literature. Further, the LIVE/DEAD test was also conducted on bacteria after electrical measurements on CMG-gold-bacteria device. The bacterial cells atop silica were found to be alive after the application of an average of 4V (DC) for 1.6 seconds, while the cells atop gold electrodes died (Figure 2.3). This

magnitude and the duration of the voltage are the typical values used for the IV-measurements on the devices.

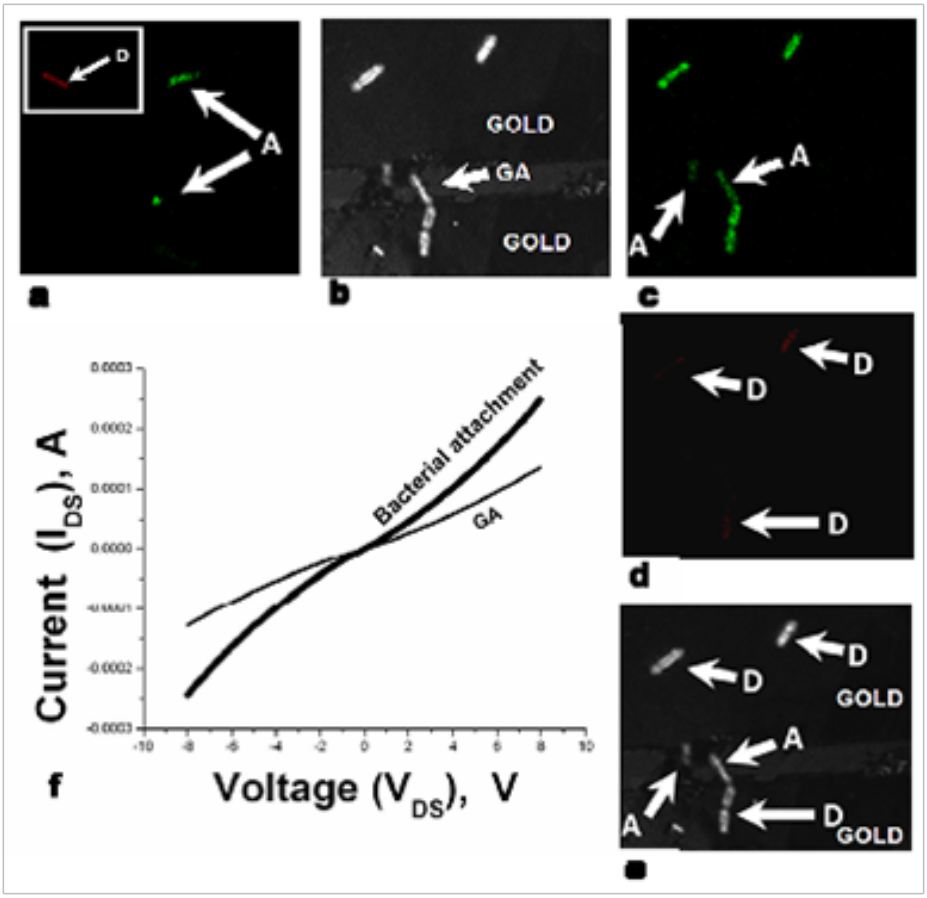

Figure 2-3 (a) LIVE/DEAD test with confocal images after Syto-9 and PI stained bacteria after their electrostatic deposition onto GA. The confocal image indicates that most of the bacteria are live (A); while there are some dead cells (D) as well. (b, c, d) Optical and confocal images of Syto-9+PI stained bacteria on GA after conducting the electrical measurements. The images indicate that the bacteria atop GA remains alive after the electrical measurements; whereas the bacteria atop gold electrodes died. (e) The duplicated optical image of (b) indicating all the live and dead bacteria marked up as A and D respectively. (f) Electrical measurements on the GA-bacteria ensemble shown in (b, c, d) illustrating an increase in the conductivity of GA after the bacterial deposition.

Preparation of GO-bacteria ensembles via Concanavalin-A tethers

Concanavalin - A protein conjugated with FITC was tethered onto GO. Upon immersion in the bacterial solution, the bacterial deposition on this hybrid was found to be highly-selective and of high affinity. This high selectivity and affinity is attributed to the strong concanavalin–A/teichoic acid interaction. These large numbers of bacteria were stained with Syto-9 to confirm their attachment on the concanavalin-GO-hybrid under confocal-microscope (Figure 2.4).

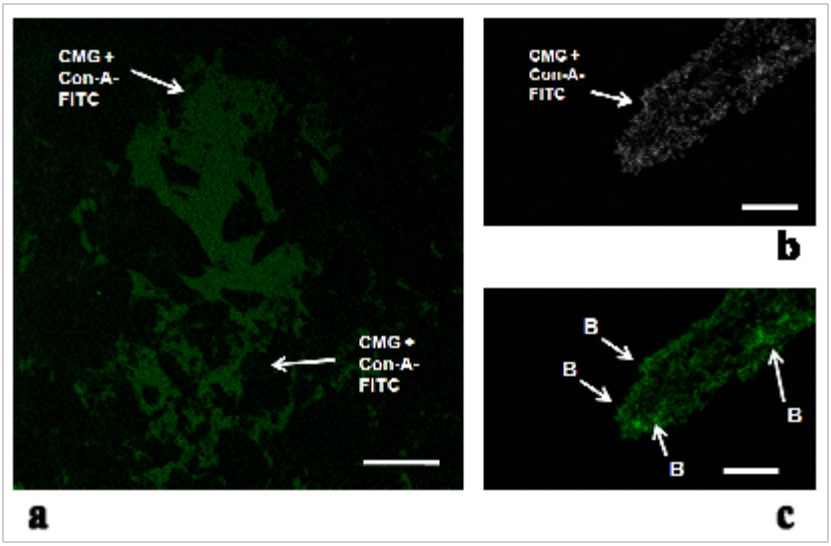

Figure 2-4 (a) Confocal images confirming the successful tethering of the FITC-conjugated-Concanavalin-A on CMG. (b, c) Optical and the confocal images of the Syto-9 stained bacteria (B) attached on the FITC-Concanavalin-A-CMG conjugate. Scale bar = 30 microns

Preparation of Protein/Bacteria ensemble on GA

After 14 hours of culture in 25ml of nutrient broth media, the *Bacillus cereus* cells were partly lysed and pelleted by centrifuging at 13000 rpm in a microcentrifuge for 2 minutes and the pellet dissolved in 500 µl of DI water. The GA chips were immersed in this soup for 10 minutes and then washed gently with DI water for 10 seconds and dried.

Results and Discussion

Figure 2.5 shows the atomic force microscope (AFM) images of the GO sheets. The thickness of most GO sheets varied from 1 to 5 nm. The GO sheet scanned in Figure 2.5a had a thickness of 2 nm (Figure 2.5a (top inset)), which corresponds to an approximately four atom thick layer of GO. This small thickness of GO confirms the effectiveness of the Hummer's method to cleave ultrathin graphene sheets and functionalizing them with negative charge [13]. GO's surface scanned by the AFM and imaged by optical microscopy revealed the presence of sharp wrinkles (Figure 2.5a bottom inset), which were 6−8 nm in height, 30−50 nm in width, and several micrometers long (Figure 2.5a, top right inset). The lack of directional preference of these wrinkles indicated that they were entropically formed [36, 37].

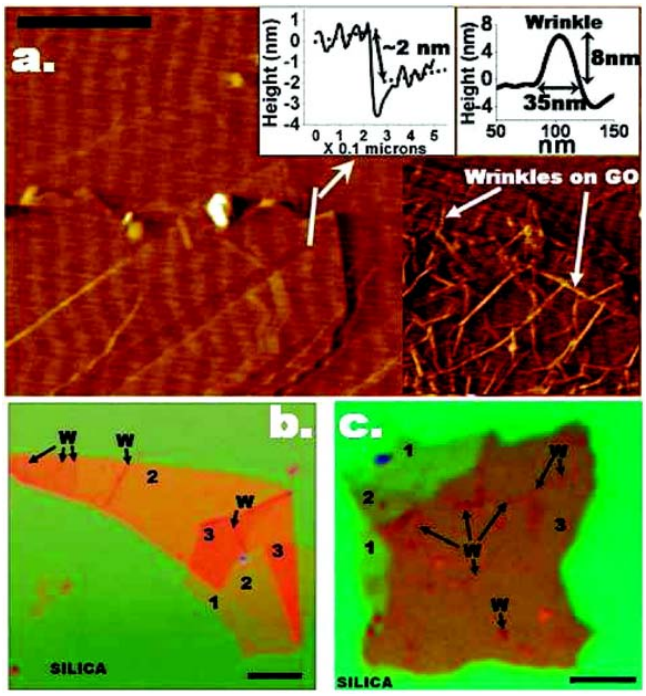

Figure 2-5 (a) AFM image (3.1 × 1.9μm2) of GO sheets deposited on silica substrate. Top left inset shows the thickness of a GO sheet to be 2 nm (approximately four atoms thick). Bottom inset shows an AFM image showing the several wrinkles on the GO's surface. Top right inset shows the height and width of a typical wrinkle on GO. (b, c) Optical microscope images (inverted colors) of GO on 300 nm silica substrate are shown. Here 1, 2, and 3 represent the relative thickness of GO sheets and W represents the wrinkles. Bar size = 5 μm.

Further, these long wrinkles were observed in a greater quantity on larger GO sheets (>20 μm) than on the smaller ones (<510 μm) and more at the center than on the edges. These results indicate that the wrinkle formation was a result of multiple-point electrostatic anchoring of GO sheets, producing wrinkles in the middle. The AFM and the optical microscopy images also showed the presence of folds and multilevel layering of sheets (Figure 2.5b). In Figure 2.5b we have marked the regions of different relative thicknesses (not the number of layers) of GO sheets, thus illustrating the multilevel structure of GO. PGA was synthesized either by exposing the graphite flakes to ammonia (or nitrogen plasma) followed by exfoliation via sonication in water or by exposing the GO sheets immobilized on a silica substrate to hydrogen plasma followed by ammonia (or nitrogen) plasma.

The GO sheets immobilized on silica were used as templates to selectively and covalently tether single-stranded DNA to build the G-DNA hybrid. The GO–silica substrate was immersed in a solution mixture of 5′-pentamine-terminated DNA with 20 bases (amine-AAC TGC CAG CCT AAG TCC AA) and O-(7-azabenzotriazole-1-yl)-N,N,N,N′-tetramethyluronium hexafluorophosphate (HATU) (an amide-coupling reagent), at room temperature for 8 h in an incubator. Since this DNA's terminal amine group bonds covalently with the carboxylic group on GO and not with the amine groups on silica, the reaction resulted in selective DNA tethering on the GO sheets. The physically adsorbed DNA molecules were removed by a 1% sodium dodecyl sulfate (SDS) wash for 30 min. The tethering of this target DNA was verified by hybridizing it with a fluorescent cDNA probe (dye-TTG GAC TTA GGC TGG CAG TT) terminated with 3′-rhodamine green dye (522 nm emission). The hybridization process was conducted by placing a drop of the probe DNA on the G-DNA substrate followed by incubation at room temperature for 4 h. The nonspecifically bound DNA was removed by a 30 min wash with 1% SDS solution.

Under a confocal microscope, fluorescence at 522 nm confirmed the successful synthesis of G-DNA hybrids (Figure 2.6, panels a and b) with DNA tethered on its surface. The confocal images (Figure 2.6, panels a and b) further show that the DNA preferentially tethers on thicker layers (including folds) and on wrinkles of GO as depicted by a higher fluorescence intensity in these regions. This was verified by the z-stack images from the confocal microscope. The insets of panels a and b of Figure 2.6 show the optical image of the corresponding G-DNA. Since the dye molecules are at least 7.2 nm (20 base DNA + seven-carbon chain) from the GA surface, the

observed florescence contrast is not due to quenching, [38] electromagnetic enhancement,[38] or background overlapping. The bottom-left inset of Figure 2.6a shows the effect of GO thickness on the relative fluorescence intensity and thus the DNA density. This contrast in DNA density can be attributed to dissimilar surface potential at different layer thicknesses caused by a difference in the magnitude of intrinsic screening of the interfacial traps or defects on silica surface [39]. This causes a higher surface potential on thicker surfaces, which in turn lead to more favorable DNA binding. This variable surface potential for different thicknesses has been shown for pristine graphene [39]. Similarly, the higher DNA density on the surface wrinkles can be attributed to the local field enhancement at the sharp edges of the wrinkles [40, 41]. Furthermore, the absence of enhanced fluorescence at the G-DNA edges indicates that, for a particular GO thickness, the carboxylic acid groups are uniformly distributed [42] on GO surface with no selectivity for the edge, contrary to the earlier report [17, 43]. Similar uniform functionalization of carboxylic group has been reported for carbon nanotubes [44, 45]. Two control experiments by omitting (a) the probe-DNA attachment step and (b) the target-DNA attachment step showed no fluorescence under confocal microscope, thus validating the results (Figure 2.6, panels c and d). Omitting HATU-reagent from the process led to a sharp decrease in the florescence intensity on G-DNA, indicating that the presence of HATU is crucial for stronger DNA binding.

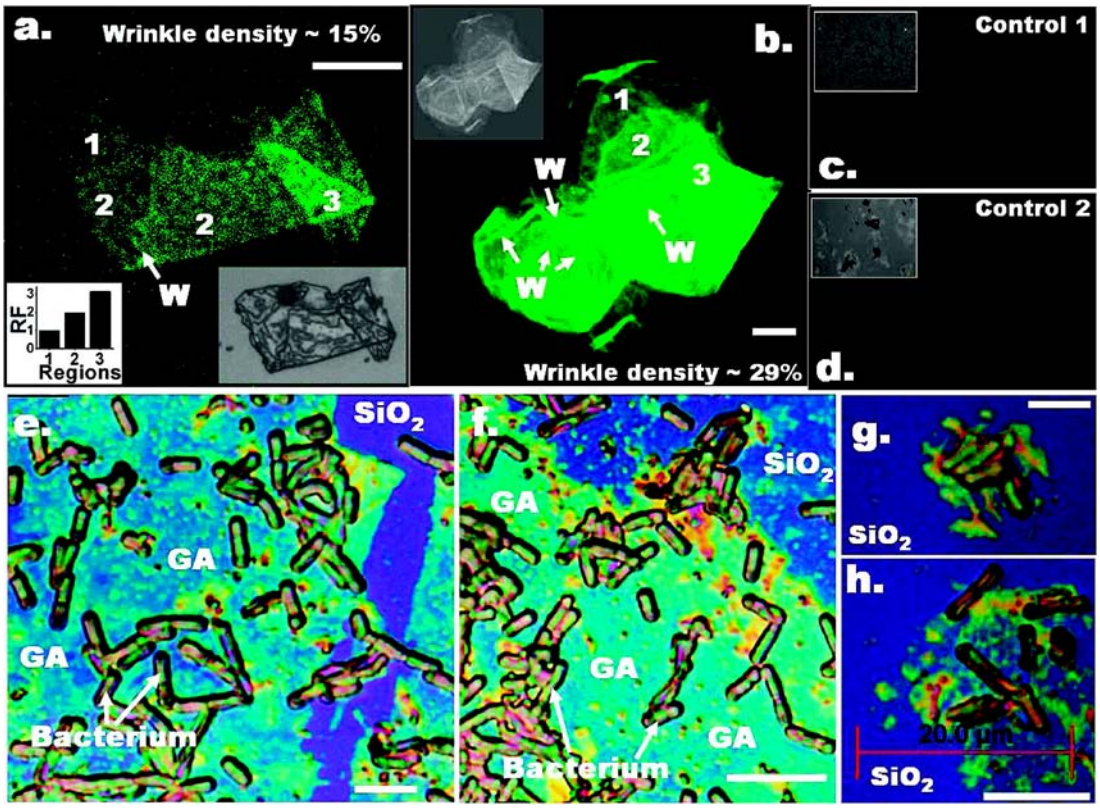

Figure 2-6 (a, b) Confocal images showing florescent-labeled probe-DNA hybridized on the target-DNA covalently attached on GO sheets. The folds and wrinkles on G-DNA sheets are easily visible via florescence-contrast. 1, 2, and 3 represent the relative thickness of G-DNA sheets and W represents wrinkles (confirmed by *z*-stack). The bottom-right inset of (a) and the top inset of (b) show the optical images of the corresponding G-DNA sheets; while the bottom-left inset of (a) shows the relative intensities in regions 1, 2, and 3 of (a). (c) and (d) Control-confocal images for no probe-DNA and no target-DNA, respectively. (e) and (f) Microscope images showing selective attachment of bacterial cells on GA. (g) and (h) Selective deposition of bacteria on smaller GA sheets. Bar size = 10 µm.

The CMG/bacteria hybrid was built by selectively assembling microscale negatively charged bacterial cells on positively charged GA scaffolds synthesized by amination of the immobilized GO sheets on silica substrate. A high selectivity of bacterial assembly was achieved by making the silica substrate hydrophobic by treating it with valeric acid and HATU. This process tethers a five-carbon-chain molecule on silica. The GO to GA conversion was achieved by immersing the substrate in a solution mixture of ethylenediamine (EDA) and HATU for 8 h at

room temperature. In this reaction, one amine group of the EDA molecule bonds with the carboxylic groups on GO, while the other amine group remains unreacted on the surface, thus producing positively charged GA sheets surrounded by hydrophobic silica substrate (Figure 2.7a, bottom inset).

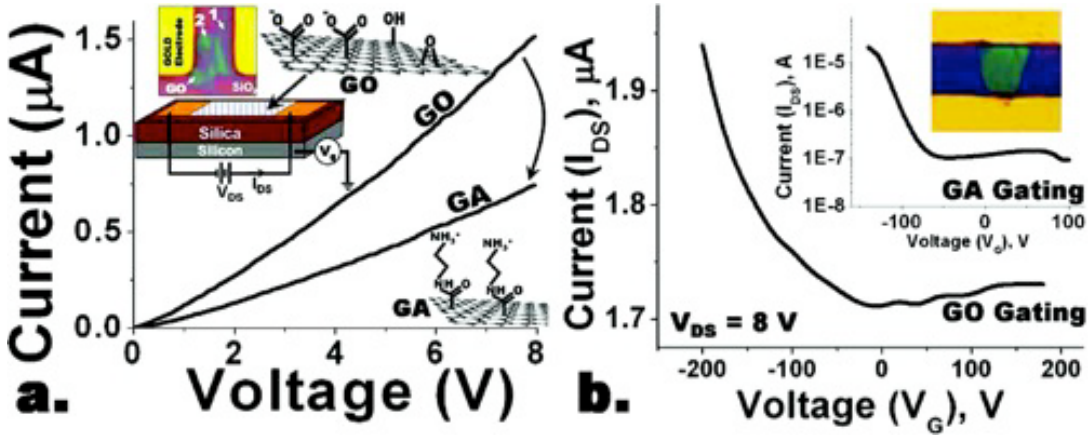

Figure 2-7 (a) Current−voltage behavior of the GO and GA devices. GA devices always show lower conductivity than their parent GO devices. The increase in conductivity with voltage is slightly nonlinear for both GO and GA devices. The insets show the device with GO/GA between gold electrodes and a schematic of the GO and GA's chemical structure. (b) Electrical gating of GO and GA shows that they are p-type semiconductors. The top inset shows the postdeposited gold electrodes on a GO sheet.

The Gram-positive *Bacillus cereus* cells were employed to fabricate the bacteria/CMG ensembles. These cells possess a highly negatively charged surface due to the polyteichoic acid molecules densely tethered on their cell wall [3, 46]. The Bacillus cereus cells were first cultured in LB media in an incubator shaker at 37 °C for 14 h (log phase). The cells were subsequently washed five times by centrifuging (2000 rpm (400g), 5 min) and resuspending in DI water. With a strong cell wall, these bacterial cells do not undergo lysis in DI water [2, 3, 46]. The previously prepared GA substrate was immediately immersed in the purified bacterial suspension for 5 min, followed by washing with DI water and drying in a jet of dry nitrogen. This led to electrostatic deposition of the bacterial cells on GA as shown in Figure 2.6, panels e and f. Further, the hydrophobicity of silica surface enhanced the selectivity of deposition (Figure 2.6, panels g and h) on GA. This indicates that the adhesion of bacteria on GA is not governed by the (sticky)

surface protein and is purely electrostatic. There were also no signs of bacterial lysis, with the cells retaining their integrity on GA. Further, to determine whether the bacteria deposited on GA were live, a LIVE/DEAD test was conducted by staining the bacteria on the samples with Syto-9 and PI for 1 min. Under confocal microscopy, the bacteria which were alive appear green in color (syto-9 staining) and the ones which were dead appear red in color (PI staining). It was confirmed that most of the cells on GA were alive (Figure 2.8a, inset 3) after their deposition, an observation similar to an earlier report [3]. The bacteria, however, die after about 4 h. The deposition of bacteria of all sizes (or life cycle stages) indicates that their negative charge polarity is not size dependent. No preferential deposition of these relatively large sized (4–5 μm) bacterial cells was observed with respect to the wrinkles or the edges of the GA sheets, indicating uniformity of the charge on GA at a larger scale. The deposited bacteria did not detach from the surface when washed with DI water at room temperature, thus illustrating the strong binding between bacteria and the CMG. However, rigorous washing with DI water at 80 °C did cause the bacteria to peel off. Further, to increase the affinity and specificity of bacterial attachment on CMG, GO was tethered with concanavalin, a biomolecule with highly specific affinity to the teichoic acid on the peptidoglycan membrane of the bacterial cell wall. The bacterial attachment density on this CMG-concanavalin conjugate was found to be extremely high and very specific. Confocal microscopy was used to confirm the tethering of the concanavalin-FITC conjugate on GO and to confirm the subsequent attachment density of the bacterial cells.

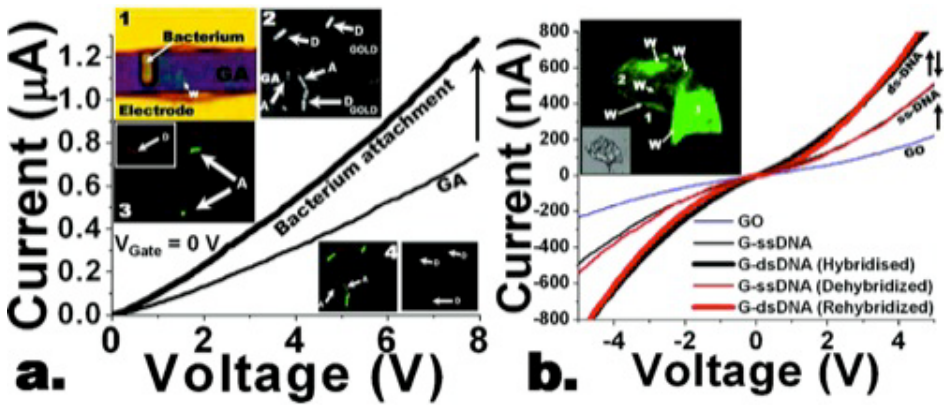

Figure 2-8 (a) The conductivity of the p-type GA device increases upon attachment of a single bacterial cell on the surface of GA (inset 1). LIVE/DEAD confocal microscopy test on the bacteria deposited on GA confirmed that most of the bacteria were alive after the electrostatic deposition (inset 3). A = alive and D = dead. The LIVE/DEAD test conducted immediately after the electrical measurements on the GA−gold−bacteria device (inset 2 and inset 4) showed that the bacterial cells on GA atop silica remain alive, while the bacteria deposited on the GA atop gold electrodes die after electrical measurements (inset 4 (right)). (b) DNA transistor: ss-DNA tethering on GO increases the conductivity of the device. Successive hybridization and dehybridization of DNA on the G-DNA device results in completely reversible increase and restoration of conductivity. Inset shows a G-DNA(ds) sheet with wrinkles and folds clearly visible.

Electrical measurements of GO and GA sheets immobilized on silica substrate with predeposited or postdeposited gold electrodes (Figure 2.7 top inset) and silicon as backgate were conducted to determine the semiconductor characteristics of the CMGs. Here, the GA devices were produced by direct aminization of the GO devices (as explained above). Both GO and GA exhibited a slightly nonlinear current−voltage behavior (Figure 2.7a) in dry nitrogen atmosphere, with the GA device always having a lower conductivity than the parent GO devices (Figure 2.7a). Both the GO and GA devices were p-type semiconductors (Figure 2.7b). For the device shown in Figure 2.7a, top inset, the hole mobilities for GO and GA were 0.0297 ± 0.0017 $cm^2/V{\cdot}s$ and 5.882 ± 0.098 $cm^2/V{\cdot}s$, respectively, while the electron mobilities were 0.00198 ± 0.0002 and 0.00747 ± 0.00178 $cm^2/V{\cdot}s$, respectively. These carrier mobilities ($\mu_{Carrier}$) were calculated from the following expression

$$\mu_{\text{Carrier}} = (\Delta I_{DS}/\Delta V_G)/(C_G(l/w)V_{DS}) \qquad (1)$$

Here, ΔI_{DS} and V_{DS} are the source−drain current and voltage, CG is the capacitance of the silica gate, and l and w are the length and width of the CMG sheets between electrodes. The higher hole mobility of GA can be attributed to the relatively large distance between the charged amine group and the graphene base as compared to the distance between carboxylic group and the graphene base for GO. The density of holes in GA is 2100-fold less than that in GO. Further, the hole mobility of GA was always higher than that of the parent GO device and increases with increasing aminization time scale. Devices with postdeposited gold electrodes on GO produced similar results (Figure 2.7b, top inset).

Bacterial attachment on a GA device was tested for CMG's microbial interfacing sensitivity and resolution. The GA device exhibited a sharp 42% increase in conductivity upon attachment of a single bacterial cell on GA (method explained above) (Figure 2.8a). This can be attributed to the p-type characteristic of GA, where the attachment of a negatively charged species such as bacteria, is equivalent to a negative potential gating which increases the hole density and thus the conductivity of GA. The hole density increase due to the bacterium attachment (Figure 2.8a, top inset) was calculated to be 3.53 × 1010 cm^{-2} ($R_{1|GA}$ = 10.85 ± 0.51 MΩ, $R_{2|Bacteria}$ = 6.3 ± 0.4 MΩ). This corresponds to a generation of 1400 holes per bacterium in GA. The change in hole density (Δq) was calculated by the expression

$$\Delta q = (R_2^{-1} - R_1^{-1})/((l/w)\mu_p) \qquad (2)$$

Here R_2 and R_1 are the final and initial resistances of the device. Since all the measurements were conducted in a dry nitrogen atmosphere, with bacteria not touching both electrodes simultaneously, there was no ionic conductivity from bacteria. Also application of electric field for long durations did not change the conductivity as expected for ionic conductivity. This further shows that the chemical gating on GA was partially a result of the compensation of the positive charge of the amine groups on GA by the negative charge of the polyteichoic acid molecules on the bacterial surface. Further, the LIVE/DEAD test on a bacterial device after electrical measurements showed that the bacteria on GA atop silica remain alive immediately after an electrical measurement; however the cells deposited on GA atop gold

electrodes died (Figure 2.8a, inset). A typical IV electrical measurement comprises of an application of an average of 4 V (dc) for a net time of 1.6 s (total time of 10 min). The electrical measurements and the nitrogen atmosphere did not have any visible effect on the integrity of the bacterium's structure as against the CNT network devices [12]. These results show a proof-of-concept of a highly sensitive graphene-based biodiagnostic tool with single-bacterium resolution. Further, some advantages of the CMG/bacteria device over the optical-detection methods are that (a) the CMG/bacteria device does not require the lengthy process of florescent [47] or magnetic [48] labeling of bacteria required for some optical methods, (b) it does not require high computation power for image analysis [47, 49] necessary for most optical methods, (c) the optical methods require expensive optics such as CCDs, lasers, etc [47-50], and (d) to attract the bacteria most optical methods are coupled with external ultrasonic standing wave generators [50]. A CMG/bacteria device would not require external instruments for bacterial trapping, which can be achieved by electrophoresis [51] by application of a small ac voltage on the device electrodes. Further, as shown earlier, high specificity can be achieved by the CMGs devices by tethering them with biomolecules, like concanavalin, with high affinity to the bacterial cell wall.

Electrical characterization of the G-DNA hybrids was conducted to examine CMG's viability and sensitivity as a biomolecular transistor. First, selective tethering of the single-stranded DNA on GO to form G-DNA was carried out (method explained earlier). This led to a 128% increase in the conductivity, partially attributed to the attachment of the negatively charged DNA on the p-type GO (Figure 2.8b). Subsequently, hybridization with cDNA was conducted on the G-DNA device (explained earlier). This led to a 71% increase in conductivity ($R_{1|DNA}$ = 9.86 ± 0.24 MΩ; $R_{2|dsDNA}$ = 5.77 ± 0.17 MΩ) (Figure 2.8b). The robustness of this device was tested by dehybridizing the cDNA from G-DNA (see Appendix A), which resulted in the restoration of G-DNA's original conductivity (Figure 2.8b). Further, multiple hybridization−dehybridization runs showed consistent increase and restoration of the conductivity. The increase in the hole density upon DNA hybridization was $+5.61 \times 10^{12}$ cm^{-2} (eq 2), which in turn implies that one quanta of hole is generated or removed by hybridization or dehybridization of approximately six DNA molecules (see Appendix A). This figure is calculated assuming a carboxylic acid density on GO of 1.623×10^{14} cm^{-2},[52] a DNA attachment efficiency of 25%, and a hybridization efficiency of 90% [53]. The generation of holes is attributed to the negative-charge molecular gating from the phosphate ions of the

complementary DNA. The change in conductivity due to hybridization/dehybridization varied from 60% to 200% for different G-DNA samples. Immersing the G-DNA device in a solution of non-complementary DNA did not change the conductivity. Even though the DNA hybridization/dehybridization measurements were made in dry nitrogen conditions, they were effective in producing the negative-charge-gating. These results further elucidate the high sensitivity of CMG-nanostructures which function effectively as a label-free DNA detector and a molecular transistor.

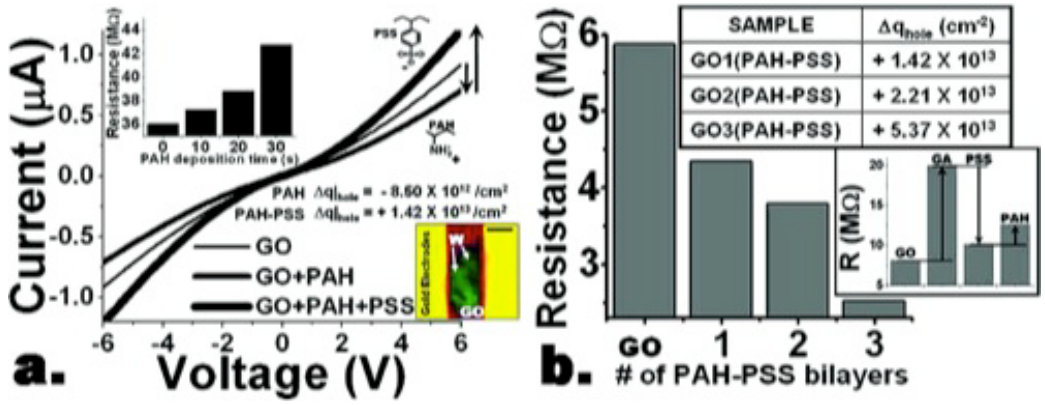

Figure 2-9 (a) The conductivity and the hole density of GO decreases and increases with attachment of PAH and PSS, respectively. Top inset: Increasing the areal density of attached PAH on GO, by increasing deposition time, leads to increase in gating of GO between the electrodes (bottom inset), reducing its conductivity. Bottom inset's bar size = 4 μm. (b) Resistance reduces (negative potential gating) with increase in the number of PAH−PSS bilayer. The top inset shows the change in the hole density. The bottom inset shows the change in resistance of a GO device functionalized to a GA device followed by attachment of a PSS monolayer and subsequent attachment of a PAH monolayer.

To examine the CMG molecular transistor's specificity to polarity, a positively charged PAH monolayer [54] (70000 Da; 2.5 mg/mL; 10 min deposition) was deposited on GO. This led to an increase in its resistance corresponding to a decrease in hole density ($R_{1|GO}$ = 5.88 ± 0.3 MΩ, $R_{2|GO\text{-}PAH}$ = 7.47 ± 0.31 MΩ, $\Delta q_h = -8.5 \times 10^{12}$ cm^{-2}) (Figure 2.9a). It was calculated (Eq 3) that on an average 1 PAH monomer is electrostatically attached on 3 nm^2 of GO surface.

$$n = (4\pi(h^2/dl_P)_{PAH} W^2 \Delta I_{DS})/(e\mu V_{DS}) \qquad (3)$$

Here h, d, and l_P are the height, the width, and the length of a PAH monomer. This further implies that attachment of approximately four PAH monomers reduces a single quantum of hole (see Appendix A). Furthermore, the PAH attachment (Figure 2.9a inset (top)) showed a monotonous decrease in conductivity with an increase in duration of attachment, reaching saturation in 3 min. This is attributed to a continuous decrease in number of holes as more and more PAH deposits on GO. Attaching a monolayer of negatively charged PSS (70000 Da, 2.5 mg/mL, 10 min) on the GO–PAH device increased the conductivity corresponding to an increase in hole density, equivalent to a negative-potential gating (Figure 2.9a) ($R_{1|GO\text{-}PAH}$ = 7.47 ± 0.31 MΩ; $R_{2|GO\text{-}PAH\text{-}PSS}$ = 4.41 ± 0.43 MΩ, $\Delta q_h = +1.42 \times 10^{13}$ cm^{-2}). This shows that the GO device undergoes a polarity specific gating with increase or decrease in conductivity upon attachment of negatively or positively charged species, respectively. This further shows that the CMG gating is sensitive to molecular adsorption at distances more than that of a single polyelectrolyte monolayer. Indeed attachment of two more layers of PAH and PSS each (six monolayers with a thickness of 13.6 nm [54]) led to continued gating of the underlying GO (Figure 2.9b, top inset). The non-unidirectional (increase and decrease) change in conductivity observed by differently charged molecules negates the phenomenon originating from a change in ionic conductivity, contact resistance, or thermal effects, where the response is expected to be unidirectional. GA devices also show similar results for molecular attachment. Electrostatic attachment of PSS followed by PAH on a GA device led to an increase and decrease in conductance, respectively ($R_{1|GO}$ = 8.11 ± 0.5 MΩ; $R_{2|GA}$ = 20.0 ± 0.5 MΩ; $R_{3|GA\text{-}PSS}$ = 10.1 ± 0.6 MΩ; $R_{4|GO\text{-}PSS\text{-}PAH}$ = 12.6 ± 0.51 MΩ). These results show that (a) response direction of CMG transistors is polarity specific, (b) CMGs can be designed to respond to any polarity, and (c) CMG gating is sensitive over several multilayers of adsorption. PGA synthesized by nitrogen–helium plasma treatment of graphite also showed a p-type nature and polyelectrolyte attachment sensitivity similar to GA (see Appendix A).

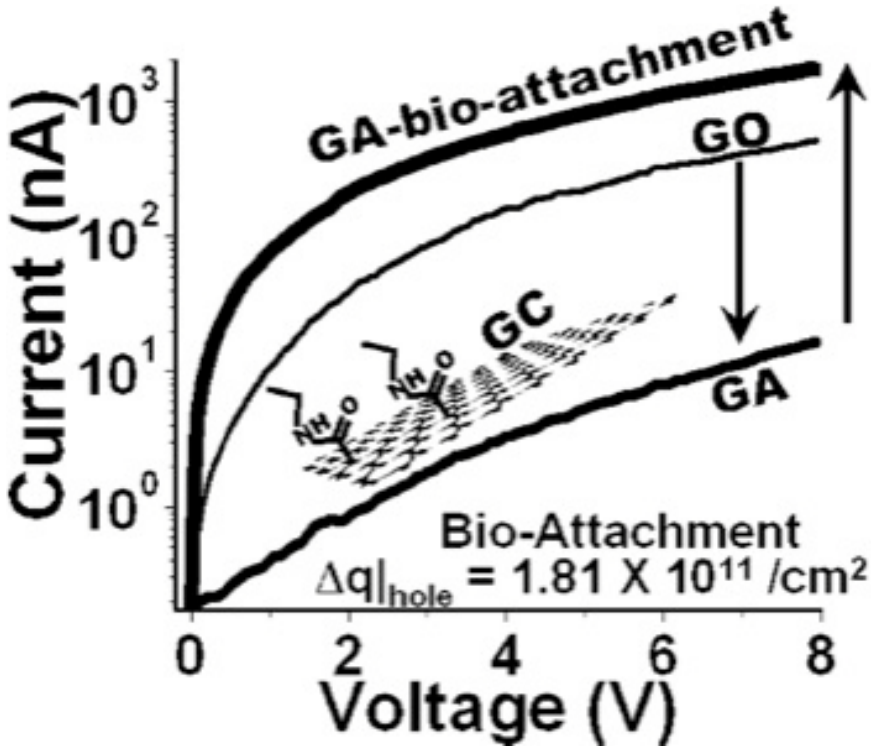

Figure 2-10 GA produced from extensive aminization of GO, via covalent attachment of the ethylenediamine, led to 30-fold reduction in conductivity. Further electrostatic attachment of negatively charged bacterial protein and DNA on the GA device led to 100-fold increase in conduction due to negative charge gating. The inset shows a CMG of graphene carbonitrile (GC).

A study of a protein transistor was conducted to establish the relationship between device sensitivity and fabrication process. GA produced from extensive amination of parent GO underwent a high 30-fold increase in resistance ($R_{1|GO}$ = 26.67 ± 0.9 MΩ; $R_{2|GA}$ = 800.1 ± 2 MΩ). Electrostatic adsorption of a mixture of negatively charged bacterial DNA and proteins extracted from Bacillus cereus (see Appendix A) on this GA device led to a sharp 2 orders of magnitude decrease in resistance ($R_{1|GA}$ = 800.1 ± 2 MΩ; $R_{2|GA\text{-}Bacteria\text{-}proteins}$ = 5.34 ± 0.2 MΩ, Δq_h = +1.81 × 10^{11} hole/cm^2) (Figure 2.10). This extremely high sensitivity of GA is attributed to the extensive amination of GO to form GA, where the EDA bonding on GO partially acts as a gating process for the base graphene-carbonitrile (GC) sheets (Figure 2.10, inset). Generally, the GA devices which underwent a larger decrease in conductivity after amination, or a higher positive gating (partial) of the GC base, have higher sensitivity to negative species attachment. Since the

aminization process can be controlled by deposition time, it provides the ability to tune CMG's sensitivity.

Conclusion

In conclusion, we have demonstrated the viability of CMGs as sensitive building blocks for bioelectronics at both microbial and molecular levels. Specifically, we demonstrated (i) a single bacterium resolution interfacial device, (ii) a label-free, reversible DNA detector, and (iii) a polarity-specific molecular transistor for protein/DNA adsorption. We also illustrated the ability to control the sensitivity, polarity specificity, and the extent of gating of the CMGs. This study will potentially motivate the development of a tool kit of graphene derivatives to apply them in building next-generation systems and devices such as biodriven electronic devices, biodetection tools, biobatteries, smart electrochemical circuitry, and molecular electronic systems.

Acknowledgements

V.B. would like to thank Kansas State University for the start-up funds. We would like to thank Jose Armesto, Ashvin Nagaraja, and Kabeer Jasuja for help with plasma treatment of graphite, bacterial samples, and electrical measurements, respectively.

References

1. Liao, H. W., Nehl, C. L., Hafner, J. H. Biomedical applications of plasmon resonant metal nanoparticles *Nanomedicine* **1** 201-208 (2006)

2. Berry, V.; Rangaswamy, S., Saraf, R. F. Highly selective, electrically conductive monolayer of nanoparticles on live bacteria *Nano Lett.* **4** 939-942 (2004)

3. Berry, V.; Saraf, R. F. Self-assembly of nanoparticles on live bacterium: An avenue to fabricate electronic devices *Angew. Chem., Int. Ed.* **44** 6668-6673 (2005)

4. Cai, H., Cao, X. N.; Jiang, Y., He, P. G., Fang, Y. Z. Carbon nanotube-enhanced electrochemical DNA biosensor for DNA hybridization detection *Anal. Bioanal. Chem.* **375** 287-293 (2003)

5. Cui, Y., Wei, Q. Q., Park, H. K., Lieber, C. M. Nanowire nanosensors for highly sensitive and selective detection of biological and chemical species *Science* **293** 1289-1292 (2001)

6. Patolsky, F., Zheng, G. F., Lieber, C. M. Nanowire-based biosensors *Anal. Chem.* **78** 4260-4269 (2006)

7. Cai, H., Xu, C., He, P. G., Fang, Y. Z. Colloid Au-enhanced DNA immobilization for the electrochemical detection of sequence-specific DNA *J. Electroanal. Chem.* **510** 78-85 (2001)

8. Le, J. D., Pinto, Y., Seeman, N. C., Musier-Forsyth, K., Taton, T. A., Kiehl, R. A. DNA-templated self-assembly of metallic nanocomponent arrays on a surface *Nano Lett.* **4** 2343-2347 (2004)

9. Cai, H., Xu, C., He, P. G., Fang, Y. Z. Colloid Au-enhanced DNA immobilization for the electrochemical detection of sequence-specific DNA *J. Electroanal. Chem.* **510** 78-85 (2001)

10. Cui, Y., Wei, Q. Q., Park, H. K., Lieber, C. M. Nanowire nanosensors for highly sensitive and selective detection of biological and chemical species *Science* **293** 1289-1292 (2001)

11. Patolsky, F., Zheng, G. F., Lieber, C. M. Nanowire-based biosensors *Anal. Chem.* **78** 4260-4269 (2006)

12. So, H. M., Park, D.-W., Jeon, E.-K., Kim, Y.-H., Lee, C.-K., Choi, S. Y., Kim, S. C., Chang, H., Lee, J.-O Detection and titer estimation of Escherichia coli using aptamer-functionalized single-walled carbon-nanotube field-effect transistors *Small* **4** 197-201 (2008)

13. Gilje, S., Han, S., Wang, M., Wang, K. L., Kaner, R. B. A chemical route to graphene for device applications *Nano Lett.* **7** 3394-3398 (2007)

14. Stankovich, S., Dikin, D. A., Dommett, G. H. B., Kohlhass, K. M., Zimney, E. J., Stach, E. A., Piner, R. D., Nguyen, S. T., Ruoff, R. S. Graphene-based composite materials *Nature* **442** 282-286 (2006)

15. Hod, O., Peralta, J. E., Scuseria, G. E. Edge effects in finite elongated graphene nanoribbons *Phys. Rev. B* **76** 233401 (2007)

16. Gomez-Navarro, C., Weitz, R. T., Bittner, A. M., Scolari, M., Mews, A., Burghard, M., Kern, K. Electronic transport properties of individual chemically reduced graphene oxide sheets *Nano Lett.* **7** 3499-3503 (2007)

17. Park, S., Lee, K.-S., Bozoklu, G., Cai, W., Nguyen, S. T., Ruoff, R. S. Graphene oxide papers modified by divalent ions - Enhancing mechanical properties via chemical cross-linking *ACS Nano* **2** 572-578 (2008)

18. Yan, Q. M., Huang, B., Yu, J., Zheng, F., Zang, J., Wu, J., Gu, B.-L., Liu, F., Duan, W. Intrinsic current-voltage characteristics of graphene nanoribbon transistors and effect of edge doping *Nano Lett.* **7** 1469-1473 (2007)

19. Obradovic, B. Analysis of graphene nanoribbons as a channel material for field-effect transistors *Appl. Phys. Lett.* **88** (2006)

20. Barone, V., Hod, O., Scuseria, G. E. Electronic structure and stability of semiconducting graphene nanoribbons *Nano Lett.* **6** 2748-2754 (2006)

21. Novoselov, K. S., Geim, A. K., Morozov, S. V., Jiang, D., Zhang, Y., Dubonos, S. V., Grigorieva, I. V., Firsov, A. A. Electric field effect in atomically thin carbon films *Science* **306** 666-669 (2004)

22. Novoselov, K. S., Geim, A. K., Morozov, S. V., Jiang, D., Katsnelson, M. I., Grigorieva, I. V., Dubonos, S. V., Firsov, A. A. Two-dimensional gas of massless Dirac fermions in graphene *Nature* **438** 197-200 (2005)

23. Berger, C., Song, Z., Li, X., Wu, X., Brown, N., Naud, C., Mayou, D., Li, T., Hass, J., Marchenkov, A. N., Conrad, E. H., First, P. N., de Heer, W. A. Electronic confinement and coherence in patterned epitaxial graphene *Science* **312** 1191-1196 (2006)

24. Zhou, S. Y., Gweon, G.-H., Graf, J., Fedorov, A. V., Spararu, C. D., Diehl, R. D., Kopelevich, Y., Lee, D.-H., Louie, S. G., Lanzara, A. First direct observation of Dirac fermions in graphite *Nat. Phys.* **2** 595-599 (2006)

25. Geim, A. K., Novoselov, K. S. The rise of graphene *Nat. Mater.* **6** 183-191 (2007)

26. Schedin, F. Detection of individual gas molecules adsorbed on graphene *Nat. Mater.* **6** 652-655 (2007)

27. Jian-Hao, Chen et al. Printed Graphene Circuits. *Adv. Mater.* **19**, 3623-3627 (2007).

28. Wu, Y. Q. Top-gated graphene field-effect-transistors formed by decomposition of SiC *Appl. Phys. Lett.* **92** 092102 (2008)

29. Liu, Q., Liu, Z., Zhang, X., Zhang, N., Yang, L., Yin, S., Chen, Y. Organic photovoltaic cells based on an acceptor of soluble graphene *Appl. Phys. Lett.* **92** 223303 (2008)

30. Wang, X. Transparent carbon films as electrodes in organic solar cells *Angew. Chem., Int. Ed.* **47** 2990-2992 (2008)

31. Becerril, H. A., Mao, J., Liu, Z., Stoltenberg, R. M., Bao, Z., Chen, Y. Evaluation of solution-processed reduced graphene oxide films as transparent conductors *ACS Nano* **2** 463-470 (2008)

32. Wang, X., Zhi, L. J., Mullen, K. Transparent, conductive graphene electrodes for dye-sensitized solar cells *Nano Lett.* **8** 323-327 (2008)

33. Blake, P., Brimicombe, P. D., Nair, R. R., Booth, T. J., Jiang, D., Schedin, F., Ponomarenko, L. A., Morozov, S. V., Gleeson, H. F., Hill, E. W., Geim, A. K., Novoselov, K. S. Graphene-Based Liquid Crystal Device *Nano Lett.* **8** 1704-1708 (2008)

34. Hummers, W. S., Offeman, R. E. Preparation of Graphitic Oxide *J. Am. Chem. Soc.* **80** 1339 (1958)

35. Blake, P., Hill, E. W., Castro Neto, A. H., Novoselov, K. S., Jiang, D., Yang, R., Booth, T. J., Geim, A. K. Making graphene visible *Appl. Phys. Lett.* **91** 063124 (2007)

36. Meyer, J. C., Geim, A. K., Katsnelson, M. I., Novoselov, K. S., Booth, T. J., Roth, S. The structure of suspended graphene sheets *Nature* **446** 60-63 (2007)

37. Meyer, J. C., Geim, A. K., Katsnelson, M. I., Novoselov, K. S., Obergfell, D., Roth, S., Girit, C., Zettl, A. On the roughness of single- and bi-layer graphene membranes *Solid State Commun.* **143** 101-109 (2007)

38. Stoermer, R. L., Keating, C. D. Distance-dependent emission from dye-labeled oligonucleotides on striped Au/Ag nanowires: Effect of secondary structure and hybridization efficiency *J. Am. Chem. Soc.* **128** 13243-13254 (2006)

39. Datta, S. S., Strachan, D. R., Mele, E. J., Johnson, A. T. C..Surface Potentials and Layer Charge Distributions in Few-Layer Graphene Films. *Nano Lett.* **9** 7-11 (2009).

40. Kokkorakis, G. C., Xanthakis, J. P. Local electric field and enhancement factor around nanographitic structures embedded in amorphous carbon *Surf. Interface Anal.* **39** 135-138 (2007)

41. Ferris, K. F., Risser, S. M. Surface Defect Enhancement of Local Electric-Fields in Dielectric Media *Chem. Phys. Lett.* **234** 359-366 (1995)

42. Mermoux, M., Chabre, Y., Rousseau, A. FTIR and C-13 NMR-Study of Graphite Oxide *Carbon* **29** 469-474 (1991)

43. He, H. Y., Riedl, T., Lerf, A., Klinowski, J. Solid-state NMR studies of the structure of graphite oxide *J. Phys. Chem.* **100** 19954-19958 (1996)

44. Holzinger, M., Vostrowsky, O., Hirsch, A., Hennrich, F., Kappes, M., Weiss, R., Jellen, F. Sidewall functionalization of carbon nanotubes *Angew. Chem., Int. Ed.* **40** 4002-4004 (2001)

45. Jiang, K. Y., Schradler, L. S., Siegel, R. W., Zhang, X., Terrones, M. Protein immobilization on carbon nanotubes via a two-step process of diimide-activated amidation *J. Mater. Chem.* **14** 37-39 (2004)

46. Berry, V., Gole, A., Kundu, S., Murphy, C. J., Saraf, R. F. Deposition of CTAB-terminated nanorods on bacteria to form highly conducting hybrid systems *J. Am. Chem. Soc.* **127** 17600-17601 (2005)

47. Matsunaga, T., Nakayama, H., Okochi, M., Takeyama, H. Fluorescent detection of cyanobacterial DNA using bacterial magnetic particles on a MAG-microarray *Biotechnol. Bioeng.* **73** 400-405 (2001)

48. Baldrich, E., Munoz, F. X. Enzyme shadowing: using antibody-enzyme dually-labeled magnetic particles for fast bacterial detection *Analyst* **133** 1009-1012 (2008)

49. Bloem, J., Veninga, M., Shepherd, J. Fully-Automatic Determination of Soil Bacterium Numbers, Cell Volumes, and Frequencies of Dividing Cells by Confocal Laser-Scanning Microscopy and Image-Analysis *Appl. Environ. Microbiol.* **61** 926-936 (1995)

50. Zourob, M., Hawkes, J. J., Coakley, W. T., Treves Brown, B. J., Fielden, P. R., McDonnell, M. B., Goddard, N. J. Optical leaky waveguide sensor for detection of bacteria with ultrasound attractor force *Anal. Chem.* **77** 6163-6168 (2005)

51. Beck, J. D., Shang, L., Marcus, M. S., Hamers, R. J. Manipulation and real-time electrical detection of individual bacterial cells at electrode junctions: A model for assembly of nanoscale biosystems *Nano Lett.* **5** 777-781 (2005)

52. Stankovich, S., Dikin, D. A., Piner, R. D., Kohlhaas, K. A., Kleinhammes, A., Jia, Y., Wu, Y., Nguyen, S. T., Ruoff, R. S. Synthesis of graphene-based nanosheets via chemical reduction of exfoliated graphite oxide *Carbon* **45** 1558-1565 (2007)

53. Peterson, A. W., Heaton, R. J., Georgiadis, R. M. The effect of surface probe density on DNA hybridization *Nucleic Acids Res.* **29** 5163-5168 (2001)

54. Decher, G. Fuzzy nanoassemblies: Toward layered polymeric multicomposites *Science* **277** 1232-1237 (1997)

Chapter 3 - Impermeable graphenic encasement of bacteria

Abstract

Transmission electron microscopy (TEM) of hygroscopic, permeable, and electron-absorbing biological cells has been an important challenge due to the volumetric shrinkage, electrostatic charging, and structural degradation of cells under high vacuum and fixed electron beam. Here we show that bacterial cells can be encased within a graphenic chamber to preserve their dimensional and topological characteristics under high vacuum (10^{-5} Torr) and beam current (150 A/cm^2). The strongly repelling π-clouds in the interstitial sites of graphene's lattice reduce the graphene-encased-cell's permeability from 7.620 nm/s to 0 nm/s. The C−C bond flexibility enables conformal encasement of cells. Additionally, graphene's high Young's modulus retains cell's structural integrity under TEM conditions, while its high electrical and thermal conductivity significantly abates electrostatic charging. We envision that the graphenic encasement approach will facilitate real-time TEM imaging of fluidic samples and potentially biochemical activity.

Published as

Mohanty, N., Fahrenholtz, M., Nagaraja, A., Boyle, D., and Berry, V., "Impermeable graphenic encasement of bacteria." *Nano Letters* **11** 1270-1275 (2011)

Introduction

For the last 80 years, TEM imaging has been a key component in the evolution of science and technology [1-3]. Currently, there are two common routes to conduct room-temperature TEM imaging of wet cells:[1-3] (1) Environmental TEMs (ETEMs), where cells are imaged at low vacuum (1 Torr), thereby reducing the pressure drop between the intracellular and extracellular regions of the cell; [4-10] (2) microfluidic TEM where thin, impermeable, and electron transparent chambers are fabricated lithographically and the cells are trapped within it [11-19]. While, ETEM has shown tremendous promise in native cell imaging, the low vacuum is high enough to shrink the cells [1, 2]. On the other hand, the microfluidic encasement achieves wet-phase imaging even with a regular TEM. However, the technique requires extensive lithography, and does not provide a conductive sink to reduce charging [1, 20]. Alternatively, cryogenic solid-phase TEM imaging of biological cells has received great attention due to its ease of use;[1, 2] here, the sample is frozen/solidified and therefore retains its volatile content. However, this technique does not allow "liquid-phase" imaging.

A solution to the above-mentioned challenge is to confine the cells within an easy-to-apply impermeable and electron-transparent encasement, which retains the cellular water content while enabling TEM imaging. This work shows that few-atoms-thick graphenic sheets have a unique combination of properties (mentioned above and more), making it an ideal candidate for cellular encasement for TEM imaging [15-20]. The following properties of graphenic sheets are leveraged: (a) impermeability,[15, 21] the close-packing of carbon atoms in graphene leaves ultrasmall interstitial space with high π-electron density restricting the passage of even the small atoms, such as helium; (b) high electron transparency,[22] high-momentum electrons can transmit through monolayer or multilayer (~10 nm) graphene, which enables facile TEM imaging; (c) flexibility [17, 18] (which enables graphene to be rolled into carbon nanotubes) allows the sheets to conformally wrap the cells or other macroscale particles; (d) mechanical strength,[16, 23] graphene's high yield strength enables it to sustain the high-pressure differences, similar to that between the intracellular region and external vacuum of a TEM; (e) high electrical conductivity,[19, 22] the mobile π electrons of graphene significantly reduce the electrostatic charge buildup under electron microscopy (EM); and (f) high thermal conductance,[20, 22] graphene's high phonon conductivity dissipates the heat generated from electron bombardment. Clearly, this unique combination of properties makes graphene an ideal

nanomaterial for wet-phase imaging under TEM, while preserving intracellular volatile content of the cell under high vacuum.

This paper demonstrates that protein-functionalized graphene (PFG) can specifically wrap bacteria, thus completely encasing them. The wrapping subsequently facilitates their effective wet-phase TEM imaging. This technique is shown for Gram-positive bacteria, Bacillus subtilis. These bacteria have about 70% water content (volumetric) with a cell wall thickness of 16−30 nm [24] and were kept unstained (see Appendix B). Briefly, an aqueous suspension of graphene oxide (GO) sheets with area between 20 and 600 μm^2 was prepared via the modified Hummer's method [25, 26]. To enhance wrapping, the GO was covalently bonded to the amine groups on membrane-binding protein, [25] concanavalin-A (CA), which has specific-affinity to the polyteichoic acid moieties on the bacterial cell wall [27]. These protein-covered sheets are referred to as PFGs in this paper. To confirm CA functionalization, fluorescein isothiocyanate (FITC) dye labeled CA was used. Substrate-deposited PFGs showed a faint green fluorescence (owing to quenching by GO [28]), confirming the successful functionalization (Figure 3.1).

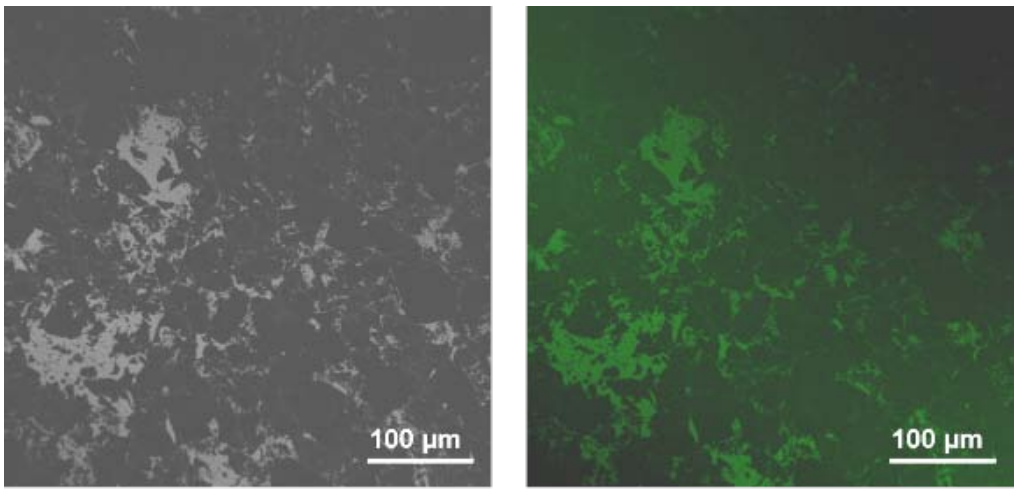

Figure 3-1 Optical microscope (a) and confocal images (b) of the PFGs with FITC-tagged concanavalin – A. The green fluorescence confirms the successful attachment of concanavalin - A molecules to the PFGs.

Purified bacterial cell suspension (cultured overnight in nutrient agar media, pelleted down, washed, and diluted to 10^3 cells/mL in deionized (DI) water) was mixed with a fresh PFG suspension (10 mg/mL). This led to a visible clouding of the suspension, which we attribute to the bacterial encasement by the PFGs. It is expected that the large area of PFG sheets will strengthen its interfacing with bacteria. The PFG encasement/wrapping mechanism is proposed to be a sequential multipoint attachment process, as favored by minimization of Gibbs energy

$$\sum_{i=1}^{n}(\mu_{G+i}N_{G+i} + \mu_{B-i}N_{B-i}) > \sum_{i=1}^{n}(\mu_{GB\pm i}N_{GB\pm i})$$

where μ is the chemical potential, N is the number of sites, and the subscripts G+ and B− are the CA and teichoic acid sites on PFG and bacteria, respectively) [29]. Further, the sizable reduction of free energy originating from the reduction of chemical potential via the highly specific ligand−receptor interaction is expected to offset the ligand−receptor b ond stretching during wrapping [29]. The anticipated wrapping process is depicted in panels a−e of Figure 3.2. The negative control experiments with GO in the absence of CA yielded no wrapping, attributed to the increase in free energy with the proximity between negatively charged GO and teichoic acid.

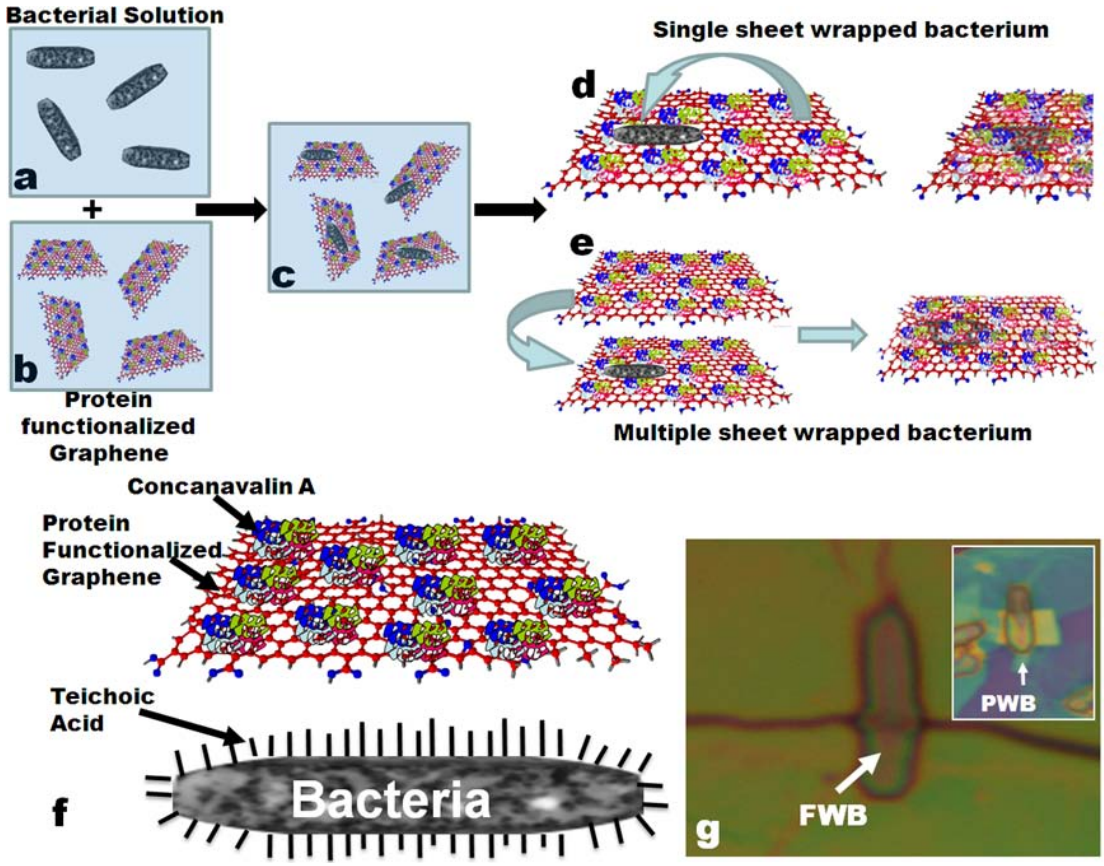

Figure 3-2 (a – e) Schematic diagram showing the steps involved in the bacterial wrapping by the PFG sheets. (f) A schematic showing the highly specific interaction between the CA on the PFG sheets and the teichoic acid moieties on the bacterial cell-wall. (g) An optical microscope image of a fully wrapped bacterium (FWB) and a partially wrapped bacterium (PWB, top right inset).

Experimental methods

Preparation of Protein-functionalized graphene (PFGs)

GO was synthesized from mesh 7 graphite flakes (Sigma-Aldrich Inc.) via the modified Hummer's method to produce a stable, aqueous suspension of 10 mg/ml GO sheets with an average areal distribution around ~ 400 μm^2. 7 grams of mesh 7 graphite flakes (Cat # 332461, Sigma Aldrich Inc.) were suspended in a mixture of 200 ml of 96 % sulfuric acid and 33 ml of 68 % Nitric acid in a 4 °C water bath and stirred for about 30-45 minutes. Then 30 g of potassium permanganate was added slowly onto the mixture while maintaining the temperature

of the mixture at 4 C with constant agitation. Subsequently the temperature of the mixture was raised to 40 °C (with a ramp of 1 C per minute) and held constant for 6 hours. The mixture was then cooled down to 4 °C in an ice bath and 30 % H_2O_2 (in DI water) is added slowly drop-by-drop with adequate mixing to neutralize the excess potassium permanganate. Upon cessation of the reaction, the resulting GO solution was left undisturbed overnight, after which the GO sheets were spun down (11, 000 g, 60 min, 300 K), washed with DI water followed by HCl and then again by water. The washing step was repeated at least 2 more times after which the aqueous suspension of GO was dialyzed in copious amounts of DI water for a week.

A 0.05 mg/ml solution of CA was prepared from the lyophilized protein powder in 1X PBS. 1 ml of this CA solution was mixed with 9 ml of the GO suspension in DI water in addition to 1mg of the coupling agent HATU in 10 µl DMF and incubated at 37 °C in an incubator shaker for 6 hours. This reaction produced PFG sheets with CA attached to the carboxylic acid / hydroxyl groups via the amide linkage. The PFG sheets were then pelleted down via centrifugation (11,000 g, 60 minutes, 300 K), washed multiple times and re-suspended in fresh DI water via intermittent sonication, serially diluted to have a final concentration of 10 mg/ml.

Preparation of Bacteria

Bacillus subtilis cells were cultured in the nutrient broth media (Sigma-Aldrich Inc.) and incubated in an incubator-shaker (New Brunswick Inc.) at 37 °C for 12 hours. The mature bacterial cells were then pelleted down via centrifugation (500 g, 6 minutes, 300 K), washed multiple times with 1X PBS and finally re-suspended (after requisite serial dilution) in 1 ml of DI water to obtain a concentration of 10^3 cells / ml.

Wrapping of Bacteria

1 ml of the re-suspended bacterial cells was mixed with a freshly sonicated 1 ml sample of PFGs (conc. ~ 10 mg/ml). Instantaneous (less than a minute) wrapping of the bacterial cells was observed.

Immobilization of wrapped bacteria on silica substrate / Si_3N_4 grids

300 nm thick silica wafers were first cleaned with organic solvents (acetone, isopropanol and ethanol) and then treated with oxidizing plasma (O_2 Plasma, 2 mbar, 300 K, 5 minutes). Subsequently the wafers were passivated via treatment with the hydrogen plasma (H_2 Plasma, 2

mbar, 300 K, 2 minutes). To immobilize the wrapped bacteria onto the wafers, 500 µl of the suspension containing the wrapped bacteria was drop casted onto the clean, passivated wafers and left undisturbed for 10 minutes in a laminar flow hood. The wafer is first dried using a nitrogen flow, washed with DI water and again dried. The wafer was visually inspected under an optical microscope (Olympus BX41) to locate the fully wrapped bacteria.

For immobilization onto a Si_3N_4 TEM window, the grid was dipped in the suspension containing the wrapped bacteria for 5-10 minutes.

Live-Dead test

Live – dead test was carried out on the bacteria by incubating them in a solution containing 0.1 mg/ml each of syto – 9 and propidium Iodide (PI) in 1X PBS for 2 minutes, followed by a thorough washing step and subsequent observation under the confocal microscope (Zeiss LSM 5 PASCAL). Image analysis was carried out using the Image J software in concert with GIMP. Note that, the live-dead test was carried out on the bacterial cells just before the wrapping process and NOT on the wrapped bacteria due to the impermeability of the PFG, as has been shown in the TEM studies.

FESEM imaging

The instrument used was a Zeiss Leo 1550 scanning electron microscope in UHV conditions at a 8 kV EHT with a working distance of 6 mm using both the in-lens and the below-lens Everhart-Thornley Detector. The images were pseudo-coloured using Image J and overlayed using GIMP image processing software.

TEM imaging

The instrument used was a Philips CM100 TEM equipped with a AMT digital image capturing system, accelerating voltages up to 100 kV, low-dose capabilities, compuStage and a cold finger. The TEM imaging was carried out on the wrapped and the un-wrapped bacteria at 100 kV accelerating voltage, 1 pA probe current, 1.5 micron diameter illumination (Spotsize of 6) and a typical magnification of 13500 X.

TEM tomography on wrapped bacteria

The wrapped bacteria were spun down from the suspension via centrifugation (500 x g, 10 minutes, 300 K) in a table top micro-centrifuge re-suspended in 2 % paraformaldehyde and 2.5 % glutaraldehyde fixative in 0.1 M sodium cacodylate buffer at pH 7.4 and left undisturbed for 1 hour at 300 K. The fixed cells were washed 3 times with the sodium cacodylate buffer and subsequently re-suspended in a DI water solution of 1% osmium tetroxide and 1.5 % potassium ferrocyanide. After an hour of incubation in the dark at 300 K , the cells were washed with DI water for 4 times. The samples were then resuspended in a solution of 1% Uranyl Acetate in DI water, left undisturbed for 30 minutes and subsequently washed with DI water for 3 times. Sequential dehydration was carried out via re-suspension and incubation (10 minutes, 300 K) with 30%, 40 %, 50 %, 60 %, 70 %, 80%, 90% and 100 % ethanol. The samples were then resuspended in propyleneoxide for an hour after which the same volume of epoxy resin (EMbed 812, Product # 14120, EMS Inc.) was added to the suspension for infiltration and left undisturbed for 30 minutes. The infiltrated samples were spun down and put in the embedding mold of freshly prepared epoxy resin and allowed to polymerize in a 333 K oven for 24 hours.

It is interesting to note that whereas: the whole embedding process / negative-staining takes > 24 hours; and the cryo-sample preparation takes > 1 hour and involves use of special cryo-stages, the wrapping process can be carried out in < 5 minutes.

The embedded samples were then mounted in an ultra-microtome (Leica EM UC7) and gold (~90 nm thin) sections were cut using a diamond knife (Du Pont Inc.). Serial sections were collected on lacey carbon TEM grids and observed in a CM100 TEM (FEI Company, Hillsboro, OR) (see supplementary videos: 3SV1 and 3SV2).

Results and Discussion

The cross section of the PFG-wrapped bacteria was characterized by cutting 90 nm thick sections (slices) of wrapped bacteria using a microtome (EM UC7, Leica, Inc.) (see supplementary videos: 3SV1 and 3SV2). These sections were analyzed under the TEM (CM100, 100 kV, FEI Inc.). 90 ± 10% of the bacteria were fully wrapped (Figures 3.3), while the others were partially wrapped.

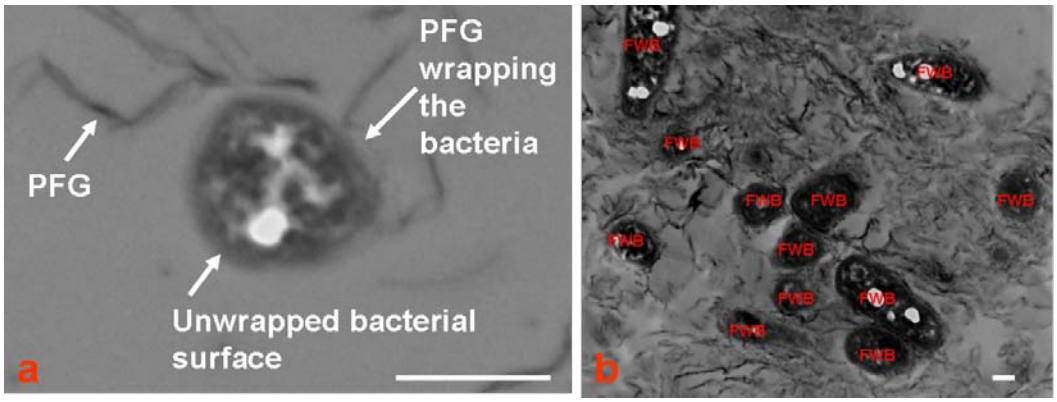

Figure 3-3 (a) High resolution cross-sectional TEM images showing clear distinction between unwrapped and wrapped surface of a bacterium. (b) Sample TEM image of the resin-embedded bacterial cross-sections showing the fully wrapped bacterium (FWB) and the partially wrapped bacterium (PWB): On an average 90 % of the wrapped bacteria were fully wrapped.

The high wrapping efficiency of the process is attributed to (a) the larger area (~2000 μm^2) of the PFG sheets, compared to the bacterial surface area (~2 μm^2) (see supplementary videos: 3SV1 and 3SV2) and (b) the higher concentration of PFGs in comparison to bacteria. A majority of the cells were wrapped with multilayered PFG sheets 2 to 5 nm thick (corresponding to 1 to 7 GO layers (CA is 1 nm) [30]) as shown in Figure 3.4a (also see Figure 3.5).

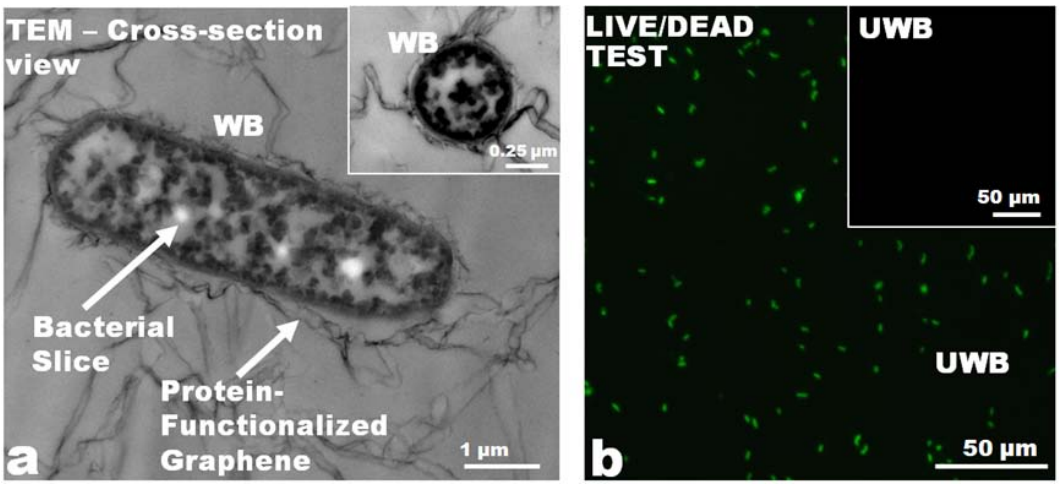

Figure 3-4 (a) TEM images of the 90 nm sections of wrapped bacteria showing the hermetic nature of the PFG wraps. Inset shows a lateral cross section of a wrapped bacterium. (b)

Live/dead tests on the bacteria just before wrapping via Syto-9 (green fluorescence, live, shown by panel b) and PI (red fluorescence, dead: shown by inset) staining showing most of the bacteria to be alive.

The thicker sheets are expected to exhibit a higher impermeability, while maintaining electron transparency [21, 22]. Further, the wrapped sheets conformed to the cell geometry (Figure 3.4a and inset; also see Figure 3.5), as expected for thin graphenic sheets due to their relatively flexible C−C bonds [16]. Since the bacterial sections in Figure 3.4a are open, they dehydrate in TEM vacuum, producing wrinkles on PFGs and gaps between PFGs and bacterial cell walls [31].

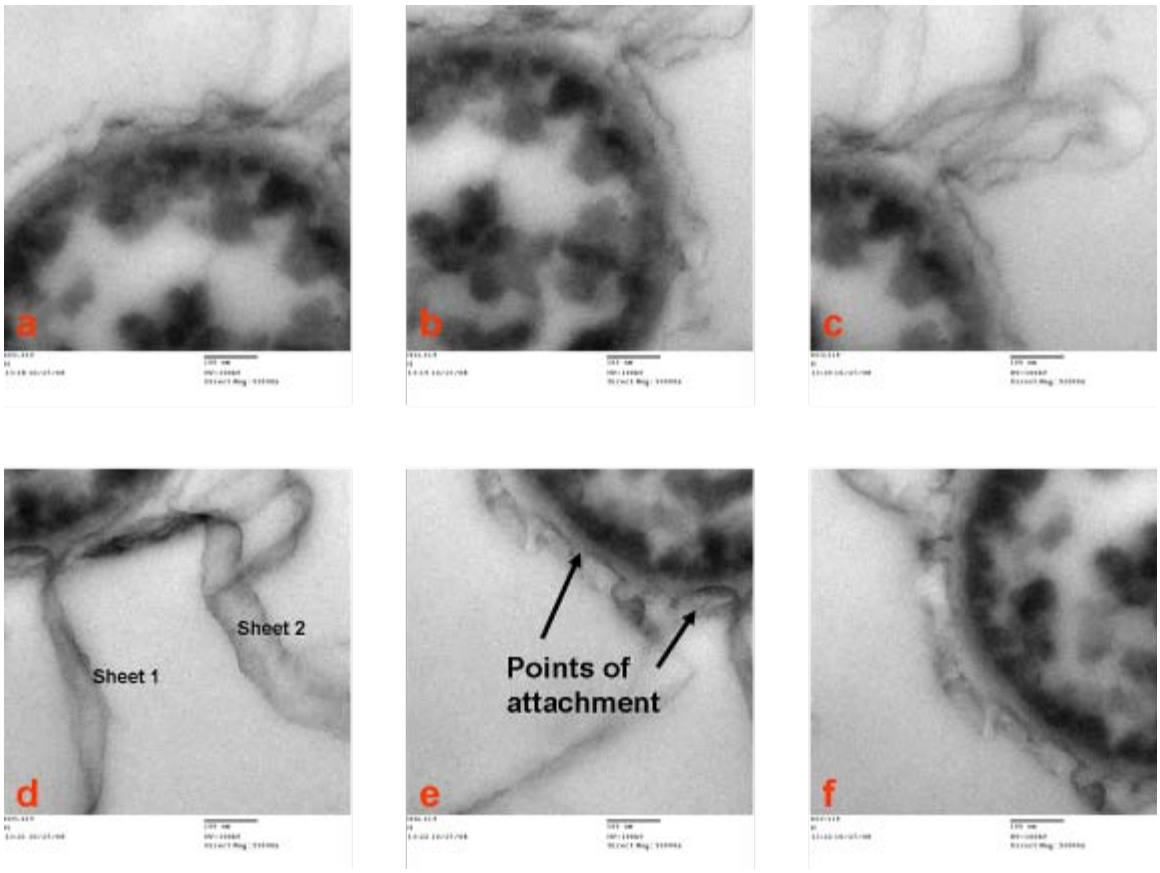

Figure 3-5 (a-e) Series of high resolution cross-sectional TEM images showing close ups of the surface of the PFG-wrapped bacteria shown in Figure 3.4a – top inset. These images demonstrate the hemetic nature of the PFG wraps. Scale bars correspond to 500 nm.

A live/dead test was conducted on the bacteria immediately before the wrapping process to confirm that the bacteria were alive (Figure 3.4b, inset) with intact cell wall [32]. This was important to make sure that the bacteria studied were completely hydrated. Owing to the impermeability of the PFG wraps, a live/dead test could not be conducted postwrapping.

For studying the effectiveness of graphenic wrapping under TEM conditions, the cells were immobilized on 100 nm thick silicon nitride (Si_3N_4) windows, followed by encasing the exposed face with PFG sheets. In a typical experiment, 20 wrapped or unwrapped bacteria (from a fresh culture), immobilized on the Si_3N_4 window, were analyzed. It is important to note that, even in the same culture, different bacteria are at different stages of the cell cycle resulting in slight variations in their spatial dimensions [32]. The average dimensions of the native bacteria were first recorded via an optical microscope at atmospheric pressure. The TEM micrographs were subsequently obtained after 5 (minimum time to start collecting images after stage insertion and microscope focus/contrast optimization), 15, and 20 min with the following conditions: vacuum of 10^{-5} Torr, incident current density of 150 A/cm^2, 100 kV electron beam, 1 pA probe current, 13500X magnification, spot size 1.5 μm illumination diameter (CM100 spot size # 6). For study of the electron-beam-induced damage, the side of the window with the bacteria was oriented toward the electron beam with the electron beam on at all times, while for exclusive vacuum study, the samples were oriented such that the electrons hit the Si_3N_4 layer before the bacteria, with the only electron flux exposure during image acquisition (30 s for the 1024 × 1024 pixels). Under TEM, the samples were examined for (a) ability to resolve the cell wall, (b) retention of the bacterial dimensions, and (c) permeability (under vacuum and vacuum plus electron bombardment).

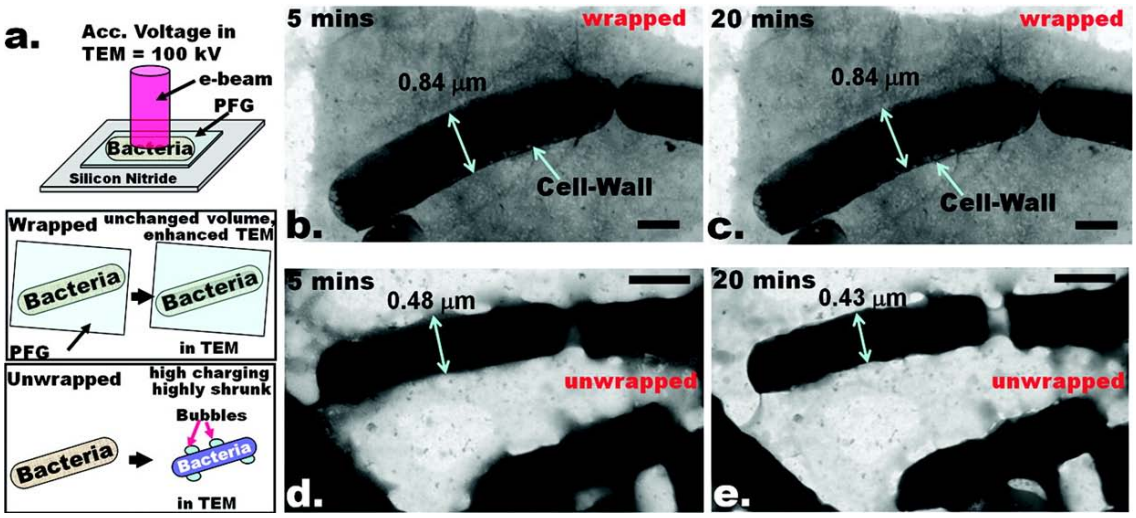

Figure 3-6 (a) PFG wrapping of bacteria prohibits shrinking under TEM. (b, c) Representative TEM images of wrapped bacterium (WB on 100 nm thick Si_3N_4 windows) exhibits no shrinkage from the original size after 5 and 20 min exposure. (d, e) Representative unwrapped bacteria (UWB) exhibit 75% shrinkage after only 5 min under TEM vacuum (minimum time to obtain micrograph). Extensive bubbling is also observed during imaging, attributed to boiling of the volatile component of the cell's intracellular region (see videos 3SV3, 3SV4, 3SV5, 3SV6 and 3SV7). Scale bar = 500 nm. Note that under the same conditions, the cell wall of the wrapped bacteria is clearly discernible. This is attributed to significantly reduced charge accumulation due to the conductive PFGs (π electrons are highly conductive).

The TEM micrographs of the PFG wrapped bacteria show that the bacterial cell wall and intracellular structure are clearly discernible (Figure 3.6, see Figure B1 in Appendix B). This is attributed to (a) the high density of conductive π electrons in the PFG sheets, which reduces the localized charge buildup, [22, 33] and (b) the high thermal conduction of the PFG sheet, which dissipates the heat generated from electron bombardment [9, 22, 33]. In contrast, the TEM micrographs of the unwrapped bacteria under the same conditions exhibited charging, as evident from the dark images of the bacteria. Further, the cell wall and the other intracellular structure of the bacteria are unrecognizable.

Table 3-1 Average dimensions of the wrapped / unwrapped *Bacillus subtilis* immobilized on Si_3N_4 grids upon exposure to high vacuum and electron beam exposed environment of the TEM. All dimensions are in µm.

	Average Dimensions of Wrapped bacteria upon exposure to a conjoined effect of UHV and electron beam			Average Dimensions of Un-Wrapped bacteria upon exposure to a conjoined effect of UHV and electron beam		
	Length	Breadth	Area	Length	Breadth	Area
No exposure	3.438 ± 0.028	0.843 ± 0.159	2.897 ± 0.525	3.233 ± 0.586	0.846 ± 0.151	2.735 ± 0.959
~ 5 minutes exposure	3.310 ± 0.095	0.753 ± 0.139	2.492 ± 0.138	2.867 ± 0.234	0.459 ± 0.057	1.316 ± 0.017
~ 15 minutes exposure				2.761 ± 0.235	0.459 ± 0.057	1.267 ± 0.019
~ 20 minutes exposure				2.761 ± 0.194	0.450 ± 0.057	1.242 ± 0.003

Table 3-2 Average dimensions of the wrapped / unwrapped *Bacillus subtilis* immobilized on Si_3N_4 grids upon exposure to UHV environment of the TEM. All dimensions are in µm.

	Average Dimensions of Wrapped bacteria upon exposure to the exclusive effects of UHV			Average Dimensions of Un-Wrapped bacteria upon exposure to the exclusive effects of UHV		
	Length	Breadth	Area	Length	Breadth	Area
No exposure	3.438 ± 0.028	0.843 ± 0.159	2.897 ± 0.525	3.233 ± 0.586	0.846 ± 0.151	2.735 ± 0.959
~ 5 minutes exposure	3.164 ± 0.063	0.828 ± 0.128	2.620 ± 0.356	2.864 ± 0.210	0.545 ± 0.034	1.619 ± 0.086
~ 15 minutes exposure				2.794 ± 0.115	0.490 ± 0.047	1.378 ± 0.06
~ 20 minutes exposure				2.718 ± 0.120	0.489 ± 0.05	1.339 ± 0.04

Next, we analyzed unwrapped and wrapped cells for their size consistency under TEM. As mentioned above, the first TEM micrograph for each sample was obtained after the sample had resided in the TEM chamber for 5 min under a vacuum of 10^{-5} Torr; thus it depicts only the effect of vacuum on the bacteria. For the unwrapped bacteria, the initial average areal size (20

cells) at atmospheric pressure was 2.73 ± 0.96 μm^2 (3.23 ± 0.59 × 0.85 ± 0.15 μm^2), which reduced to 1.32 ± 0.02 μm^2 (2.87 ± 0.23 × 0.46 ± 0.06 μm^2) and 1.24 ± 0.003 μm^2 (2.76 ± 0.19 × 0.45 ± 0.06 μm^2) after 5 and 20 min of exposure to vacuum and continuous electron beam exposure (Figure 3.6 and Table 3.1). The observed 76% reduction in volume is attributed to the efflux of the internal hygroscopic intracellular molecules due to exposure to the high vacuum in the TEM column (10^{-5} Torr) and due to the electron beam induced damage of the cell wall. Further, as shown in supplementary videos 3SV4, 3SV5, 3SV6 and 3SV7, the unwrapped bacteria also produced bubbles on the cell wall, attributed to the "boiling" of the intracellular volatile components under high vacuum [31, 33]. The high bubble formation in the unwrapped bacteria along with the charge buildup mentioned above indicate that the bacterial cell wall was being damaged significantly more than for the wrapped bacteria [2]. In stark contrast, no change in the area (2.897 ± 0.565 μm^2 (3.438 ± 0.028 × 0.843 ± 0.159μm ^{2})) or structure was observed for fully wrapped bacteria after 20 min of vacuum and electron beam exposure (Figure 3.6; see supplementary video 3SV3 and Tables 3.1 and 3.2). The least count of our measurements was 10 nm (for FEI-CM100 TEM). After 20 min of vacuum/electron-beam exposure, the unwrapped bacteria were expected to be dry. This was vindicated by the experimentally observed volume percentage of volatile matter in bacteria of 76% (assuming isotropic cross-sectional shrinkage), consistent with literature [32, 34]. Further assuming that the majority of volatile matter is water, the water retention achieved by PFG wrapping was 350% volume (dry basis). This retention of intracellular volatile matter by the ultrathin graphenic wrapping is attributed to (a) the high impermeability of the graphenic lattice, where the high π-electron density on the carbon rings repels molecules and does not allow even helium to pass through [16] and (b) high yield strength of graphene, where the lattice atoms are covalently linked in honeycomb structure, bestowing it with high stiffness [16, 17, 23]. Expectedly, for the partially wrapped bacteria we observed 5−10% volume shrinkage (assuming the bacterial shrinkage to be radially isotropic), which was attributed to the out-diffusion through unwrapped regions between the overlapping sheets and through the vacancy defects on GO from the harsh acid treatment (see supporting video 3SV7 and Figure B1 in the Appendix B).

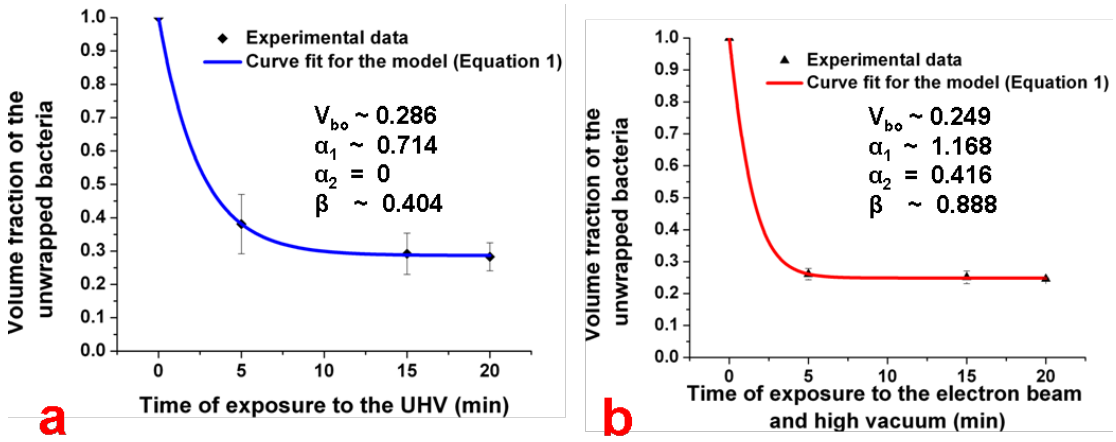

Figure 3-7 Efflux of intracellular matter in partially wrapped/unwrapped bacteria. (a, b) Curve fit of the model described in eq 1 with the normalized volume fraction shrinkage for the unwrapped bacteria exposed to vacuum and to vacuum plus electron beam. The error bars are the standard deviation of 20 measurements.

The mass-transfer (MT) resistance for release of volatile intracellular components from the bacteria is inversely proportional to the Darcian permeability, k, of the bacterial membrane [35]. Further, the electron-flux-induced damage of cell wall is expected to open more MT channels, thus increasing the effective permeability. A simple bacterial-shrinkage model was constructed

$$\mathrm{MT} \propto \frac{k}{R} C_w + \frac{AI}{\lambda} C_w C_T$$

where k is the Darcian permeability, A is the electron-beam damage factor, C_w and C_T are the water and total concentration in a bacterium, R is the radius of the bacterium, I is the electron beam current, and λ is the latent heat of vaporization. This gives

$$V = \frac{V_{B0} + \alpha_1 \exp(-\beta t)}{1 + \alpha_2 \exp(-\beta t)} \qquad (1)$$

where V_{B0} is the volume fraction of completely dehydrated bacteria, α_1 and β are constants inversely proportional to membrane permeability, and α_2 is a constant proportional to

the additional permeability caused by electron-beam-induced membrane damage. Additionally, the initial rate of volume shrinkage

$$\left.\frac{dV}{dt}\right|_{t=0} = (V_{B0} + \alpha_1)\frac{\alpha_2\beta}{(1+\alpha_2)^2} - \frac{\alpha_1\beta}{(1+\alpha_2)} = P^D$$

gives combined permeability (P^D, Darcian and electron-beam induced permeability).

For unwrapped bacteria, the values of V_{B0}, α_1, α_2, and β were 0.29, 0.71, 0, and 0.40 min^{-1} for the effects of vacuum. Further, the Darcian permeability (with $\alpha_2 = 0$) is calculated to be 7.6×10^{-9} m/s (consistent with literature, [36] see Appendix B for details). For the combined effect of the electron beam and vacuum, the values of V_{B0}, α_1, α_2, and β were 0.25, 1.17, 0.42, and 0.89 min^{-1} (Figure 3.7, see Appendix B). The combined permeability, P^D 20.5×10^{-9} m/s, was an order of magnitude higher than that for the only vacuum exposure, reaffirming the adverse effects of the electron beam. It is important to note that the curve fits shown in Figure 3.7 are an extrapolation of the three data points, which were used to measure the Darcian permeability. The wrapped bacteria exhibited no discernible volume change; therefore the permeability was practically zero. Theoretically, if a monolayer graphene sheet wraps a bacterium under 10^{-5} Torr pressure, it experiences 1 atm pressure difference. Under this pressure difference, graphene (strain = 0.26%) [16] will stretch by 4.38 nm. With an elastic modulus of 400 N/m, the average lateral force on graphene will then be 1.752 μN (=EAx) an d the net force across the membrane of a bacterium would be 0.46 μN (=ΔP $A_{bacteria}$). In the current study, the graphenic multilayers with or without defects are expected to exhibit a higher resistance to stretching than graphene monolayers [21]. This extrapolation from *Bunch et al* [16] is consistent with the observed retention of the original volume of the PFG-encased bacteria under TEM (Figure 3.6). This further indicates that there was no slippage of the sheets either from the substrate or between different layers in the time scale of our measurements. It is pertinent to note that the electron transparency of graphene can cause electron-bombardment-induced hydrolysis of bacterial water to produce hydrogen (see Appendix B) [33]. However, further studies are required to evaluate the effect of hydrolysis. Futuristically, the graphene-

encased systems could benefit from covalently sealing (bonding) the overlapped graphene sheets to reduce intralayer diffusion (from between sheets).

Conclusion

In conclusion, we have demonstrated that bacteria can be encased within graphenic chamber by wrapping them with PFG. The unique structural, chemical, and electrical properties of graphene can then be applied to significantly improve their TEM imaging as compared to imaging native unwrapped cells: for example, (a) "wet" state TEM imaging of cells can be achieved; (b) bacteria can be imaged with original, uncontracted dimensions; (c) the bacterial volatile content can be retained; (d) internal bacterial structures, such as the cell wall, can be clearly distinguished in comparison to unwrapped bacteria under similar TEM conditions; (e) electrostatic charge buildup can be significantly reduced. Under similar TEM imaging, the unwrapped bacteria shrank by 76% and exhibited significant charge buildup. Postwrapping, the Darcian permeability of bacteria reduced from ~720 nm/s to practically zero. The specific graphenic properties which enable the above results include high impermeability, electron transparency, high conductivity, structural strength, and conforming flexibility. We envision that encasing wet samples within graphenic chambers will potentially enable real-time imaging of fluid dynamics, liquid suspensions of nanoparticles, proteins, and live cell's biochemical activity.

Acknowledgements

V.B. is grateful for the financial support from NSF (CMMI-0939523), Terry C. Johnson Center for Basic Cancer Research, and KSU start-up. V.B. thanks Dr. Praveen Vadlani (KSU) for providing the Bacillus subtilis samples and Dr. David Moore (KU) for help with TEM and FESEM.

References

1. Williams, D.B., Carter, C.B. Transmission electron microscopy (*Springer*, 2009).

2. Cellular electron microscopy, Volume 79 (Methods in Cell Biology) (ed. Mcintosh, J.R.) (*Academic Press*, 2007).

3. Ayache, J., Beaunier, L., Boumendil, J., Ehret, G. & Laub, D. Sample preparation handbook for transmission electron microscopy: techniques (*Springer*, 2010).

4. Geim, A.K. & Novoselov, K.S. The rise of graphene. *Nat. Mater.* **6**, 183-191 (2007).

5. Bunch, J.S., Verbridge, S.S., Alden, J.S., van der Zande, A.M., Parpia, J.M., Craighead, H.G. Impermeable atomic membranes from graphene sheets. *Nano Lett.* **8**, 2458-2462 (2008).

6. Gomez-Navarro, C., Burghard, M. & Kern, K. Elastic properties of chemically derived single graphene sheets. *Nano Lett.* **8**, 2045-2049 (2008).

7. Tsoukleri, G., Parthenios, J., Papagelis, K., Jalil, R., Ferrari, A.C., Geim, A.K. Subjecting a graphene monolayer to tension and compression. *Small* **5**, 2397-2402 (2009).

8. Castro Neto, A.H., Guinea, F., Peres, N.M.R., Novoselov, K.S. & Geim, A.K. The electronic properties of graphene. *Rev. Mod. Phys.* **81**, 109-162 (2009).

9. Balandin, A.A., Ghosh, S., Bao, W.Z., Calizo, I., Teweldebrhan, D., Miao, F. et al. Superior thermal conductivity of single-layer graphene. *Nano Lett.* **8**, 902-907 (2008).

10. Parsons, D.F., Matricardi, V.R., Mortez, R.C. & Turner, J.N. Electron microscopy and diffraction of wet unstained and unfixed biological objects. *Adv. Biol. Med. Phys.* **15**, 161-270 (1974).

11. Hui, S.W. & Parsons, D.F. Electron-diffraction of wet biological membranes. *Science* **184**, 77-78 (1974).

12. Parsons, D.F. Structure of wet specimens in electron-microscopy. *Science* **186**, 407-414 (1974).

13. Gai, P.L. Development of wet environmental TEM (Wet-ETEM) for in situ studies of liquid-catalyst reactions on the nanoscale. *Microsc. Microanal.* **8**, 21-28 (2002).

14. Heide, H.G. Electron microscopic observation of specimens under controlled gas pressure. *J. Cell Bio.* **13**, 147-152 (1962).

15. Williamson, M.J., Tromp, R.M., Vereecken, P.M., Hull, R. & Ross, F.M. Dynamic microscopy of nanoscale cluster growth at the solid-liquid interface. *Nat. Mater.* **2**, 532-536 (2003).

16. Daulton, T.L., Little, B.J., Lowe, K. & Jones-Meehan, J. In situ environmental cell-transmission electron microscopy study of microbial reduction of chromium(VI) using electron energy loss spectroscopy. *Microsc. Microanal.* **7**, 470-485 (2001).

17. Liu, K.L., Wu, C.C., Huang, Y.J., Peng, H.L., Chang, H.Y., Chang, P. et al. Novel microchip for in situ TEM imaging of living organisms and bio-reactions in aqueous conditions. *Lab on a chip* **8**, 1915-1921 (2008).

18. de Jonge, N., Poirier-Demers, N., Demers, H., Peckys, D.B. & Drouin, D. Nanometer-resolution electron microscopy through micrometers-thick water layers. *Ultramicroscopy* **110**, 1114-1119 (2010).

19. Peckys, D.B., Veith, G.M., Joy, D.C. & de Jonge, N. Nanoscale imaging of whole cells using a liquid enclosure and a scanning transmission electron microscope. *PLoS ONE* **4**, (2009).

20. de Jonge, N., Peckys, D.B., Kremers, G.J. & Piston, D.W. Electron microscopy of whole cells in liquid with nanometer resolution. *Proc. Natl. Acad. Sci. U.S.A.* **106**, 2159-2164 (2009).

21. Leenaerts, O., Partoens, B. & Peeters, F.M. Graphene: A perfect nanoballoon. *App. Phys. Lett.* **93**, (2008).

22. Wilson, N.R., Pandey, P.A., Beanland, R., Young, R.J., Kinloch, I.A., Gong, L. et al. Graphene Oxide: Structural analysis and application as a highly transparent support for electron microscopy. *ACS nano* **3**, 2547-2556 (2009).

23. Lee, C., Wei, X.D., Kysar, J.W. & Hone, J. Measurement of the elastic properties and intrinsic strength of monolayer graphene. *Science* **321**, 385-388 (2008).

24. Beveridge, T.J. & Murray, R.G.E. How thick is the *bacillus-subtilis* cell-wall. *Curr. Microbiol.* **2**, 1-4 (1979).

25. Mohanty, N. & Berry, V. Graphene-based single-bacterium resolution biodevice and DNA transistor: interfacing graphene derivatives with nanoscale and microscale biocomponents. *Nano Lett.* **8**, 4469-4476 (2008).

26. Hummers, W.S. & Offeman, R.E. Preparation of graphitic oxide. *J. Am. Chem. Soc.* **80**, 1339-1339 (1958).

27. Archibal, A.R. & Coapes, H.E. The interaction of concanavalin-A with teichoic Acids and bacterial walls. *Biochem. J.* **123**, 665-667 (1971).

28. Kim, J., Cote, L.J., Kim, F. & Huang, J.X. Visualizing graphene based sheets by fluorescence quenching microscopy. *J. Am. Chem. Soc.* **132**, 260-267 (2010).

29. Prausnitz, J.M., Lichtenthaler, R.N., Azevedo, E.G. Molecular thermodynamics of fluid-phase equilibria (*Prentice Hall*, 1998).

30. Bouckaert, J., Loris, R., Poortmans, F. & Wyns, L. Crystallographic structure of metal-free concanavalin A at 2.5 angstrom resolution. *PROTEINS: Structure, Function, and Bioinformatics* **23**, 510-524 (1995).

31. Egerton, R.F., Wang, F. & Crozier, P.A. Beam-induced damage to thin specimens in an intense electron probe. *Microsc. Microanal.* **12**, 65-71 (2006).

32. Lodish, H., Berk, A., Zipursky, L., Matsudaira, P., Baltimore, D., Darnell, J. Molecular cell biology (*W. H. Freeman*, 1999).

33. Egerton, R.F., Li, P. & Malac, M. Radiation damage in the TEM and SEM. *Micron* **35**, 399-409 (2004).

34. Bratbak, G., Dundas, I. Bacterial dry-matter content and biomass estimations. *Appl. Environ. Microbiol.* **48**, 755-757 (1984).

35. Incropera, F.P. Fundamentals of heat and mass transfer (*Wiley*, 2006).

36. deMaranon, I.M., Gervais, P. & Molin, P. Determination of cells' water membrane permeability: Unexpected high osmotic permeability of Saccharomyces cerevisiae. *Biotechnol. Bioeng.* **56**, 62-70 (1997).

37. Meyer, J.C., Girit, C.O., Crommie, M.F., Zettl, A. Imaging and dynamics of light atoms and molecules on graphene, *Nature* **454**, 319-322 (2008)

Chapter 4 - Bio-compatible, robust free-standing paper composed of TWEEN/graphene composite

Abstract

A stable, biocompatible, free-standing "paperlike" material composed of polyoxyethylene sorbitan laurate (TWEEN) and reduced graphene oxide platelets is presented. The TWEEN paper is highly stable in water (no leakage of TWEEN) and sufficiently robust to be handled by hand without breaking. Furthermore, the material is noncytotoxic to three mammalian cell lines and inhibits nonspecific binding of Gram-positive bacteria.

Published as

Park, S., Mohanty, N., Suk, J.W., Nagaraja, A., An, J., Piner, R.D., Cai, W., Dreyer, D.R., Berry, V., Ruoff, R.S., "Biocompatible, robust free-standing paper composed of a TWEEN/Graphene composite." *Advanced Materials*, **6** 1736-1740 (2010)

Introduction

Nonspecific binding (NSB), a random adsorption of biocomponents such as proteins and bacteria on noncomplementary materials, is one of the biggest problems in biological applications including biosensors, protein chips, surgical instruments, drug delivery, and biomedicine. Polyoxyethylene sorbitan laurate (TWEEN), a commercially available chemical with aliphatic ester chains, has shown promise as a medical material and in overcoming problems associated with NSB [1–4]. However, stability during solution-based processing and uniformity of the materials that have TWEEN coating on flat substrates or nanomaterials using the selfassembled-monolayer (SAM) method has been an important issue. Further, biocompatible materials with high strength are important for several medical applications including stents, nail implants, and strong invasive instruments. Here, we present the production of a free-standing "paperlike" material composed of TWEEN and reduced graphene oxide (RGO) platelets and obtained by simple filtration of a homogeneous aqueous colloidal suspension of TWEEN/RGO hybrid. The "TWEEN paper" was highly stable in water without leakage of TWEEN and is compliant and sufficiently robust to be handled by hand without breaking. Furthermore, the TWEEN paper was noncytotoxic to three mammalian cell lines and biocompatible, inhibiting nonspecific binding of Gram-positive bacteria [5]. In contrast, RGO paper without TWEEN showed nonspecific bacterial binding.

TWEEN is composed of three chemical parts (Figure 4.1a): aliphatic ester chains that can prevent NSB of biomolecules, three-terminal hydroxyl groups that are hydrophilic and can be chemically modified for further applications, and an aliphatic chain that can easily be adsorbed on a hydrophobic surface by noncovalent interaction. Protein microarrays on flat substrates with SAM of TWEEN [4] and highly sensitive biosensors, [1–3] built using field-effect transistor (FET) behavior of individual carbon nanotube (CNT) strands coated with TWEEN, have demonstrated that TWEEN can be effectively used to overcome NSB.

Graphene, an atom-thick layer composed of sp^2 carbons, has recently gained interest owing to its outstanding electrical, mechanical, and thermal properties [6–8]. Bioapplications using graphene sheets have been suggested for fundamental research as well as practical applications [9–11]. Hydrophobic graphene sheets, which are exfoliated from graphite/graphite-derivatives or produced by reduction of graphene oxide, have shown noncovalent adsorption by surfactants, resulting in the generation of their homogeneous colloidal suspensions [12–14]

Consequently, we thought that TWEEN might easily adsorb on the basal planes of graphene sheets. The high specific surface area of graphene (the calculated value is 2630 m^2 g^{-1}, which includes both surfaces) would also benefit its applications as a highly sensitive sensor for gas or biomolecules.

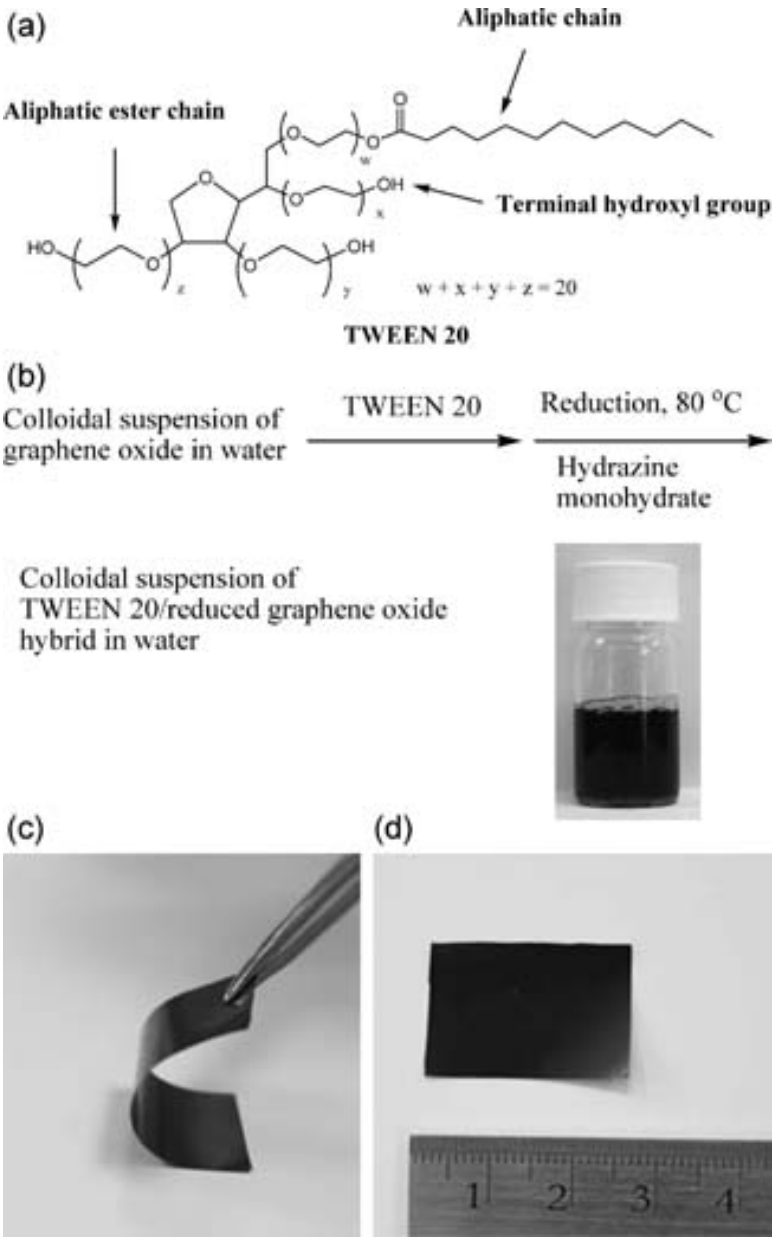

Figure 4-1 (a) The chemical structure of TWEEN 20. (b) Reaction scheme for the production of an aqueous colloidal suspension (photo, bottom right) of TWEEN/RGO-hybrid particles. (c,d) Photos of a TWEEN paper sample (scale in (d), cm).

Experimental methods

Production of colloidal suspension of TWEEN/RGO hybrid

GO was synthesized from natural graphite (SP-1, Bay Carbon, MI) by the modified Hummers method. Light brown colloidal suspensions (concentration, 1 mg GO/ 4 ml of water) of individual graphene oxide sheets in purified water (17.4 MΩ resistance) were prepared with the aid of ultrasound (*Fisher Scientific FS60 ultrasonic cleaning bath*) in 20-ml batches. TWEEN 20 (1 ml for 20 mg GO, *Sigma-Aldrich*) was added to the aqueous suspension of graphene oxide, producing a stable light brown suspension. After stirring with a Teflon-coated stirring bar for 10 min, hydrazine monohydrate (1 ml for 3 mg of GO, 98%, *Aldrich*) was subsequently added to the suspension. Additional stirring at 80 ^{o}C for 12 h yielded a black suspension of TWEEN/RGO hybrid (pH: ~7).

Production of TWEEN paper materials

After cooling the suspension above to room temperature, paper samples of TWEEN/RGO hybrid were made by filtration of the colloidal suspension through an Anodisc® membrane filter (47 mm in diameter, 0.02-μm pore size, *Whatman, Middlesex, UK*). The resulting papers were rinsed by addition of purified water and filtered 3 times. After the filtration, the papers were suction-dried for a day.

Stability test of TWEEN paper in water

We tested the stability of the TWEEN paper by weighing before and after washing it with water. As described in the manuscript, we first made TWEEN paper, then air-dried and weighed it (sample #0, 18.2 mg). Then we soaked sample #0 in water to find out if residual TWEEN molecules would leach out of the sample. The sample was soaked in water for 1 day, then was air-dried for 3 days and was weighed. This procedure was done 4 times, totally 4 days soaking (sample #0-1 (1 time washed, 17.6 mg), sample #0-2 (2 times washed, 17.6 mg), sample #0-3 (3 times washed, 17.6 mg), sample #0-4 (4 times washed, 17.6 mg)). After first time washing, the weight was decreased (18.2 mg vs. 17.6 mg) by possibly washing residual TWEEN out. Then, the sample was reached to steady state without further leakage of TWEEN molecules. Consequently, we washed other samples for totally 4 days (1 day for each soaking in clean bath, no drying after each soaking, 4 times) without measuring weight at each steps. After this

washing then air-drying for 3 days, we measured the weight of the paper sample (sample #1). Then, we again soaked sample #1 in water to test stability. After soaking in water for consecutive 4 days followed by drying under air for 3 days, the resulting paper sample (sample #2) showed the same weight as sample #1 did prior to this 4-days exposure in water (our balance is good to 0.1 mg).

Methods for cytotoxicity test

Three cell lines representing a broad range of characteristics viz. (1) Vero Cells (African Green Monkey Kidney Cells, *ATCC Cat. No.CCL-81*), (2) Embryonic Bovine Cells (*EB, Kansas State University*), (3) Crandell-Rees feline kidney (CRFK, *ATCC Cat. No. CCL-94*). Healthy frozen stocks of the Vero and the CRFK cell lines were thawed and passaged along with healthy, proliferating primary culture of EB cells, in freshly prepared multi-antibiotic laced Dulbecco's Modified Eagle's Medium (D-MEM) media with 7% fresh Fetal Bovine Serum (FBS), for adherent growth in sterile culture tubes Submitted to 3 (Fisher Inc.). After the first passage and the ensuing growth in a 5% CO_2 incubator maintained at 37 °C, with a relative humidity (RH) > 95% for 48 h, the adherent cells were detached via trypsinization and washed with fresh media and then Phosphate Buffer Saline (PBS) for at least 3 times. The paper samples were placed in a fresh multi-well culture plate in duplicates. A small quantity of the afore-obtained cells was seeded on the paper with concomitant addition of sterile media. The culture plates were placed in an incubator for 48 h, after which the cells were initially visualized under an upright optical microscope (*BX41, Olympus Inc.*). The cells were then stained with Calcein (shows green fluorescence on live cells by binding with calcium) and with Propidium Iodide (shows red fluorescence on dead cells by intercalating between the strands of DNA and RNA) for the confirmatory Live-Dead test. The stained cells were washed, fixed and observed under a Spinning Disc Confocal Microscope (*Olympus Inc.*).

Methods for blood agar test

A commercially obtained blood agar (5% sheep blood, *Cole- Parmer Inc.*) plate was incubated with the paper samples for 48 h to assess the potential hemolytic activity of the paper. The blood agar plate was then observed under an upright stereo-microscope (*Leica Inc.*) for signs of hemolysis (discolouration of the agar underneath and around the paper).

Methods for bacteria repellant test

Bacillus cereus cells (*ATCC 21634*) were cultured overnight in a nutrient broth media at 37 ^{o}C with constant agitation in an incubator-shaker (*Fisher-scientific Inc.*). The matured cells were pelleted down by centrifuging at 2000 rpm for 2 min in a table top micro-centrifuge (*Fisher-scientific Inc.*), washed repeatedly with deionized (DI) water (18.6 MΩ) and re-suspended in fresh DI water. The paper sample held tweezers was submerged completely in the DI water suspension of the Bacillus cereus cells for one min and subsequently washed with excess DI water for 10 sec and dried in a jet of dry nitrogen gas. The paper was observed under an optical microscope (*BX41, Olympus Inc.*) for further analysis. To further test the possible absence of bacteria on the paper, the after-treatment- paper was seeded in a fresh sterile liquid suspension of nutrient broth. After incubation at 37^{o} C in an incubator-shaker for 16 h, the culture was checked for bacterial growth by centrifuging at 11,000 g for 10 min in a table-top micro-centrifuge and monitoring for presence of a pellet.

Results and discussion

Graphite oxide (GO) was synthesized from natural graphite (*SP-1, Bay Carbon, MI, USA*) by the modified Hummers method [15]. A homogeneous black suspension of TWEEN 20/RGO hybrid with no particles visible to the naked eye has been produced by chemical reduction of an aqueous colloidal suspension of graphene oxide and TWEEN using hydrazine monohydrate (Fig. 4.1b, see Appendix C for details). On the other hand, reduction of aqueous graphene oxide suspension using hydrazine monohydrate without TWEEN produced black agglomerates that could not be redispersed by sonication or stirring [16]. This indicates that TWEEN plays a role as a surfactant for helping dispersion of RGO sheets in water. We confirmed that the chemical structure of TWEEN was not changed by the reaction with hydrazine monohydrate (see Appendix C, Figure 4.2). The presence of individual RGO sheets in the hybrid was confirmed by non-contact-mode atomic force microscopy (AFM; see Appendix C, Fig. 4.2).

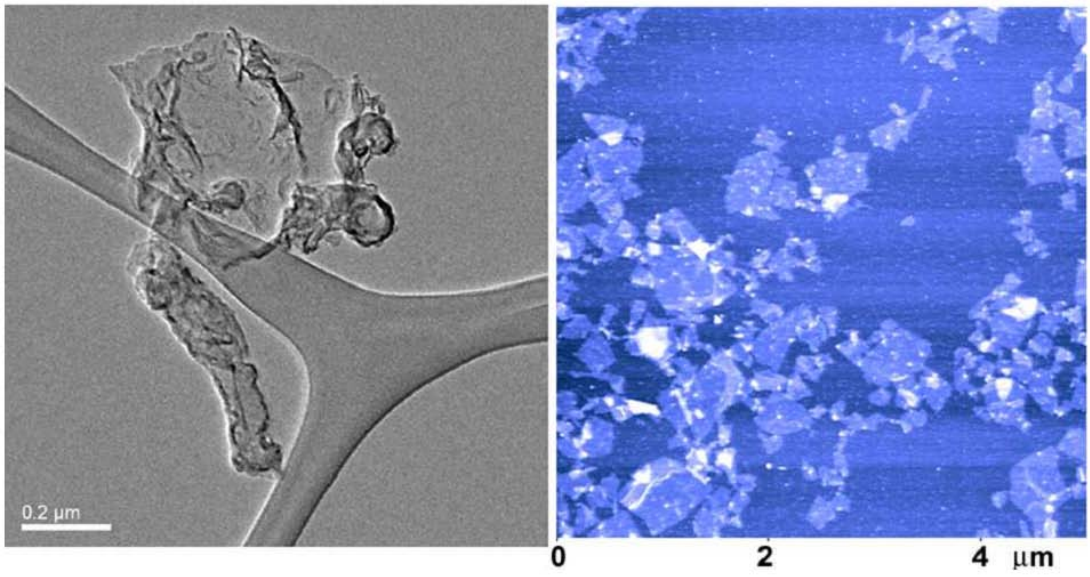

Figure 4-2 Left, a TEM image and right, an AFM image of the composite

Shiny black and compliant TWEEN-paper samples (Fig. 4.1 c,d) composed of the TWEEN/RGO particles were fabricated by filtration of the homogeneous aqueous suspension of TWEEN/RGO hybrid. Using the homogeneous suspension provides a very promising method for generating uniform performance of such paper-like materials. After harsh rinsing with water and subsequent air-drying, the weight of the resulting TWEEN paper was higher than that of the starting GO (e.g., 51.1 mg of TWEEN paper from 30.0 mg of starting GO material and 17.6 mg from 12.0 mg). The leakage of TWEEN, which is adsorbed on the hydrophobic surfaces, from materials is an important issue in terms of stability [4, 17]. To check the stability of the TWEEN paper in water, the washed and air-dried paper sample was further soaked for 4 days in water and then air-dried for 3 days. The weight of the resulting TWEEN paper was the same as that of the sample before further soaking in the measuring range of our balance (measurable to 0.1 mg), so TWEEN molecules are not leaked from the paper sample in water, or the leak is negligible.

The weight ratio of chemically reduced graphene oxide (without TWEEN, other conditions were the same as that for production of TWEEN/RGO hybrid describe above) relative to starting GO was ~65%, as measured for several separate reactions in our laboratory. That is, 19–20 mg of chemically reduced graphene oxide has usually been produced by reduction of

30 mg of starting GO. The weight ratio of RGO in the TWEEN paper relative to the starting GO would be similar to that of RGO in the system without TWEEN, meaning that ~51 mg of paper, which is produced from 30 mg of starting GO, contains 19–20 mg (37–39 wt%) of RGO. Thus, ~31–32 mg (61–63 wt%) in the TWEEN paper (~51 mg) should be contributed by TWEEN 20 and possibly trapped solvents in the paper samples. The thermogravimetric analysis (TGA) curve (Figure 4.3) of the air-dried TWEEN paper sample showed almost no weight loss before 100 °C. A weight loss (~48 wt% relative to the starting material) from 100 to 300 °C and a smaller weight loss (~14 wt% relative to the starting material) from 300 to 550 °C could be caused by loss of CO, CO_2, and H_2O by the decomposition of C-C and C=O bonds in TWEEN 20 and/or labile oxygen functional groups of RGO [15, 16] and, possibly, by evaporation of water molecules trapped in the paper sample. The remaining material (~38 wt% of the starting mass) at 550 °C in the TGA curve is close to that (37–39 wt%, calculated by the ratio of weight of the RGO to the starting material, see above) of RGO in the TWEEN paper sample.

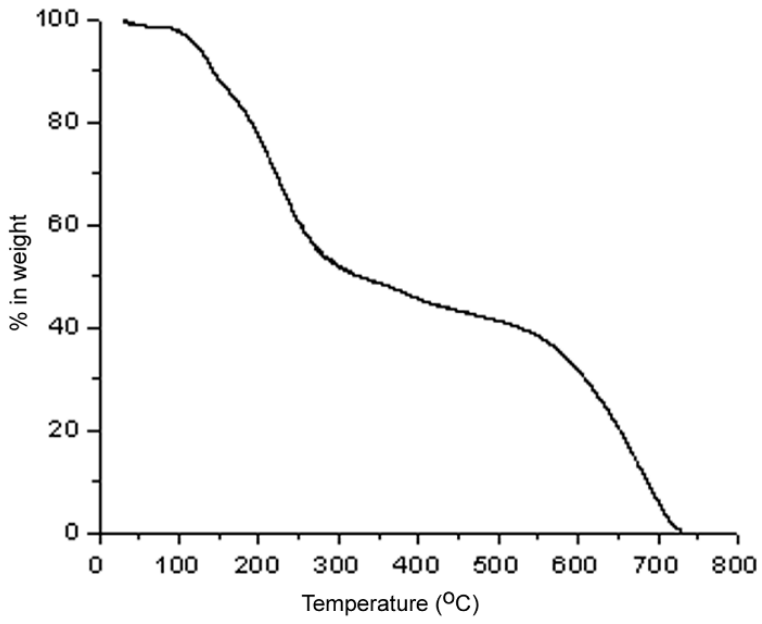

Figure 4-3 TGA curve of air-dried *TWEEN* paper sample

The TWEEN paper samples were sufficiently robust to be handled by hands and tweezers without breaking. We have measured the mechanical properties of the air-dried paper materials

weighing ~51 mg by tensile testing (five samples; Figure 4.4a and the Appendix C, Table C1). The TWEEN papers were brittle, similar to other graphene-based paper materials [8, 11, 18] and had a modulus in the range of 1.2–2.3 GPa in the "linear region" (this region is almost linear, thus here we refer to it as the linear region). The tensile strength of the TWEEN papers was 3.4–6.2 MPa and their strain was 0.2–0.4% (see Appendix C, Table C1).

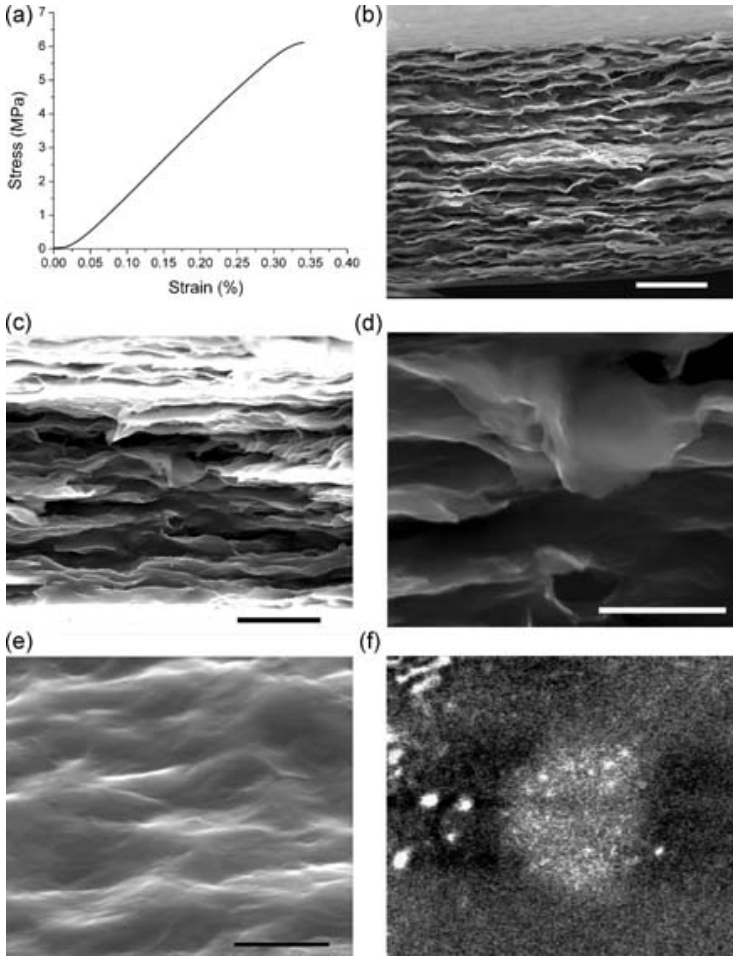

Figure 4-4 Mechanical properties of a TWEEN paper sample and images of SEM and Raman spectroscopy. (a) A stress–strain curve of the paper sample by tensile test. b–d) SEM images of a cross-section of broken sample by tensile test (b) (scale bar, 10 µm) and a sample fractured by tweezers at room temperature (c,d) (scale bars, 5 µm (c) and 2 µm (d)). (e,f) Surface images of the paper sample: an SEM image (e) (top view at an angle; scale bar, 2 µm), and a mapping image by micro-Raman spectroscopy (f) (scale bar, 6 µm).

While the surface of the RGO paperlike sample is electrically conductive,[19] the surface of TWEEN paper is electrically insulating. This could be caused by complete coating of electrically insulating TWEEN molecules on RGO platelets. Scanning electron microscopy (SEM) images of the cross-section of such an air-dried TWEEN paper samples (broken by the tensile test, Figure 4.4b, and separately fractured by tweezers, Fig. 4.4c and d, at room temperature) exhibited overall a layered structure of TWEEN/RGO hybrid (Figure 4.4b,c). However, determining the structural nature between TWEEN matrices and RGO platelets could be an interesting challenge for the future. The existence of thin "graphene sheets" in the composites was frequently found by SEM (Figure 4.4d). The thickness of a sample broken by the tensile test was ~30 μm (Figure 4.4b). The Raman spectrum of the surface of the air-dried paper sample showed two broad peaks at around 1345 and 1580 cm^{-1}. These two peaks would be contributed mainly by a D-band and a G-band from embedded RGO sheets, respectively [19, 20]. The Raman spectrum of free TWEEN 20 exhibited two weak broad peaks, only, at around 1290 and 1475 cm^{-1}, Although the surface of the TWEEN paper sample (Figure 4.4e) was slightly rough, the mapping images of the surface at around 1345 cm^{-1} and separately 1580 cm^{-1} showed uniform dispersion of RGO platelets in the TWEEN matrices at the surface of the paper sample (Figure 4.4f).

Cytotoxicity analysis of the TWEEN paper was carried out by investigating cell growth and proliferation [11] on the surface of the papers. Three cell lines representing a broad range of characteristics in cell growth were employed: i) Vero cells (African green monkey kidney cells)—robust cells with high propensity of growth and proliferation, ii) embryonic bovine (EB) cells—primary culture with a limited lifespan resembling the cells in vivo, and iii) Crandell–Rees feline kidney cells (CRFK)—finicky, delicate cells with relatively low growth rate and proliferation. After washing the cells with phosphate buffer saline (PBS), followed by their incubation on the TWEEN paper in the presence of a fresh culture media for 48 h, the three cell lines were analyzed for growth, structural properties, and vitality. A rough estimate of cell death is inferred from the transformation of the cell's native structure into a spherical shape and the floating of cells detached from the surface of the paper upon washing. The confirmatory live–dead test (calcein and propidium iodide staining) on the cells growing on the TWEEN paper

confirmed its noncytotoxicity, with >90% of the cells being alive after 48 h of exposure to the paper and forming a confluent monolayer on its surface (Figure 4.5), indicating cell vitality during growth.

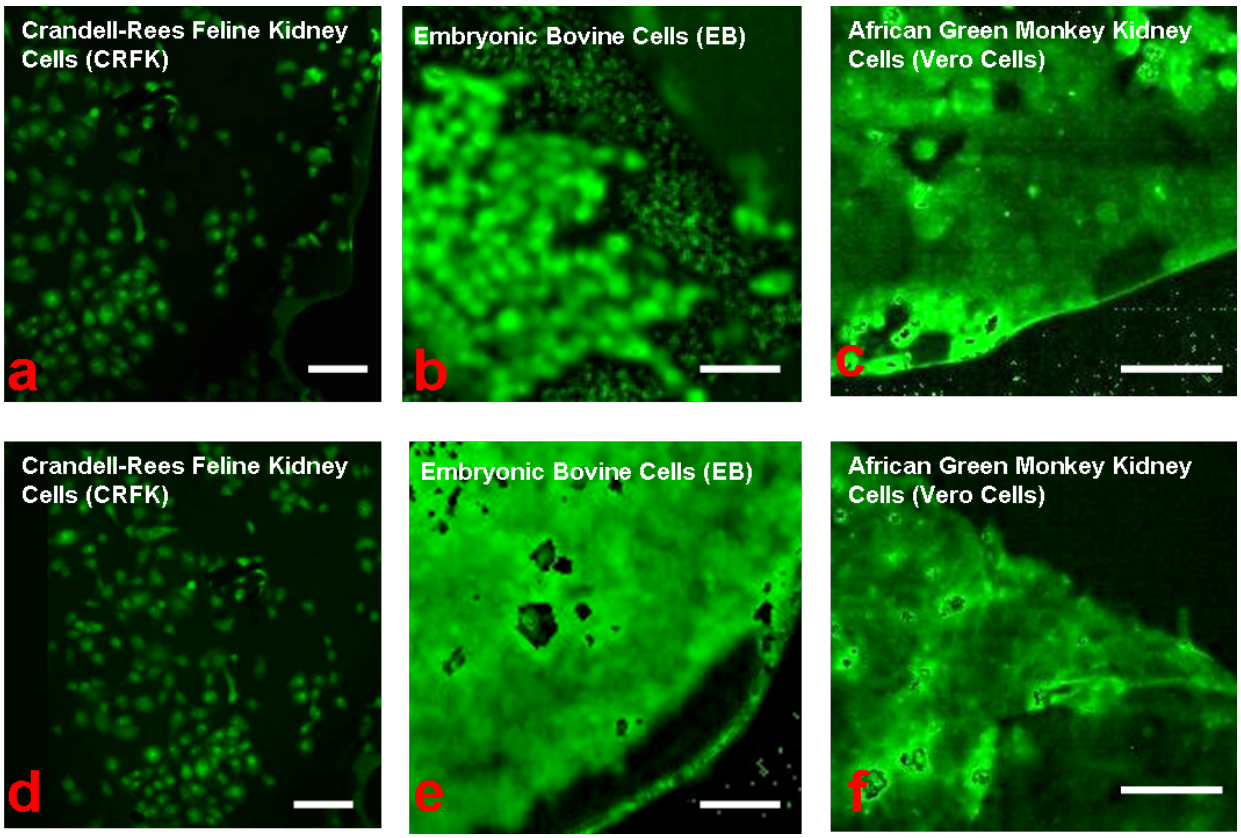

Figure 4-5 Cytotoxicity test for the TWEEN paper and the pristine RGO paper. Composite confocal microscopy images of the CRFK (a,d), the primary EB (b,e) and the Vero cells (c,f), grown for 48 h on TWEEN-paper (a–c) and RGO-paper (d–f) substrates, respectively, and subsequently stained with calcein (green) and propidium iodide (red) as a part of the standard live–dead test (scale bars, 20 µm).

Although TWEEN is known to degrade the cell membranes, the noncytotoxicity of TWEEN paper could be attributed to its firm incorporation into the RGO paper. These cytotoxicity tests were also conducted on the RGO paper without TWEEN, produced with the method explained in a previous publication [19]. As expected, the papers showed a consistent cell growth and proliferation with the cells retaining their native shape, and forming a confluent monolayer as

observed by the live–dead test. The observed noncytotoxicity of the RGO paper is consistent with an earlier report by *Chen et al.*, where mouse fibroblast cells were used [11]. Further, the two papers (TWEEN, and RGO paper) were non-hemolytic in blood-agar experiments (Figure 4.6). Blood cells in the agar exposed to the papers were found to be stable without any sign of lysis (and discoloration).

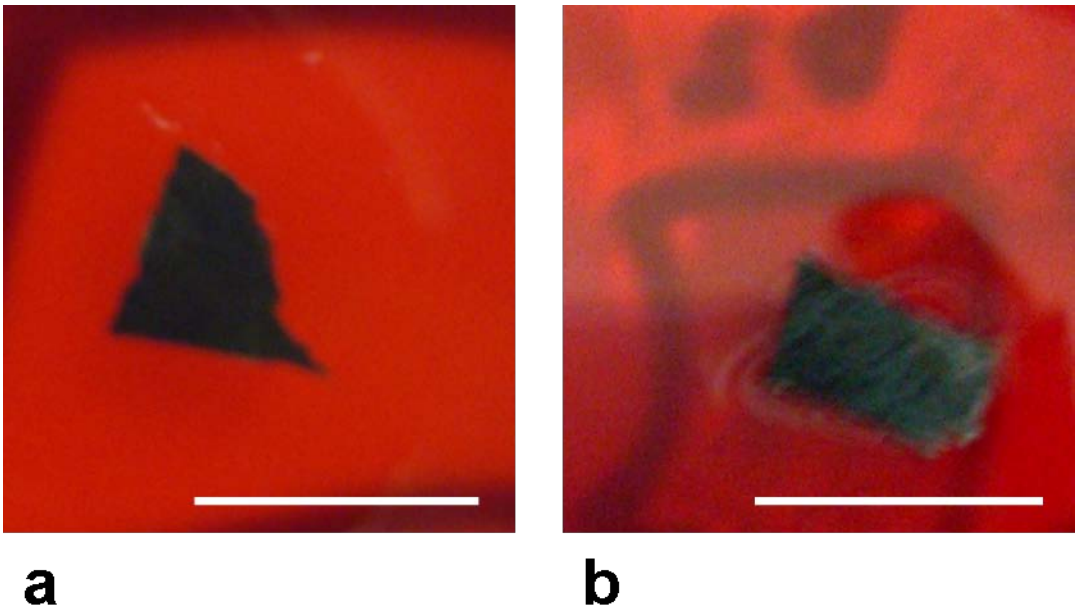

Figure 4-6 An optical microscope image of a sheep-blood-agar plate with (a) TWEEN paper and (b) RGO paper, showing non-hemolytic activity of both the papers (all scale bars correspond to 2 cm).

To study their NSB to microbes, the two papers were tested for bacterial interfacing. While the TWEEN paper inhibited NSB of Gram-positive bacteria, the RGO paper exhibited bacterial binding. Here, the papers were submerged in a suspension of washed Bacillus cereus cells in deionized (DI) water for 1 min and for 10 h (Figure 4.7, 4.8), rinsed with excess DI water for 10 s, dried in a slow jet of nitrogen and observed under an optical microscope. No bacterial cells attached on the surface of the TWEEN paper [3, 4] (Figure 4.7). To further confirm the absence of bacteria, the exposed papers were seeded in separate nutrient-broth media (10 mL) and incubated at 37 °C in an incubator-shaker for 16 h, followed by centrifugation

(11000 g (13 000 rpm) for 10 min) of the media-solution. No bacterial growth was observed, as deduced from the absence of pellet formation after centrifugation.

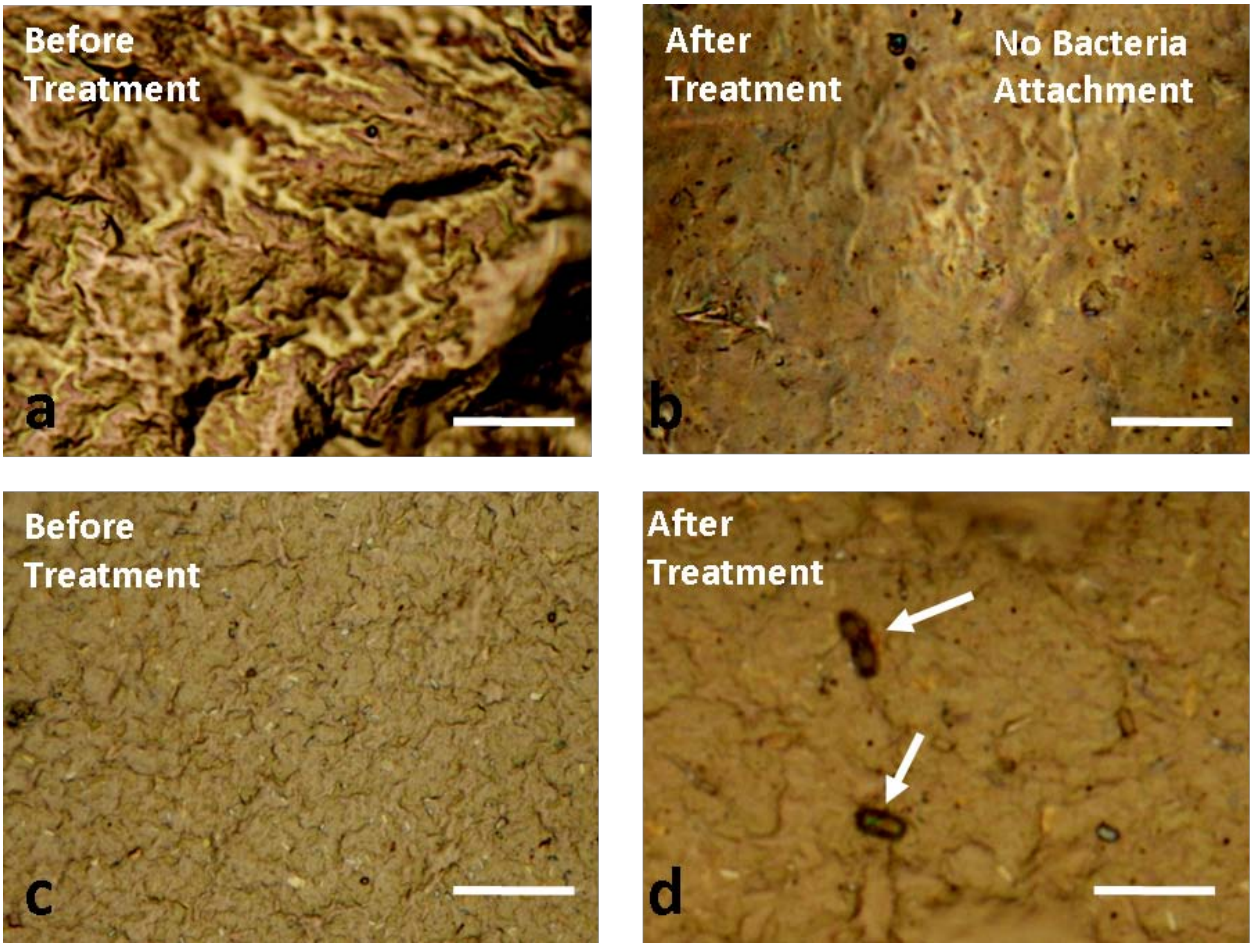

Figure 4-7 (a,b) Optical microscopy image of the TWEEN paper before and after the treatment with a DI-water suspension of the mature *Bacillus cereus* cells. The TWEEN paper shows no bacterial attachment. (c,d) Optical microscopy image of the RGO paper before and after the bacterial treatment. The RGO paper shows bacterial attachment (marked by arrows). All scale bars are 10 μm.

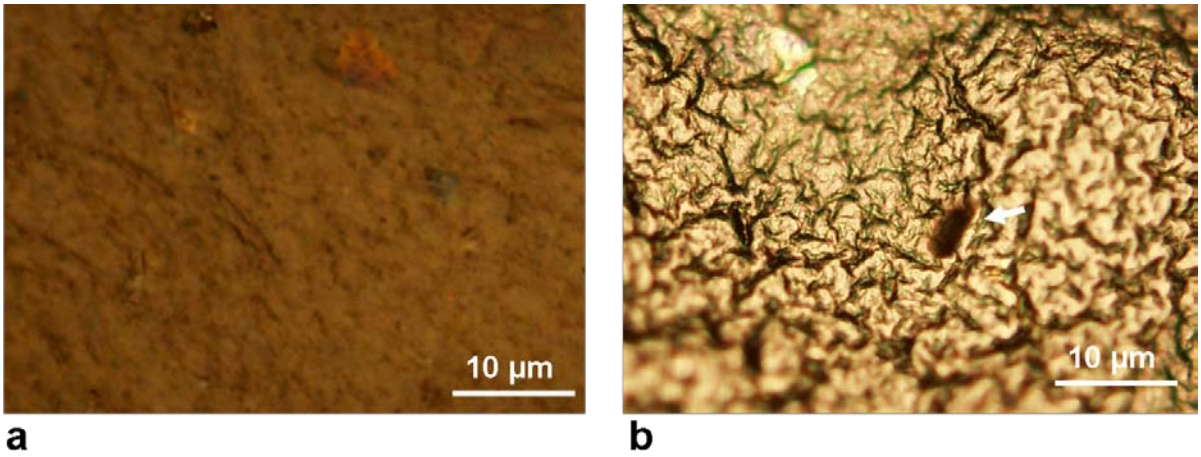

Figure 4-8 Optical micrographs of the TWEEN paper and RGO paper after the 10 hours of bacterial treatment. (a) Optical microscope image of the TWEEN paper after the treatment with a Nutrient broth suspension of the *Bacillus cereus* cells for 10 hours. The TWEEN paper shows no bacterial attachment. (b) Optical microscope image of the RGO paper after the treatment. The RGO paper shows bacterial attachment (marked by an arrow).

In contrast, the RGO paper exhibited bacterial attachment and subsequent bacterial growth in a sterile media solution. The difference in the cell adhesion properties between the bacterial cells and the mammalian cells for the TWEEN paper can be attributed to the dissimilarities between the Gram-positive-bacteria cell wall (thick, rigid peptidoglycan layer with teichoic acid moieties) and the cell membrane of the mammalian cells (lipid membrane with cell adhesion molecules (CAMs), including immunoglobulins, integrins, cadherins, selectins, and/or lymphocyte receptors) [21–23]. Further, after reducing the density of the CAMs on the Vero cells via trypsinization (tripsin proteolysis) of the CAMs, followed by a short exposure (1 min) to the papers, no cell adhesion was detected on the TWEEN and the RGO paper (see Appendix C, Figure C1). In conclusion, the TWEEN paper reduces the NSB of the bioentities, including the Gram-positive bacterial cells; while it allows adhesion and proliferation of the mammalian cells, which use CAMs to stick to the TWEEN paper [3, 4]. More work is necessary to confirm the bacterial cytotoxicity of TWEEN paper and to thoroughly characterize its interaction with the cell's surface proteins, teichoic acids, and peptidoglycan membrane.

Conclusion

In summary, we have fabricated a strong and biocompatible free-standing paper composed of TWEEN 20 and chemically reduced graphene oxide and demonstrated that the paper exhibits excellent stability in water and is compliant and is robust enough to be handled by hand without breaking. The TWEEN paper and the RGO paper were noncytotoxic to three mammalian cell lines, while only the TWEEN paper inhibited the NSB of bacterial cells. These results show that the macroscopic TWEEN-based paper materials and its derivatives can potentially function as effective components for medical applications including transplant devices, invasive instruments, and implants.

Acknowledgements

This work was supported by a startup package to R.S.R. by The University of Texas at Austin and by the Texas Nanotechnology Research Superiority Initiative (TNRSI)/SWAN. The work was also supported by a startup package to V.B. by Kansas State University.

References

1. So, H.-M. et al. Single-walled carbon nanotubes biosensors using aptamers as molecular recognition elements. *J. Am. Chem. Soc.* **127**, 11906-11907 (2005).

2. Byon, H.R. & Choi, H.C. Network single-walled carbon nanotube-field effect transistors (SWNT-FETs) with increased Schottky contact area for highly sensitive biosensor applications. *J. Am. Chem. Soc.* **128**, 2188-2189 (2006).

3. Chen, R.J. et al. Noncovalent functionalization of carbon nanotubes for highly specific electronic biosensors. *PNAS* **100**, 4984-4989 (2003).

4. Chi, Y.S., Byon, H.R., Choi, H.C. & Choi, I.S. A noncovalent approach to the construction of Tween 20-based protein microarrays. *ChemBioChem* **8**, 1380-1387 (2007).

5. Kleinsmith, L.J. & Kish, V.M. Principles of cell and molecular biology (New York, 1995).

6. Park, S. & Ruoff, R.S. Chemical methods for the production of graphenes. *Nat. Nanotechnol.* **4**, 217-224 (2009).

7. Geim, A.K. & Novoselov, K.S. The rise of graphene. *Nature Mater.* **6**, 183-191 (2007).

8. Dikin, D.A. et al. Preparation and characterization of graphene oxide paper. *Nature* **448**, 457-460 (2007).

9. Liu, Z., Robinson, J.T., Sun, X. & Dai, H. PEGylated nanographene oxide for delivery of water-insoluble cancer drugs. *J. Am. Chem. Soc.* **130**, 10876-10877 (2008).

10. Mohanty, N. & Berry, V. Graphene-based single-bacterium resolution biodevice and DNA transistor: Interfacing graphene derivatives with nanoscale and microscale biocomponents. *Nano Lett.* **8**, 4469-4476 (2008).

11. Chen, H., Muller, M.B., Gilmore, K.J., Wallace, G.G. & Li, D. Mechanically Strong, Electrically Conductive, and Biocompatible Graphene Paper. *Adv. Mater.* **20**, 3557-3561 (2008).

12. Li, X., Wang, X., Zhang, L., Lee, S. & Dai, H. Chemically derived, ultrasmooth graphene nanoribbon semiconductors. *Science* **319**, 1229-1232 (2008).

13. Xu, Y., Bai, H., Lu, G., Li, C. & Shi, G. Flexible graphene films via the filtration of water-soluble noncovalent functionalized graphene sheets. *J. Am. Chem. Soc.* **130**, 5856-5857 (2008).

14. Stankovich, S. et al. Stable aqueous dispersions of graphitic nanoplatelets via the reduction of exfoliated graphite oxide in the presence of poly(sodium 4-styrenesulfonate). *J. Mater. Chem.* **16**, 155-158 (2006).

15. Park, S. et al. Aqueous suspension and characterization of chemically modified graphene sheets. *Chem. Mater.* **20**, 6592-6594 (2008).

16. Stankovich, S. et al. Synthesis of graphene-based nanosheets via chemical reduction of exfoliated graphite oxide. *Carbon* **45**, 1558-1565 (2007).

17. Sigal, G.B., Mrksich, M. & Whitesides, G.M. Using surface plasmon resonance spectroscopy to measure the association of detergents with self-assembled monolayers of hexadecanethiolate on gold. *Langmuir* **13**, 2749-2755 (1997).

18. Park, S. et al. Graphene oxide papers modified by divalent ions--Enhancing mechanical properties via chemical cross-linking. *ACS Nano* **2**, 572-578 (2008).

19. Park, S. et al. Colloidal suspensions of highly reduced graphene oxide in a wide variety of organic solvents. *Nano Lett.* **9**, 1593-1597 (2009).

20. Yang, D. et al. Chemical analysis of graphene oxide films after heat and chemical treatments by X-ray photoelectron and Micro-Raman spectroscopy. *Carbon* **47**, 145-152 (2009).

21. Klebe, R.J. et al. Fibronectin-mediated attachment of mammalian-cells to polymeric substrata *Proteins at Interfaces: Physicochemical and Biochemical Studies*, Vol. **343** (Eds: J. L.Brash, T. A.Horbett), American Chemical Society, Washington DC p. 615 (1987)

22. Khoo, X. Et al. Directed assembly of PEGlated-peptide coatings for infection-resistant titanium metal J. Am. Chem. Soc. 131, 10992 (2009)

23. Dexter, S.J. et al. . A comparison of the adhesion of mammalian cells and Staphylococcus epidermidis on fibronectin-modified polymer surfaces *Biomed. Mater. Res. A* **56**, 222 (2001)

Chapter 5 - High-throughput, ultrafast synthesis of solution-dispersed graphene via a facile hydride chemistry

Abstract

Graphene's superior electrical, optical & mechanical characteristics and its continuously growing applications require concomitant development of graphene-processing-technology. Recently, graphene solution-dispersions have received great attention as they offer the possibility of easy graphene processing and directly employing graphene from solution into applications such as sensors, solar cells, biodevices, FETs etc. Here, we leverage the ability of sodium hydride to act both as a reducing agent and as a deprotonator to instantaneously (in few seconds) reduce graphene-oxide (GO) in methanol to graphene sheets and to deprotonate methanol to methoxy ions, where the methoxy ions then stabilize the graphene sheets in the residual methanol suspension at a yield of ~ 68 %. Further, this novel chemistry was found to be effective in producing reduced graphene oxide (RGO) with a higher ratio of sp^2 to sp^3 carbon densities, where the average sp^2 domains size increases from 2 nm to 3.5 nm after reduction. The graphene sheets exhibited a carrier mobility of 300-600 $cm^2/V{\cdot}s$.

Published as

Mohanty, N., Nagaraja, A., Armesto, J., and Berry, V., "High-throughput, ultrafast synthesis of solution-dispersed graphene via a facile hydride chemistry." *SMALL* **6** 226-231 (2010)

Introduction

Graphene is a single-atom-thick two-dimensional macromolecule with sp^2-bound carbon atoms [1] arranged in a honeycomb lattice. Recently, graphene has emerged as an attractive candidate for several applications, including ultrafast nanoelectronic devices, [2, 3] tunable spintronics, [4] ultracapacitors, [5] transparent conducting electrodes, [6, 7] single-molecule chemical sensors, [8] ultrasensitive biodevices, [9] and nanomechanical devices [10]. These applications have evolved from its atypical properties, such as weakly scattered ballistic transport of charge carriers behaving as massless fermions at room temperature, [3, 11] magneto-sensitive transport, [12–14] tunable bandgap,[15] quantum Hall effect at room temperature,[12–14] tunable optical transitions,[16, 17] exceptional mechanical strength,[18] megahertz characteristic frequency,[10] carrier collimation, and ultrahigh stiffness.

Graphene can be (1) synthesized on-substrate, (2) deposited on-substrate via mechanical processes, or (3) deposited on-substrate from solution. On-substrate synthesis includes high-temperature (>1000 °C) epitaxial growth on SiC, [19, 20] ruthenium [21] or chemical vapor deposition on nickel [22] and copper, [23] while mechanical deposition includes adhesive-tape exfoliation of highly oriented pyrolytic graphite (HOPG) and the ensuing transfer. The third process, which is based on on-substrate deposition from a graphene suspension, has several advantages including the large-scale production of reduced graphene oxide (RGO) and easy-to-apply chemical and physical manipulations for functionalization and directed deposition [24–28]. Graphene suspension synthesis methods include 1) π–π intercalation or graphite intercalation compound (GIC)-based exfoliation of graphite flakes into graphene sheets, [24, 25, 29, 30] and 2) in-solution reduction of graphite oxide prepared by Hummers method [15, 31, 32] with hydrazine [26–28, 33]. The π–π intercalation and GIC-based methods produce high-quality graphene; however, the yield is low with relatively low stability of the graphene solution, in which the graphene sheets have a tendency to settle down. The graphene suspension prepared by in-solution or 180 °C solvothermal reduction of graphene oxide (GO) in hydrazine produces a higher yield and stability; however, the process takes several days for completion [34]. Supercritical water has been used for the reduction of GO into graphene, for which high pressures and temperatures are required in a closed system, and the process takes about 6 h for completion [35]. Recently, sodium borohydride and concentrated sulfuric acid have been used to

reduce GO sheets via a two-step reduction process, which takes about 3 days for completion [36, 37].

Herein, we present a novel route to reduce GO and stabilize RGO in dispersions in a methanol suspension using common reagents via an ultrafast (less than a minute), high-throughput, single-step process. Sodium hydride acts both as a reducing agent to reduce GO to RGO and as a deprotonator to convert methanol to methoxy ions. These methoxy ions then stabilize the RGO sheets in the bulk methanol. Multilayer RGO sheets as large as >10 000 μm^2 with high sp^2 to sp^3 ratio and low defect density were obtained with conductivities of 4500–10, 625 S/m with electron and hole mobilities of 100–400 and 300–600 $cm^2/V{\cdot}s$, respectively. These values are comparable with the highest values reported for multilayer RGO [38].

Experimental methods

GO sheets suspended in water were synthesized from mesh 7 graphite flakes (Sigma–Aldrich) via a modified Hummers acid oxidation method, which produces one- to four-atom-thick sheets of partially oxidized graphene with the surface containing negatively charged hydroxyl, epoxy, and carboxylic acid groups, which electrostatically stabilize the GO sheets in suspension. The addition of the electronegative oxygen and the removal of unsaturated π electrons cause the GO sheets to be distorted due to the introduction of nonplanar sp^3 bonds (Figure 5.1, top). The GO suspension samples were centrifuged (11, 000 g, 60 min, 20 °C) and resuspended in 99% methanol with intermittent sonication [39]. Methanol-dispersed GO was then exposed to pure sodium hydride powder (final concentration ≈100 mg m/L), which instantaneously (a few seconds) reduced GO to RGO, while generating hydrogen gas bubbles. Further, sodium hydride deprotonates methanol to methoxy ions, [40] which is expected to stabilize the RGO sheets in methanol. Finally, a dark black, highly stable (about one month) solution of RGO was produced. Based on the initial weight of the graphite flakes, the process gave a yield of ≈68% with most RGOs having one to four layers. The yield for the NaH-based GO to RGO reduction process was close to 100%. The chemistry is shown below: [40]

$$\text{graphene oxide (GO)} \overset{NaH}{\Rightarrow} \text{reduced graphene oxide (RGO)} + H_2 \quad ((1))$$

$$CH_3OH \overset{NaH}{\Rightarrow} CH_3O^- + H_2 \quad ((2))$$

The relatively low exothermicity (T_{rxn}< 350 K, $T_{autoignition}$ ≈ 858 K; *source: NIST*) of the reaction at the experimental volumes reduces the fire hazard from the hydrogen gas produced during the reaction. The RGO suspension was highly stable with no visible settling, which can be attributed to the adsorbed methoxide ion ($Na^+CH_3O^-$)-induced electrostatic repulsion between individual RGO sheets in methanol [41].

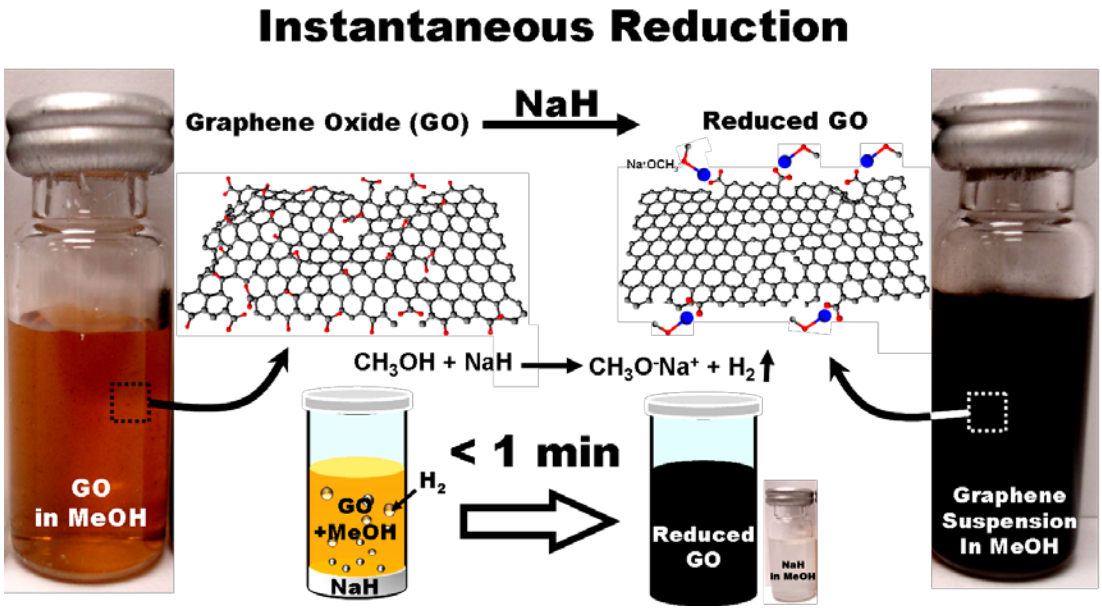

Figure 5-1 Schematic diagram of the hydride reduction process. Photographs of glass vials containing a dispersion of the GO in methanol (left) and a stable dispersion of RGO in bulk methanol (right). Center right, bottom: picture of a vial with NaH in methanol. The dark black color of the stabilized RGO in contrast to the yellow color of the GO indicates the partial restoration of the interlayer π network of the RGO sheets. The cartoon and the three-dimensional (3D) chemical structures (the gray, red, and blue balls denote the carbon, oxygen, and sodium atoms, respectively, in the ball-and-stick model) show the reduction process of GO to RGO via hydride chemistry, the associated release of hydrogen gas, and the ensuing solution stabilization of the RGO by sodium methoxide ions.

Results and discussion

Field-emission scanning electron microscopy (FESEM) images of the RGO sheets immediately after the hydride reaction show dendritic structures of sodium methoxide deposited

on the RGO surface, the chemical composition of which was confirmed by energy-dispersive X-ray (EDX) analysis (see Figure 5.2).

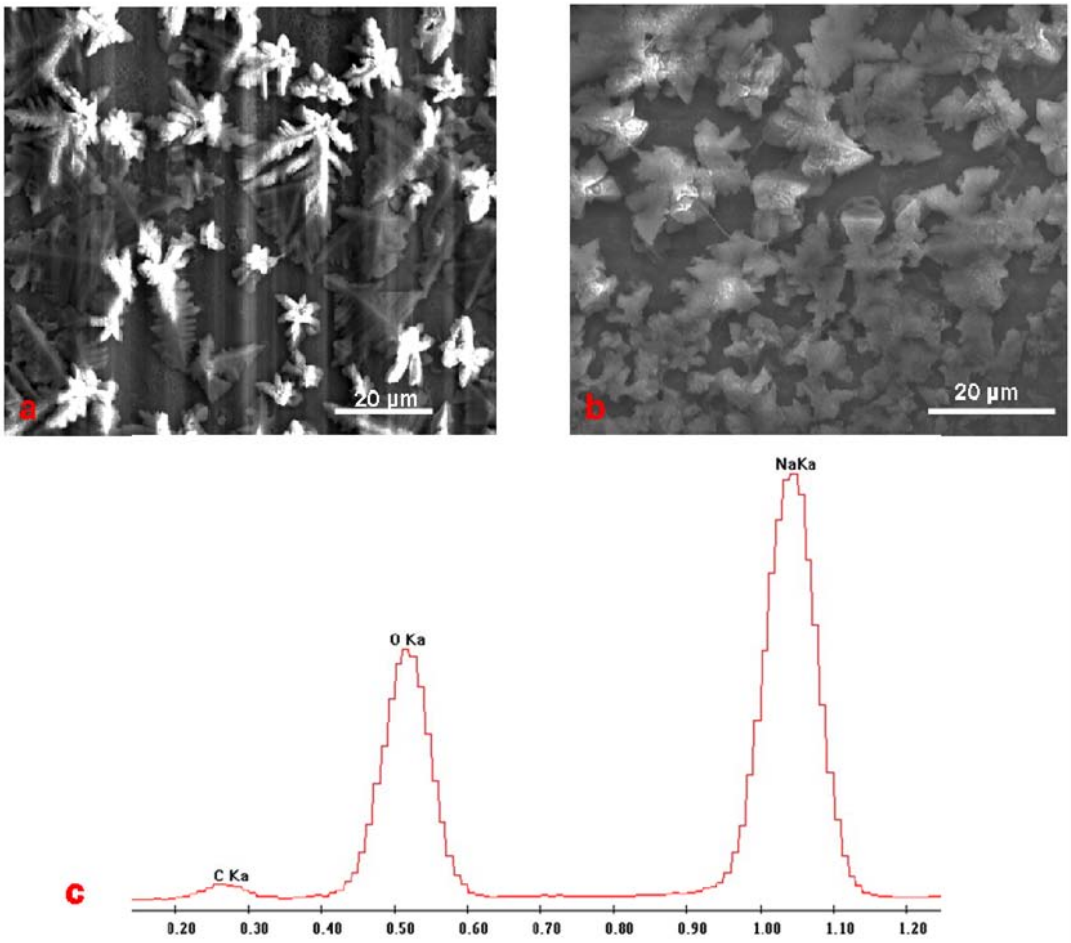

Figure 5-2 Field Emission – Scanning Electron Microscope (FESEM) images of the reduced graphene oxide (RGO) sheets before washing. (a, b) FESEM images of the RGO sheets drop casted onto silica substrate before washing showing the dendritic micro-structures formed by the $NaOCH_3$ depositions (c) Energy Dispersive X-ray analysis (EDX) image of the dendritic micro-structure showing the fingerprint peaks for Na, O and C.

Addition of deionized (DI) water to the suspension destabilizes the solution resulting in the formation of large clusters, which slowly settle down. This finding can be attributed to the removal of the stabilizing methoxide ions from the RGO surface. EDX studies confirmed complete sodium removal, which also made the RGO surfaces smooth as observed by FESEM (see Figure 5.3; Figure 5.4b, inset).

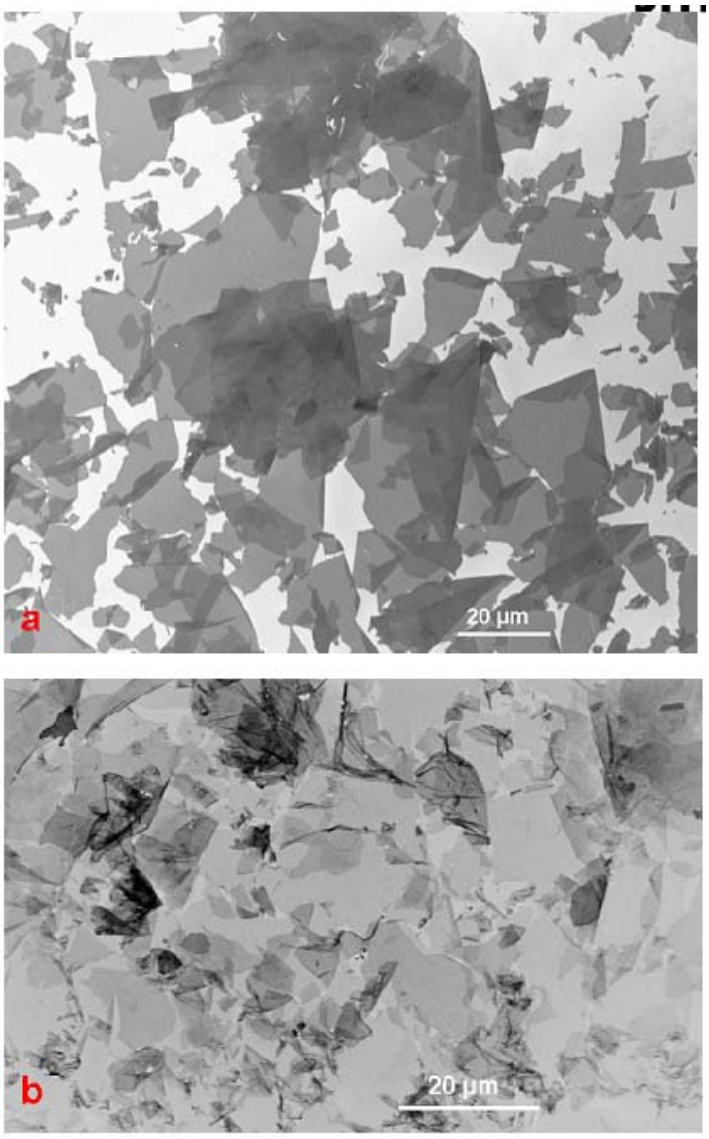

Figure 5-3 Field Emission – Scanning Electron Microscope (FESEM) images of the reduced graphene oxide (RGO) sheets after washing. (a, b) FESEM images of the RGO sheets drop casted onto silica substrate after washing with de-ionized water (DI water) showing the clean, flat surfaces vindicating the success of the washing process

More studies are needed to completely characterize this process. When a 300-nm-thick silicon dioxide substrate is contacted with a RGO solution for 10 min, a large areal RGO coverage is achieved, as observed by FESEM and optical microscopy (Figure 5.4c; see Appendix D, Figure D1 and D2).

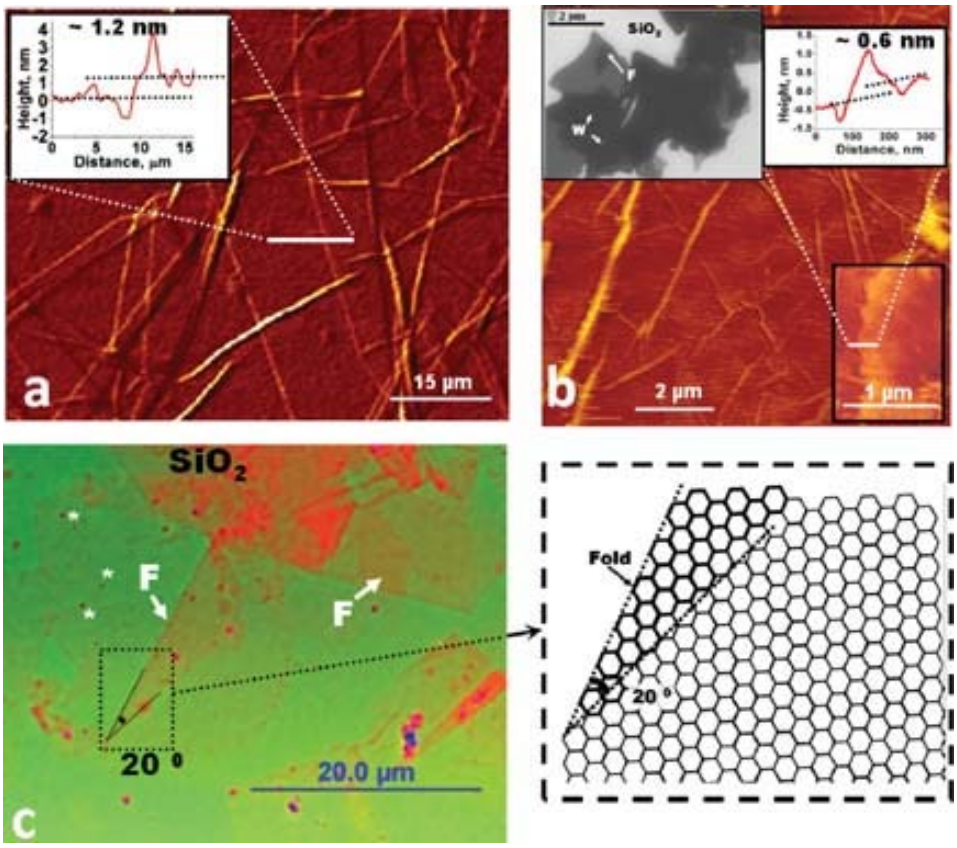

Figure 5-4 (a,b) Atomic force microscopy (AFM) images of the GO sheets (a) and RGO sheets (b) spin-coated on 300-nm-thick silica wafers. Insets: the height profiles indicate that the thickness of the GO monolayer is ≈1.2 nm (a), while that for the RGO monolayer is 0.6 nm (top right inset (b)). The top left inset in (b) shows an FESEM image of the washed RGO sheets deposited on a 300-nm-thick silica substrate. The sheets form wrinkles (W) and folds (F). c) Optical image of RGO sheets deposited on a 300-nm-thick silica substrate, which shows large-area coverage of the sporadically folded (F) RGO sheets. The stars indicate the probable residual sodium methoxide deposits on the RGO sheets and on the substrate. The schematic diagram of the carbon structure (right) depicts a possible folding conformation of the RGO sheets on the atomic scale.

AFM studies on deposited GO and RGO sheets showed that RGO has a smaller thickness (≈0.6 nm) than the parent GO, which is higher than the theoretical thickness, also reported by other groups (Figure 5.4a,b; Appendix D, Figure D2) [38]. This can be attributed to either

partially unreduced nonplanar oxy-functional groups, remnant sp^3 CC bonds, or gas/solvent molecules trapped between the substrate and the RGO sheets [42]. Furthermore, RGO was found to show a large density of folds, which is expected because of π–π interaction energy within the sheets. A rough schematic (Figure 5.4c, right) shows one possible folding mechanism using the angle of fold (=20°) shown (Figure 5.4c, left). The RGO sheets form wrinkles, however the wrinkle density is less than that for GO [9]. Moreover, the RGO sheets deposited on a substrate do not agglomerate during deposition. This is attributed to the negatively charged methoxide adsorption on the RGO surfaces, which repel each other.

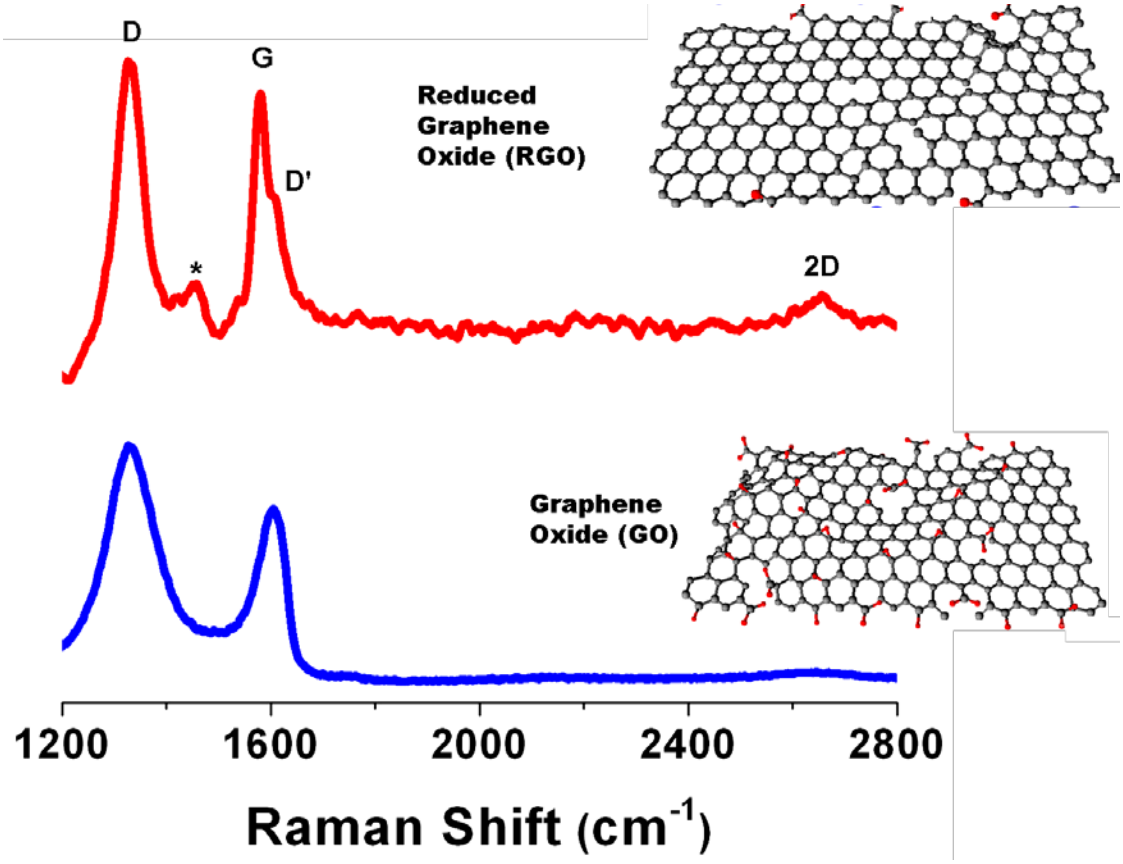

Figure 5-5 Comparison of the Raman spectra of the GO and RGO sheets. TheI_D/I_G and I_D'/I_G ratios for RGO decrease after the reduction process, which suggests the establishment of a long-range crystallographic order of the sp^2 carbon atoms in the RGO structure. The peak marked (*) in the RGO spectrum can be attributed to residual surface-adsorbed sodium methoxide molecules. The 3D chemical structures on the right depict the GO and RGO sheets.

The RGO sheets were analyzed by Raman (Figure 5.5), UV/Vis, and Fourier transform infrared (FTIR) spectroscopy (Figure 5.7) to study the reduction of GO to RGO and to investigate the change in the sp^2 to sp^3 ratio. UV/Vis absorption measurements showed that there was a red shift in the absorbance peak from GO (≈270 nm) to RGO (330 nm), which suggests a restoration of the π network of the carbon atoms (sp^2 hybridization) during a reduction of sp3 to sp^2 bonding (Figure 5.1). The presence of an absorbance peak at ≈330 nm compares well with the values reported by other groups (Figure 5.7b) [38]. The Raman spectra of the GO and RGO samples were recorded on a spot area of ≈1 μm^2, which was far from the sheet edges to avoid signals from the edge defect, and at a low power of ≈5 mW to reduce localized heating (Figure 5.5). The Raman peaks at ≈1355 cm^{-1} (D band) and at ≈1590 cm^{-1} (G band) agree well with the literature [15, 33, 43]. The slight increase in the position of the G peak compared to that for pristine graphene can be attributed to the remnant n-doping in RGO [44, 45].

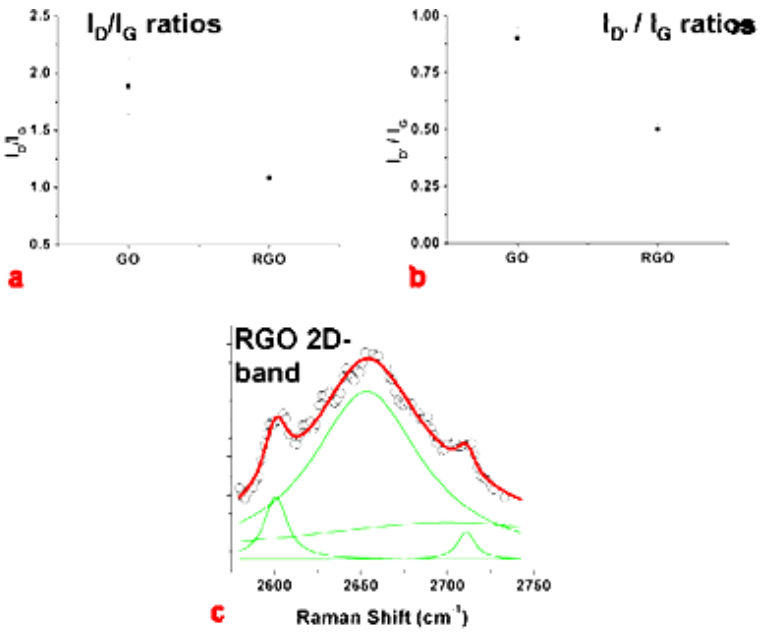

Figure 5-6 Raman characteristics of GO and RGO. (a) D/G intensity ratios; (b) D'/G intensity ratios for GO and RGO showing a decrease in both cases suggesting a decrease in defect density. Error bars are based on Raman spectra analysis for multiple samples. (c) A 4 peak lorentzian fit into the 2D band in the Raman spectra of the RGO channel in the FET depicted in Figure 5.8 d (inset) implying the presence of a bilayer.

The I_D/I_G ratios, which quantify the relative content of the intervalley scattering producing defects (D peak) and the graphenic region (G pea k), were calculated from the spectra after baseline correction and integration. While the I_D/I_G ratio for GO was found to be $\approx 1.88 \pm 0.25$, as expected for GO, the I_D/I_G ratio for RGO was$\approx 1.08 \pm 0.15$, which implies a substantial hydride-induced reduction in the relative content of the sp^3 carbon atoms and the oxidized molecular defects, vacancies, etc. (Figure 5.6). This lower value of I_D/I_G is comparable to that achieved by the supercritical-water-based reduction process ($I_D/I_G \approx 0.9$) and to the recently reported 180 °C solvothermal reduction process ($I_D/I_G \approx 0.9$), and can be attributed to the mild, low exothermic nature of the reduction process. In contrast, the hydrazine reduction of GO [46] exhibits an I_D/I_G ratio of 1.44. Furthermore, the $I_{D'}/I_G$ ratio, which quantifies the ratio of the weak defects, induced intravalley scattering (D' peak) and the graphenic region (G peak) also decreased after reduction to RGO (see Figure 5.6). Using the empirical *Tuinstra–Koenig* relation, which relates the I_D/I_G ratio to the crystallite size of the carbonaceous graphitic samples, the size of the ordered graphitic regions in GO was calculated to be≈ 4 nm^2, as expected for a large areal density of sp^3 carbon atoms and defects [47]. For RGO, the areal crystallite density with defect-free segments of sp^2 carbon atoms increased threefold and corresponded to a domain size of ≈ 12.25 nm^2. The presence of the D/D' band on the entire RGO can be attributed to vacancy defects from the loss of the carbon atoms due to the reduction of the highly oxidized carbon atoms on the parent GO [48]. Furthermore, the relatively weak 2D band intensity in RGO spectra can be attributed to the fractional non-sp^2 carbon domains, in contrast to the solely sp^2 carbon atoms in the pristine graphene [49].

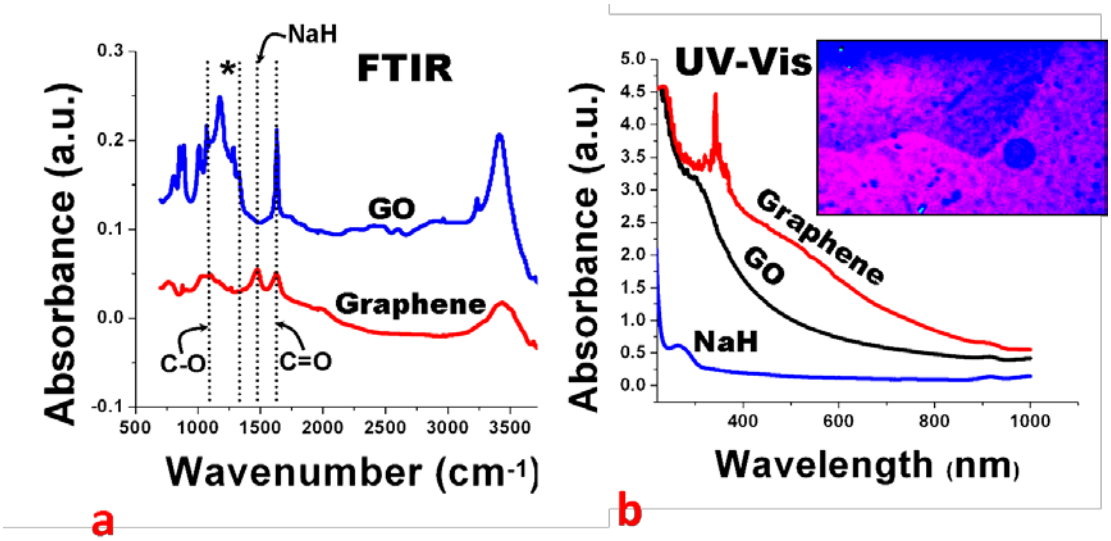

Figure 5-7 (a) The FTIR spectra of the RGO and GO samples depict the characteristic peaks for the inherent chemical structure. The starred peak (*), which corresponds to the fingerprint region for the amorphous carbon, undergoes a sharp decrease in intensity after reduction of GO to RGO, which implies an increased crystallinity of RGO. (b) The UV/Vis spectra of RGO, GO, and NaH exhibit the characteristic red shift for RGO, which indicates the restoration of the π-electron network (solvent is methanol). Inset: optical image of a monolayer of RGO spin-coated on a 300-nm-thick silica substrate.

FTIR studies were conducted to illustrate the chemical structure of the RGO sheets. The RGO and GO sheets were dried in an inert atmosphere (99.9% He, 200 °C) to obtain powders for characterization. The spectrum for GO agrees well with the values reported in the literature [50]. The absorbance peak for GO at≈1375 cm^{-1} (appears as a shoulder to the broad peak at ≈1150 cm^{-1}), which corresponds to the fingerprint region of amorphous carbon, is greatly reduced in the RGO spectrum, thus signifying the restoration of the honeycomb lattice of carbon atoms. The spectrum for RGO shows a residual peak at≈1100 cm^{-1} corresponding to stretching of the CO bond, which could arise from adsorbed methoxide or defects on the RGO lattice. Furthermore, the intensity of the absorbance peak for GO at≈1650 cm^{-1}, which corresponds to stretching of the carbonyl group, reduces by 3.33 in RGO, thus confirming its reduction.

The electrical properties of the thus-produced RGO were studied to determine the charge-carrier properties. RGO sheets were deposited on prepatterned silica (300 nm thermally grown)

on n^+ silicon substrates with gold electrodes 5 µm apart. The samples were thoroughly washed with DI water and dried in a vacuum. To discern the layer thickness of the RGO channel, the D band from the Raman spectrum acquired earlier (Figure 5.5) was fitted with the Lorentzian model. A four-peak Lorentzian fit of the D-band-signal curve implied that the sheet was a graphene bilayer [51] (Figure 5.5b; see Figure 5.6 for the 2D band fits) [52]. Similarly, a GO test device was also prepared. The n^+ silicon layer was used as a back gate for the field-effect measurements and the 300-nm silica layer functioned as the gate oxide (Figure 5.8a).

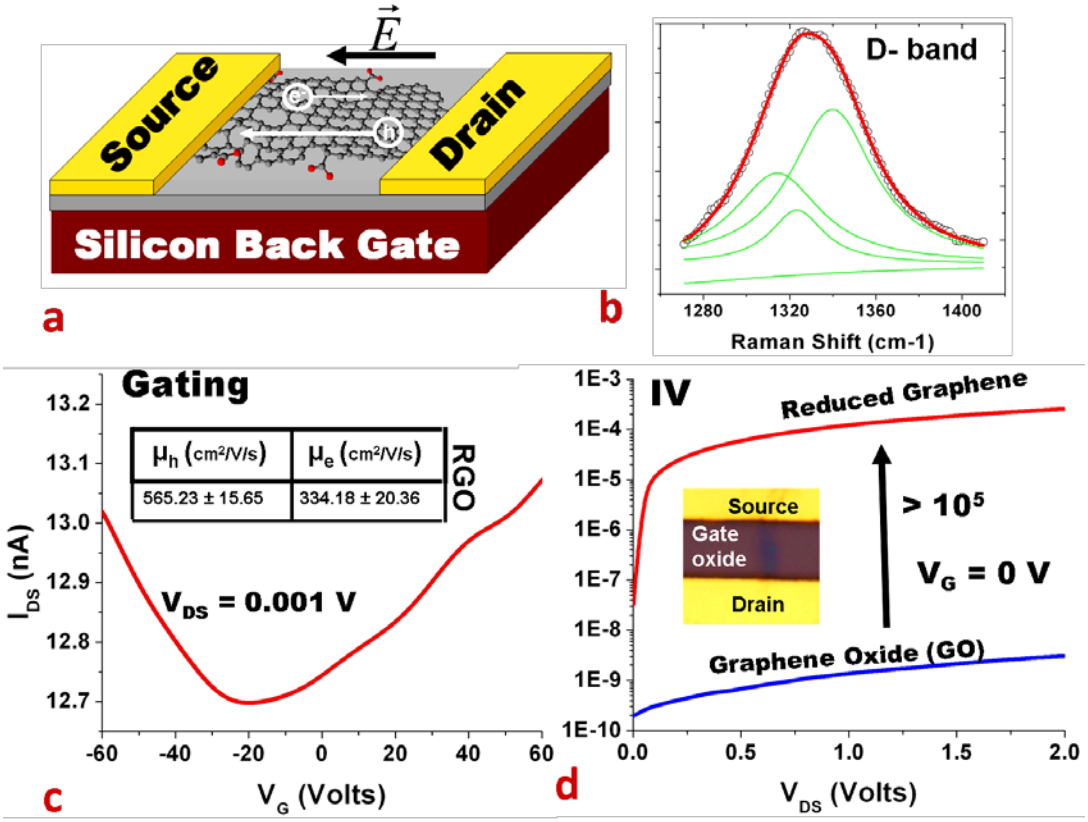

Figure 5-8 (a) Schematic diagram of the back-gated field-effect transistor (FET) for studying the electrical properties of RGO. $\vec{E}$ denotes the electric field; e and h denote electrons and holes, respectively. (b) Four-peak Lorentzian fit of the D band from the Raman spectra acquired for the RGO channel in the RGO FET demonstrates a bilayer. c) Electrical gating data for the RGO-based back-gated FET show a slight n-type characteristic. Inset: tabulated values of the calculated carrier mobilities for this RGO bilayer. d) Current–voltage measurements across the source and drain electrodes of a GO

sheet, which exhibit a five orders of magnitude increase in conductivity after NaH-induced reduction. Inset: optical image of the RGO FET.

The samples were placed in a $\approx 10^{-4}$ Torr vacuum probe station at room temperature. Figure 5.8d shows the typical source–drain characteristics of the RGO and GO test devices. The RGO bilayer sheets (prepared by reduction in less than a minute) exhibited conductivities of ≈4500–10, 625 S/m, which were five orders of magnitude higher than those of the GO sheets [28, 38, 48]. Furthermore, a GO test device after treatment with sodium hydride solution for 1 min exhibited a three orders of magnitude increase in conductivity, owing to the partial (single side) reduction of GO (Figure 5.9).

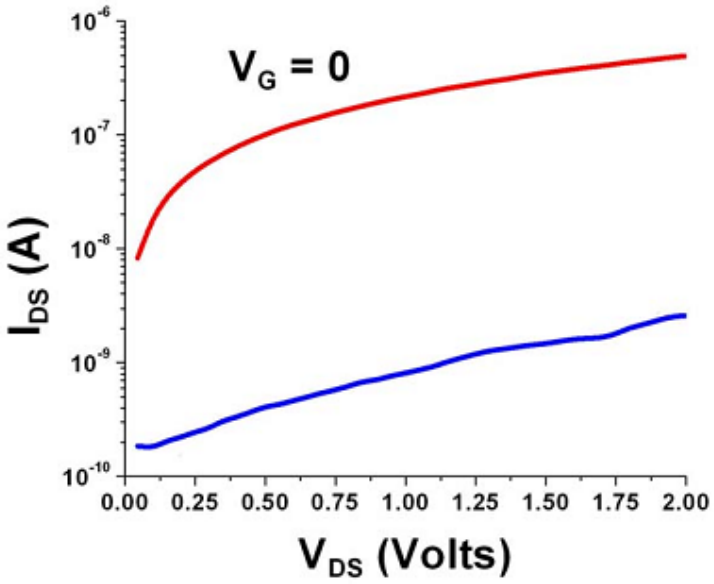

Figure 5-9 I-V of GO and RGO (on-substrate-reduction). Electrical conductivity of GO (Blue) and partially reduced GO after hydride treatment (Red) showing 3 orders of increase.

Electrical gating studies conducted under vacuum showed that the RGO exhibits a slight n-type characteristic, in contrast to the strongly p-type characteristic of the GO sheets [9]. The slight asymmetry in the gating curve (Figure 5.8) can be attributed to the residual sodium methoxide ions adsorbed on RGO and the charged impurities transferred from the unpassivated

silica substrate [48, 53, 54]. Furthermore, upon prolonged washing (6 h) of the as-prepared FET with DI water, near ambipolar carrier density of graphene was restored (Figure 5.10).

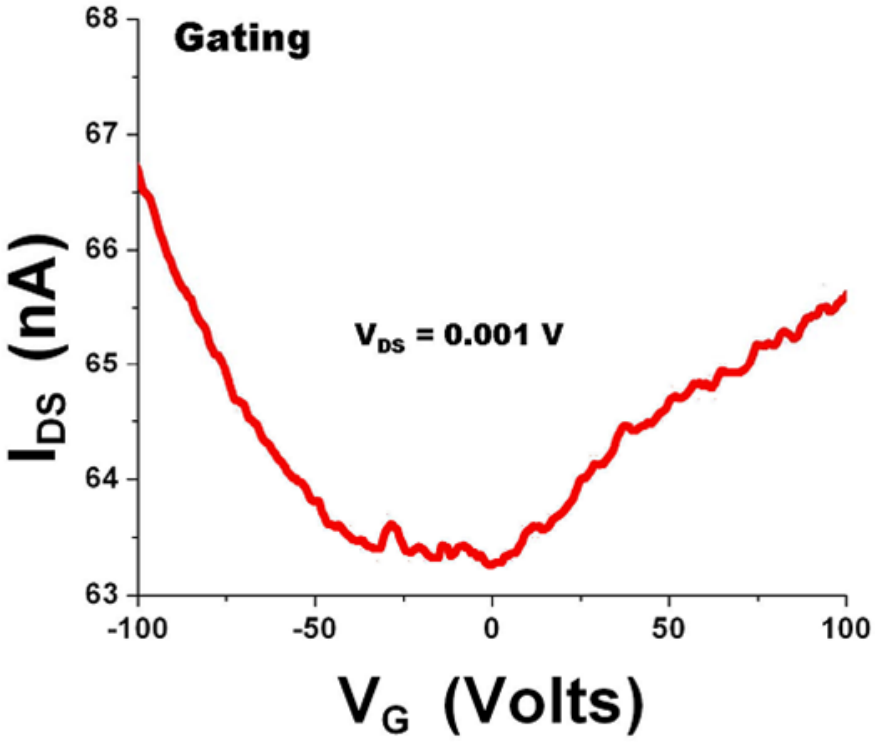

Figure 5-10 Electrical gating studies. Electrical gating on a few-layer RGO FET, washed for a prolonged duration in DI water, showing a near complete restoration of the ambi-polar carrier density

The electron and hole mobilities for the RGO were computed from the gating data by using the expression:

$$\mu_{carrier} = (\Delta I_{DS}/\Delta V_G)/(C_G(l/w) \times V_{DS}) \qquad ((3))$$

where C_G is the silica gate capacitance, l is the length of the graphene channel, and w is its width. Owing to the bilayer nature of the RGO channel, the gating effect is expected to be screened by the graphene layers [55]. The electron and hole mobilities were calculated to be 100–400 and 300–600 $cm^2/V{\cdot}s$, respectively, which are several orders of magnitude higher than those reported for GO [55, 56]. This further confirms the reduction-induced augmentation of ordered sp^2 domains (also observed previously in Raman studies), which in turn increases the

carrier scattering distance and thus the carrier mobility. Furthermore, the I_{DS}–V_{DS} curves for RGO were found to have nonlinear exponential characteristics (Figure 5.11), which, in conjunction with the limited ordered graphenic domain size (~25 nm^2), suggests a two-dimensional variable-range hopping conduction mechanism, thus vindicating the presence of conducting graphenic domains separated by defects in the RGO sheets [26, 27, 48, 57]. However, further studies are needed to characterize this in detail.

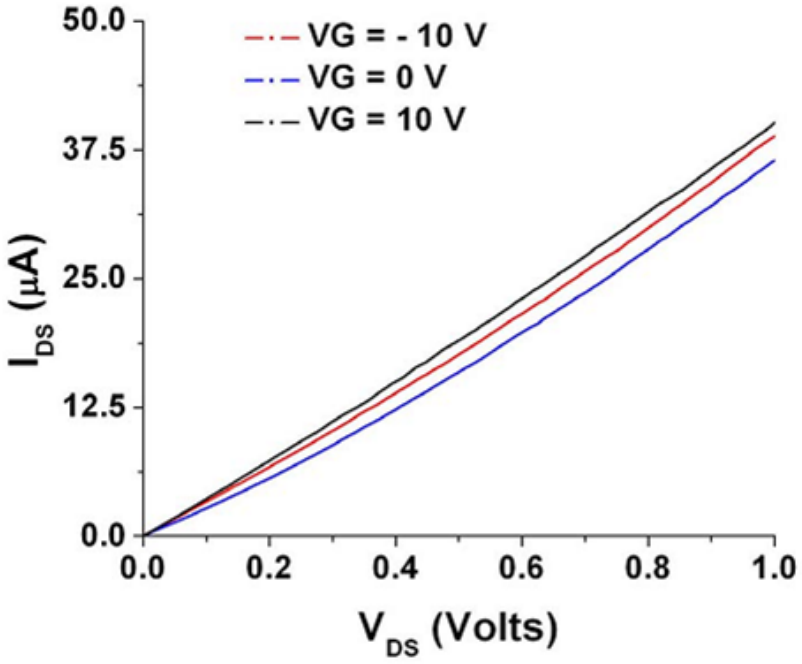

Figure 5-11 Typical VRH characteristics. I_{DS} vs. V_{DS} curves at varying V_G for a bilayer RGO-FET at 300 K showing non-linear, exponential characteristics.

Conclusion

In summary, we have demonstrated a novel, ultrafast, and high-yield process to synthesize highly stable RGO dispersions and have illustrated the spectroscopic and electrical characterization of the RGO sheets. The facile hydride chemistry process, which uses commonly available reagents, effectively restores the planar sp^2-hybridized structure of graphene, with relatively low defects confirmed by Raman and UV/Vis spectroscopy. The high carrier mobility and the bipolar carrier density in RGO further confirm the increased crystalline sp^2 regions in

RGO with lower scattering distances. These results suggest that this process can a) enable improved handling of graphene dispersions, b) deliver high-quality graphene on demand for electronic, mechanical, and other applications, and c) develop next-generation solution-based graphene functionalization schemes.

Acknowledgements

We thank Dr. Paula Spencer and Dr. Charles Ye for help with Raman characterization. We also thank Myles Ikenberry and Dr. Keith Hohn for help with FTIR spectroscopy. We thank Dr. David Moore and Heather Shinogle for help with FESEM. V.B. thanks NSF (contract CMMI-0939523) and KSU for financial support.

References

1. Geim, A. K., Novoselov, K. S., The rise of graphene. *Nat. Mater.* **6** 183–191 (2007)

2. Novoselov, K. S., Jiang, D., Schedin, F., Booth, T. J., Khotkevich, V. V., Morozov, S. V., Geim, A. K., Two-dimensional atomic crystals. *Proc. Natl. Acad. Sci. USA*. **102** 10451–10453 (2005)

3. Novoselov, K. S., Geim, A. K., Morozov, S. V., Jiang, D., Katsnelson, M. I., Grigorieva, I. V., Dubonos, S. V., Firsov, A. A., Two-dimensional gas of massless Dirac fermions in graphene *Nature* **438** 197–200 (2005)

4. Abanin, D. A., Lee, P. A., Levitov, L. S., Charge and spin transport at the quantum Hall edge of graphene. *Solid State Commun.* **143** 77–85 (2007)

5. Stoller, M. D., Park, S., Zhu, Y., J. An, Ruoff, R. S., Graphene-based ultracapacitors. *Nano Lett.* **8** 3498–3502 (2008)

6. Wang, X., Zhi, L. J., Tsao, N., Tomovic, Z., J. L. Li, Mullen, K., Transparent carbon films as electrodes in organic solar cells *Angew. Chem*. **120** 3032–3034 (2008); *Angew. Chem. Int. Ed.* **47** 2990–2992 (2008)

7. Wang, X., Zhi, L. J., Mullen, K., Transparent, conductive graphene electrodes for dye-sensitized solar cells *Nano Lett.* **8** 323–327 (2008)

8. Schedin, F., Geim, A. K., Morozov, S. V., Hill, E. W., Blake, P., Katsnelson, M. I., Novoselov, K. S., Detection of individual gas molecules adsorbed on graphene. *Nat. Mater.* **6** 652–655 (2007)

9. Mohanty, N., Berry, V., Graphene-Based Single-Bacterium Resolution Biodevice and DNA Transistor: Interfacing Graphene Derivatives with Nanoscale and Microscale Biocomponents. *Nano Lett.* **8** 4469–4476 (2008)

10. Bunch, J. S., van der Zande, A. M., Verbridge, S. S., Frank, I. W., Tanenbaum, D. M., Parpia, J. M., Craighead, H. G., McEuen, P. L., . Electromechanical resonators from graphene sheets. *Science* **315** 490–493 (2007)

11. Novoselov, K. S., Geim, A. K., Morozov, S. V., Jiang, D., Zhang, Y., Dubonos, S. V., Grigorieva, I. V., Firsov, A. A., Electric field effect in atomically thin carbon films. *Science* **306** 666–669 (2004)

12. Abanin, D. A., Novoselov, K. S., Zeitler, U., Lee, P. A., Geim, A. K., Levitov, L. S., Dissipative quantum Hall effect in graphene near the Dirac point. *Phys. Rev. Lett.* **98** 196806 (2007)

13. Novoselov, K. S., Jiang, Z., Zhang, Y., Morozov, S. V., Stormer, H. L., Zeitler, U., Maan, J. C., Boebinger, G. S., Kim, P., Geim, A. K., *Science* **315** 1379 (2007)

14. Novoselov, K. S., McCann, E., Morozov, S. V., Fal'ko, V. I., Katsnelson, M. I., Zeitler, U., Jiang, D., Schedin, F., Geim, A. K., Room-temperature quantum hall effect in graphene. *Nat. Phys.* **2** 177–180 (2006)

15. Stankovich, S., Dikin, D. A., Piner, R. D., Kohlhaas, K. A., Kleinhammes, A., Y. Jia, Y. Wu, Nguyen, S. T., Ruoff, R. S., Synthesis of graphene-based nanosheets via chemical reduction of exfoliated graphite oxide. *Carbon* **45** 1558–1565 (2007)

16. Blake, P., Hill, E. W., Neto, A. H. C., Novoselov, K. S., Jiang, D., Yang, R., Booth, T. J., Geim, A. K., Making graphene visible. *Appl. Phys. Lett.* **91** 063124 (2007)

17. Huang, Y. C., Chang, C. P., Lin, M. F., Magnetic and quantum confinement effects on electronic and optical properties of graphene ribbons. *Nanotechnology* **18** 495401 (2007)

18. Lee, C., Wei, X. D., Kysar, J. W., Hone, J., Measurement of the elastic properties and intrinsic strength of monolayer graphene. *Science* **321** 385–388 (2008)

19. Berger, C., Song, Z. M., Li, X. B., Wu, X. S., Brown, N., Naud, C., Mayo, D., T. B. Li, Hass, J., Marchenkov, A. N., Conrad, E. H., First, P. N., de Heer, W. A., Electronic confinement and coherence in patterned epitaxial graphene. *Science* **312** 1191–1196 (2006)

20. Emtsev, K. V., Bostwick, A., K. Horn, Jobst, J., Kellogg, G. L., L. Ley, J. L. McChesney, Ohta, T., Reshanov, S. A., J. Rohrl, Rotenberg, E., Schmid, A. K., Waldmann, D.,

Weber, H. B., Seyller, T., Towards wafer-size graphene layers by atmospheric pressure graphitization of silicon carbide. *Nat. Mater.* **8** 203–207 (2009)

21. Sutter, P. W., Flege, J. I., Sutter, E. A., Epitaxial graphene on ruthenium. *Nat. Mater.* **7** 406–411 (2008)

22. Kim, K. S., Zhao, Y., Jang H., Lee S. Y., Kim J. M., Kim K. S., Ahn J. H., Kim P., Choi Y., Hong B. H., Large-scale pattern growth of graphene films for stretchable transparent electrodes. *Nature* **457** 706–710 (2009)

23. Li, X. et al Large Area Synthesis of High-quality and uniform graphene films. *Science* (2009)

24. Li, X., Zhang G., X. Bai, Sun X., Wang X., Wang E., Dai H., Highly conducting graphene sheets and Langmuir-Blodgett films. *Nat. Nanotechnol.* **3** 538–542 (2008)

25. Hernandez, Y. et al., High-yield production of graphene by liquid-phase exfoliation of graphite. *Nat. Nanotechnol.* **3** 563–568 (2008)

26. Gilje, S., Han S., Wang M., Wang K. L., Kaner, R. B., A chemical route to graphene for device applications. *Nano Lett.* **7**, 3394–3398 (2007)

27. Kaiser, A. B., Gomez-Navarro, C., Sundaram R. S., Burghard M., Kern, K., Electrical Conduction Mechanism in Chemically Derived Graphene Monolayers. *Nano Lett.* **9** 1787–1792 (2009)

28. Y. Si, Samulski E. T., Synthesis of water soluble graphene. *Nano Lett.* **8** 1679–1682 (2008)

29. Valles, C., Drummond, C., Saadaoui, H., Furtado, C. A., M. He, Roubeau, O., L. Ortolani, Monthioux M., Penicaud A., Solution of negatively charged graphene sheets and ribbons. *J. Am. Chem. Soc.* **130** 15802–15804 (2008)

30. Lee, J. H., Shin D. W., Makotchenko V. G., Nazarov A. S., Fedorov V. E., Y. H. Kim, Choi J. Y., Kim J. M., Yoo J. B., One-step exfoliation synthesis of easily soluble graphite and transparent conducting graphene sheets. *Adv. Mater.* **21** 1–5 (2009)

31. Hummers, W. S., Offeman, R. E., Preparation of Graphitic Oxide. *J. Am. Chem. Soc.* **80** 1339 (1958)

32. Luo, Z., Y. Lu, L. Somers, A., Johnson, A. T. C., High Yield Preparation of Macroscopic Graphene Oxide Membranes. *J. Am. Chem. Soc.* **131** 898–8899 (2009)

33. Gomez-Navarro, C., Weitz, R. T., Bittner, A. M., Scolari , M., Mews ,A., Burghard, M., Kern, K., Electronic transport properties of individual chemically reduced graphene oxide sheets. *Nano Lett.* **7** 3499–3503 (2007)

34. Wang, H., Robinson, J. T., Li, X., Dai, H., Solvothermal Reduction of Chemically Exfoliated Graphene Sheets. *J. Am. Chem. Soc.* **131** 666–669 (2009)

35. Zhou, Y., Bao, Q., L. Tang, A. L., Zhong, Y., Loh, K. P., Hydrothermal Dehydration for the ôGreenö Reduction of Exfoliated Graphene Oxide to Graphene and Demonstration of Tunable Optical Limiting Properties. *Chem. Mater.* **21** 2950–2956 (2009)

36. Bourlinos, A. B., Gournis, D., Petridis, D., Szabo, T., Szeri A., Dekany, I., Graphite Oxide: Chemical Reduction to Graphite and Surface Modification with Primary Aliphatic Amines and Amino Acids. *Langmuir* **19** 6050–6055 (2003)

37. Gao, W., Alemany, L. B., L. Ci, Ajayan, P. M., New insights into the structure and reduction of graphite oxide. *Nat. Chem.* **1** 403–408 (2009)

38. Li, D., Muller, M. B., Gilje, S., Kaner, R. B., Wallace, G. G., Processable aqueous dispersions of graphene nanosheets. *Nat. Nanotechnol.* **3** 101–105 (2008)

39. Paredes, J. I., Villar-Rodil, S., Marti¦ünez-Alonso, A., Tasco¦ün, J. M. D., Graphene Oxide Dispersions in Organic Solvents. *Langmuir* **24** 10560–10564 (2008)

40. Brown ,H. C., Krishnamurthy, S., 40 Years of Hydride Reductions. *Tetrahedron* **35** 567–607 (1979)

41. Chen, H., Muller, M. B., Gilmore, K. J., Wallace, G. G., Li D., Mechanically strong, electrically conductive, and biocompatible graphene paper. *Adv. Mater.* **20** 3557–3561 (2008)

42. Ishigami, M., Chen, J. H., Cullen, W. G., Fuhrer, M. S., Williams, E. D., Atomic structure of graphene on SiO_2. *Nano Lett.* **7** 1643–1648 (2007)

43. Kudin, K. N., Ozbas, B., Schniepp, H. C., Prud'homme, R. K., Aksay, I. A., Car, R., Raman spectra of graphite oxide and functionalized graphene sheets. *Nano Lett.* **8** 36–41 (2008)

44. Ferrari, A. C., Meyer, J. C., Scardaci, V., Casiraghi, C., Lazzeri, M., Mauri, F., S. Piscanec, Jiang, D., Novoselov, K. S., Roth, S., Geim, A. K., Raman spectrum of graphene and graphene layers. *Phys. Rev. Lett.* **97** 187401 (2006)

45. Casiraghi, C., Pisana, S., Novoselov, K. S., Geim, A. K., Ferrari, A. C., Raman fingerprint of charged impurities in graphene. *Appl. Phys. Lett.* **91** 233108 (2007)

46. Zhou, Y., Bao Q., L. Tang, A. L., Zhong, Y., Loh, K. P., Hydrothermal dehydration oft he „green“ reduction of exfoliated graphene oxide to graphene and demonstration of tunable optical limiting properties. *Chem. Mater.* **21** 2950–2956 (2009)

47. Tuinstra, F., Koenig, J. L., Raman Spectrum of Graphite. *J. Chem. Phys.* **53** 1126–1130 (1970)

48. Tung, V. C., Allen, M. J., Yang, Y., Kaner, R. B., High-throughput solution processing of large-scale graphene. *Nat. Nanotechnol.* **4** 25–29 (2009)

49. Malard, L. M., Pimenta, M. A., Dresselhaus, G., Dresselhaus, M. S., Raman spectroscopy in graphene. *Phys. Rep.* **475** 51–87 (2009)

50. Sreeprasad, T. S., Samal, A. K., Pradeep, T., Tellurium Nanowire-Induced Room Temperature Conversion of Graphite Oxide to Leaf-like Graphenic Structures. *J. Phys. Chem. C* **113** 1727–1737 (2009)

51. Gupta, A. K., Russin, T. J., Gutierrez, H. R., Eklund, P. C., Probing Graphene Edges via Raman Scattering. *ACS Nano* **3** 45–52 (2008)

52. Gupta, A., Chen, G., Joshi, P., Tadigadapa, S., Eklund, P. C., Raman scattering from high frequency phonons in supported n-graphene layer films. *Arxiv preprint cond-mat/0606593* (2006)

53. Shemella, P., Nayak, S. K., Electronic structure and band-gap modulation of graphene via substrate surface chemistry. *Appl. Phys. Lett.* **94** 032101 (2009)

54. Jasuja, K., Berry, V., Implantation and Growth of Dendritic Gold Nanostructures on Graphene Derivatives: Electrical Property Tailoring and Raman Enhancement. *ACS Nano* **3** 2358–2366 (2009)

55. Reina, A., Jia X., Ho J., Nezich D., Son, H., Bulovic, V., Dresselhaus, M. S., Kong, J., Large area, few-layer graphene films on arbitrary substrates by chemical vapor deposition. *Nano Lett.* **9** 30–35 (2009)

56. Gu, G., Nie, S., Feenstra, R. M., Devaty, R. P., Choyke, W. J., Chan, W. K., Kane, M. G., Field effect in epitaxial graphene on a silicon carbide substrate. *Appl. Phys. Lett.* **90** 253507 (2007)

57. Ohta, T., Bostwick, A., Seyller, T., Horn, K., Rotenberg, E., Controlling the electronic structure of bilayer graphene. *Science* **313** 951–954 (2006)

Chapter 6 - High efficiency production of long, high-quality graphene nanoribbons with narrow width

Abstract

Graphene nano-ribbons (GNRs) – *single atom thick strips of sp^2 hybridized carbon atoms* – exhibit width dependent band-gap with potential for scalar potential-mediated coupling of states in distinct bands, and room temperature ballistic transport. Since GNR's exophysical attributes define its properties, they are a new variety of graphene. The sub-10 nm wide GNRs (both *zig-zag* and *arm-chair*) and the relatively wider arm-chair edged GNRs (15 nm - 90 nm wide) are semiconducting: a key requirement for traditional CMOS architecture. However, the realization of their potential in electronics requires a route to produce GNRs with precise and reproducible dimensions at high-throughput. Currently, achieving high-throughput synthesis of pristine GNRs with 'pre-determined' width is challenging. In this report, we demonstrate a large-scale production route (10^8 ribbons/hour) for GNRs with narrow width-distribution, length of several microns, and smooth-edges, achieved by nanotomy (nanoscale cutting) of highly oriented pyrolytic graphite (HOPG) into graphite nano-blocks (GNBs), and their subsequent exfoliation. This simple process produces the narrowest distribution of the ribbon-width (standard deviation ~ 3 – 15 nm for 20 – 80 nm GNRs) with the modal width pre-determinable between 5 nm and 600 nm. The overall yield of the process is ~ 80 % (nanotomy = 100 % and exfoliation ~ 80 %). Thin films of the as-fabricated pristine GNRs show semiconducting nature with bandgaps of ~ 30 ± 10 meV for films of 15 nm wide GNRs and significant carrier mobilities of ~ 20 ± 4 $cm^2/V{\cdot}s$ for films of 15 and 25 nm GNRs. This inexpensive, high-throughput method for the synthesis of the high quality, narrow GNRs and GNR films will produce a quantum leap in the GNR applications and research.

To be submitted to *Nature* as

Mohanty, N., Moore, D., Nagaraja, A., and Berry, V., "High Efficiency Production of Long, High-Quality Graphene Nanoribbons with Narrow Width"

Introduction

The lateral quantum confinement of the electron wave-functions and lattice termination effects in the narrow GNRs, result in the opening up of a finite energy gap, which can be leveraged in graphene electronics and optoelectronics [1-8]. Current techniques for production of GNRs are based on: lithography; chemical and sonochemical methods; unzipping of carbon nanotubes (CNTs) [8]; bottom up chemical routes [9]; and templated epitaxial growth on SiC steps. While the lithographic methods are limited by low throughput and low efficiency, the chemical and the sonochemical methods are limited by restricted lateral and longitudinal dimensions or broad width-distributions. The multi-walled carbon nanotubes (MWCNTs) when unzipped produce GNRs with a broad distribution of widths (resulting from the difference in outer and inner circumference) or are partially oxidized (referred as reduced graphene oxide nanoribbons (RGONR)). The bottom-up chemical routes are applicable only for GNRs with ultrasmall length-scale and small width (< 2 nm widths). Finally, the templated epitaxial growth of GNRs on SiC steps affords limited control on the width. Thus, a high-yield strategy for producing high-quality, long GNRs with pre-determined widths and facile processability is desired.

Here, we present a top-down strategy for high-throughput GNR production from HOPG blocks, a source of columnar stacked graphene layers (*ZYA* grade, 0.4 ± 0.1 mosaic spread, Figure 6.1a, b). We performed diamond-knife based serial cleaving of the HOPG along the plane perpendicular to the graphene planes to produce narrow graphite nano-blocks (GNBs) (Figure 6.1, 6.2, Supporting Video 6SV1 and 6SV2). Typically, the GNBs were ~1 mm long and ~1 mm thick; thus, consisted of millions of columnar-stacked GNRs with similar dimensions. These were chemically exfoliated in superacid to generate a stable suspension of the GNRs with narrow width distribution (Figure 6.1d, e and 6.2).

The diamond-knife-nanotomy process is embedding-free, one step process for direct synthesis of GNBs (and subsequently the GNRs) from HOPG. Here, a HOPG block (SPI Inc.) is rigidly attached to a cuboidal block of araldite resin using cyanoacrylate (Superglue) and is firmly mounted on the sample holder of a nanotome (PT-XL Microtome, Boeckeler Instruments Inc.; Figure 6.1c and 6.2) with the graphene plane oriented perpendicular to the knife-edge (Figure 6.1b, 6.2): the araldite resin mounting gives structural support to the HOPG block during

the cleaving process (see methods section and supporting information for details). The sample is precisely aligned with the edge of the ultra-sharp diamond knife (Du Pont Inc., 45^0 included

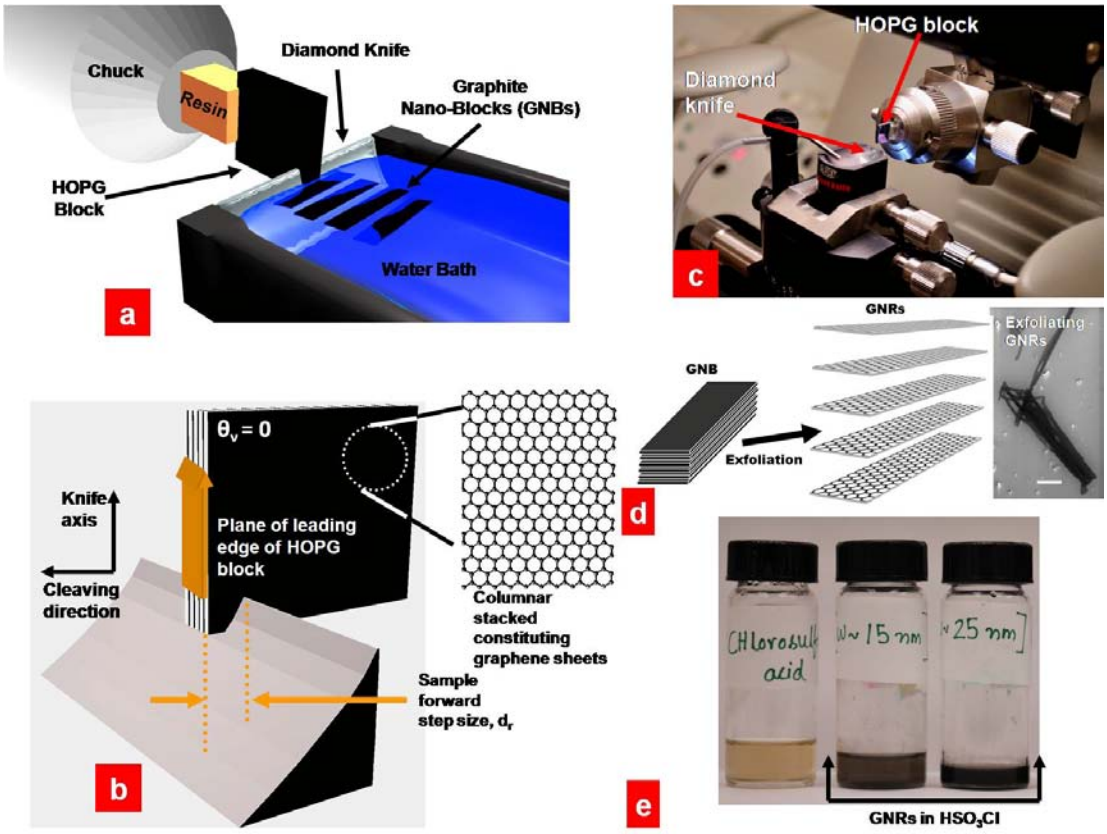

Figure 6-1 (a) A cartoon showing the manufacturing process of the Graphene nano-ribbons (GNRs) from a HOPG block using a simple mechanical cleaving process in a precision diamond knife-based nanotome. This process produces the GNBs (d) which are subsequently exfoliated by the superacid (chlorosulfonic acid) based exfoliation method to generate the uniform width, ultra-long GNRs. D-inset shows the Field Emission Scanning Electron Microscope (FESEM) image of the constant width (w ~ 200 nm) GNRs exfoliating from a GNB (Scale bar = 2 µm). (b) A schematic diagram of the close up of the nanoscale cleaving process showing process parameters: the d_r and the θ_v (c) A Nikon D60 image of the nanotome with the HOPG sample mounted before the start of the cleaving process. (e) A picture of the glass vials containing pure chlorosulfonic acid, w ~ 15 nm and 25 nm GNRs. The dark color of the GNR-sample containing vials shows successful exfoliation of the corresponding GNBs.

angle), at a 50° clearance angle, a 400 rake angle and with a controlled angle between the plane of the leading edge of the HOPG block and the knife axis (θ_v) (Figure 6.1 b) (see methods section for a detailed alignment procedure). Throughout this report, $\theta_v = 0$ has been used in order to maximize the GNR output by utilizing the full cross-section of the cuboidal HOPG block for the cleavage. By changing the forward step size, d_r of the sample arm, GNBs with different widths were cleaved serially from the parent HOPG block (Figure 6.1a, b; Supporting Video 6SV1 and 6SV2), which were collected in the water trough on the back side of the diamond knife (Figure 6.2c). After alignment, the yield for the synthesis of the GNBs was found to be close to 100 %: suggesting the overall yield of the GNR fabrication process to be limited by the efficiency of the GNB-exfoliation step. These GNBs can be exfoliated via any of the reported graphene exfoliation methods [10-15]. In order to synthesize pristine GNRs at high yield, we employed the recently reported superacid based exfoliation strategy (Figure 6.1e, see methods section for details) [16]. The maximum efficiency of superacid exfoliation strategy was found to be ~ 80 % of starting GNBs (see Appendix E for details), which translates to ~ 10^8 GNRs per hour (for 50 cutting cycles in 1 hour, see Appendix E) per nanotome. This is a significantly higher yield than that of most current processes. Two other exfoliation strategies, viz. the Hummer's acid exfoliation and PCA-based π-intercalation exfoliation [17], were also tested to demonstrate the versatility of this process. It is important to note that a variant of the nanotomy process has been previously employed by the Whitesides' group to produce gold nanostructures [18-20].

Experimental methods

Cleavage of HOPG

We affixed a 7 X 7 X 1 mm HOPG block (*ZYA* Grade, *SPI Inc.*) onto a cuboidal piece of hardened araldite resin using superglue, with an orientation as shown in Figure 6.1 (also see Figure 6.2). The resin-HOPG ensemble was allowed to dry at room temperature for several days before being mounted onto the nanotome sample chuck as shown in Figure 6.2 and 6.3. The chuck was then mounted onto the nanotome and bolted to position on the sample arm. The diamond knife was then mounted on the nanotome with a 5º clearance angle and 40º rake angle (see below for a detailed mounting procedure).

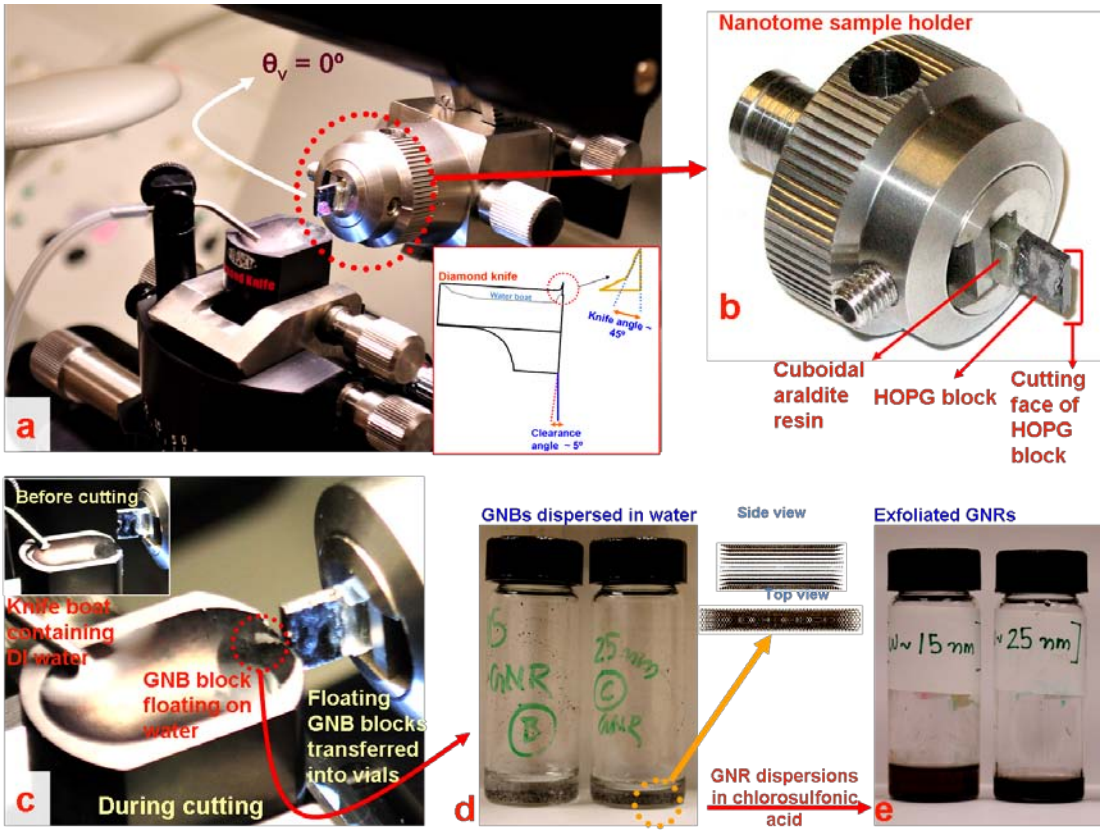

Figure 6-2 Schematic diagram of the nanotomy process. (a) A Nikon D60 image of the nanotome with the HOPG sample mounted before commencement of the cutting cycle. As can be seen from the figure (and from Figure 6.1b), by using $\theta_v = 0$ we ensure using the whole cross section of the cutting face of HOPG. Bottom inset shows a schematic diagram of the diamond knife and the various knife parameters. (b) A close up of the sample holder chuck showing the HOPG rigidly attached (using superglue) to the araldite resin block. The cutting edge of the HOPG shows a metallic hue after the priming as discussed in the methods section of the manuscript. (c) Optical images just before and after a single cutting cycle showing the generation of a GNB after cleavage (also see Supporting Video 6SV1). The cleaved GNBs float in water and are later scooped up into glass vials after completion of cutting process. (d) Optical image of a glass vial containing scooped up GNBs for w ~ 15 and 25 nm. Right inset shows a cartoon depicting the structure of the GNBs, which comprise of stacked GNRs. (e) Vials containing the stably-dispersed GNRs after the exfoliation of GNBs into GNRs using chlorosulfonic acid.

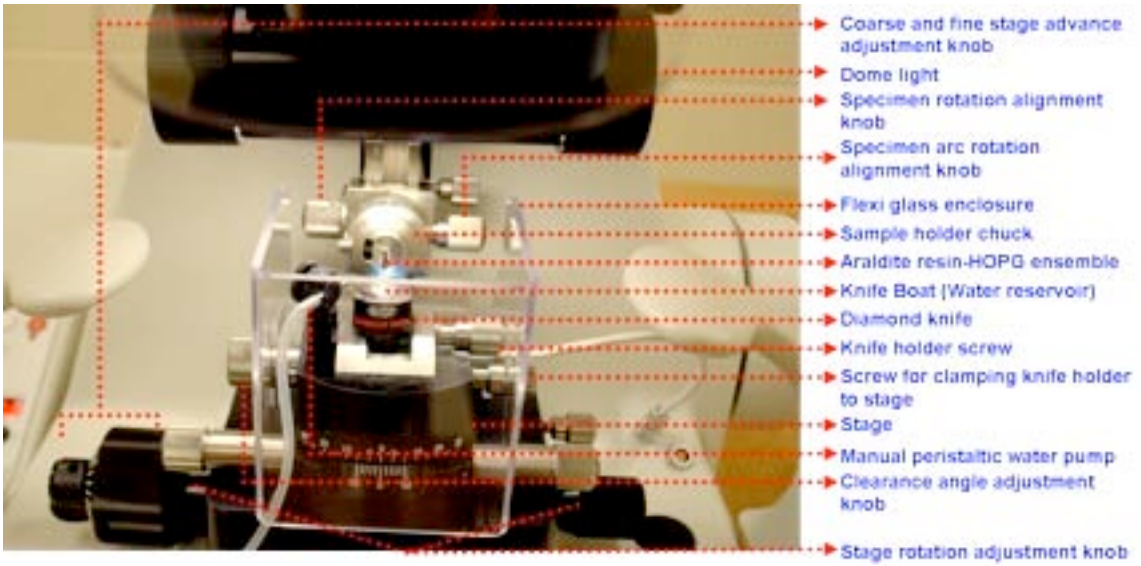

Figure 6-3 Details of the nanotome (Model # PT-XL, Boeckeler Instruments Inc.; 3 mm edge width Du Pont Diamond Knife) used in the manuscript. A second knife of similar parameters from RMC products was also used in this report.

Subsequently, assiduous alignment of the cutting face of the HOPG was carried out with respect to the knife (at $\theta_v = 0^0$) by following the three step procedure described by *Xu et al* [28] (see below for details). During the whole alignment routine extreme care was taken so as not to bump onto the diamond knife edge. Then the knife boat was filled with DI water level and the level adjusted by the water pump (Figure 6.3) so as to have an angle of contact of 30-50^0 with the back of the knife edge as shown in Figure 6.1a. With a pre-determined sample-forward stepsize (d_r) and a specimen-arm speed of 0.4 mm/sec, the HOPG block was cleaved repeatedly to obtain the Graphene nano-Blocks (GNBs) (see figure 6.2c and Supporting Video 6SV1 and 6SV2).

The GNBs slid and got collected in the knife boat. The GNB dispersion in water was collected in clean tubes (Figure 6.2d) and heated at 100 °C under an Ultra High Pure (UHP) argon atmosphere (20 psi) for 1 hour to evaporate all the water in order to obtain the dry GNBs. Due to the high significance of the sample alignment for high quality cleaving, to achieve best results, we used a higher d_r in the beginning of the cleavage process to prime-up the HOPG block before proceeding onto finer cleavage (The initial samples were usually discarded.)

Mounting of diamond knife

The diamond knife (internal knife angle ~ 45º) was attached to the knife holder (Figure 6.3) while making sure it is horizontal using a leveler. Then the knife is clamped tight to the knife holder using the knife holder screw shown in Figure 6.3. Subsequently, we adjusted the clearance angle adjustment knob so as to have a 5^0 clearance angle (and 40^0 rake angle). Then the knife holder was securely clamped down to the stage using the screws shown in Figure 6.3.

Alignment of cutting face of HOPG with respect to diamond knife edge

We used a modified version of the full alignment procedure described by *Xu et al* [28] tailored for our instrument. A similar procedure can be used for any nanotome.

First, only the stage LEDs were switched on (The dome light was kept turned off.) to enhance the shadows which will be used in the alignment procedure. The sample arm containing the HOPG block was parked at the same height as that of the diamond knife edge using the handwheel. Then, while viewing through the stereoscope, the knife stage was moved forward closer to the HOPG block edge, first within a few mm using the course adjustment knob and then closer (a few hundred microns) using the fine adjustment knob. Then the following 3 step process was employed to align the knife edge with respect to the HOPG cutting face.

Alignment of the bottom edge of HOPG block parallel to the edge of the knife: The HOPG block was slowly moved past the knife edge back-and-forth (using the handwheel) while the shadow was observed that appears at the bottom of the cutting face of HOPG and disappears at the top. If the top and the bottom edges of the HOPG are parallel to the knife edge, then the shadow should first appear at the bottom of the face, move across the entire length and disappear at the top of the face. If the shadow appears at the lower edge of one side of the HOPG block before the other, then the cutting face is not parallel. The alignment of the HOPG block was adjusted using the specimen rotation alignment knob (Figure 6.3) until the shadow appears evenly.

Alignment of knife edge parallel to the block face across the width of block: The HOPG block was moved past the knife back-and-forth slowly using the handwheel while observing the height of the reflection across the width of the cutting face. The reflection should be of uniform height across the whole length of the cutting face of the block. If it was higher on

one side than the other, the knife alignment was changed using the stage rotation adjustment knobs (Figure 6.3) until height uniformity was achieved.

Alignment of the HOPG cutting face with knife edge along its whole length: The HOPG block was moved past the knife edge back-and-forth slowly using the handwheel while observing the shadow formed at the cutting face of the HOPG. The shadow is expected to maintain the same height all along the length of the face of the HOPG. If it is not, then the specimen arc rotation alignment knob (Figure 6.3) was used to achieve height uniformity.

During all the above alignment steps extreme caution should be taken so as not to bump into the diamond knife edge. The diamond knife edge is very fragile to lateral stresses and extreme care should be taken while handling it at all times.

Exfoliation of the GNBs

The GNB exfoliation process was carried out via the recently reported superacid exfoliation strategy unless mentioned otherwise. The other two strategies used in this report were the Hummer's acid exfoliation strategy and the Pyrene Carboxylic Acid (PCA) based π-intercalation exfoliation. The experimental details are as follows:

Superacid-based exfoliation of the GNBs: The dried GNBs in glass vials were dispersed in 5 ml of > 99 % Chlorosulfonic acid inside a glove box (< 1 ppm Water Vapor, < 1 ppm Oxygen) (Figure 6.1e, 6.2 d, e). The vials were then placed in a shaker (inside the glove box) for ~ 8 hours at room temperature for the exfoliation process to go to completion as inferred from the dark black color of the suspension phase with no solid residue left over. For characterization purposes, the GNR-suspension was quenched in DI water (1:200) as per the procedure described by *Behabtu et al* [21].

Hummer's acid oxidation based exfoliation followed by hydrazine reduction: A modified Hummer's acid oxidation as described in a previous report by our group (*Mohanty et al*, Nano Letters, 2008: Chapter 2) was used for exfoliating the GNRs. The as-produced GONRs were reduced by the solution-phase hydrazine reduction, washed in DI water and substrate immobilized for further characterization.

Pyrene Carboxylic Acid (PCA) based π-intercalation exfoliation: We also used a modified version of the PCA based exfoliation strategy as reported by *An et al*. In brief, dehydrated GNBs were dispersed in 1 mg/ml solution of PCA in DMF, left undisturbed for ~ 8

hours and subsequently sonicated for 60 seconds resulting in the formation of light-grey colored suspension. The exfoliated GNRs were then washed several times in methanol, followed by DI water and immobilized onto substrates for further studies.

Sample preparation for FESEM, TEM, XPS and Raman spectroscopy

The samples for the FESEM, XPS and Raman spectroscopy were fabricated by immobilizing the quenched GNRs via drop-casting on freshly cleaned n-type Silicon wafers (*University Wafers Inc.*) and drying in an 20 psi UHP Ar atmosphere followed by annealing at 200 C in vacuum (base pressure of 10^{-5} Torr) for 2 hours. The cleaning procedure of the silicon wafers involved organic cleaning (acetone and iso-propanol) followed by native oxide etching with a solution of H_2O:HF (10:1) and washing with iso-propanol. FESEM imaging was carried out in a *FEI* NovaNano FESEM, XPS was carried out in a *Perkin Elmer* XPS and Raman spectroscopic analyses was carried out in a *Renishaw* InVia microRaman spectroscope equipped with a 514.5 nm laser line using a 100 X objective (NA 0.9).

The samples for TEM imaging were fabricated by dipping the lacey carbon 400 mesh grids (*SPI Inc.*) in the freshly quenched GNR solution and drying. TEM imaging was carried out in the Philips CM 100 TEM. The HRTEM images were provided by the *FEI Inc.* (imaging was conducted in a FEI Titan TEM at Hillsboro, OR).

Methods for fabrication of GNR-films

The dilute suspension (~ 0.2 mg/l) of the quenched GNRs was vacuum filtered over 600 nm pore size polycarbonate filter papers (*SPI Inc.*) on a Büchner funnel over a Büchner flask (Figure 6.4). After filtration, the polycarbonate filters were dried over *Drierite* at room temperature for 2 days and then cut as desired. For AFM and FESEM analysis of the GNR film, the polycarbonate filter containing the GNR-film was templated on a freshly cleaned silicon wafer and clamped down using conductive carbon paint. FESEM imaging was carried out using the beam deceleration feature of the *FEI* NovaNano FESEM with landing voltages of < 1 KV. AFM imaging was carried out in tapping mode using the easyScan 2 AFM system from *NanoScience Instruments Inc*.

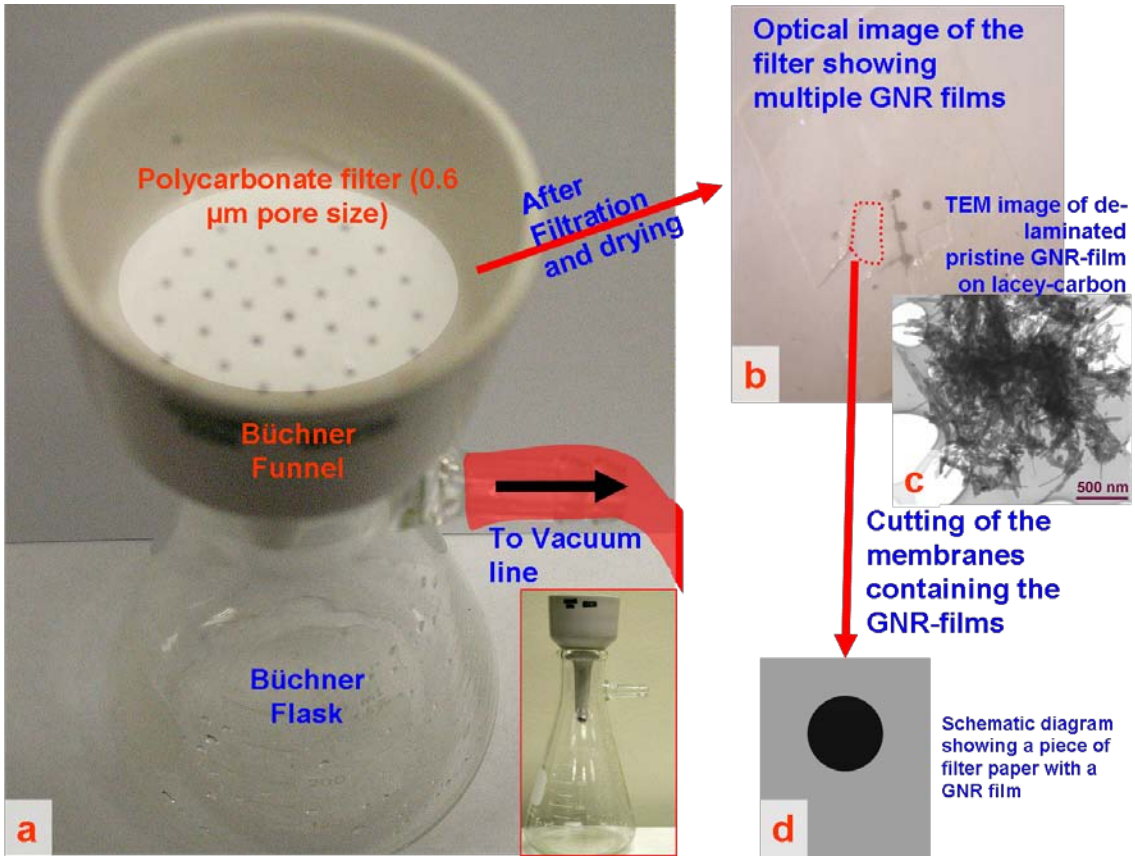

Figure 6-4 Schematic diagram showing the vacuum filtration apparatus and the steps followed for fabricating GNR films. (a) A hybrid of schematic diagram and optical images showing the Büchner filtration apparatus and the polycarbonate filter on the Büchner funnel. After filtration the membrane is dried in an Argon atmosphere at room temperature for 2 days. (b) Optical image showing one such filter paper after the filtration process. Several GNR films (each similar in dimensions to the Büchner funnel pore size ~ 0.4 mm) were observed on the filter, which was then cut out for further characterization. (c) TEM image of de-laminated pristine-GNR film (by dissolution of the polycarbonate filter in 99 % chloroform) immobilized on 400 mesh Lacey carbon grids showing the random arrangement of GNRs in the film. (d) Schematic diagram of the cut out portion of a single GNR film on the polycarbonate filter substrate.

Fabrication of thin-film pristine GNR devices

We used the GNR films on polycarbonate filter substrate directly for device fabrication. 0.2 mm wide polyethylene strips were used as shadow-mask (to define the channel) while source and drain Au:Pd (3:2) electrodes were deposited via sputtering. Then the mask was removed and

the sample checked under an optical microscope to ensure proper deposition of electrodes and channel integrity. For back-gated electrical studies, the film (with source and drain deposited) was immobilized mechanically using a PDMS stamp on a gold coated silicon dioxide wafer. Here, the polycarbonate substrate acts as the gate oxide and the gold coating on the wafer acts as the back gate (Figure 6.11). Electrical characterization was carried out in a *Janis ST100 cryostat* connected to a turbomolecular pump and a liquid nitrogen line.

Results and discussion

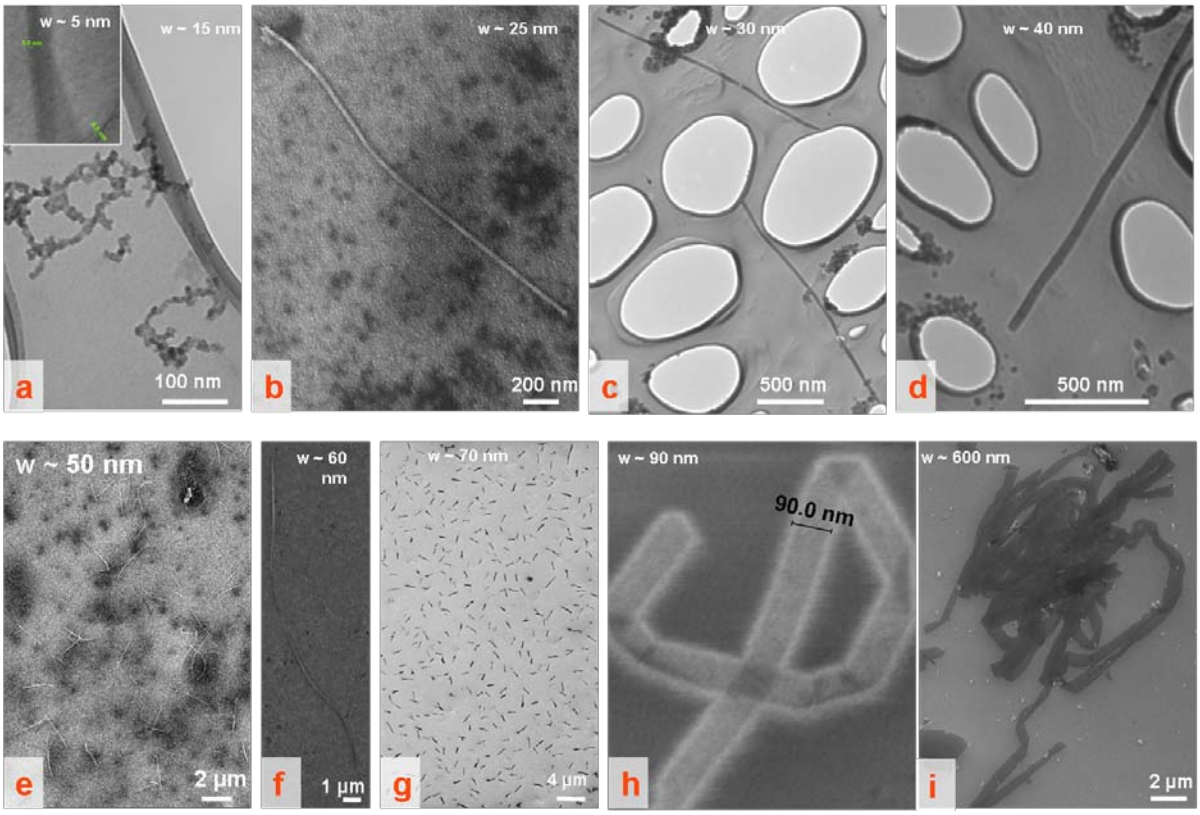

Figure 6-5 Assorted FESEM and TEM images of GNRs with varying widths demonstrating the versatility of our GNR-production process. (a, c, d) TEM images of w ~ 15, 30 and 40 nm GNRs immobilized on 400 mesh Lacey carbon TEM grids (a – top inset, b, e, f, g, h, i) FESEM images of w ~ 5, 6.5, 25, 50, 60, 70, 90 and 600 nm GNRs immobilized on silicon substrates

We templated the as-exfoliated GNRs on n-type silicon wafers or immobilized on 400 mesh lacey carbon TEM grids for FESEM and TEM analyses, respectively (see methods section for details). The thinnest ribbons produced by this setup had a width of ~ 5 nm (Figure 6.5a, top inset), similar to or a significant improvement over the current GNR fabrication strategies.

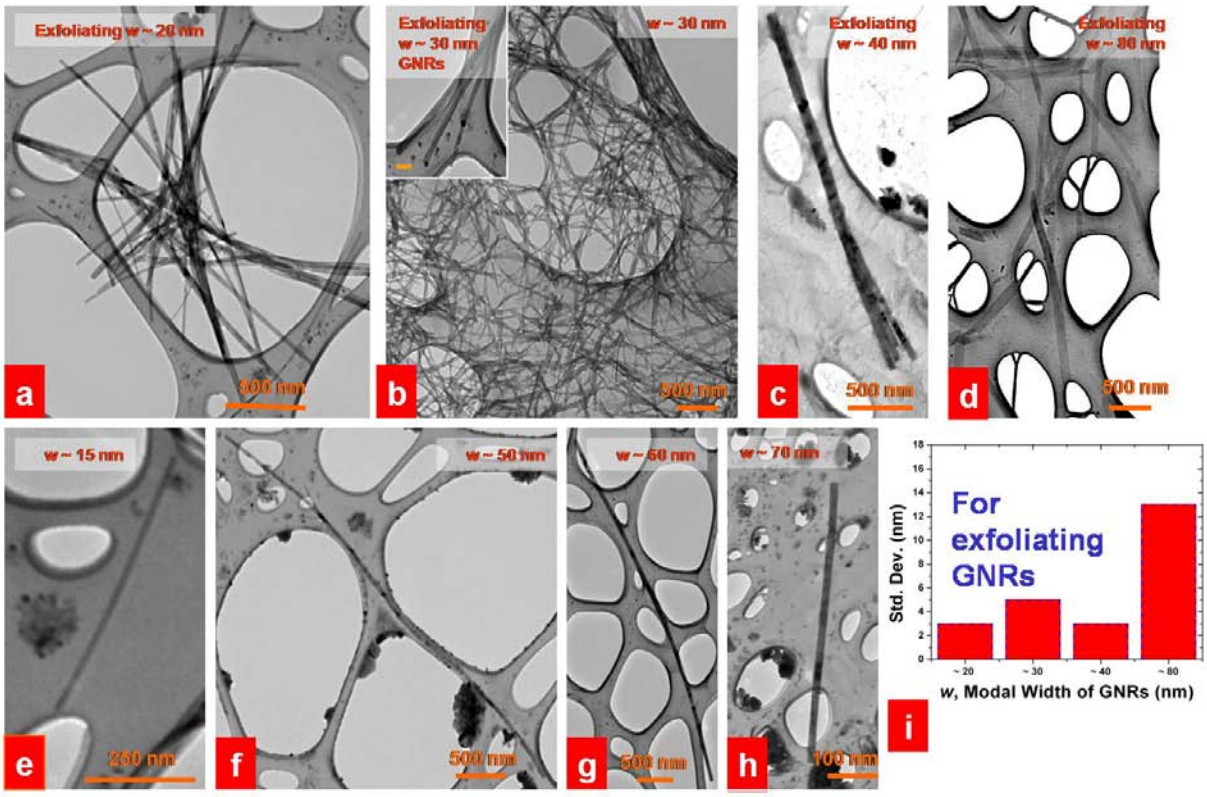

Figure 6-6 (a – d; b-inset) TEM images of still-exfoliating w ~ 20, 30, 40 and 80 nm GNRs templated on 400 mesh lacey carbon TEM grids (*SPI Inc.*). (e - h) High resolution TEM images of w ~ 15, 50, 60 and 70 nm GNRs templated on 400 mesh Lacey carbon TEM grids (*SPI Inc.*). The assortment of images shows the ability of the nanotomy process to pre-determine the width of the GNRs with high aspect ratio (large longitudinal dimensions). (i) Width analysis of the images in panel a – d showing the variation of Standard Deviation with respect to the modal width of the GNRs. The observed standard deviations in width from 3 – 15 nm for w ~ 20 – 80 nm GNRs is, to the best of our knowledge, one of the narrowest width distributions reported till date for narrow GNRs.

Figures 6.6a-d shows a collection of TEM images of still-exfoliating 20, 30, 40 and 80 nm wide GNRs; Figure 6.6e-h show a collection of high resolution TEM images of 15, 50, 60 and 70 nm GNRs. The GNRs are uniform with high aspect ratio in the longitudinal direction. Further, the assorted images demonstrate the versatility of our process to produce pre-determined GNR widths (w) from ~ 5 nm to 600 nm (see Figure 6.5). The TEM images in Figure 6.6a-d were analyzed for the variation in width. For the w ~ 20 nm, ~ 30 nm, ~ 40 nm and ~ 80 nm GNRs, the standard deviation in width was found to be ~ 10 nm, ~ 5 nm, ~ 3 nm and ~ 15 nm, respectively (Figure 6.6i). For GNR widths in the 20-80 nm range in large solvent concentrations (> 10^8/ml), these GNR width distributions are the narrowest. AFM scans on the GNRs templated on 300 nm thick silicon dioxide substrate showed typical bilayer or monolayer nature of the GNRs (Figure 6.7; this is consistent with the results reported by Ref. 21 on graphene superacid dispersions).

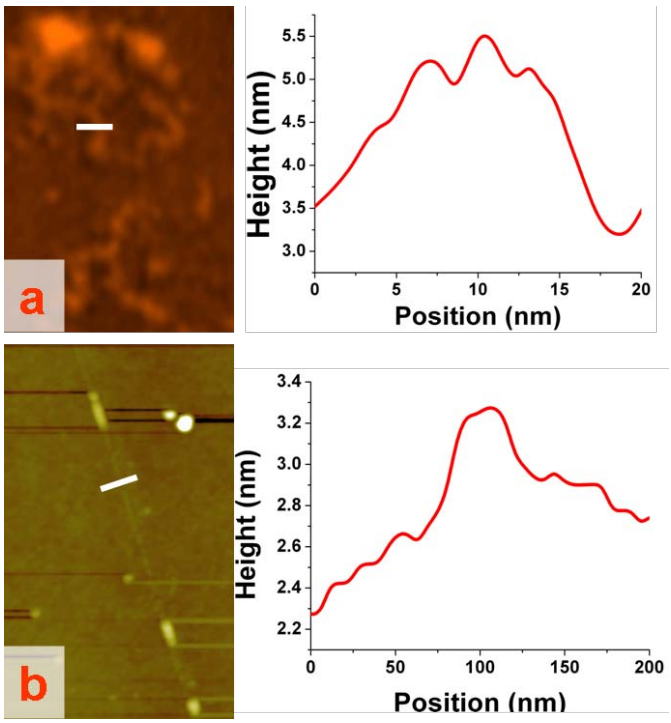

Figure 6-7 AFM images of w ~ 15 nm and 50 nm GNRs showing a typical thickness of 1.5 nm (bilayer) and 0.6 nm (monolayer), respectively

We also employed high-resolution-transmission–electron-microscopy (HR-TEM) for characterization of the atomistic-lattice and the edge crystallography of narrow (w ~ 15 nm wide)

GNRs deposited on lacey carbon grids (*SPI Inc.*) (Figure 6.8). The GNRs were found to have a uniform width in the longitudinal direction, with the diffraction pattern displaying the crystallographic signature of the honeycomb graphitic lattice attesting to their high quality. Atomistic edge crystallographic orientation of the studied GNRs was between zig-zag and arm-chair chirality. In theory, our process can achieve some degree of control the edge crystallography provided it is done on an HOPG with large grain-size; since then the direction of nanotomy can be controlled to provide a desired edge-chirality.

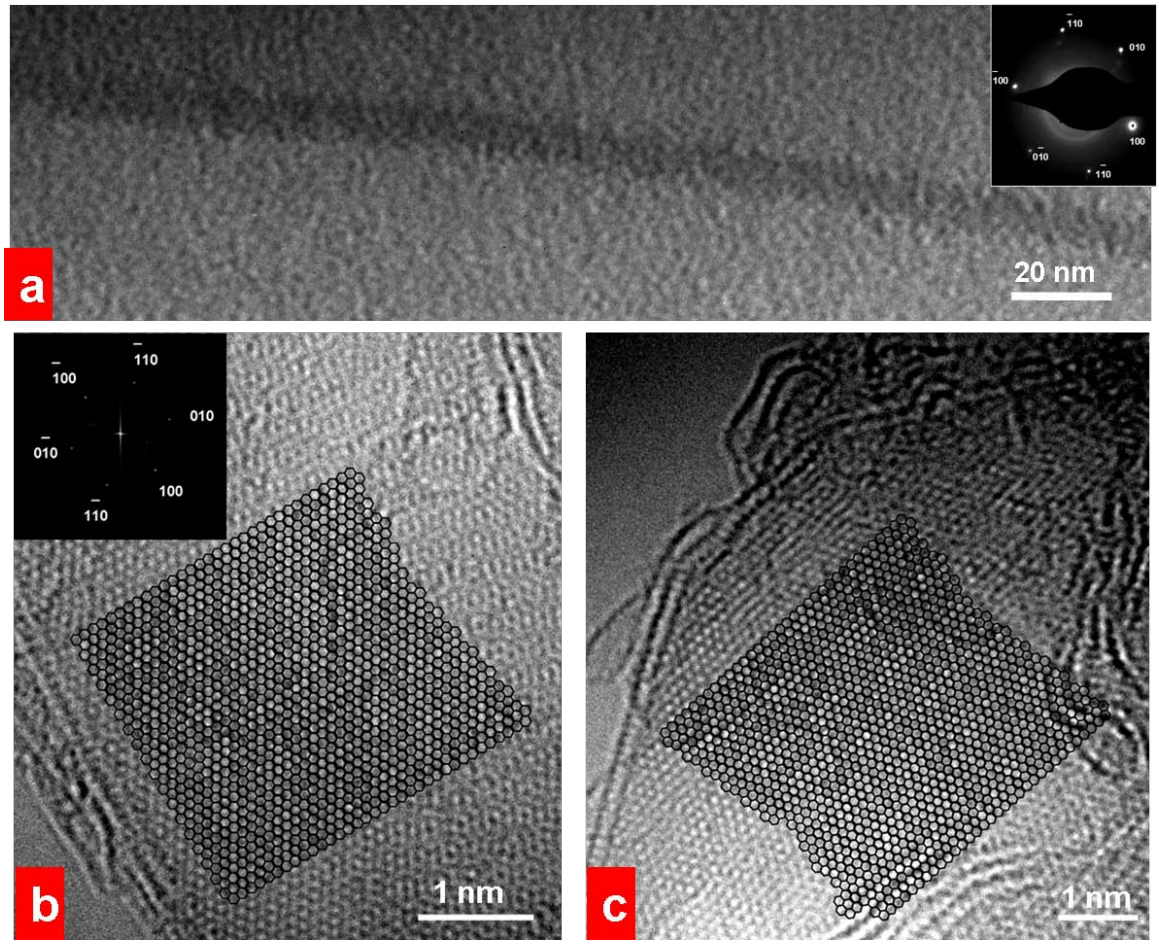

Figure 6-8 HRTEM image of the GNRs. (a) HRTEM image of a w ~ 15 nm wide GNR showing width uniformity vindicating the high quality nature of the production process. A selected area electron diffraction (SAED) on the GNR shows a hexagonal pattern confirming its crystalline structure and its high quality. (b, c) Aberration corrected HRTEM image of the edge of a multilayer w ~ 15 nm wide GNR showing mixed edges (superimposed cartoon showing the graphene structure is a guide for the eye). Left image

inset shows a Fourier transform of the image showing an expected hexagonal pattern attesting to the crystallinity of the structure.

We also used X-ray photoelectron spectroscopy (XPS) to characterize the chemical structure of the GNRs. High resolution C 1s spectra for the GNRs, showed an absence of any carbon bound to other functional groups. Only the sp^2 carbon peak at 284.5 eV was observed, indicating pristine graphenic lattice (Figure 6.9h). This is consistent with the earlier results reported for similar graphenic dispersions in organic and inorganic solvents [11, 21, 23]. The XPS survey scan also detected trace amounts of sulfur (< 1 atomic percent) on the surface of the GNRs, which was attributed to the sulfonation of the edges (Figure 6.9h – insets) induced by the chlorosulfonic acid treatment [21, 22] (Figure E.2, see Appendix E for details). Next, we employed Raman spectroscopy (514.5 nm, < 5 mW) for analyzing the quality of the as-produced GNRs [24]. Sample GNRs (post-exfoliation, followed by quenching and centrifugation-based concentrating) with widths ~ 15, 25 and 50 nm, as determined by the TEM images and the FESEM images were drop-casted as films on a heavily doped n-type silicon substrate, dried in a 20 psi UHP argon atmosphere and calcinated at 200 C for 2 hours in vacuum (10^{-5} Torr). The $I_{D/G}$ ratios, which determine the relative density of the edge roughness/defects, including dangling bonds and crystallographic randomness [25], were used to analyze the GNRs. Since the laser beam diameter was ~ 0.4 μm the Raman spectrum provides the average quality of the GNRs (and accounts for the relative broad nature of peaks especially the short and broad 2D peak). The $I_{D/G}$, ranged from ~ 0.22 – 0.28 for the as-synthesized GNRs, with the narrower ribbons having relatively higher $I_{D/G}$ (Figure 6.9 a, c, e). On comparing with the literature data on GNRs with similar dimensions, these values are close to that reported for GNRs produced *via* sonochemical unzipping of CNTs and are considerably lower than that for other nanoribbon production technique (Figure 6.9g) [8, 25-27]. This indicates a high smoothness of the edges of the produced GNRs. Further, conformal Raman mapping of the individual bi-layer GNRs immobilized on SiO_2 substrate was also recorded. The average $I_{D/G}$ ratio for the w ~ 15 nm GNRs was 0.4-0.5 (see Appendix E, Figure E.3), comparable to the GNRs of similar widths synthesized by sonochemical unzipping of CNTs and much lower than those produced by lithographic methods ($I_{D/G}$ ~ 1.5) or oxidative unzipping of CNTs ($I_{D/G}$ ~ 1).

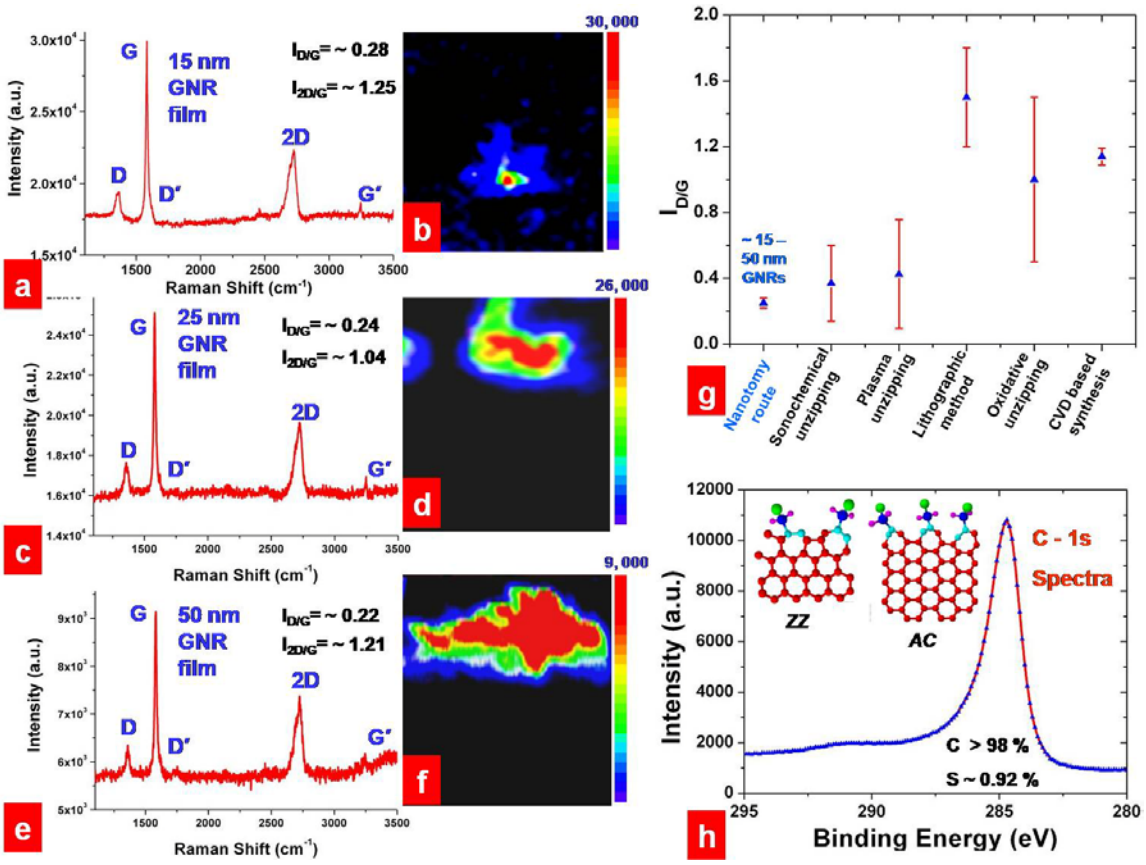

Figure 6-9 (a,b; c, d; e, f) Raman spectra and G-band scans of the w ~ 15, ~ 25 and ~ 50 nm drop casted GNRs showing substantially low $I_{D/G}$ ratios signifying a high quality (low edge roughness and edge defects). As expected the $I_{D/G}$ ratios showed scaling behavior with respect to the width, with narrower ribbons showing higher $I_{D/G}$ due to higher percentage of edges. The close to unity values of the $I_{2D/G}$ ratios suggests heavy doping attributed to the adsorbates during synthesis process. (g) Graph showing the comparison of the $I_{D/G}$ data obtained for our GNRs with the literature values. With the exception of the sonochemical unzipping method, all other methods had higher $I_{D/G}$ suggesting comparatively higher edge defect density [8, 25-27]. (h) Typical high resolution XPS spectra for the C 1s binding energies of the GNRs showing the sp^2 carbon peak at 284.5 eV. The absence of any peaks for other carbon-bound functional groups suggests pristine nature of our GNRs. XPS survey showed trace amounts of sulfur which were confirmed from the high resolution scans for S 2p binding energies (see Appendix E and Figure E.2) Inset shows the schematic diagram of the probable edge sulfonation of predominantly *arm-chair (AA)* and *zig-zag (ZZ)* GNR edges.

The mechanism of nanotomy of GNBs is proposed to be a cleavage-fracture process (see Appendix E for details). The first step of this process is known to involve initiation of a crack in the HOPG from the compressive forces at the first contact point with the diamond knife [28, 29]. The hard and brittle nature of HOPG (Young's modulus = 5-25 GPa) is expected to aid the crack generation, which were found to range from 1-100 μm in length depending on the sample-forward stepsize (d_r) (Figure 6.10c shows the typical data). In a process similar to the wedge-based cleaving of macroscopic brittle materials such as wood, these cracks propagate ahead of the knife aided by the craze formations in HOPG to produce the GNBs. These crazes, which develop from the tensile stresses arising from knife advance, were found to have a strong bearing on the edge quality of GNBs and hence the GNRs (Figure 6.10). Thus the large crazes from high tensile stresses of a faster cleaving speed (i.e. a higher specimen-arm velocity (SAV)) are expected increase the roughness of the edges. This was indeed verified by mapping the average Raman I_D/I_G ratio with the cleaving speed. I_D/I_G ratio = ~ 0.83 for fast (1 mm/sec) compared to ~ 0.22 for slow (0.4 mm/sec) for w ~ 15 nm GNRs. After completion of a cleaving cycle, the GNB slices slide down the back of the diamond knife lubricated by the water molecules from the water reservoir in the knife boat (see Figure 6.2c and 6.10a). If the cleaving process is carried out in absence of the water reservoir, extensive breaking and chipping of GNBs was observed. Therefore, water lubrication is important for reducing the friction and the compressive/bending stresses on the cleaving sections. Further, we found that an angle of contact of ~ 30 - 50º between the water meniscus and the knife edge is important to efficiently collect the cleaved GNBs without any GNBs-buildup at knife edge.

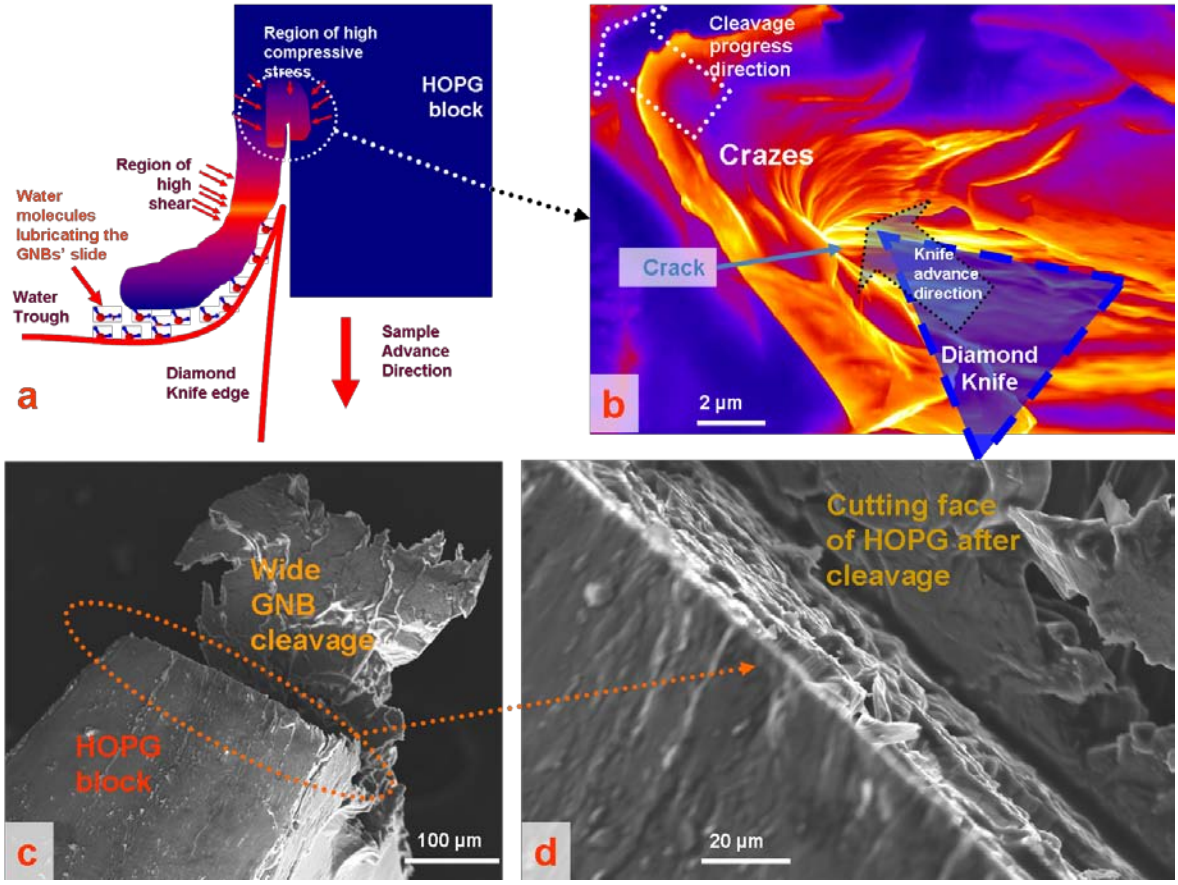

Figure 6-10 Cleavage of GNBs from the HOPG (a) Schematic diagram showing the cleavage of the GNBs from the parent HOPG block. The red colored regions show the areas with high mechanical stresses. The diagram also shows the crucial role played by the water molecules in lubricating the sliding of the GNBs on back of the knife edge, hence reducing friction and bending stresses. (b) False colored FESEM micrographs of the crack generated in the HOPG upon initiation of the cutting process. The respective arrows show the direction of the relative movement of the diamond knife and the direction of propagation of the crack. The crack propagation is known to be aided by the generation of the crazes as shown in the figure. The red colored areas show the areas expected to experience high tensile forces and compressive / shear stresses. (c, d) FESEM micrographs of the side and top views of partially-cut GNB, still attached to the HOPG block, showing good mesoscopic uniformity of the cutting face.

The width-tunable bandgap of the graphene nanoribbons make them excellent channel-material for Field Effect Transistor (FET) fabrication. The high-throughput of this nanoribbon fabrication process was leveraged to fabricate macroscopic thin-films of pristine, narrow GNRs (thickness ~ 50 nm, Figure 6.11f; w ~ 50, 25 and 15 nm GNRs used for film synthesis) with potential applications in flexible electronic/optoelectronics. Recently, films with functionalized-wide-reduced-GONRs were produced *via* oxidative unzipping of nanotubes [30]. Thin films of fixed width GNRs were fabricated from their respective dilute aqueous dispersions (~ 0.2 mg/l) using the standard vacuum filtration technique on 600 nm pore size polycarbonate filters (*SPI Inc.*, Figure 6.11b, c inset, see Figure 6.4). For several (10) such films, FESEM surveys and AFM scans (typical film surfaces shown in Figure 6.11e and 6.11f) showed a uniformly smooth and homogenous surface topography without any significant aggregation, positive attributes for transistor channel material. Sheet resistance of the GNR-films, as determined from the four point probe measurements (see supporting information), was found to be 2.2 – 5.1 MΩ/□ with no apparent dependence on the width of GNRs constituting the film (3 devices were tested for each width). Next, we fabricated GNR-film based FETs by sputter-coating gold-palladium (3:2) source and drain electrodes onto the films directly on the polycarbonate filter paper substrate using resist-free shadow-masking (~ 200 μm channel length and ~ 400 μm channel width) (see methods section and Appendix E for details) (Figure 6.11g).

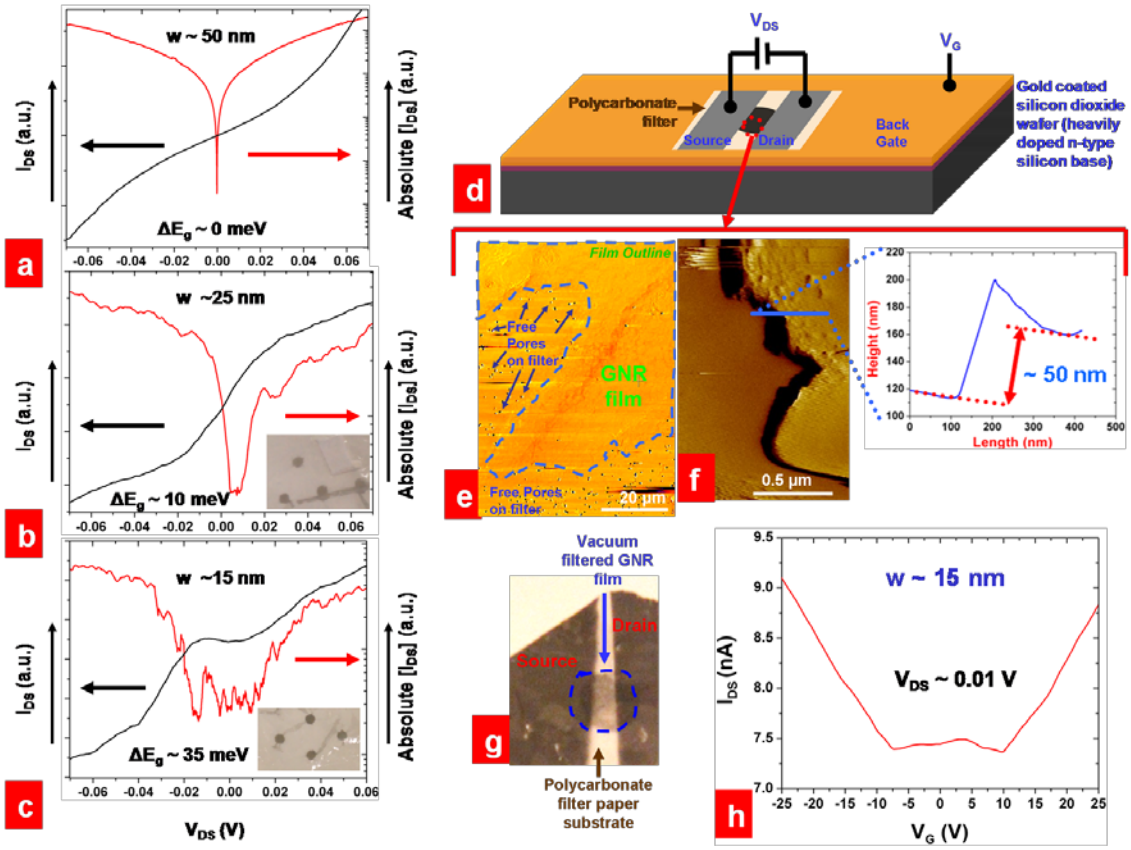

Figure 6-11 (a, b, c) Typical high vacuum (10^{-5} Torr), low temperature (80 K) I_{DS} versus V_{DS} characteristics (linear scale) of the w ~ 50, ~ 25 and ~ 15 nm GNR-film devices (as shown in the schematic diagram (d) and in the optical image of (g)) and the corresponding Absolute [I_{DS}] vs V_{DS} curves (logarithmic scale) showing the non-linear transport. The edges of the bandgap were determined by the steep increase of the current in the logarithmic scale. Owing to the relatively large channel lengths in our GNR film devices, the channel length dependence of the non linear transport gap is expected to be inconsequential. A clear bandgap scaling was observed for the different GNR films: the bandgaps for the as shown w ~ 50 , 25 and 15 nm GNR films were estimated to be ~ 0 meV, ~ 10 meV and ~ 35 meV respectively. (b) and (c) insets show an optical image of the respective GNR films on the polycarbonate filter after drying. (e) FESEM image of a typical GNR film (as shown w ~ 15 nm GNR film) on a polycarbonate filter substrate. (f) Tapping mode AFM image of the GNR film showing typical thickness of ~ 50 nm (right inset). (h) Low temperature (80 K) transfer characteristics of a typical w ~ 25 nm GNR film showing decreasing OFF current upon reduction in the temperature.

In addition to ensuring the absence of any short-channel effects, the relatively long channel dimensions were used to warrant bulk limited transport without any significant influence of the contact-characteristics [31, 32]. For electrical gating, gold surface was used as bottom gate and the polycarbonate filter substrate as the gate oxide ($\varepsilon_r^{Polycarbonate} \sim \frac{3}{4}\varepsilon_r^{SiliconDioxide}$) (see methods section and Appendix E for details) (Figure 6.11d). In air transfer characteristics of the devices showed n-type doping effects attributed to physisorbed chemical species during fabrication steps (Figure 6.12).

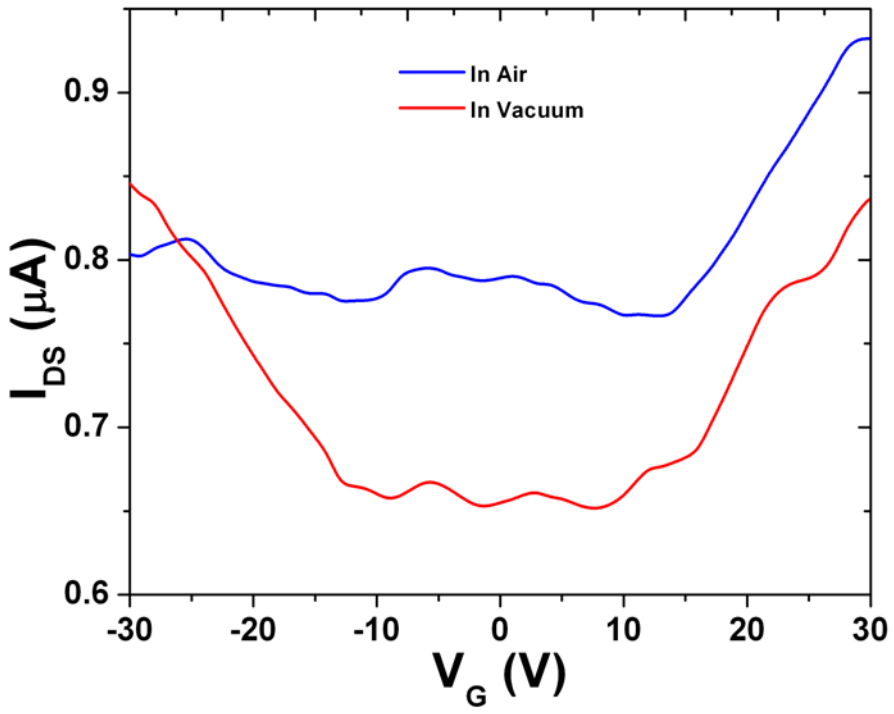

Figure 6-12 Typical back-gated transfer characteristics of a GNR film (the above example is for a w ~ 15 nm GNR film) device with L ~ 0.2 mm, W ~ 0.4 mm and V_{SD} ~ 0.1 V in air and in vacuum.

This was consistent with the close to unity values of I_{2D}/I_G and red shift of 2D peak in the Raman spectra [33] (Figure 6.9a, c, e). The devices were electrically annealed in vacuum (10^{-5} Torr base pressure) to remove all adsorbates (as described in ref. 34), resulting in the recovery of the ambipolar transfer characteristics with symmetric electron and hole transports resembling pristine-graphene (Figure 6.12). The carrier mobilities were calculated to be 20 ± 4 $cm^2/V{\cdot}s$ for

the GNR-films (all widths) which are significantly higher than that reported for typical functionalized-wide-reduced-GONR films [30], confirming high quality (see Appendix E). However, these values are two orders of magnitude lower than the highest mobilities reported for single GNRs (~ 1500 $cm^2/V{\cdot}s$) [25]. The low mobilities here are attributed to carrier scattering at randomly distributed GNR overlap junctions. High vacuum (10^{-5} Torr), low temperature (80 K) current-voltage characteristics (I_{DS} vs V_{DS}) of the w ~ 50 nm, 25nm and 15 nm GNR films at zero gate ($V_G = 0$) exhibited a semiconductor-like non-linear behavior near zero source-drain bias (V_{DS}). With the source-drain gap determined by the edges of the steep logarithmic increase of current, a clear bandgap scaling was observed for the respective GNR films: ~ 0 meV for w ~ 50 nm, ~ 10 meV for w ~ 25 nm and ~ 35 meV for w ~ 15 nm GNR films (Figure 6.11 a-c) [31, 35]. It is imperative to note that owing to the relatively long channel lengths in the GNR film devices, the channel length dependence of the non-linear bandgap [35] is expected to be inconsequential. It is remarkable that the transport spanning multiple GNRs exhibited a measurable bandgap opening. In view of the pristine nature of the GNRs, we attribute the generation of these bandgaps to the quantum confinement in the constituent GNRs, contrary to the functionalized-wide-reduced-GONR films [30]. In order to independently confirm these results, we analyzed the temperature dependent transport behavior for w ~ 15 and w ~ 25 nm GNR-films [36]. Figure 6.11h shows the typical transfer characteristics of the w ~ 25 nm GNR film with respect to the temperature. Arrhenius plots for temperature dependent F current followed the simple exponential relation $I_{OFF} \propto e^{\frac{-E_g}{2k_BT}}$ (Eqn. 1) at higher temperatures. The average thermal activation energies, E_g corresponding to the respective bandgaps were measured to be ~ 6 meV and ~ 30 meV for w ~ 25 and 15 nm GNR films, comparable to those determined from nonlinear transport characteristics.

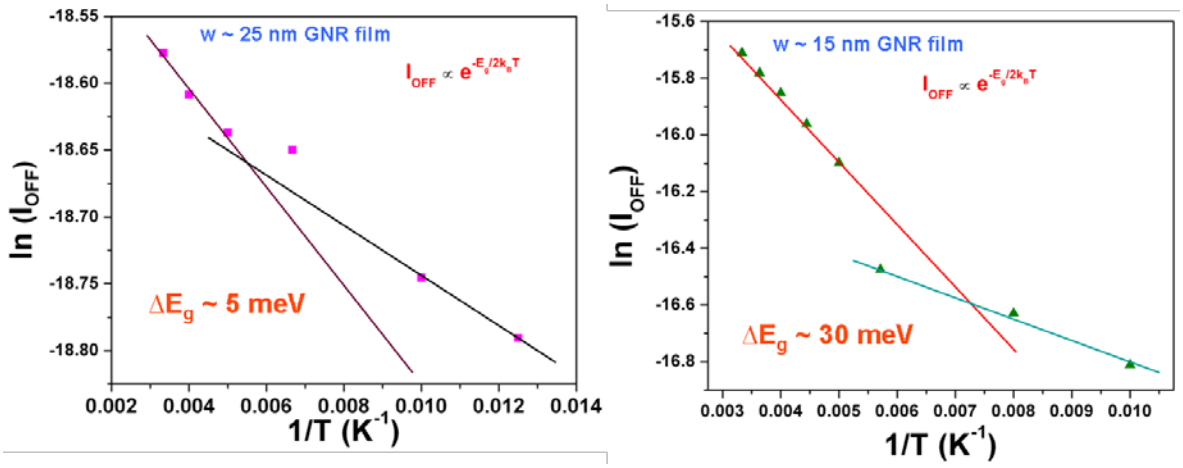

Figure 6-13 Typical temperature dependent transfer characteristics of the GNR-films (a shows a w ~ 25 nm GNR film; b shows a w ~ 15 nm GNR film) showing two different regimes of transport, one at high temperatures T> T^* and other at low temperatures T < T^*. This is characteristic of VRH transport model.

At lower temperatures the F current was observed to deviate from the simple activation behavior given by Eqn. 1, decreasing more slowly, a characteristic of variable range hopping (VRH) behavior. We fit the VRH model given by, $I_{OFF} \propto e^{-(\frac{T_0}{T})^{\gamma}}$ into the low temperature data. For both $\gamma = 1/3$ and $\gamma = 1/4$, similar standard deviations were obtained suggesting hopping in 2 and 3 dimensions including through randomly distributed scattering sites at the overlays of the GNRs and through multiple layers [37].

Conclusion

In conclusion, we demonstrate a novel nanotomy route to controllably synthesize high-density, long, smooth-edged GNRs with pre-determined widths and narrowest width distribution reported till date. The structural and electrical properties characterized *via* TEM, HRTEM, SAED, Raman and gating measurements confirm the pristine nature of GNRs and control on width. We also demonstrate that this process can produce pristine GNR films with band-gap controlled by GNR-width. These structurally defined GNRs and the robust synthesis process will potentially enable rational design of GNR applications and will further evolve GNR research. We envision that the nanotomy process could be applied on large-grain HOPG with known crystallographic orientation to produce GNRs with defined chirality. Also, the edge smoothness

could be further improved by reducing the environmental vibration during nanotomy, by using ultrasonic diamond knives [38, 39].

Acknowledgements

VB thanks the financial support from NSF-CAREER CMMI-1054877; CMMI-0939523 and KSU-Startup. VB thanks DM and the KU materials characterization facility for equipment usage support. VB thanks FEI Inc for providing HRTEM images of the GNRs. VB thanks Dr. Daniel Boyle for help with TEM imaging and microtomy; and Dr. Dr. Qiang (Charles) Ye for help with Raman.

References

1. Ritter,K.A. & Lyding,J.W. The influence of edge structure on the electronic properties of graphene quantum dots and nanoribbons. *Nature Materials* **8**, 235-242 (2009).

2. Han,M.Y., Ozyilmaz,B., Zhang,Y.B., & Kim,P. Energy band-gap engineering of graphene nanoribbons. *Phys. Rev. Lett.* **98**, 206805 (2007).

3. Kinder,J.M., Dorando,J.J., Wang,H., & Chan,G.K.L. Perfect Reflection of Chiral Fermions in Gated Graphene Nanoribbons. *Nano Letters*109-625 .

4. Liang,G., Neophytou,N., Nikonov,D.E., & Lundstrom,M.S. Performance projections for ballistic graphene nanoribbon field-effect transistors. *IEEE Transactions on Electron Devices* **54**, 677-682 (2007).

5. Obradovic,B. *et al.* Analysis of graphene nanoribbons as a channel material for field-effect transistors. *Appl. Phys. Lett.* **88**, 142102 (2006).

6. Wang,X. *et al.* Room-temperature all-semiconducting sub-10-nm graphene nanoribbon field-effect transistors. *Phys. Rev. Lett.* **100**, 206803 (2008).

7. Yang,L., Park,C.H., Son,Y.W., Cohen,M.L., & Louie,S.G. Quasiparticle Energies and Band Gaps in Graphene Nanoribbons. *Phys. Rev. Lett.* **99**, 186801 (2007).

8. Jiao,L., Zhang,L., Wang,X., Diankov,G., & Dai,H. Narrow graphene nanoribbons from carbon nanotubes. *Nature* **458**, 877-880 (2009).

9. Cai,J. *et al.* Atomically precise bottom-up fabrication of graphene nanoribbons. *Nature* **466**, 470-473 (2010).

10. Li,X.L., Wang,X.R., Zhang,L., Lee,S.W., & Dai,H.J. Chemically derived, ultrasmooth graphene nanoribbon semiconductors. *Science* **319**, 1229-1232 (2008).

11. Hernandez,Y. *et al.* High-yield production of graphene by liquid-phase exfoliation of graphite. *Nature Nanotechnology* **3**, 563-568 (2008).

12. Li,X.L. *et al.* Highly conducting graphene sheets and Langmuir-Blodgett films. *Nature Nanotechnology* **3**, 538-542 (2008).

13. Liu,N. *et al.* One-Step Ionic-Liquid-Assisted Electrochemical Synthesis of Ionic-Liquid-Functionalized Graphene Sheets Directly from Graphite This project was sponsored by the Scientific Research Foundation for Returned Overseas Chinese Scholars, the State Education Ministry, and the Scientific Innovation Foundation for Undergraduates, Northeast Normal University. Supporting Information is available online from Wiley InterScience or from the author. *Advanced Functional Materials* **18**, (2008).

14. Valle s,C. *et al.* Solutions of negatively charged graphene sheets and ribbons. *Journal of the American Chemical Society* **130**, 15802-15804 (2008).

15. Hao,R., Qian,W., Zhang,L., & Hou,Y. Aqueous dispersions of TCNQ-anion-stabilized graphene sheets. *Chemical Communications* **2008**, 6576-6578 (2008).

16. Xu,Y., Bai,H., Lu,G., Li,C., & Shi,G. Flexible graphene films via the filtration of water-soluble noncovalent functionalized graphene sheets. *Journal of the American Chemical Society* **130**, 5856-5857 (2008).

17. An,X. *et al.* Stable Aqueous Dispersions of Noncovalently Functionalized Graphene from Graphite and their Multifunctional High-Performance Applications. *Nano Letters* **10**, 4295-4301 (2010).

18. Xu,Q., Bao,J., Capasso,F., & Whitesides,G.M. Surface Plasmon Resonances of Free-Standing Gold Nanowires Fabricated by Nanoskiving. *Angewandte Chemie International Edition* **45**, 3631-3635 (2006).

19. Xu,Q., Gates,B.D., & Whitesides,G.M. Fabrication of Metal Structures with Nanometer-Scale Lateral Dimensions by Sectioning Using a Microtome. *Journal of the American Chemical Society* **126**, 1332-1333 (2004).

20. Xu,Q., Perez-Castillejos,R., Li,Z., & Whitesides,G.M. Fabrication of High-Aspect-Ratio Metallic Nanostructures Using Nanoskiving. *Nano Letters* **6**, 2163-2165 (2006).

21. Behabtu,N. *et al.* Spontaneous high-concentration dispersions and liquid crystals of graphene. *Nature Nanotechnology* **5**, 406-411 (2010).

22. Cremlyn,R.J.W. *Chlorosulfonic acid: a versatile reagent*(Springer Us/Rsc,2002).

23. Lotya,M., King,P.J., Khan,U., De,S., & Coleman,J.N. High-Concentration, Surfactant-Stabilized Graphene Dispersions. *Acs Nano* **4**, 3155-3162 (2010).

24. Ferrari,A.C. Raman spectroscopy of graphene and graphite: Disorder, electron-phonon coupling, doping and nonadiabatic effects. *Solid State Communications* **143**, 47-57 (2007).

25. Jiao,L., Wang,X., Diankov,G., Wang,H., & Dai,H. Facile synthesis of high-quality graphene nanoribbons. *Nature Nanotechnology* **5**, 321-325 (2010).

26. Campos-Delgado,J. *et al.* Bulk production of a new form of sp(2) carbon: Crystalline graphene nanoribbons. *Nano Letters* **8**, 2773-2778 (2008).

27. Kosynkin,D.V. *et al.* Longitudinal unzipping of carbon nanotubes to form graphene nanoribbons. *Nature* **458**, 872-876 (2009).

28. Xu,Q., Rioux,R.M., Dickey,M.D., & Whitesides,G.M. Nanoskiving: A New Method To Produce Arrays of Nanostructures. *Accounts of Chemical Research* **41**, 1566-1577 (2008).

29. Acetarin,J.D., Carlemalm,E., Kellenberger,E., & Villiger,W. Correlation of some mechanical properties of embedding resins with their behaviour in microtomy. *J. Elec. Microsc. Tech.* **6**, 63-79 (1987).

30. Zhu,Y. & Tour,J.M. Graphene Nanoribbon Thin Films Using Layer-by-Layer Assembly. *Nano Letters* **10**, 4356-4362 (2010).

31. Eda,G., Fanchini,G., & Chhowalla,M. Large-area ultrathin films of reduced graphene oxide as a transparent and flexible electronic material. *Nature Nanotechnology* **3**, 270-274 (2008).

32. Kittel,C. & McEuen,P. *Introduction to solid state physics*(Wiley New York,1986).

33. Casiraghi,C., Pisana,S., Novoselov,K.S., Geim,A.K., & Ferrari,A.C. Raman fingerprint of charged impurities in graphene. *Appl. Phys. Lett.* **91**, 233108 (2007).

34. Moser,J., Barreiro,A., & Bachtold,A. Current-induced cleaning of graphene. *Appl. Phys. Lett.* **91**, (2007).

35. Han,M.Y., Brant,J.C., & Kim,P. Electron Transport in Disordered Graphene Nanoribbons. *Phys. Rev. Lett.* **104**, 056801 (2010).

36. Chen,Z.H., Lin,Y.M., Rooks,M.J., & Avouris,P. Graphene nano-ribbon electronics. *Physica E-Low-Dimensional Systems & Nanostructures* **40**, 228-232 (2007).

37. Jin,M. *et al.* Graphene oxide thin film field effect transistors without reduction. *Journal of Physics D: Applied Physics* **42**, 135109 (2009).

38. Jθsior,J.C. Use of low-angle diamond knives leads to improved ultrastructural preservation of ultrathin sections. *Scanning microscopy. Supplement* **3**, 147 (1989).

39. Studer & Gnaegi Minimal compression of ultrathin sections with use of an oscillating diamond knife. *Journal of Microscopy* **197**, 94-100 (2000).

Chapter 7 - High throughput production of graphene quantum dots (GQDs) with tunable size and shape

Abstract

Graphene Quantum Dots (GQDs) – *single atom thick nano-sheets of graphene with dimensions approaching the Bohr exciton radii* – have elicited intense interest owing to facile carrier modulation via spatial (3D) quantum confinement and edge lattice-terminations, unlike their 2D parent *Graphene*. Theoretical and experimental studies have shown this phenomenon to induce exciting new carrier transportation and optical properties, dependent on the GQD shape, size and the edge crystallography. However, the current GQD synthesis strategies for yielding precise dimensions and geometry are challenging. Here, we present a novel nano-mechanical route for high throughput production of GQDs with predetermined spatial dimensions (50 nm till > 100 nm), controllable geometry (squares, rectangles, trapezoids and triangles) and smooth edges. Similar in principle to the chopping of an onion, a 2 axes nano-scale cutting process was employed in an ultra-microtome to produce graphene nano-blocks (GNBs) from HOPG. Comprising of millions of *AB* stacked GQDs, these GNBs were exfoliated via the superacid exfoliation strategy to produce a mono-dispersion of GQDs (Efficiency ~ 80 %). These mono-dispersions of GQDs displayed spatial dimension-dependent band-gap and corresponding photoluminescence emission peaks. To the best of our knowledge, this is the first instance of high-throughput fabrication of GQDs with both controlled dimensions and pre-determined shape and the experimental demonstration of the rational engineering of the GQDs' optical property.

Introduction

Since its isolation in 2004, Graphene, *consisting of a monolayer of sp^2 bonded carbon atoms arranged in a honey comb lattice*, has generated intense excitement owing to its unparalleled properties[1-8]. Reduction of the size of graphene close to its *Bohr exciton* radii results in the formation of a new class of graphene called Graphene quantum dots (GQDs) and leads to the emergence of several new phenomena unavailable to the parent graphene [2, 4, 7, 9-18]. Crucial among those are the bandgap generation and the unique optical properties such as the emergence of new absorption bands and photoluminescence emission spectra [11-13, 18]. Theoretical and experimental studies have found these properties to be sensitively dependent on the dimensions and edge lattice terminations of the GQDs [9-13, 15, 17, 18]. Despite the plethora of research into the production of the 2D graphene, the progress in the synthesis of GQDs has lagged far behind. The current methods of fabrication include the top down strategies of chemical [9, 18], sono-chemical [11] and lithographic strategies [15]; and the bottom-up chemical condensation strategy [12, 13]. While the chemical and sono-chemical methods produce GQDs with restricted dimensions and rough edges, the lithographic methods are limited by the extreme low throughput. The bottom-up chemical condensation of halocyclic precursors, even-though promising, fails for GQDs with dimensions > 3 nm. To enable the rational engineering of the optical properties of GQDs, a new large-scale production strategy is mandated with better control on the GQD dimensions and edge structure.

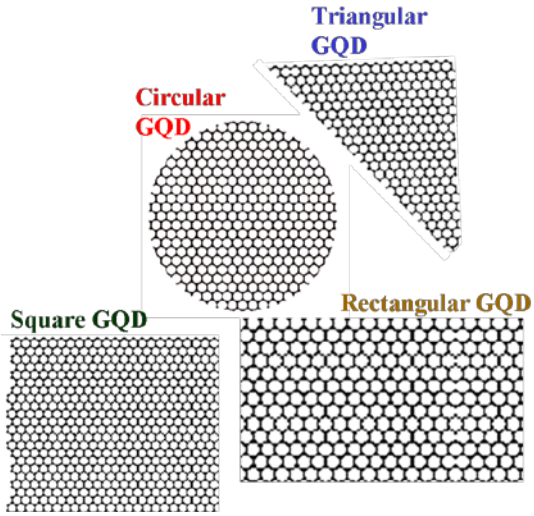

Figure 7-1 Schematic diagram of GQDs of various shapes

In this report we demonstrate a novel nanotomy-based (nanoscale cutting) production strategy for large scale synthesis of GQDs with tunable dimensions and shape from commercially acquired highly oriented pyrolytic graphite (HOPG) blocks. Similar in principle to the chopping of an onion (a macroscopic layered material), we employ two-step-two-axes nanotomy of HOPG, using an ultrasharp diamond knife (*Boeckeler Inc.*, edge radius ~ 5 nm) mounted on a ultramicrotome (*Boeckeler Instruments, Inc.*), to produce nanoblocks of graphene (see methods section for details). Upon assiduous alignment routines (see methods section for details), each cutting cycle was found to be successful in producing a cut. The efficiency of cutting was found to be ~ 99 % (for ~ 200 cutting cycles in each step: *see methods section and Appendix F for details*). The as-produced graphene nanoblocks (GNBs) comprise of millions of *AB*-stacked GQDs which were then exfoliated using the recently reported chlorosulfonic superacid exfoliation strategy[19] (Figure 7.3). With the exfoliation efficiency ~ 60 %, the overall efficiency of the GQD synthesis strategy is ~ 59 %. This translated to ~ 10^{10} GQDs per hour per nanotome per HOPG (see Appendix F for details).

Experimental Methods

Priming the HOPG block

A commercially obtained HOPG block (*ZYA* grade, *SPI Inc.*; Size 7 X 7 X 1 mm) was cleaved using a stainless steel knife into 2 mm X 2 mm X 1 mm pieces (due to the limitations imposed by the dimensions of the diamond knife: Knife edge length 3 mm) and the cut blocks embedded in Paraffin Wax molds at 80 C and then allowed to cool to room temperature for 4 hours. Paraffin wax provides structural support during the cutting process (Figure 7.2 a-c).

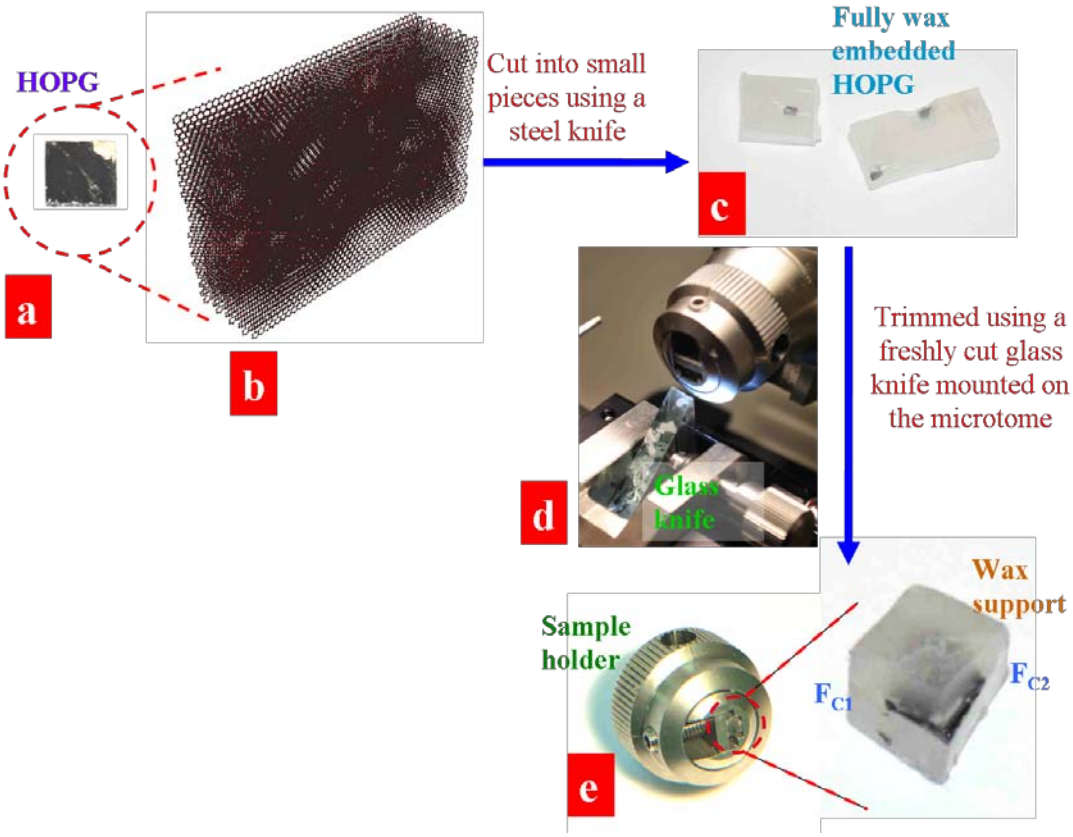

Figure 7-2 (a, b) Optical image and schematic diagram of a HOPG block. (c) Optical image of fully embedded cut-HOPG blocks in wax. (d) Nikon D60 image of the trimming setup using a freshly sharpened glass knife mounted on a microtome. A closer look at the figure reveals the wax trims on the user-side of the knife. (e) Optical image of the trimmed HOPG-embedded-in-wax showing the F_{C1} and the F_{C2} faces.

The wax-embedded sample is then mounted onto the sample holder as shown in the Figure 7.2 d. The sample is then primed for the cutting step by serially trimming the wax using a freshly sharpened glass knife so as to expose the HOPG block on 2 sides (Figure 7.2d, e) for the serial 2-step-2-axes cutting process.

Cutting process

Similar to the chopping of an onion, a 2-step-2-axes cutting process was carried out in order synthesize the quantum dots (Figure 7.3 a, b). After the priming process, the wax-embedded HOPG is mounted on the sample holder with the first cutting face, F_{C1} facing the

diamond knife, as shown in Figure 7.3 a and e. Careful alignment routines similar to that described in Chapter 6, *Methods section* are employed to ensure that F_{C1} and the diamond knife edge are parallel. For the first step, the HOPG was cut partially (the vertical displacement during

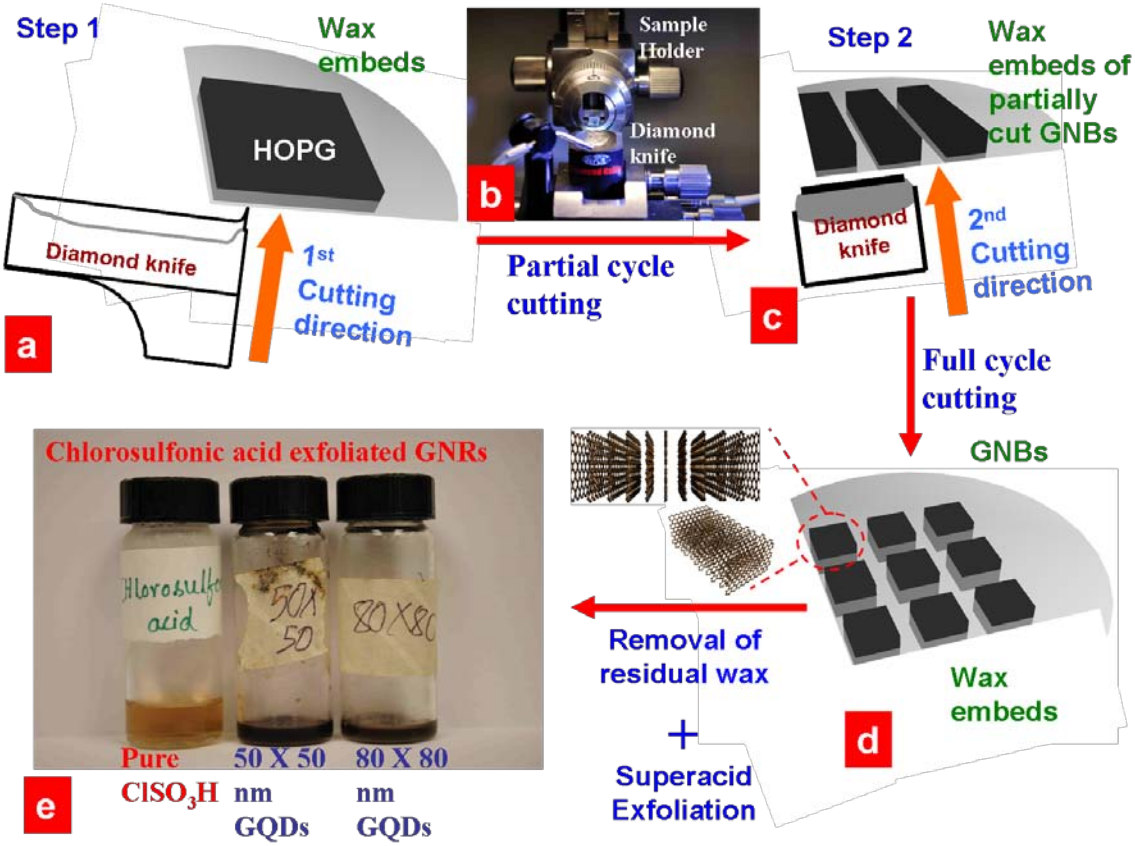

Figure 7-3 (a, c, d) Schematic diagram of the high-throughput GQD production strategy via nano-scale 2-step-2-axes cutting of HOPG blocks (embedded in wax) in an ultra-microtome. First, partial cutting of the HOPG block was carried out along the 1st axis (a), followed by cutting in the 2nd axis (b), to produce the GNBs (c). The GNBs comprise of millions of AB stacked GQD sheets as shown in the cartoon in d. (e) A Nikon D 60 image of the ultra-microtome setup employed in the GQD production process. (f) The as-obtained GNBs were exfoliated into their constituent GQDs via the recently reported super-acid exfoliation strategy. The figure shows optical images of the glass vials containing a mono-dispersion of 50 X 50 and 80 X 80 nm GQDs dispersed stably in chlorosulfonic acid.

cutting being equal to the thickness of HOPG block embedded in wax i.e. ~ 1 mm without cleaving the wax support on the top surface of HOPG) while moving forward in steps of predetermined d_{r1} (this corresponds to the length of the GQDs eventually produced).

It is imperative to note that, partial cutting is important in the first step to enable the cut blocks to be still embedded in wax for the second axes cutting (see Figure 7.3 b). Without the partial cutting action, the first step was found result in de-lamination of the GNBs from wax leading to the formation of GNRs instead of GQDs. With the cutting action being successful in every cutting cycle, the efficiency of the cutting was estimated to be ~ 100 % owing to the partial cutting. Then, the partially-cut-HOPG-wax ensemble is rotated by an angle $\theta_{GQD} \sim 90^{o}$ (or any other angle depending on the desired shape of GQDs, Figure 7.4) in the horizontal plane as shown in Figure 7.3b, aligned assiduously as per the procedure described before, and the second full cycle cutting step is carried out in steps of d_{r2} (the breadth of the GQDs) producing the GNBs with dimensions d_{r1} X d_{r2}: the cut GNBs fell free from the wax embeds onto the water bath behind the diamond knife. The angle, θ_{GQD} determines the shape of the GQDs. As can be seen from Figure 7.4, varying the θ_{GQD} and the d_{r1} and d_{r2} different shapes and sizes of GQDs could be obtained.

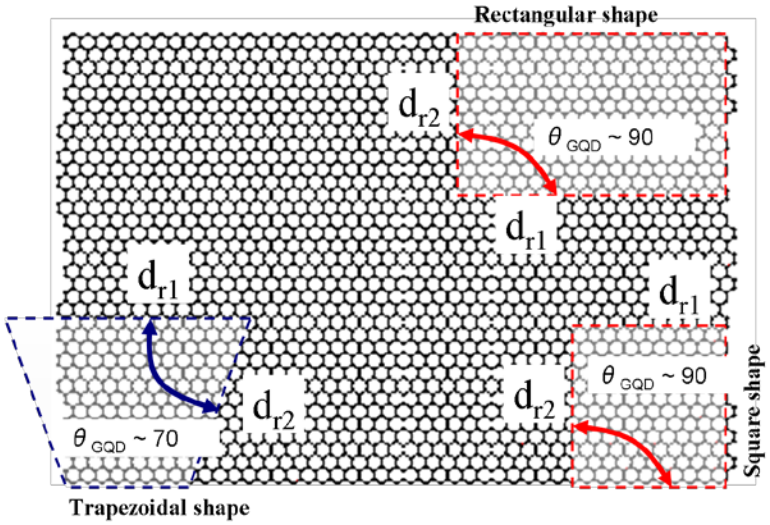

Figure 7-4 Schematic diagram showing the various parameters during the cutting process and their effect in producing different shapes of GQDs

We would like to draw attention to the fact that after the second axes (F_{C2}) cutting step, owing to the limited number of cutting cycles from the first axis (F_{C1}) cutting steps non en-compassing the whole length of the HOPG block, GNRs are produced concomitantly with GQDs (see Appendix F for a detailed discussion). The GQDs are separated from the GNRs using high-speed centrifugation based processing as described in later sections.

Collection of GNBs and exfoliation

The free GNBs in the water bath were collected via aspiration using a pipette and stored in a glass vial. The glass vials were heated at 200 °C for 2 hours to remove residual wax and evaporate the water. The as-obtained GNBs could potentially be exfoliated using any of the reported graphene exfoliation strategies [20]. For this work, we chose to employ the recently reported chlorosulfonic acid based exfoliation [19] owing to its high efficiency and its capability in producing pristine exfoliated GQDs. 2 ml of 98 % chlorosulfonic acid was dispensed into the glass vials and put in a shaker at room temperature for ~ 8 hours to facilitate exfoliation into the constituent GQDs (Figure 7.3 f). The liquid phase in the vials turned black demonstrating the successful exfoliation of the GNBs into the constituent GQDs (and the GNR contaminants). The as-produced GQD-dispersions were found to be stable for over several months (> 2 months).

Separation of GNRs from the GQDs

The exfoliated mixture of GNR contaminants and the GQDs in chlorosulfonic superacid were centrifuged at 13, 300 g for 3 hours at room temperature in a table top centrifuge. Subsequently, the top layer of superacid, which contained enriched GQDs, was extracted. Throughout this report, thus enriched samples of GQDs were employed for further analyses unless otherwise mentioned.

Results and Discussions

The exfoliated GQDs were quenched in DI water (1:200) and were templated on 300 mesh lacey-carbon TEM grids for TEM analyses. Figure 7.5 shows an assortment of TEM images of the GQDs produced by our nano-scale cutting strategy. The images demonstrate the versatility of our process in producing GQDs with controlled dimensions from 50 nm till > 100 nm and pre-determined regular shapes (square, rectangular, trapezoidal and triangular). Dimensional analysis was carried out for the 50 X 50 GQDs displayed in Figure 7.5 a and the standard deviation was determined to be ~ 5 nm, which showed good mono-dispersity of the GQD suspensions. This is comparable to or surpasses most GQD production strategies that have been reported this far.

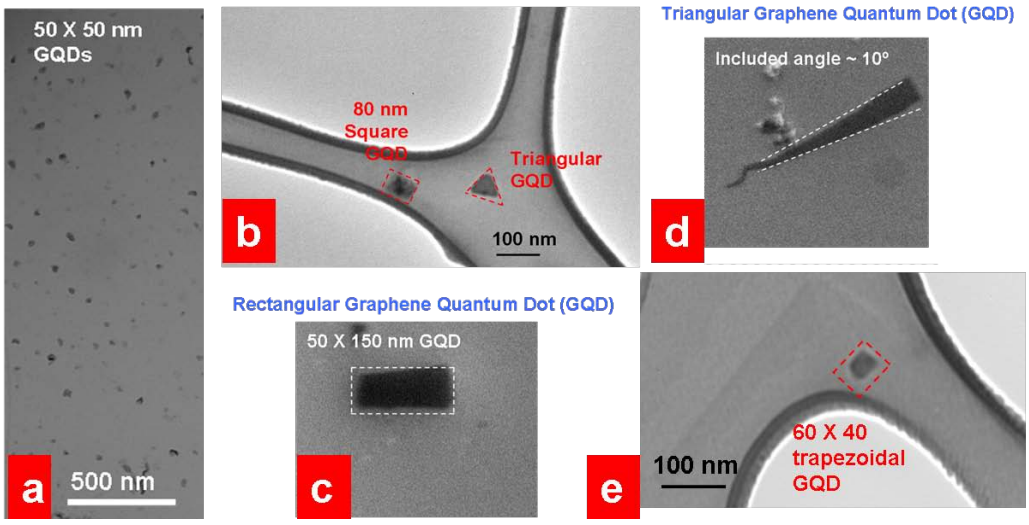

Figure 7-5 (a-e) Assorted TEM images of GQDs immobilized on 300 mesh lacey-carbon TEM grids demonstrating the versatility of our synthesis strategy with regard to the dimensions and shape

We employed X-ray photoelectron spectroscopy (XPS) for analysing the chemical properties of the superacid exfoliated GQDs. C 1s spectra on the GQD films, immobilized on silicon dioxide substrate via dropcasting, showed the lone peak at 284.5 eV characteristic to sp^2 bonded carbon (Figure 7.6 a) [21]. This absence of the XPS spectral peaks corresponding to the sp^3 bonded carbon demonstrates the predominantly pristine nature of our GQDs. However, full scale survey scans showed the presence of < 1 % sulphur, which we attribute to probable edge sulfonation considering the excellent propensity of chlorosulfonic acid to sulfonate phenylic groups [22, 23]. This inability of the C 1s spectra in detecting edge sulfonation is due to the low atomic percentage of sulphur and is not without precedence, has in fact been observed by *Behabtu et al* [19] in their study on exfoliation of graphene. High resolution scans for sulphur 2p displayed two peaks, one at ~ 169 eV corresponding to sulphur at high oxidation states such as sulfonates and the other at ~ 164 eV corresponding to unbound disulfide or thiols (adsorbed residual acid / sulphur compounds) [24] (Figure 7.6 b). Theoretical analysis on the fraction of edge carbon atoms with respect to the basal surface ones for a 50 X 50 nm GQD caps the maximum possible sulphur atomic percentage at 8 % (assuming total sulfonation of the edge associated carbon stoms), consistent with the experimental results (see Chapter 6 - Appendix E for details).

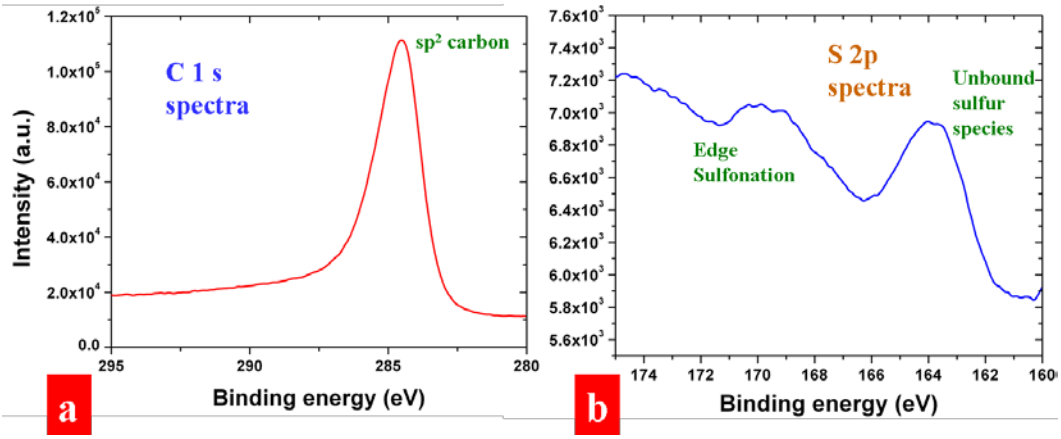

Figure 7-6 (a) Typical C 1s XPS spectra for the 50 X 50 nm GQDs showing the presence of the lone peak at ~ 284.5 eV corresponding to the crystalline sp^2 bonded carbon. The absence of peaks corresponding to the functionalized sp^3 bonded carbon demonstrates the pristine nature of our chlorosulfonic superacid exfoliated GQDs. (b) High resolution S 2p spectra for the GQDs showing the presence of trace amounts of sulphur attributed to the probable edge sulfonation (peak at ~ 169 eV) and adsorbed residual acid (peat at ~ 164 eV)

We studied the optical properties of two families of GQDs with similar shapes: the 50 X 50 nm square GQDs and the 80 X 80 nm square GQDs quenched in DI water, for the ease of comparison (Figure 7.7). Theoretical studies have predicted the emergence of several unique optical properties due to pronounced effects of the quantum confinement and edge lattice effects in view of smaller dimensions (< 100 nm) of the GQDs [2, 10, 11, 15, 18, 25, 26]. Experimental UV-Vis absorbance spectra of both the GQD families showed one concurrent peak typically at ~ 230 nm which was attributed to the $\pi - \pi^*$ electronic transitions of the pristine aromatic sp^2 domains [8, 11]. New characteristic peaks at ~ 276 nm (~ 4.49 eV) for 50 X 50 nm GQDs and at ~ 308 nm (~ 4.02 eV) for 80 X 80 nm GQDs, were also observed without any precedence in the parent graphene [2, 4].

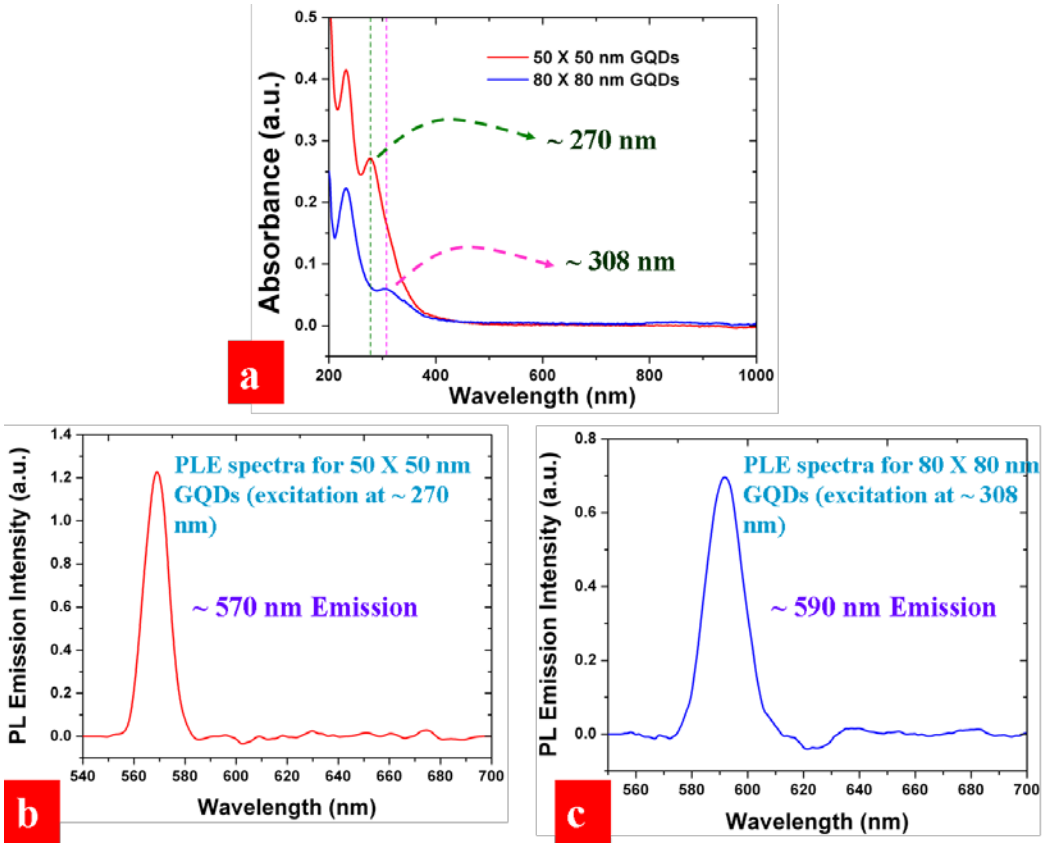

Figure 7-7 (a) UV-Vis absorption spectra for the two families of GQDs viz. 50 X 50 nm GQDs and 80 X 80 nm GQDs showing the unique spectral features absent in the parent graphene. (b, c) Photoluminescence emission spectra for the excitation at the characteristic absorption peaks for the respective GQD families.

Photoluminescence emission spectra of the GQDs for excitation at the corresponding characteristic absorption band showed a strong green luminescence: for 50 X 50 nm GQDs PL emission at 570 nm was observed for excitation at 270 nm i.e. a stokes shift of 300 nm (2.32 eV); and for 80 X 80 nm GQDs PL emission at 590 nm was observed for excitation at 308 nm corresponding to a stokes shift of ~ 282 nm (1.92 eV) (Figure 7.7 b, c). The observed red-shift in the PL emissions upon increase in GQD dimensions is in sync with the theoretical predictions [10, 11, 18]. The respective PL emission peaks were found to be excitation dependent, with the most intense peak being for excitation at the characteristic absorption band, similar what has been reported earlier by *Pan, D. et al* [11]. The PL emission spectra was found to be independent of the pH of the solution, discounting the involvement of emissive free *zig-zag* sites of the GQDs [11, 26, 27]. The PL excitation spectra for the respective emission peaks showed only one sharp

peak corresponding to the characteristic absorption peaks (see Appendix F, Figure F2). In contrast to the results by *Pan, D. et al* [11], this suggests for a different origin for the photoluminescence other than the carbene-like triplet ground states in free *zig-zag* sites of GQDs. Further studies need to be conducted on determining the exact origin of our photoluminescence peaks.

Conclusion

In conclusion, we have demonstrated a novel nano-scale 2-step-2-axes cutting strategy for high throughput fabrication of GQDs with controlled dimensions, shapes and smooth edges. The structural and optical properties of the resulting mono-dispersed suspension of GQDs were characterized via TEM, UV-Vis spectroscopy and Photoluminescence spectroscopy, providing a clear demonstration of the effects of quantum confinement for two size families. We expect this facile synthesis process to enable rational design of the electro-optical properties of GQDs for applications in electronics and optics.

Acknowledgements

VB thanks the financial support from NSF-CAREER CMMI-1054877, NSF-CMMI-0939523 and the KSU. We thank Dr. John Tomich for providing us access to the fluorometer for PL measurements.

References

1 Andre Geim and Konstantin Novoselov land nobel prize for discovering graphene *ChemSusChem* **3**, 1224-1224 (2010)

2 Geim, A.K. Graphene: status and prospects *Science* **324**, 1530-1534 (2009)

3 Fal'ko, V., Geim, A., Das Sarma, S., MacDonald, A. & Kim, P. Special issue recent progress in graphene studies preface *Solid State Communications* **149**, 1039-1040 (2009)

4 Geim, A.K. & Novoselov, K.S. The rise of graphene *Nat. Mater.* **6**, 183-191 (2007)

5 Geim, A.K. & MacDonald, A.H. Graphene: exploring carbon flatland *Physics Today* **60**, 35-41 (2007)

6 Fal'ko, V.I. & Geim, A.K. Graphene: emerging matter in two dimensions *European Physical Journal-Special Topics* **148**, 1-3 (2007)

7 Novoselov, K.S., Jiang, D., Schedin, F., Booth, T.J., Khotkevich, V.V., Morozov, S.V. & Geim, A.K. Two-dimensional atomic crystals *Proc. Natl. Acad. Sci. U.S.A.* **102**, 10451-10453 (2005)

8 Novoselov, K.S., Geim, A.K., Morozov, S.V., Jiang, D., Zhang, Y., Dubonos, S.V., Grigorieva, I.V. & Firsov, A.A. Electric field effect in atomically thin carbon films *Science* **306**, 666-669 (2004)

9 Lu, J., Yeo, P.S.E., Gan, C.K., Wu, P. & Loh, K.P. Transforming c-60 molecules into graphene quantum dots *Nat. Nanotechnol.* **6**, 247-252 (2011)

10 Li, L.S. & Yan, X. Colloidal graphene quantum dots *J. Phys. Chem. Lett.* **1**, 2572-2576 (2010)

11 Pan, D.Y., Zhang, J.C., Li, Z. & Wu, M.H. Hydrothermal route for cutting graphene sheets into blue-luminescent graphene quantum dots *Adv. Mater.* **22**, 734-+ (2010)

12 Yan, X., Cui, X., Li, L. Synthesis of large, stable colloidal graphene quantum dots with tunable size *J. Am. Chem. Soc.* **132**, 5944-5945 (2010)

13 Yan, X., Cui, X., Li, B., Li, L. Large, solution-processable graphene quantum dots as light absorbers for photovoltaics *Nano Lett.* **10**, 1869-1873 (2010)

14 Libisch, F., Stampfer, C. & Burgdorfer, J. Graphene quantum dots: beyond a dirac billiard *Phys. Rev. B* **79**, (2009)

15 Ponomarenko, L.A., Schedin, F., Katsnelson, M.I., Yang, R., Hill, E.W., Novoselov, K.S. & Geim, A.K. Chaotic dirac billiard in graphene quantum dots *Science* **320**, 356-358 (2008)

16 Trauzettel, B., Bulaev, D.V., Loss, D. & Burkard, G. Spin qubits in graphene quantum dots *Nat. Phys.* **3**, 192-196 (2007)

17 Silvestrov, P.G. & Efetov, K.B. Quantum dots in graphene *Phys. Rev. Lett.* **98**, (2007)

18 Li, Y., Hu, Y., Zhao, Y., Shi, G.Q., Deng, L.E., Hou, Y.B. & Qu, L.T. An electrochemical avenue to green-luminescent graphene quantum dots as potential electron-acceptors for photovoltaics *Adv. Mater.* **23**, 776-+ (2011)

19 Behabtu et al Spontaneous high-concentration dispersions and liquid crystals of graphene *Nature Nanotechnol.* **ASAP**, (2010)

20 Zhu, Y.W., Murali, S., Cai, W.W., Li, X.S., Suk, J.W., Potts, J.R. & Ruoff, R.S. Graphene and graphene oxide: synthesis, properties, and applications *Adv. Mater.* **22**, 3906-3924 (2010)

21 Zhu, Y. & Tour, J.M. Graphene nanoribbon thin films using layer-by-layer assembly *Nano Lett.* **10**, 4356-4362 (2010)

22 Kosynkin, D.V., Lu, W., Sinitskii, A., Pera, G., Sun, Z.Z. & Tour, J.M. Highly conductive graphene nanoribbons by longitudinal splitting of carbon nanotubes using potassium vapor *ACS Nano* **5**, 968-974 (2011)

23 Cremlyn, R.J. Chlorosulfonic acid, *RSC* (2002)

24 Lee, M.T., Hsueh, C.C., Freund, M.S. & Ferguson, G.S. Air oxidation of self-assembled monolayers on polycrystalline gold: the role of the gold substrate *Langmuir* **14**, 6419-6423 (1998)

25 Li, X.Y., Wang, H.Q., Shimizu, Y., Pyatenko, A., Kawaguchi, K. & Koshizaki, N. Preparation of carbon quantum dots with tunable photoluminescence by rapid laser passivation in ordinary organic solvents *Chem. Comm.* **47**, 932-934 (2011)

26 Sun, Y.P., Zhou, B., Lin, Y., Wang, W., Fernando, K.A.S., Pathak, P., Meziani, M.J., Harruff, B.A., Wang, X., Wang, H.F. et al. Quantum-sized carbon dots for bright and colorful photoluminescence *J. Am. Chem. Soc.* **128**, 7756-7757 (2006)

27 Radovic, L.R. & Bockrath, B. On the chemical nature of graphene edges: origin of stability and potential for magnetism in carbon materials *J. Am. Chem. Soc.* **127**, 5917-5927 (2005)

Chapter 8 - Conclusions and future work

In this dissertation we synthesized various structural and chemical derivatives of graphene, characterized them in detail and employed them in applications as diverse as ultrasensitive sensing, thin film transistors, physiological coatings in biomedical engineering and as a protective swaddle for TEM imaging of bacteria. Chapter 1 presented a brief overview of the wonder material graphene, some of its exceptional properties that make graphene a truly table top quantum material and the current fabrication methods for producing graphene. It also made an attempt to contextualize the results in chapters 2 – 7 in view of the overall landscape of graphene science.

Chapter 2 demonstrated the first working graphene based bacterial / DNA sensor. Using a novel HATU-catalyzed reaction of Graphene oxide (GO), an oxy-functional derivative of graphene, bio-functionalized graphene (both peptide and probe DNA functionalized) was synthesized which were employed as sensitive building blocks for bioelectronics at both microbial and molecular level with single quanta sensitivity. We demonstrated a single bacterium bio-device, where 1400 charge carriers were generated in the functionalized graphene sensor; and a DNA / protein and polyelectrolyte chemical transistor, where hybridization of a single DNA strand to its complementary probe reversibly increased the hole density by 5.61 X 10^{12} cm^{-2}. We believe this work to lead to the development of various graphene derivatives and their application in highly sensitive molecular detection tools, bio-batteries, bio-driven electronics and molecular electronic systems.

Chapter 3 extends this work to the next level where a single live bacterium (at the time of wrapping) was hermetically wrapped with a protein-functionalized graphene sheet. The exceptional structural, chemical and electrical properties of graphene were leveraged to protect the dimensional and topological integrity of the bacterial cells in ultrahigh vacuum (~ 10^{-5} Torr) and high beam current (~ 150 A/cm^2) of the TEM column. Unlike unwrapped bacterium which shrunk by ~ 76 % upon exposure to the TEM column during imaging, the impermeable graphenic encasements of the wrapped bacterium enabled ~ 350 % wet volume retention, protected the internal bacterial structures including cell wall and significantly abated electrostatic charging. This enabled facile “native state” imaging of the bacterial cells in a TEM without the traditionally lengthy sample preparation procedures. We believe this work to enable real-time

imaging of fluid dynamics, liquid protein suspensions and elucidation of live cell biochemical activity.

The fabrication of biocompatible, robust free-standing TWEEN/Graphene paper is demonstrated in chapter 4. In addition to demonstrating excellent chemical stability and mechanical strength (robust enough to be handled by hand), the TWEEN/Graphene paper was non-toxic towards three mammalian cell lines (African green monkey kidney cells (Vero Cells), Embryonic bovine (EB) cells, and Crandell–Rees feline kidney cells (CRFK)) tested while simultanelously inhibiting the non-specific binding of bacterial cells (*Bacillus cereus*). These results show that TWEEN/Graphene composites could potentially be used for biomedical applications including artificial skin, transplant device coatings, invasive instrument coatings and implants.

Chapter 5 addresses the issue of extreme toxicity of reductants employed in reduced graphene oxide (RGO) production by demonstrating a novel, ultra-fast and high-yield process for synthesizing highly stable RGO dispersions in methanol via a facile sodium hydride based reduction of GO. The abilities of sodium hydride to act as a reducing agent to reduce GO to RGO and as a deprotonator to convert methanol to methoxy ions which stabilize the RGO sheets in bulk methanol are leveraged in this process. The RGO sheets produced displayed high carrier mobilities (as high as 600 $cm^2/V{\cdot}s$) and a low degree of sp^3 defects (Raman $I_{D/G} \sim 1.08$), demonstrating the high efficiency of the reduction process. Owing to its benignness, we expect an ubiquitous application of our hydride reduction strategy for chemical synthesis of graphene.

In chapter 6, we have addressed one of the key problems withholding the ubiquitous application of graphene nanoribbons (GNRs), *1 dimensional semiconducting derivatives of graphene*, in electronics. We demonstrate a novel high-throughput ($\sim 10^8$ GNRs / hr / nanotome) nanotomy (nanoscale cutting) route to synthesize GNRs with controllable width and smooth edges (Raman $I_{D/G} \sim 0.22 – 0.28$) from commercially available highly oriented pyrolytic graphite (HOPG) blocks using an ultra-sharp (edge radius ~ 5 nm) diamond knife. The minimum standard deviation of the widths (modal width pre-determinable between ~ 5 nm till 600 nm) obtained was ~ 4 nm which is one of the narrowest width distributions reported till date. Thin films of the pristine GNRs for varying widths displayed an ambipolar semiconducting nature (bandgaps ~ 30 ± 10 meV for films of 15 nm wide GNRs) and high carrier mobilities (~20 ± 4 $cm^2/V{\cdot}s$ for films of 15 and 25 nm GNRs). With every researcher having easy access to a mictotome, we expect

wide-spread adoption of our GNR synthesis strategy and a resulting quantum leap in GNR applications and research.

Chapter 7 extends this work by demonstrating a modified version of the nanoscale cutting strategy, a 2-step-2-axes cutting process for high throughput fabrication of GQDs with controlled dimensions, shapes and smooth edges. The structural and optical properties of the resulting mono-dispersed suspension of GQDs were characterized via TEM, UV-Vis spectroscopy and Photoluminescence spectroscopy, providing a clear demonstration of the effects of quantum confinement. We expect this facile synthesis process to enable rational design of the electro-optical properties of GQDs for applications in electronics and optics.

To conclude this dissertation, inspite of several key findings and the resulting high-impact publications, in our opinion has just skimmed the surface of the sea of graphene science. Much further studies wait to be done both in breadth and depth before the importance of graphene can be tangibly appreciated. The enormous potentialities offered by graphene need to be actualized, or they would be forever lost as one of the numerous intangibles in the academia. Taking a cue from Jon Von Neumann, one of the founding fathers of modern science & technology, who has famously talked about the ever accelerating pace of technological revolution enabling advancements in rapidly decreasing time scales: unlike Silicon, the material at the heart of current technology (both digital and analog), which needed a generation of research before its mainstream applications; those of graphene, in view of the exponentially increasing research efforts, might not be that far in the future: atleast not a generation.

References

1 Novoselov, K.S., Jiang, D., Schedin, F., Booth, T.J., Khotkevich, V.V., Morozov, S.V. & Geim, A.K. Two-dimensional atomic crystals *Proc. Natl. Acad. Sci. U.S.A.* **102**, 10451-10453 (2005)

2 Novoselov, K.S., Geim, A.K., Morozov, S.V., Jiang, D., Katsnelson, M.I., Grigorieva, I.V., Dubonos, S.V. & Firsov, A.A. Two-dimensional gas of massless dirac fermions in graphene *Nature* **438**, 197-200 (2005)

3 Novoselov, K.S., Geim, A.K., Morozov, S.V., Jiang, D., Zhang, Y., Dubonos, S.V., Grigorieva, I.V. & Firsov, A.A. Electric field effect in atomically thin carbon films *Science* **306**, 666-669 (2004)

4 Geim, A.K. Graphene: status and prospects *Science* **324**, 1530-1534 (2009)

5 Geim, A.K. & Novoselov, K.S. The rise of graphene *Nat. Mater.* **6**, 183-191 (2007)

6 Geim, A.K. & MacDonald, A.H. Graphene: exploring carbon flatland *Physics Today* **60**, 35-41 (2007)

7 Fal'ko, V., Geim, A., Das Sarma, S., MacDonald, A. & Kim, P. Special issue recent progress in graphene studies preface *Solid State Comm.* **149**, 1039-1040 (2009)

8 Das Sarma, S., Geim, A.K., Kim, P. & MacDonald, A.H. Exploring graphene - recent research advances - foreword *Solid State Comm.* **143**, 1-2 (2007)

9 Friedman, T.L. The world is flat: a brief history of the twenty-first century , (2007)

10 Barth, A. & Marx, W. Graphene - a rising star in view of scientometrics *arXiv.org* **arXiv:0808.3320**, (2008)

11 Du, X., Skachko, I. & Andrei, E.Y. Towards ballistic transport in graphene *International J. Mod. Phys. B* **22**, 4579-4588 (2008)

12 Bolotin, K.I., Sikes, K.J., Jiang, Z., Klima, M., Fudenberg, G., Hone, J., Kim, P. & Stormer, H.L. Ultrahigh electron mobility in suspended graphene *Solid State Comm.* **146**, 351-355 (2008)

13 Balandin, A.A., Ghosh, S., Bao, W.Z., Calizo, I., Teweldebrhan, D., Miao, F. & Lau, C.N. Superior thermal conductivity of single-layer graphene *Nano Lett.* **8**, 902-907 (2008)

14 Lee, C., Wei, X.D., Kysar, J.W. & Hone, J. Measurement of the elastic properties and intrinsic strength of monolayer graphene *Science* **321**, 385-388 (2008)

15 Bunch, J.S., Verbridge, S.S., Alden, J.S., van der Zande, A.M., Parpia, J.M., Craighead, H.G. & McEuen, P.L. Impermeable atomic membranes from graphene sheets *Nano Lett.* **8**, 2458-2462 (2008)

16 Nair, R.R., Blake, P., Grigorenko, A.N., Novoselov, K.S., Booth, T.J., Stauber, T., Peres, N.M.R. & Geim, A.K. Fine structure constant defines visual transparency of graphene *Science* **320**, 1308-1308 (2008)

17 Morozov, S.V., Novoselov, K.S. & Geim, A.K. Electron transport in graphene *Physics-Uspekhi* **51**, 744-748 (2008)

18 Katsnelson, M.I. & Novoselov, K.S. Graphene: new bridge between condensed matter physics and quantum electrodynamics *Solid State Comm.* **143**, 3-13 (2007)

19 Castro Neto, A.H., Guinea, F., Peres, N.M.R., Novoselov, K.S. & Geim, A.K. The electronic properties of graphene *Rev. Mod. Phys.* **81**, 109-162 (2009)

20 Stoller, M.D., Park, S.J., Zhu, Y.W., An, J.H. & Ruoff, R.S. Graphene-based ultracapacitors *Nano Lett.* **8**, 3498-3502 (2008)

21 Zhang, Y.B., Tan, Y.W., Stormer, H.L. & Kim, P. Experimental observation of the quantum hall effect and berry's phase in graphene *Nature* **438**, 201-204 (2005)

22 Dikin, D.A., Stankovich, S., Zimney, E.J., Piner, R.D., Dommett, G.H.B., Evmenenko, G., Nguyen, S.T. & Ruoff, R.S. Preparation and characterization of graphene oxide paper *Nature* **448**, 457-460 (2007)

23 Stankovich, S., Dikin, D.A., Dommett, G.H.B., Kohlhaas, K.M., Zimney, E.J., Stach, E.A., Piner, R.D., Nguyen, S.T. & Ruoff, R.S. Graphene-based composite materials *Nature* **442**, 282-286 (2006)

24 Blake, P., Brimicombe, P.D., Nair, R.R., Booth, T.J., Jiang, D., Schedin, F., Ponomarenko, L.A., Morozov, S.V., Gleeson, H.F., Hill, E.W. et al. Graphene-based liquid crystal device *Nano Lett.* **8**, 1704-1708 (2008)

25 Hill, E.W., Geim, A.K., Novoselov, K., Schedin, F. & Blake, P. Graphene spin valve devices *IEEE Transactions on Magnetics* **42**, 2694-2696 (2006)

26 Subrina, S., Kotchetkov, D. & Balandin, A.A. Heat removal in silicon-on-insulator integrated circuits with graphene lateral heat spreaders *IEEE Electron Device Lett.* **30**, 1281-1283 (2009)

27 Bunch, J.S., van der Zande, A.M., Verbridge, S.S., Frank, I.W., Tanenbaum, D.M., Parpia, J.M., Craighead, H.G. & McEuen, P.L. Electromechanical resonators from graphene sheets *Science* **315**, 490-493 (2007)

28 Park, S., Mohanty, N., Suk, J.W., Nagaraja, A., An, J., Piner, R.D., Cai, W., Dreyer, D.R., Berry, V. & Ruoff, R.S. Biocompatible, robust free-standing paper composed of a tween/graphene composite *Adv. Mater.* **22**, 1-5 (2010)

29 Mohanty, N., Nagaraja, A., Armesto, J. & Berry, V. High-throughput, ultrafast synthesis of solution- dispersed graphene via a facile hydride chemistry *Small* , (2009)

30 Mohanty, N. & Berry, V. Graphene-based single-bacterium resolution biodevice and dna transistor: interfacing graphene derivatives with nanoscale and microscale biocomponents *Nano Lett.* **8**, 4469-4476 (2008)

31 Cai, W.W., Zhu, Y.W., Li, X.S., Piner, R.D. & Ruoff, R.S. Large area few-layer graphene/graphite films as transparent thin conducting electrodes *App. Phys. Lett.* **95**, (2009)

32 Krasheninnikov, A.V., Lehtinen, P.O., Foster, A.S., Pyykko, P. & Nieminen, R.M. Embedding transition-metal atoms in graphene: structure, bonding, and magnetism *Phys. Rev. Lett.* **102**, (2009)

33 Plomp, A.J., Schubert, T., Storr, U., de Jong, K.P. & Bitter, J. Reducibility of platinum supported on nanostructured carbons *Topics in Catalysis* **52**, 424-430 (2009)

34 Blake, P., Hill, E.W., Neto, A.H.C., Novoselov, K.S., Jiang, D., Yang, R., Booth, T.J. & Geim, A.K. Making graphene visible *App. Phys. Lett.* **91**, (2007)

35 Allen, M.J., Tung, V.C. & Kaner, R.B. Honeycomb carbon: a review of graphene *Chem. Rev.* **110**, 132-145 (2010)

36 Park, S. & Ruoff, R.S. Chemical methods for the production of graphenes *Nat. Nanotechnol.* **4**, 217-224 (2009)

37 Hummers, W.S. & Offeman, R.E. Preparation of graphitic oxide *J. Am. Chem. Soc.* **80**, 1339-1339 (1958)

38 Dreyer, D.R., Park, S., Bielawski, C.W. & Ruoff, R.S. The chemistry of graphene oxide *Chem. Soc. Rev.* **39**, 228-240 (2010)

39 Tung, V.C., Allen, M.J., Yang, Y. & Kaner, R.B. High-throughput solution processing of large-scale graphene *Nat. Nanotechnol.* **4**, 25-29 (2009)

40 Si, Y. & Samulski, E.T. Synthesis of water soluble graphene *Nano Lett.* **8**, 1679-1682 (2008)

41 Stankovich, S., Dikin, D.A., Piner, R.D., Kohlhaas, K.A., Kleinhammes, A., Jia, Y., Wu, Y., Nguyen, S.T. & Ruoff, R.S. Synthesis of graphene-based nanosheets via chemical reduction of exfoliated graphite oxide *Carbon* **45**, 1558-1565 (2007)

42 Wang, G.X., Yang, J., Park, J., Gou, X.L., Wang, B., Liu, H. & Yao, J. Facile synthesis and characterization of graphene nanosheets *J. Phys. Chem. C* **112**, 8192-8195 (2008)

43 Shin, H.J., Kim, K.K., Benayad, A., Yoon, S.M., Park, H.K., Jung, I.S., Jin, M.H., Jeong, H.K., Kim, J.M., Choi, J.Y. et al. Efficient reduction of graphite oxide by sodium borohydrilde and its effect on electrical conductance *Adv. Funct. Mater.* **19**, 1987-1992 (2009)

44 Zhang, J.L., Yang, H.J., Shen, G.X., Cheng, P., Zhang, J.Y. & Guo, S.W. Reduction of graphene oxide via l-ascorbic acid *Chem. Comm.* **46**, 1112-1114 (2010)

45 McAllister, M.J., Li, J.L., Adamson, D.H., Schniepp, H.C., Abdala, A.A., Liu, J., Herrera-Alonso, M., Milius, D.L., Car, R., Prud'homme, R.K. et al. Single sheet functionalized graphene by oxidation and thermal expansion of graphite *Chem. Mater.* **19**, 4396-4404 (2007)

46 Schniepp, H.C., Li, J.L., McAllister, M.J., Sai, H., Herrera-Alonso, M., Adamson, D.H., Prud'homme, R.K., Car, R., Saville, D.A. & Aksay, I.A. Functionalized single graphene sheets derived from splitting graphite oxide *J. Phys. Chem. B* **110**, 8535-8539 (2006)

47 Zhu, Y.W., Murali, S., Cai, W.W., Li, X.S., Suk, J.W., Potts, J.R. & Ruoff, R.S. Graphene and graphene oxide: synthesis, properties, and applications (vol 22, pg 3906, 2010) *Adv. Mater.* **22**, 5226-5226 (2010)

48 Sundaram, R.S., Gomez-Navarro, C., Balasubramanian, K., Burghard, M. & Kern, K. Electrochemical modification of graphene *Adv. Mater.* **20**, 3050-3053 (2008)

49 Cote, L.J., Cruz-Silva, R. & Huang, J.X. Flash reduction and patterning of graphite oxide and its polymer composite *J. Am. Chem. Soc.* **131**, 11027-11032 (2009)

50 Salas, E.C., Sun, Z.Z., Luttge, A. & Tour, J.M. Reduction of graphene oxide via bacterial respiration *ACS Nano* **4**, 4852-4856 (2010)

51 Schwamb, T., Burg, B.R., Schirmer, N.C. & Poulikakos, D. An electrical method for the measurement of the thermal and electrical conductivity of reduced graphene oxide nanostructures *Nanotechnology* **20**, (2009)

52 Gao, W., Alemany, L.B., Ci, L.J. & Ajayan, P.M. New insights into the structure and reduction of graphite oxide *Nat. Chem.* **1**, 403-408 (2009)

53 Stankovich, S., Piner, R.D., Chen, X.Q., Wu, N.Q., Nguyen, S.T. & Ruoff, R.S. Stable aqueous dispersions of graphitic nanoplatelets via the reduction of exfoliated graphite oxide in the presence of poly(sodium 4-styrenesulfonate) *J. Mater. Chem.* **16**, 155-158 (2006)

54 Gomez-Navarro, C., Weitz, R.T., Bittner, A.M., Scolari, M., Mews, A., Burghard, M. & Kern, K. Electronic transport properties of individual chemically reduced graphene oxide sheets *Nano Lett.* **7**, 3499-3503 (2007)

55 Hernandez, Y., Nicolosi, V., Lotya, M., Blighe, F.M., Sun, Z.Y., De, S., McGovern, I.T., Holland, B., Byrne, M., Gun'ko, Y.K. et al. High-yield production of graphene by liquid-phase exfoliation of graphite *Nat. Nanotechnol.* **3**, 563-568 (2008)

56 Valles, C., Drummond, C., Saadaoui, H., Furtado, C.A., He, M., Roubeau, O., Ortolani, L., Monthioux, M. & Penicaud, A. Solutions of negatively charged graphene sheets and ribbons *J. Am. Chem. Soc.* **130**, 15802-+ (2008)

57 Hao, R., Qian, W., Zhang, L.H. & Hou, Y.L. Aqueous dispersions of tcnq-anion-stabilized graphene sheets *Chem. Comm.* , 6576-6578 (2008)

58 Liu, N., Luo, F., Wu, H.X., Liu, Y.H., Zhang, C. & Chen, J. One-step ionic-liquid-assisted electrochemical synthesis of ionic-liquid-functionalized graphene sheets directly from graphite *Adv. Funct. Mater.* **18**, 1518-1525 (2008)

59 Li, X.L., Wang, X.R., Zhang, L., Lee, S.W. & Dai, H.J. Chemically derived, ultrasmooth graphene nanoribbon semiconductors *Science* **319**, 1229-1232 (2008)

60 Behabtu et al Spontaneous high-concentration dispersions and liquid crystals of graphene *Nature Nanotechnol.* **ASAP**, (2010)

61 Sumanasekera, G.U., Allen, J.L., Fang, S.L., Loper, A.L., Rao, A.M. & Eklund, P.C. Electrochemical oxidation of single wall carbon nanotube bundles in sulfuric acid *J. Phys. Chem. B* **103**, 4292-4297 (1999)

62 Reina, A., Son, H.B., Jiao, L.Y., Fan, B., Dresselhaus, M.S., Liu, Z.F. & Kong, J. Transferring and identification of single- and few-layer graphene on arbitrary substrates *J. Phys. Chem. C* **112**, 17741-17744 (2008)

63 Reina, A., Jia, X.T., Ho, J., Nezich, D., Son, H.B., Bulovic, V., Dresselhaus, M.S. & Kong, J. Layer area, few-layer graphene films on arbitrary substrates by chemical vapor deposition *Nano Lett.* **9**, 3087-3087 (2009)

64 Sutter, P., Hybertsen, M.S., Sadowski, J.T. & Sutter, E. Electronic structure of few-layer epitaxial graphene on ru(0001) *Nano Lett.* **9**, 2654-2660 (2009)

65 Kim, K.S., Zhao, Y., Jang, H., Lee, S.Y., Kim, J.M., Kim, K.S., Ahn, J.H., Kim, P., Choi, J.Y. & Hong, B.H. Large-scale pattern growth of graphene films for stretchable transparent electrodes *Nature* **457**, 706-710 (2009)

66 Li, X.S., Cai, W.W., An, J.H., Kim, S., Nah, J., Yang, D.X., Piner, R., Velamakanni, A., Jung, I., Tutuc, E. et al. Large-area synthesis of high-quality and uniform graphene films on copper foils *Science* **324**, 1312-1314 (2009)

67 Bae, S., Kim, H., Lee, Y., Xu, X.F., Park, J.S., Zheng, Y., Balakrishnan, J., Lei, T., Kim, H.R., Song, Y.I. et al. Roll-to-roll production of 30-inch graphene films for transparent electrodes *Nat. Nanotechnol.* **5**, 574-578 (2010)

68 Hass, J., Millan-Otoya, J.E., First, P.N. & Conrad, E.H. Interface structure of epitaxial graphene grown on 4h-sic(0001) *Phys. Rev. B* **78**, (2008)

69 de Heer, W.A., Berger, C., Wu, X.S., First, P.N., Conrad, E.H., Li, X.B., Li, T.B., Sprinkle, M., Hass, J., Sadowski, M.L. et al. Epitaxial graphene *Solid State Comm.* **143**, 92-100 (2007)

70 Berger, C., Song, Z.M., Li, X.B., Wu, X.S., Brown, N., Naud, C., Mayou, D., Li, T.B., Hass, J., Marchenkov, A.N. et al. Electronic confinement and coherence in patterned epitaxial graphene *Science* **312**, 1191-1196 (2006)

71 Sprinkle, M., Soukiassian, P., de Heer, W.A., Berger, C. & Conrad, E.H. Epitaxial graphene: the material for graphene electronics *Physica Status Solidi-Rapid Research Lett.* **3**, A91-A94 (2009)

72 Kedzierski, J., Hsu, P.L., Healey, P., Wyatt, P.W., Keast, C.L., Sprinkle, M., Berger, C. & de Heer, W.A. Epitaxial graphene transistors on sic substrates *IEEE Transactions on Eectron Devices* **55**, 2078-2085 (2008)

73 Schedin, F., Geim, A.K., Morozov, S.V., Hill, E.W., Blake, P., Katsnelson, M.I. & Novoselov, K.S. Detection of individual gas molecules adsorbed on graphene *Nat. Mater.* **6**, 652-655 (2007)

74 Shao, Y.Y., Wang, J., Wu, H., Liu, J., Aksay, I.A. & Lin, Y.H. Graphene based electrochemical sensors and biosensors: a review *Electroanalysis* **22**, 1027-1036 (2010)

75 Pumera, M., Ambrosi, A., Bonanni, A., Chng, E.L.K. & Poh, H.L. Graphene for electrochemical sensing and biosensing *Trac-Tends in Analytical Chem.* **29**, 954-965 (2010)

76 Wallace, P.R. The band theory of graphite *Phys. Rev.* **71**, 622-634 (1947)

77 Handbook of semiconductor manufacturing technology, second edition , (2007)

78 Novoselov, K.S., Jiang, Z., Zhang, Y., Morozov, S.V., Stormer, H.L., Zeitler, U., Maan, J.C., Boebinger, G.S., Kim, P. & Geim, A.K. Room-temperature quantum hall effect in graphene *Science* **315**, 1379-1379 (2007)

79 Novoselov, K.S., McCann, E., Morozov, S.V., Fal'ko, V.I., Katsnelson, M.I., Zeitler, U., Jiang, D., Schedin, F. & Geim, A.K. Unconventional quantum hall effect and berry's phase of 2 pi in bilayer graphene *Nat. Phys.* **2**, 177-180 (2006)

80 Zhang, Y.B., Tang, T.T., Girit, C., Hao, Z., Martin, M.C., Zettl, A., Crommie, M.F., Shen, Y.R. & Wang, F. Direct observation of a widely tunable bandgap in bilayer graphene *Nature* **459**, 820-823 (2009)

81 Giesbers, A.J.M., Ponomarenko, L.A., Novoselov, K.S., Geim, A.K., Katsnelson, M.I., Maan, J.C. & Zeitler, U. Gap opening in the zeroth landau level of graphene *Phys. Rev. B* **80**, (2009)

82 Castro, E.V., Novoselov, K.S., Morozov, S.V., Peres, N.M.R., Dos Santos, J.M.B.L., Nilsson, J., Guinea, F., Geim, A.K. & Neto, A.H.C. Biased bilayer graphene: semiconductor with a gap tunable by the electric field effect *Phys. Rev. Lett.* **99**, (2007)

83 Gao, L.B., Ren, W.C., Liu, B.L., Wu, Z.S., Jiang, C.B. & Cheng, H.M. Crystallographic tailoring of graphene by nonmetal siox nanoparticles *J. Am. Chem. Soc.* **131**, 13934-+ (2009)

84 Rosales, L., Pacheco, M., Barticevic, Z. & Orellana, P. Conductance of armchair gnrs with side-attached organic molecules *Microelectronics J.* **39**, 1233-1235 (2008)

85 Yoon, Y. & Guo, J. Effect of edge roughness in graphene nanoribbon transistors *App. Phys. Lett.* **91**, (2007)

86 Yan, Q.M., Huang, B., Yu, J., Zheng, F.W., Zang, J., Wu, J., Gu, B.L., Liu, F. & Duan, W.H. Intrinsic current-voltage characteristics of graphene nanoribbon transistors and effect of edge doping *Nano Lett.* **7**, 1469-1473 (2007)

87 Sols, F., Guinea, F. & Neto, A.H.C. Coulomb blockade in graphene nanoribbons *Phys. Rev. Lett.* **99**, (2007)

88 Shemella, P., Zhang, Y., Mailman, M., Ajayan, P.M. & Nayak, S.K. Energy gaps in zero-dimensional graphene nanoribbons *App. Phys. Lett.* **91**, (2007)

89 Hod, O., Peralta, J.E. & Scuseria, G.E. Edge effects in finite elongated graphene nanoribbons *Phys. Rev. B* **76**, (2007)

90 Han, M.Y., Ozyilmaz, B., Zhang, Y.B. & Kim, P. Energy band-gap engineering of graphene nanoribbons *Phys. Rev. Lett.* **98**, (2007)

91 Avouris, P., Chen, Z.H. & Perebeinos, V. Carbon-based electronics *Nat. Nanotechnol.* **2**, 605-615 (2007)

92 Son, Y.W., Cohen, M.L. & Louie, S.G. Energy gaps in graphene nanoribbons *Phys. Rev. Lett.* **97**, (2006)

93 Jiao, L.Y., Zhang, L., Wang, X.R., Diankov, G. & Dai, H.J. Narrow graphene nanoribbons from carbon nanotubes *Nature* **458**, 877-880 (2009)

94 Kosynkin, D.V., Higginbotham, A.L., Sinitskii, A., Lomeda, J.R., Dimiev, A., Price, B.K. & Tour, J.M. Longitudinal unzipping of carbon nanotubes to form graphene nanoribbons *Nature* **458**, 872-U5 (2009)

95

http://www.itrs.net/Links/2009ITRS/2009Chapters_2009Tables/2009_ExecSum.pdf

96 Wang, X.R., Ouyang, Y.J., Li, X.L., Wang, H.L., Guo, J. & Dai, H.J. Room-temperature all-semiconducting sub-10-nm graphene nanoribbon field-effect transistors *Phys. Rev. Lett.* **100**, (2008)

97 Bai, J.W., Duan, X.F. & Huang, Y. Rational fabrication of graphene nanoribbons using a nanowire etch mask *Nano Lett.* **9**, 2083-2087 (2009)

98 Jia, X.T., Hofmann, M., Meunier, V., Sumpter, B.G., Campos-Delgado, J., Romo-Herrera, J.M., Son, H.B., Hsieh, Y.P., Reina, A., Kong, J. et al. Controlled formation of sharp zigzag and armchair edges in graphitic nanoribbons *Science* **323**, 1701-1705 (2009)

99 Campos-Delgado, J., Romo-Herrera, J.M., Jia, X.T., Cullen, D.A., Muramatsu, H., Kim, Y.A., Hayashi, T., Ren, Z.F., Smith, D.J., Okuno, Y. et al. Bulk production of a new form of sp(2) carbon: crystalline graphene nanoribbons *Nano Lett.* **8**, 2773-2778 (2008)

100 Wang, X.R. & Dai, H.J. Etching and narrowing of graphene from the edges *Nat. Chem.* **2**, 661-665 (2010)

101 Jiao, L., Wang, X., Diankov, G., Wang, H. & Dai, H. Facile synthesis of high-quality graphene nanoribbons *Nat. Nano.* , (2010)

102 Cai, J.M., Ruffieux, P., Jaafar, R., Bieri, M., Braun, T., Blankenburg, S., Muoth, M., Seitsonen, A.P., Saleh, M., Feng, X.L. et al. Atomically precise bottom-up fabrication of graphene nanoribbons *Nature* **466**, 470-473 (2010)

103 Sprinkle, M., Ruan, M., Hu, Y., Hankinson, J., Rubio-Roy, M., Zhang, B., Wu, X., Berger, C. & de Heer, W.A. Scalable templated growth of graphene nanoribbons on sic *Nat. Nanotechnol.* **5**, 727-731 (2010)

104 Bera, S., Arnold, A., Evers, F., Narayanan, R. & Wolfle, P. Elastic properties of graphene flakes: boundary effects and lattice vibrations *Phys. Rev. B* **82**, (2010)

105 Wei, X.D., Fragneaud, B., Marianetti, C.A. & Kysar, J.W. Nonlinear elastic behavior of graphene: ab initio calculations to continuum description *Phys. Rev. B* **80**, (2009)

106 Zhao, H., Min, K. & Aluru, N.R. Size and chirality dependent elastic properties of graphene nanoribbons under uniaxial tension *Nano Lett.* **9**, 3012-3015 (2009)

107 Michel, K.H. & Verberck, B. Theory of the evolution of phonon spectra and elastic constants from graphene to graphite *Phys. Rev. B* **78**, (2008)

108 Peres, N.M.R. The transport properties of graphene *J. Physics-Condensed Matter* **21**, (2009)

109 Peres, N.M.R., Neto, A.H.C. & Guinea, F. Dirac fermion confinement in graphene *Phys. Rev. B* **73**, (2006)

110 Gusynin, V.P. & Sharapov, S.G. Transport of dirac quasiparticles in graphene: hall and optical conductivities *Phys. Rev. B* **73**, (2006)

111 Zhu, Y., Lu, W., Sun, Z.Z., Kosynkin, D.V., Yao, J. & Tour, J.M. High throughput preparation of large area transparent electrodes using non-functionalized graphene nanoribbons *Chem. Mater.* **23**, 935-939 (2011)

112 Yin, Z.Y., Sun, S.Y., Salim, T., Wu, S.X., Huang, X.A., He, Q.Y., Lam, Y.M. & Zhang, H. Organic photovoltaic devices using highly flexible reduced graphene oxide films as transparent electrodes *ACS Nano* **4**, 5263-5268 (2010)

113 Wu, J.B., Becerril, H.A., Bao, Z.N., Liu, Z.F., Chen, Y.S. & Peumans, P. Organic solar cells with solution-processed graphene transparent electrodes *App. Phys. Lett.* **92**, (2008)

114 Park, J.S., Cho, S.M., Kim, W.J., Park, J. & Yoo, P.J. Fabrication of graphene thin films based on layer-by-layer self-assembly of functionalized graphene nanosheets *ACS Applied Mater. & Interfaces* **3**, 360-368 (2011)

115 Park, H., Rowehl, J.A., Kim, K.K., Bulovic, V. & Kong, J. Doped graphene electrodes for organic solar cells *Nanotechnology* **21**, (2010)

116 Miyasaka, Y., Nakamura, A. & Temmyo, J. Graphite thin films consisting of nanograins of multilayer graphene on sapphire substrates directly grown by alcohol chemical vapor deposition *Japanese J. Applied Pysics* **50**, (2011)

117 Matyba, P., Yamaguchi, H., Chhowalla, M., Robinson, N.D. & Edman, L. Flexible and metal-free light-emitting electrochemical cells based on graphene and pedot-pss as the electrode materials *ACS Nano* **5**, 574-580 (2011)

118 Kim, Y.K. & Min, D.H. Durable large-area thin films of graphene/carbon nanotube double layers as a transparent electrode *Langmuir* **25**, 11302-11306 (2009)

119 Kim, K.E.U.N.S.O.O., Zhao, Y.U.E., Jang, H.O.U.K., Lee, S.A.N.G.Y.O.O.N., Kim, J.O.N.G.M.I.N., Kim, K.W.A.N.G.S., Ahn, J.O.N.G.-.H.Y.U.N., Kim, P.H.I.L.I.P., Choi, J.A.E.-.Y.O.U.N.G. & Hong, B.Y.U.N.G.H.E.E. Large-scale pattern growth of graphene films for stretchable transparent electrodes *Nature (London)* **457**, 706-710 (2009)

120 Kalita, G., Masahiro, M., Uchida, H., Wakita, K. & Umeno, M. Few layers of graphene as transparent electrode from botanical derivative camphor *Mater. Lett.* **64**, 2180-2183 (2010)

121 Huang, Y.Y. & Terentjev, E.M. Transparent electrode with a nanostructured coating *ACS Nano* **5**, 2082-2089 (2011)

122 Hong, T.K., Lee, D.W., Choi, H.J., Shin, H.S. & Kim, B.S. Transparent, flexible conducting hybrid multi layer thin films of multiwalled carbon nanotubes with graphene nanosheets *ACS Nano* **4**, 3861-3868 (2010)

123 Hecht, D.S., Hu, L.B. & Irvin, G. Emerging transparent electrodes based on thin films of carbon nanotubes, graphene, and metallic nanostructures *Adv. Mater.* **23**, 1482-1513 (2011)

124 Xia, F.N., Mueller, T., Lin, Y.M., Valdes-Garcia, A. & Avouris, P. Ultrafast graphene photodetector *Nat. Nanotechnol.* **4**, 839-843 (2009)

125 Xia, F.N., Mueller, T., Golizadeh-Mojarad, R., Freitag, M., Lin, Y.M., Tsang, J., Perebeinos, V. & Avouris, P. Photocurrent imaging and efficient photon detection in a graphene transistor *Nano Lett.* **9**, 1039-1044 (2009)

126 Yan, X., Cui, X., Li, L. Synthesis of large, stable colloidal graphene quantum dots with tunable size *J. Am. Chem. Soc.* **132**, 5944-5945 (2010)

127 Yan, X., Cui, X., Li, B., Li, L. Large, solution-processable graphene quantum dots as light absorbers for photovoltaics *Nano Lett.* **10**, 1869-1873 (2010)

128 Silvestrov, P.G. & Efetov, K.B. Quantum dots in graphene *Phys. Rev. Lett.* **98**, (2007)

129 Shen, J.H., Zhu, Y.H., Chen, C., Yang, X.L. & Li, C.Z. Facile preparation and upconversion luminescence of graphene quantum dots *Chem. Comm.* **47**, 2580-2582 (2011)

130 Schumacher, S. Photophysics of graphene quantum dots: insights from electronic structure calculations *Phys. Rev. B* **83**, (2011)

131 Schnez, S., Molitor, F., Stampfer, C., Guttinger, J., Shorubalko, I., Ihn, T. & Ensslin, K. Observation of excited states in a graphene quantum dot *App. Phys. Lett.* **94**, (2009)

132 Ponomarenko, L.A., Schedin, F., Katsnelson, M.I., Yang, R., Hill, E.W., Novoselov, K.S. & Geim, A.K. Chaotic dirac billiard in graphene quantum dots *Science* **320**, 356-358 (2008)

133 Pan, D.Y., Zhang, J.C., Li, Z. & Wu, M.H. Hydrothermal route for cutting graphene sheets into blue-luminescent graphene quantum dots *Adv. Mater.* **22**, 734-+ (2010)

134 Li, L.S. & Yan, X. Colloidal graphene quantum dots *J. Phys. Chem. Lett.* **1**, 2572-2576 (2010)

135 Zhao, J., Chen, G.F., Zhu, L. & Li, G.X. Graphene quantum dots-based platform for the fabrication of electrochemical biosensors *Electrochem. Comm.* **13**, 31-33 (2011)

136 Zhang, Z.Z. & Chang, K. Tuning of energy levels and optical properties of graphene quantum dots *Phys. Rev. B* **77**, (2008)

137 Romanovsky, I., Yannouleas, C. & Landman, U. Edge states in graphene quantum dots: fractional quantum hall effect analogies and differences at zero magnetic field *Phys. Rev. B* **79**, (2009)

138 Lu, J., Yeo, P.S.E., Gan, C.K., Wu, P. & Loh, K.P. Transforming c-60 molecules into graphene quantum dots *Nat. Nanotechnol.* **6**, 247-252 (2011)

139 Libisch, F., Stampfer, C. & Burgdorfer, J. Graphene quantum dots: beyond a dirac billiard *Phys. Rev. B* **79**, (2009)

140 Katsnelson, M.I. & Guinea, F. Transport through evanescent waves in ballistic graphene quantum dots *Phys. Rev. B* **78**, (2008)

141 Joung, D., Zhai, L. & Khondaker, S.I. Coulomb blockade and hopping conduction in graphene quantum dots array *Phys. Rev. B* **83**, (2011)

142 Huang, L., Lai, Y.C., Ferry, D.K., Akis, R. & Goodnick, S.M. Transmission and scarring in graphene quantum dots *J. Physics-Cndensed Matter* **21**, (2009)

143 Li, Y., Hu, Y., Zhao, Y., Shi, G.Q., Deng, L.E., Hou, Y.B. & Qu, L.T. An electrochemical avenue to green-luminescent graphene quantum dots as potential electron-acceptors for photovoltaics *Adv. Mater.* **23**, 776-+ (2011)

Appendix A - Supporting information: Chemically modified graphene for bio/chemo-interfacing in bio-devices and DNA-sensors

Attaching DNA on graphene

The previously prepared GO-coated silica substrate was dipped in a mixture containing 5 ml of 2.5 μg/μl solution of single stranded 5' aminated DNA (20 bases, purchased from Invitrogen Inc.), having a sequence

Amine-AAC TGC CAG CCT AAG TCC AA,

mixed with 5 mg of HATU and incubated at room temperature in an incubator-shaker for 8 hours. The non-covalently bonded DNA was removed by washing with 1% SDS (1mg/ml) for 30 minutes in a shaker. This produced DNA tethered covalently on graphene.

Hybridization experiments

To hybridize this DNA tethered graphene substrate with a complementary DNA attached to a fluorescent marker, a 50 μl drop of 0.175 μg /μl probe DNA containing the 3' Rhodamine green linked dye (purchased from Invitrogen Inc.) with a complementary sequence:

Rhodamine Green – TTG GAC TTA GGC TGG CAG TT,

was put on the chip and incubated at room temperature for 4 hours after which the non-specific attachment of the probe was removed by repeated washing (2 times) with 1 % SDS for 30 minutes each. (Figure A.1)

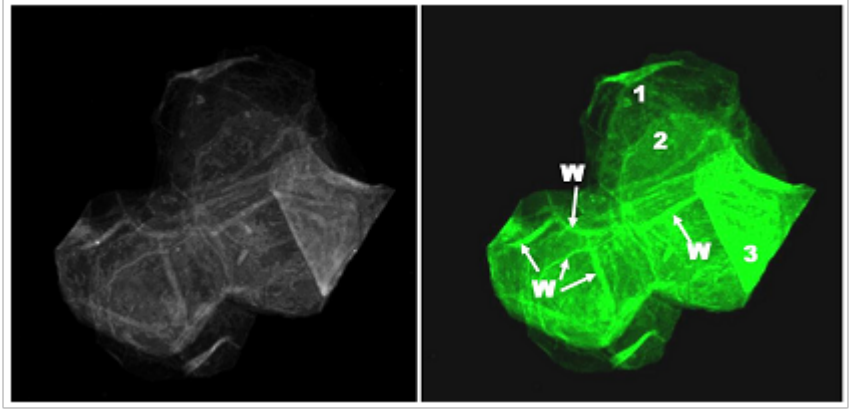

Figure A-1 Confocal image of the complementary probe DNA bound to the G-DNA showing the wrinkles (w), folds and multilayers (1, 2, 3).

De-hybridization experiments

The sample was incubated with 10 M urea at 40 ^{0}C in an incubator shaker for 3 hours followed by washing with DI water. Then the sample was dialyzed (MWCO - 2000 Daltons) for the next 24 hours to get rid of all the urea adsorbed on G-DNA.

Control experiments

For the negative control, all of the steps of the DNA attachment procedure were repeated except the probe (3' Rhodamine green dye linked DNA) hybridization step. And for the positive control, all the steps enumerated in the DNA attachment procedure were repeated except the 5' aminated DNA attachment step. (Figure A.2 – b, c)

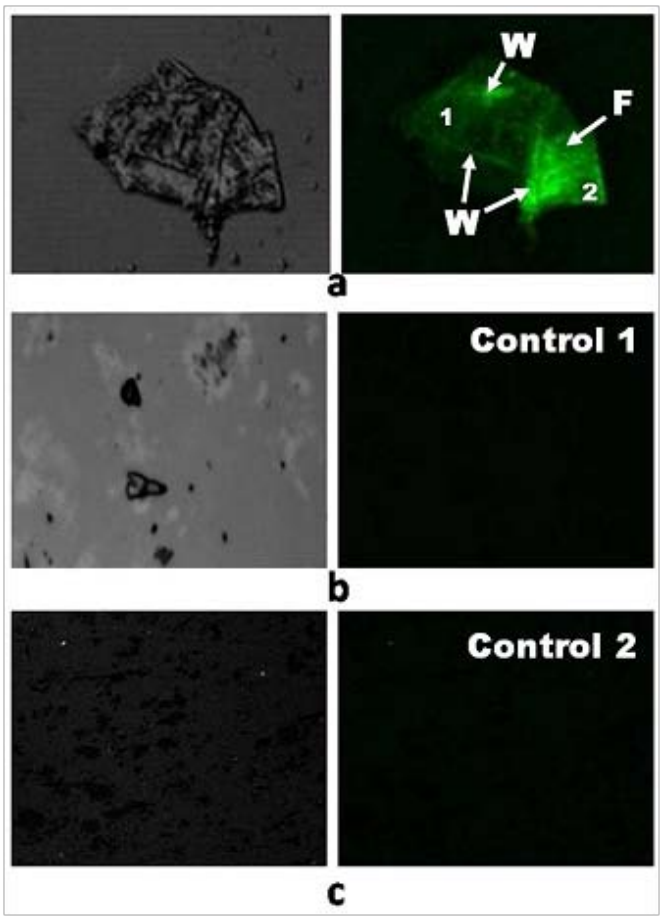

Figure A-2 a.Complementary DNA (with rhodamine green) is hybridized on graphene-DNA (G-DNA) deposited on 300 nm thick Silica substrate. Confocal microscopy image clearly shows the presence of complementary DNA hybridized. Further the folds of G-DNA can be clearly seen. The white arrows show the folds and the orange arrows show the wrinkles. b. Negative control (no probe) c. Positive control (no aminated DNA). Here 1, 2 and 3 represent the relative thickness of G-DNA sheets, F represents the folds and W represents the wrinkles.

Electrical measurements

All electrical measurements were taken at room temperature, under a steady nitrogen environment, using a *Keithley* 2612 Dual-Channel System Source Meter connected to a computer via a GPIB/IEEE-488 interface card. All observations were found to be consistent and robust over a period of multiple weeks.

Gating data for GO, PGA and GA

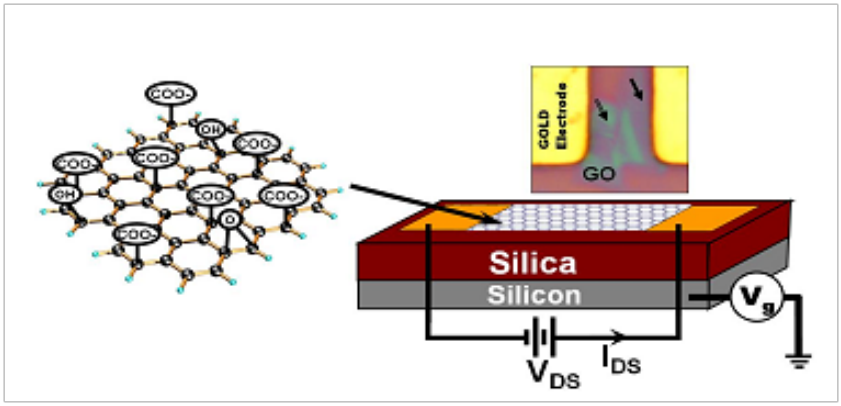

Figure A-3 Gating setup for GO, GA and PGA

Gating was performed by keeping the source-drain voltage (gold electrodes), V_{DS} = 8 V and measuring the change in conductivity with the gate voltage, which was applied to the heavy-doped silicon backgate (Figure A.3). From these measurements, the electron and hole mobilities of GA and GO were estimated as explained in the main text (FigureA.4).

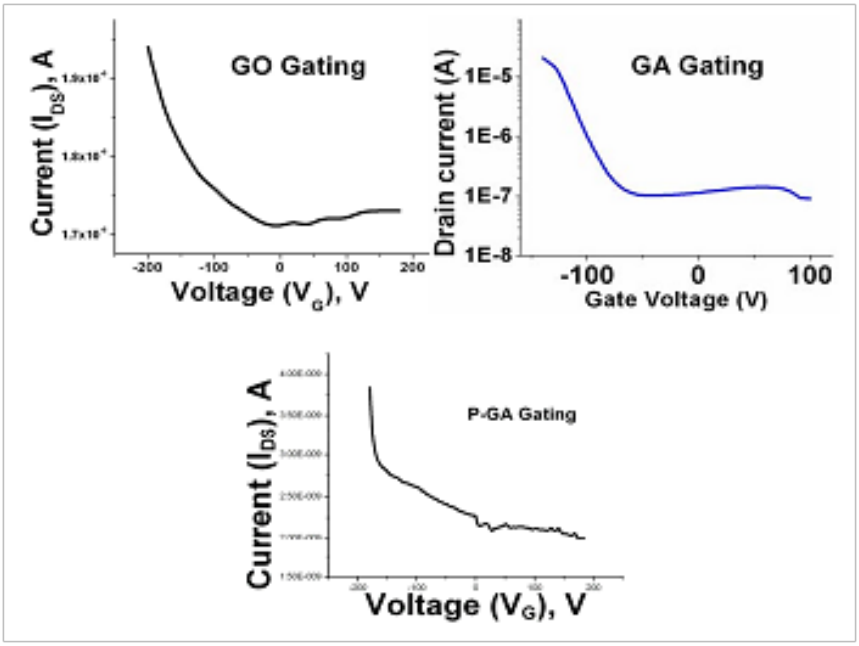

Figure A-4 Graphene-oxide, Graphene-amine and Plasma-Graphene amine gate characteristics showing the change in source-drain current versus gate potential at 8V source-drain bias.

Calculations for DNA attachments

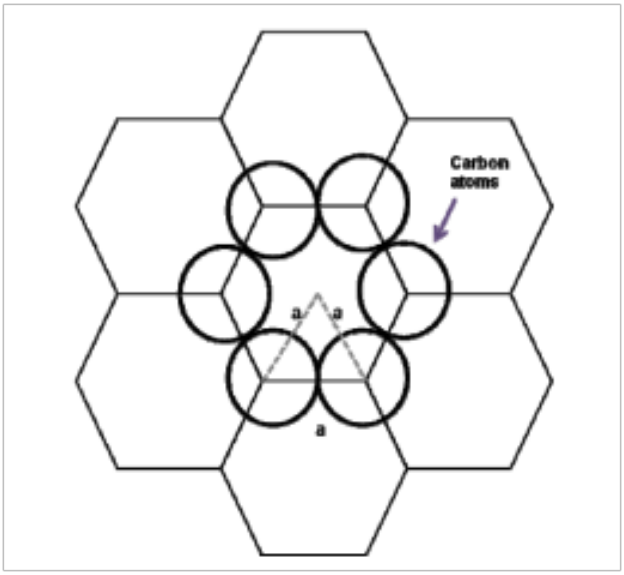

Figure A-5 A schematic of graphene's benzene ring like arrangement of carbon atoms. This schematic was used to estimate the density of DNA attached on GO.

Area of the a unit honeycomb structure ~ $\frac{1}{2} \times 3\sqrt{3}(a^2)$ where a is the bond length

For a = 0.142 nm,

Area of the unit honey comb structure = 5.239 X 10^{-16} cm^2

Number of carbon atoms per unit honey comb structure = 2,

Thus the area occupied by one carbon atom = 2.619 X 10^{-16} cm^2

Density of the [COOH] groups in graphene oxide = Number of DNA molecules attached to graphene oxide (assuming a 100 % efficiency) = 1.947 X 10^{14} cm^{-2}

Change in the number of holes for the G-DNA device = 5.61 X 10^{12} cm^{-2},

Thus the change in the number of holes per DNA = $\frac{5.61 \times 10^{12}}{1.947 \times 10^{14}} = 0.0288$

Thus, assuming a 25% efficiency, 8 DNA molecules change 1 hole.

Calculation for PAH attachment

The change in conductivity ($\frac{\Delta I}{A_{Graphene}}$) with change in charge density due to gating is given by: $\frac{\Delta I}{A_{Graphene}} = \frac{\Delta q}{V_{Graphene}} \times \mu \times \frac{V}{d}$

Where , ΔI is the change in source-drain current, Δq is the change in hole-density of graphene, μ is the hole mobility, V is the source-drain voltage, $A_{Graphene}$ is the cross-sectional area of graphene, $V_{Graphene}$ is the volume of graphene between electrodes and d is gap between the electrodes ($d = \frac{V_{Graphene}}{A_{Graphene}}$).

This further gives,:

$$\Delta I = \Delta q \times \mu \times \frac{V}{d^2}$$

The change in charge density is a result of chemical gating from attachment of the PAH molecules, which are positively charged.

Thus, $\Delta q = n \times C_{PAH} \times V_{PAH}$, where n is the number of PAH monomers, C_{PAH} is the capacitance from the positive charge on the surface of PAH monomer and V_{PAH} is the potential from the positive charge on the monomer (single charge).

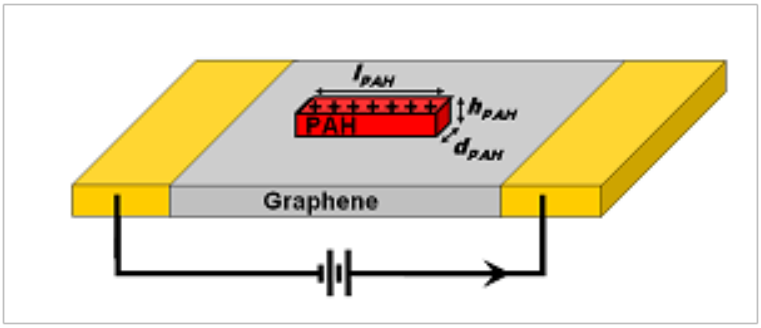

Figure A-6 A rough schematic of PAH molecule adsorbed on GO. This schematic was used to estimate the area of adsorption of a PAH monomer.

$$V_{PAH} = \frac{-e}{4\pi\kappa\varepsilon_0 h_{PAH}}$$

$$C_{PAH} = \frac{\kappa\varepsilon_0 (d_{PAH} I_{PAH})}{h_{PAH}}$$

This gives the value of charge density change to be:

$$\Delta q = n \times \frac{e(d_{PAH} I_{PAH})}{4\pi h_{PAH}^2}$$

$$\Delta I = n \times \frac{e(d_{PAH} I_{PAH})}{4\pi h_{PAH}^2} \times \mu \times \frac{V}{d^2}$$

$$n = \frac{4\pi h_{PAH}^2 d^2 \Delta I}{e(d_{PAH} I_{PAH})\mu V} = \frac{4\pi(\frac{h_{PAH}^2}{(d_{PAH} I_{PAH}})d^2 \Delta I}{e\mu V} = \frac{4\pi(\frac{h^2}{dI})_{PAH} d^2 \Delta I}{e\mu V}$$

For PAH, $(\frac{h^2}{dI})_{PAH} \sim 2$. As per our measurements, ΔI = 0.29 μA, V = 8 V, d = 5 μm, and μ is 2.269 X 10^{-6} m^2/V/s.

This gives a value of n = 1.254 X 10^7 monomers in 5 X 10^7 nm^2. This implies there is ~ 1 PAH monomer per 3 nm^2. This is not an accurate measure since it does not take into consideration the folding of PAH molecules. However it provides a lower limit to deposition and we can say that 1 monomer is attached in > 3 nm^2 area on GO.

Change in conductivity of various CMG-devices and their hybrids with polyelectrolyte attachment

Here we show the change in conductivity for the different CMGs used for building the bio-devices as well as the change in the number of holes for these devices. The conductivity change was calculated from the current-voltage curves for the CMGs and the change in the number of holes was calculated using the electrical gating data as shown above in the document.

Table A-1 The change in resistance, hole density and conductivity for different CMG-devices upon electrostatic adsorption with different polyelectrolytes

Steps	CMG	Resistance	Change in holes	Change in Conductivity
1	GO	5.88 ± 0.3 MΩ		
2	GO-PAH	7.47 ± 0.31 MΩ	-8.5×10^{12} cm^{-2}	
3	GO-PAH-PSS	4.41 ± 0.43 MΩ	$+1.42 \times 10^{13}$ cm^{-2}	
1	GO	8.11 ± 0.5 MΩ		
2	GA	20.0 ± 0.5 MΩ		-59.5%
3	GA-PSS	10.1 ± 0.6 MΩ		
4	GA-PSS-PAH	12.6 ± 0.51 MΩ		
1	GO	26.67 ± 0.9 MΩ		
2	GA	800.1 ± 2 MΩ		-96.66
3	GA-Protein	5.34 ± 0.2 MΩ	$+1.81 \times 10^{11}$ cm^{-2}	

Appendix B - Supporting information: Impermeable graphenic wrapping of bacteria

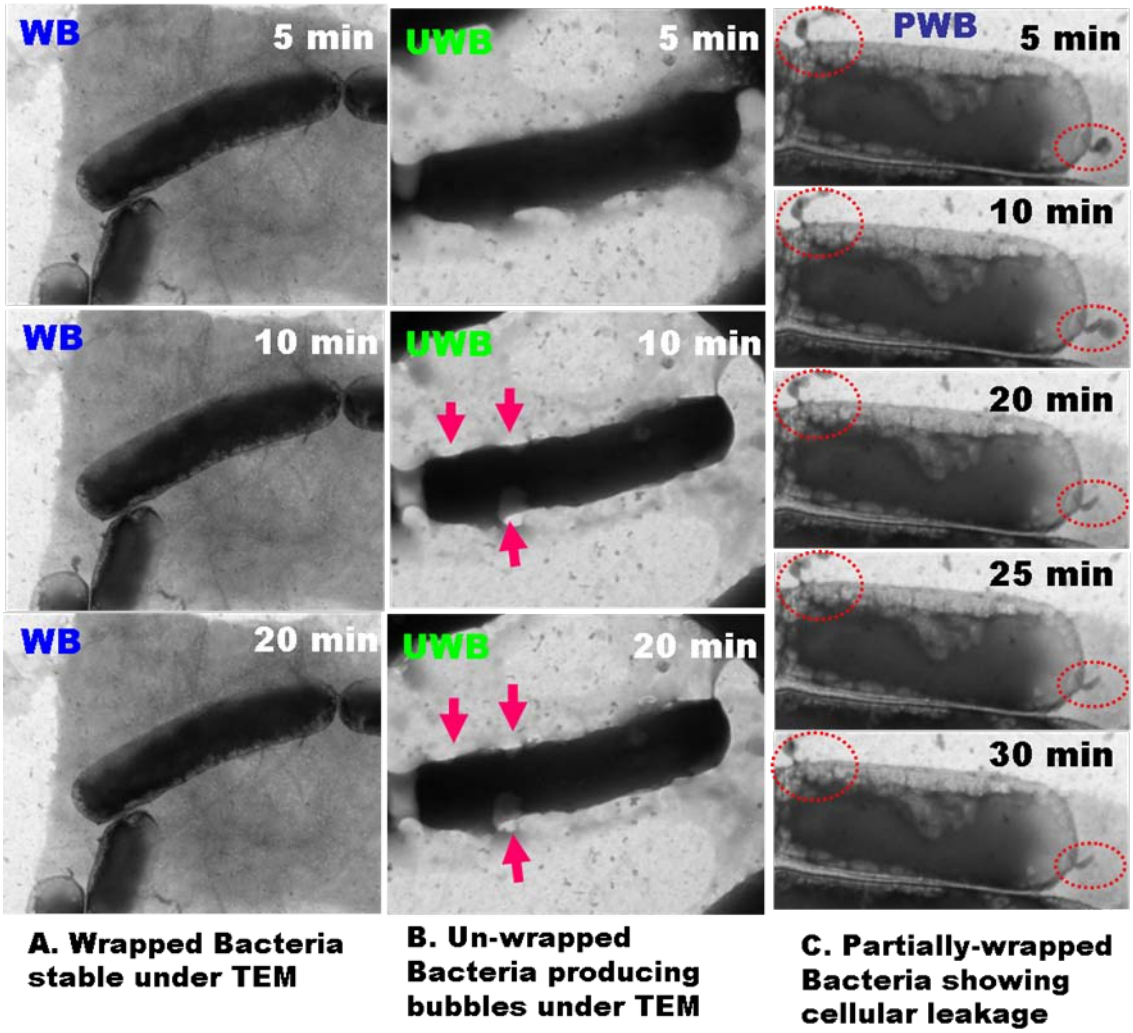

Figure B-1 The fractional shrinkage of bacteria observed as a function of time under TEM's electron beam exposure for wrapped, unwrapped bacteria and partially-wrapped immobilized on Si_3N_4 TEM-window. Clearly, the wrapped bacteria exhibit minimal shrinkage; for the unwrapped bacteria, the arrows point to the bubbles and structural defects caused due to the electron beam damage in the TEM; and for the Partially-wrapped bacteria plumes of volatile intra-cellular components escape into the TEM chamber (shown by dotted circles).

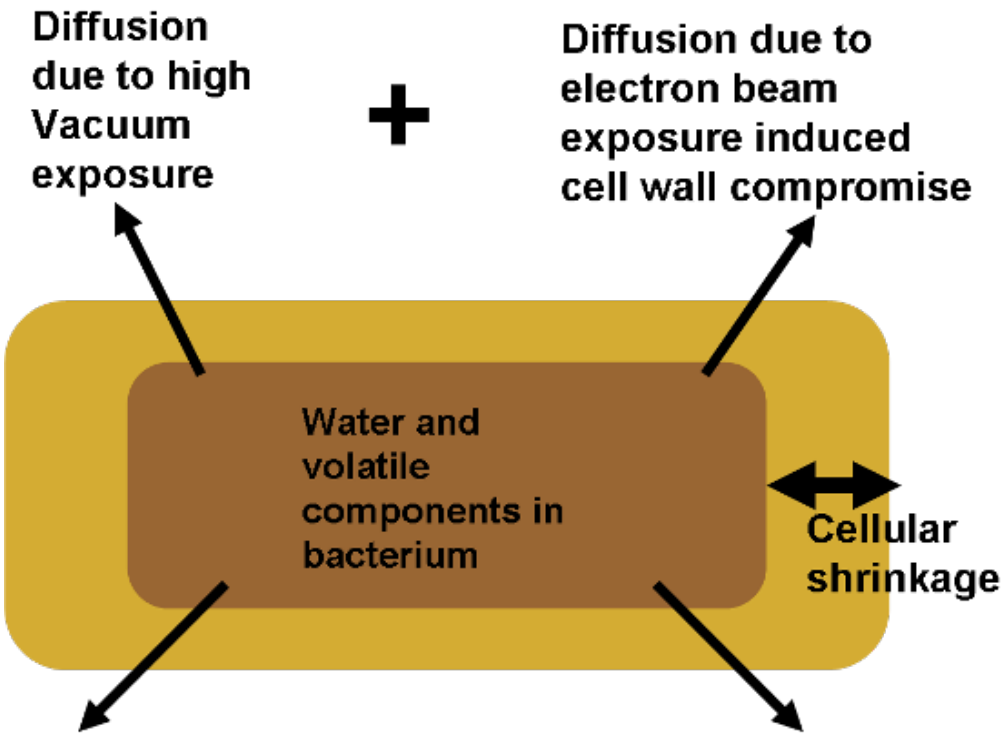

Figure B-2 Schematic diagram of the diffusion of volatile cellular components from an Si_3N_4 grid immobilized unwrapped bacterium due to exposure to the high vacuum environment of the TEM and the electron beam

Owing to exposure to the high vacuum environment of the TEM column, out-diffusion of the water and other volatile components of the un-wrapped bacterial cell were observed, leading to cellular shrinkage (Figure B.2). Further, exposure to the electron beam results in boiling off of the volatile cellular matter which in concert with vacuum mediated efflux resulting in an accelerated rate of out-diffusion. The rate of decrease of the volume fraction was found $\propto -k/R\, C_w - AI/\lambda\, C_w C_T$, where k is the permeability, A is the electron-beam boiling-factor, C_w and C_T are the water and total concentration in a bacterium, R is the radius of the bacterium, I is the electron beam current and λ is the latent heat of vaporization. Integration of this expression leads to,

$$V = \frac{V_{Bo} + \alpha_1 \exp(-\beta t)}{1 + \alpha_2 \exp(-\beta t)} \quad (1)$$

where, V_{Bo} is the volume fraction of completely dehydrated bacteria, α_1 and α_2 are arbitrarily constants proportional to the impermeability and electron beam damage resistance respectively and β is proportional to the overall volume fraction shrinkage rate.

Characterization of the exclusive effect of the high vacuum on the bacteria mandates the decoupling of the effect of the electron beam. In order to achieve this, both the unwrapped and wrapped bacteria were immobilized on 100 nm thick Si_3N_4 membrane grids, the average bacterial areal parameters determined from optical microscope images and subsequently exposed to the high vacuum of the TEM column with intermittent imaging at 5, 10 and 15 minutes (with the electron beam being kept switched off at all times other than the time required to acquire an image). Further, to reduce the effect of the electron beam, the grids were mounted on the TEM specimen holder so as to have the electron beam first hit the SiN membrane rather than the bacterial samples. Table 3.2 details the exclusive effects of the vacuum on the wrapped and the unwrapped bacterial cells. Assuming the effect of electron beam to be negligible in this setup ($\alpha_2 = 0$ in Equation 1) and fitting the curve in Origin, V_{Bo} , α_1 and β were found to be 0.286, 0.714 and 0.404 min^{-1} respectively for the unwrapped bacteria (Figure 3.7, a); in contrast insignificant change in the volume fraction of the wrapped bacteria was found signifying the high level of protection offered upon swaddling with the PFGs.

Upon studying the concerted effect of the high vacuum and the electron beam damage on the unwrapped bacteria (by keeping the electron beam switched on at all times and having the grids oriented in such a way as to have the electron beam hit the bacteria first), the V_{Bo} , α_1 , α_2 and β were found to be 0.249, 1.168, 0.416 and 0.888 min^{-1} respectively (Table 3.1, Figure 3.7, b); once again there was minuscule change in the volume fraction of the wrapped bacteria.

Permeability calculations

From equation 1, the volume fraction of an unwrapped bacterium is given by,

$$V = \frac{V_{Bo} + \alpha_1 e^{-\beta t}}{1 + \alpha_2 e^{-\beta t}} \qquad (1)$$

Upon maclaurin series expansion of the exponential terms and the denominator, followed by simplification by neglecting higher exponents for t (since we are considering initial times where the permeability is linear and the electron beam and UHV effects are additive), we obtain,

$$V = 1 + [(V_{Bo} + \alpha_1)\frac{\alpha_2 \beta}{(1+\alpha_2)^2} - \alpha_1 \beta]t \qquad (2)$$

Based on the simplistic Darcian permeability model, the darcial permeability of the bacteria is given by,

$$-P^D = (V_{Bo} + \alpha_1)\frac{\alpha_2 \beta}{(1+\alpha_2)^2} - \alpha_1 \beta \qquad (3)$$

Where, the units of P^D are in s^{-1}.

Thus, the final darcian permeability of the bacteria is given by, $\frac{P^D V_{Initial}}{S_{Initial}}$, where $V_{Initial}$ is the initial volume of the bacteria and $S_{Initial}$ is the initial surface area of the bacteria and the permeability has the final units of m/s.

For the unwrapped bacteria exposed to the exclusive effects of the UHV atmosphere, the darcian permeability was calculated to be 7.624 X 10^{-9} m/s (V_{Bo} , α_1 and β were found to be 0.286, 0.714 and 0.404 respectively, $\alpha_2 = 0$ since the effects of the electron beam are negligible, $V_{Initial} \sim$ 2.404 X 10^{-18} m^3 and $S_{Initial} \sim$ 1.516 X 10^{-12} m^2); the wrapped bacteria exhibited

negligible change in the volume. For the unwrapped bacteria exposed to the conjoined effects of the UHV and the electron beam, the darcian permeability was calculated to be 20.508 X 10^{-9} m/s (V_{Bo} , α_1 , α_2 and β were found to be 0.249, 1.168, 0.416 and 0.888 respectively, $V_{Initial} \sim 2.404 \times 10^{-18}$ m^3 and $S_{Initial} \sim 1.516 \times 10^{-12}$ m^2); wrapped bacteria again showed negligible change.

Therefore, the darcian permeability of the bacteria decreased from 7-20 nm/s to ~ 0 upon wrapping.

Empirical modeling of TEM beam damage and discussion

In order to **empirically** study the beam damage process on our PFG-wrapped samples, we considered four major pathways for the occurrence of TEM beam damage based on prior theoretical studies,: (D1) An-isotropic ballistic ejection (or sputtering) of the primary knock-on atom (PKA) facilitated by direct knock-on electron-nuclei collisions, (D2) Shear damage brought forth by the electrostatic charging induced ion migration and the ensuing repulsion, (D3) Isotropic, steady state ejection of the nuclei owing to electron-beam induced localized heating coupled with high vacuum environment inside the TEM column, and (D4) Re-configuration of the electronic and chemical structure of the organic sample via electron beam-induced excitations known as radiolysis [1-3].

D1:

Carbon, which in its crystalline form is the sole constituent of graphene and amorphous form in which it constitutes ~ 26 % of the total mass of the bacterial cells, is highly susceptible to sputtering even at 100 keV electron energies owing to its low molecular weight. The knock-on energy threshold for sputtering an in-lattice PKA carbon atom with three sp^2 bonds is 17 eV and 5-15 eV for the amorphous sp^3 bonded C-atoms or lattice-edge atoms with vacant nearest-neighbor sites). Thus, for all elastic collisions involving an energy transfer above the sputtering threshold, a carbon atom is ejected into the TEM column with the residual kinetic energy.

The maximum energy (E_{max}) that can be transferred from a 100 kV incident electron in such a collision is given by

$$E_{\max} = \frac{2E_0(E_0 + 2m_0c^2)}{Mc^2} \qquad (4)$$

where, E_0 is the kinetic energy of the incident electron, m_0 is the rest mass of en electron, c is the velocity of light in vacuum and M is the mass of the scattering atom.

In the CM100 TEM, at 100 kV electron beam irradiating the carbonaceous sample (be it crystalline or amorphous), the maximum transferable energy (E_{max}) is ~ 20 eV.

During an elastic 2-body collision between the electron and the atom, if the electron deflects by an angle θ, the energy transferred to the atom is given by,

$$E = E_{\max} \sin^2(\frac{\theta}{2}) \qquad (5)$$

Further, the differential cross section for Rutherford-type large azimuth-scattering with negligible nuclear field screening is given by,

$$\frac{d\sigma}{d\theta} = [\frac{e^2 Z}{8\pi\varepsilon_0 E_0}]^2 [\frac{(E_0 + m_0c^2)}{(E_0 + 2m_0c^2)}]^2 [\frac{2\pi \sin\theta}{\sin^4(\frac{\theta}{2})}] \qquad (6)$$

where, σ is the scattering cross-section, θ is the scattering angle, e is the charge of a single electron, Z is the atomic number and ε_0 is the dielectric constant in vacuum.

Upon integration of the expression over the scattering angle from

$\theta_{max} = \pi$ to $\theta_{min} = 2\sin^{-1}[\sqrt{\frac{E_S}{E_{max}}}]$,

with the assumption that the surface binding energy, $E_S = E_{min}$ (which is the minimum energy transferable from the beam, E_{min} = 17 eV for in-lattice sp^2 bonded C-atoms and ~ 5 - 15 eV for amorphous sp^3 bonded C-atoms or lattice-edge atoms with vacant nearest-neighbor sites), we get

$$\sigma = (2.45\times10^{-29})Z^2[\frac{(1-\frac{v^2}{c^2})}{(\frac{v^2}{c^2})^2}][\frac{E_{max}}{E_{min}}-1] \qquad (7)$$

in m^2, where v is the velocity of the incident electron given by

$v = \sqrt{\frac{2eV}{m_0}}$ (where V = 100kV).

Substituting these values, σ is calculated to be ~ 6.216 x 10^{-28} m^2 for sp^2 bonded carbon and ~ 1.174 x 10^{-27} – 10.567 x 10^{-27} m^2 for sp^3 bonded carbon or lattice-edge carbon.

The atomistic sputtering rate from elastic-electron collisions with both the exit-surface atoms and the subsurface atoms is given by,

$$S = 2c\frac{J}{e}\sigma(thickness\ of\ a\ monolayer) \qquad (8)$$

or

$$S = 2c\frac{J}{e}\sigma(\frac{uA}{\rho})^{1/3} \qquad (9)$$

where, c is the dimensionless proportionality constant depending on the sample and localized perturbations (owing to the atomistic nature of the sputtering process and the uniform composition assumptions), J is the incident electron current density (J = ~ 150 A/cm^2), e is the electronic charge, u is the atomic mass unit, A is the atomic mass number and ρ is the mass density.

Multilayered PFG- wrapped bacteria:

Owing to the multilayered structure of the PFGs comprising of functionalized outer layers and un-functionalized, crystalline graphene layers, we take the average value of the σ = 3.246 x 10^{-27} m^2 for all our calculations.

For a 3 layer PFG, the average monolayer thickness = (total thickness)/3 = 0.933 nm.

The sputtering rate is **$S = 0.0567c_1$ nm/sec,** where c1 is the proportionality constant.

Assuming the PFG wraps to conform to the structure of the bacterium, the surface area of the PFGs hermetically wrapping a bacteria is $2\pi rh$ (r is the radius of the bacterium and h is the length).

Thus the rate of volume reduction is V_{WB} (D1) = $3.563 \cdot c_1 \times 10^{-22}$ m^3 /sec

Unwrapped Bacteria:

A bacteria comprises of 26 % amorphous carbon and 70 % water, we have to account for the ejection of both the constituents (taking an weighted average).

Owing to the heterogeneity of the water molecules, the interaction of the electrons is expected to be in-elastic leading to beam damage via D2, D3 and D4.

For the amorphous carbon component,

Using the scheme as presented in 6,

We calculate, **$S = 0.0295c_2$ nm/sec**

And the rate of volume reduction is, V_{UWB}(D1) = $1.853 \cdot c_2 \times 10^{-22}$ m^3 /sec

D2:

The charging of the electrically insulating bacterial cell is caused by both elastic and in-elastic scattering events depending on the backscattering coefficient and the secondary electron yield. The current balance on the bacteria exposed to an electron beam in a TEM is given by *Egerton et al* [1, 2] as,

$$I - I_t + \frac{V_S}{R_S} = I\eta(t) + I\delta(V_S) \qquad (10)$$

where, I is the incident beam current, I_t is the transmission electron current, V_S is the surface potential, R_S is the effective electrical resistance between the irradiated and surrounding regions in the specimen, $\eta(t)$ is the reduced backscattering coefficient and $\delta(V_S)$ is the effective secondary yield when the surface potential is + V_S.

During the high resolution TEM imaging, at a high current density, the V_S becomes extremely high owing to the presence of highly energetic auger electrons leading to the creation of electric fields as high as 10^{10} V/m, more than sufficient to cause dielectric breakdown or lateral migration of ions. This migration of ions leads to electrostatic repulsion generating a shear force which in synergy with electron beam-induced heating causes membrane rupture in the specimen. However, the models accurately describing this effect are computationally intensive and are beyond the scope of this current work.

Multilayered PFG- wrapped bacteria:

With the excellent conductivity of graphene (~ 12, 000 S/m), the electrostatic charging and therefore the structural damage should be negligible. Similar observations have also been made by *Meyer et al* [3] in imaging of hydrogen atoms on graphene.

Unwrapped bacteria:

The unwrapped bacterium gets charged readily in contrast to the wrapped bacteria under similar conditions. Further, since D2 affects the cell wall/membrane integrity and hence the out-diffusion rates of intracellular material, we include this effect in a simplistic formulation in the description of the effect of D3.

D3:

The substantial energy transfer during the in-elastic collisions between incident electrons and the atomic-electrons gives rise to an increase in the specimen temperature: leading to isotropic ejection of atoms into the TEM column.

A heat-transfer balance leads to,

$$\frac{I}{e}(\frac{Et}{\lambda}) = \frac{4\pi\kappa t(T-T_0)}{[0.58+2\ln(\frac{2R_0}{d})]} + \pi(\frac{d^2}{2})\varepsilon\sigma(T^4 - T_0^4) \qquad (11)$$

i.e. the net heat transferred into the specimen from the electron beam is rejected via conduction and via radiative transfer at steady state. However, owing to the poor thermal conductivity of bacterial cells, the radiation term can be neglected, leading to

$$\Delta T = \frac{\frac{I}{e}\times(\frac{Et}{\lambda})\times[0.58+2\ln(\frac{2R_0}{d})]}{4\pi\kappa t} \qquad (12)$$

where T is the temperature of the specimen, T_0 is the temperature of the surrounding TEM column, I is the beam current, e is the electronic charge, E is the average energy loss per in-elastic electron-electron collision, λ is the mean free path of all in-elastic scattering, R_0 is the heat conduction radii, d is the beam diameter and κ is the thermal conductivity of the specimen.

Multilayered PFG- wrapped bacteria:

Owing to a high thermal conductivity of graphene (~ 5000 W/m/K), the electron beam induced heating is expected to result in negligible temperature change ($\Delta T_{theoretical}$ ~ 3.755 X 10^{-9} K) over the surrounding column temperature.

Unwrapped bacteria:

Substituting the numbers in scheme 7, I = 1 pA, R_0 = 0.5 μm, d = 1 μm, κ_{water} = 0.58 at 25 C and for 100 minutes of stationary beam exposure we get, $\Delta T_{theoretical}$ ~ 3.237 X 10^{-5} K

Thus, the effect of the electron beam induced localized heating in un-wrapped bacterium can be safely neglected for the larger beam diameters and lower beam currents. However, since water constitutes ~ 70 % of the wet mass of a bacterial cell, owing to (1) the cracks and holes in the cell wall created during the course of electron beam-induced an-isotropic sputtering and ion migration & repulsion induced shear, and (2) the high pressure difference between the

cytoplasm of the bacteria ($P_{water}^{T_0=25\ C} = 23.76$ Torr , assuming the TEM beam column to be at 25 C) and the TEM column (~ 10^{-5} torr), the water vapor is expected to slowly leech out into the TEM column resulting in the shrinkage of the bacterial cell.

Assuming the water vapor to leech out of the cell after the beam exposure at a rate depending on the amount of diffusion resistance offered by the bacterial cell wall (and cell membrane) which is being simultaneously sputtered (D1) and ruptured via the shear (D2), the reduction in volume can be calculated as follows,

Wet volume of the bacteria before beam-exposure (with cylinder approximations),

$V_{wet} = 1.571 \times 10^{-18}\ m^3$ for a 2 μm long, 0.5 μm thick bacterial cell

Since the bacteria consists of mostly water (~ 70 %) and carbon (~ 26 %), the average density of the bacterial cell can be approximated as ~ 1168 kg/m^3. Thus the weight of the bacterial cell is 1.834×10^{-15} kg.

Upon exposure to the electron beam, if $d \cdot t^n$ % (the time dependent term takes into account varying diffusion rates due to barrier compromise via D1 and D2) of water is lost via leeching from the bacterial cell, $V_{final} = (1.571 - 1.099 \times d \cdot t^n/100) \times 10^{-18}\ m^3$

Thus, theoretically upon loss of all water from the bacteria upon exposure to the TEM beam, there would be a ~ 70 % reduction in the total volume of the cell.

D4:

The inelastic collisions of the electron beam with the amorphous, organic molecules in bacteria induce intra-molecular electronic excitations resulting in an irreversible re-arrangement of the chemical bonds. This is termed Radiolysis and is usually accompanied by mass loss in form of release of low atomic number gases like hydrogen, oxygen, nitrogen, etc. Further, in the context of cells, radiolysis evokes denaturation/unfolding of proteins and destruction of the nucleic acids in the DNA and the RNA which limits the ability of the cell to replicate i.e. causes cell death.

Multilayered PFG- wrapped bacteria:

Owing to the high resonance energy of the delocalized π-electrons in the graphenic island clusters of the PFGs wrapping the bacteria, the wrapped bacteria have a higher stability under an electron beam. Further, the atomically-impermeable PFG sheets act as a diffusion barrier, thereby reducing the rate of escape of the low atomic number gases upon radiolytic damage in wrapped bacteria and increasing the probability of broken-bond annealing. Similar observations have also been reported by Fruer and Holland for carbon coated organic compounds. Thus, since the amount of information that can be extracted from the sample depends on the beam dose, increased resolution is achieved upon wrapping the bacteria before imaging.

Unwrapped bacteria:

They are exposed to the full brunt of radiolytic damage.

References

1. Egerton, R.F., Li, P. & Malac, M. Radiation damage in the TEM and SEM. *Micron* **35**, 399-409 (2004).

2. Egerton, R.F., Wang, F. & Crozier, P.A. Beam-induced damage to thin specimens in an intense electron probe. *Micros. and Microanal.* **12**, 65-71 (2006).

3. Meyer, J.C., Girit, C.O., Crommie, M.F. & Zettl, A. Imaging and dynamics of light atoms and molecules on graphene. *Nature* **454**, 319-322 (2008).

Appendix C - Supporting information: Biocompatible, robust free-standing paper composed of a TWEEN/graphene composite

Additional Details of experiments

Measurement of mechanical properties

Normal tensile tests of the paper samples were initially conducted at 35 °C for 0.5 min in controlled-force mode with a preload of 0.001N, then force was loaded with a force ramp rate of 0.05 N/min. The sample thickness was measured from SEM images of the fracture edges.

Reaction of TWEEN and hydrazine monohydrate

We carried out a control experiment in which the effect of hydrazine treatment on the chemical structure of TWEEN was investigated. Here, a reaction of TWEEN and hydrazine monohydrate in water was carried out in the absence of graphene oxide. All the reaction conditions were kept the same as those described in "Production of a colloidal suspension of TWEEN/RGO hybrid" part of experimental section. Upon completion of the reaction, water was removed by evaporation under vacuum in a water bath at room temperature for 12 h. The resultant colorless liquid was further dried under vacuum in water bath at 50 ^{o}C for 12 h. Subsequently, the ^{1}H and ^{13}C-NMR spectra of both TWEEN and hydrazine-treated TWEEN were acquired. The NMR spectra of hydrazine-treated TWEEN were found to be identical to those of TWEEN. This suggests that the chemical structure of TWEEN is not altered by the reaction with hydrazine in the reaction conditions used in this work.

Measurements of atomic force microscopy (AFM) and transmission electron microscopy (TEM)

We measured non-contact mode AFM and TEM to confirm that the RGO sheets are present as individual sheets in the hybrid. TEM samples were prepared by dip coating a Quantifoil TEM grid in a water diluted suspension of TWEEN/RGO. As can be seen from the bright field TEM (BF TEM) image in Figure 4.2, the sheets on the grid seem to be comprised of only a few layers, and are very wrinkled, and rolled at the edges. Individual reduced graphene oxide sheets could not be found by AFM scanning of dried-down deposits of

TWEEN/RGO hybrids on the mica due to TWEEN molecules adsorbed on the sheets. After heating the deposits on the mica substrate (at 200 ^{o}C, for 2 h, in the air-oven), individual flat reduced graphene oxide sheets with thickness of ~0.6 nm were frequently observed from numerous AFM images. While the thermal treated RGO sheets on the substrate are fundamentally different than the sheets in the TWEEN/RGO hybrids, the presence of ~0.6nm thick sheets after heating the dried down deposit is clear evidence that sheets do exist as individual sheets in the suspension.

Table C-1 Cell adhesion properties of TWEEN and RGO paper

	TWEEN (Long Duration)	**TWEEN (Short Duration)**	**RGO (Long Duration)**	**RGO (Short Duration)**
Bacterial	No Adhesion	No Adhesion	Adhesion	Adhesion
Mammalian Cells	Adhesion via cell adhesion molecules	No Adhesion (cell adhesion molecules absent)	Strong Adhesion	No Adhesion (cell adhesion molecules absent)

Table C-2 Mechanical properties of TWEEN paper samples

Run	E (GPa)	σ (Mpa)	ε (%) (x10^{-1})
1	2.2	6.2	3.4
2	2.3	4.4	2.8
3	1.9	5.8	3.1
4	1.4	3.5	2.4
5	1.2	3.4	3.8

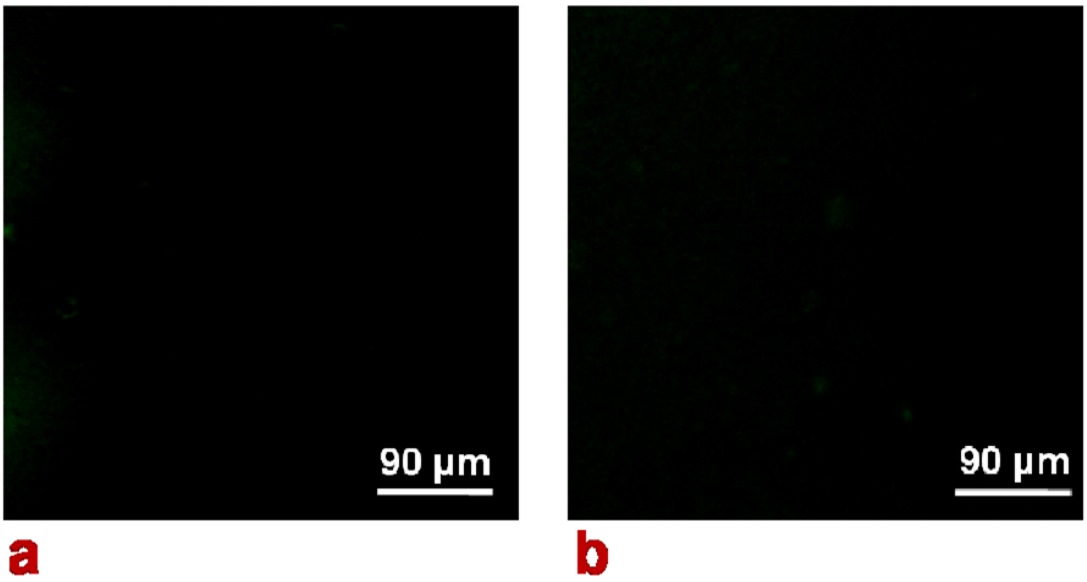

Figure C-1 Confocal microscope images of Calcein (Green fluorescence) stained CRFK cell attachment on RGO paper (a) and TWEEN-RGO paper (b). No cells were found to adhere after 1 minute of exposure to the cell suspension in either case.

Appendix D - Supporting information: High-throughput, ultra-fast synthesis of solution-dispersed graphene via a facile hydride chemistry

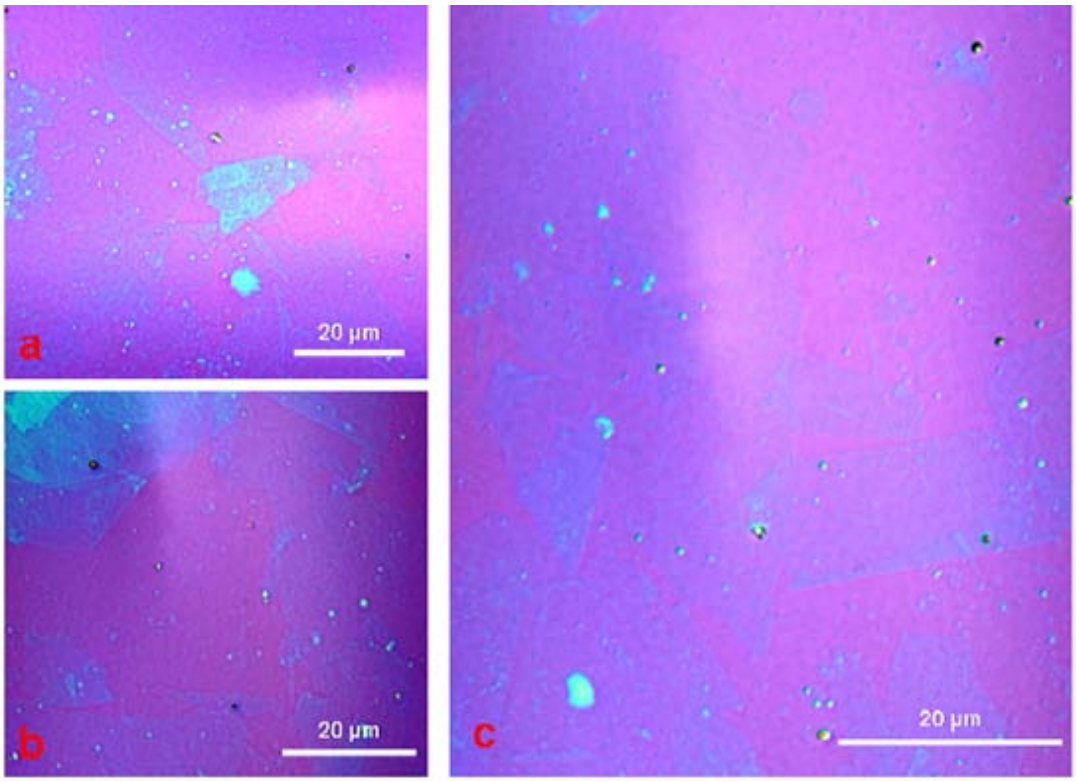

Figure D-1 (a, b, c) Optical images of the RGO sheets deposited on the 300 nm silica substrates showing single sheets, multiple sheets, folds and layers.

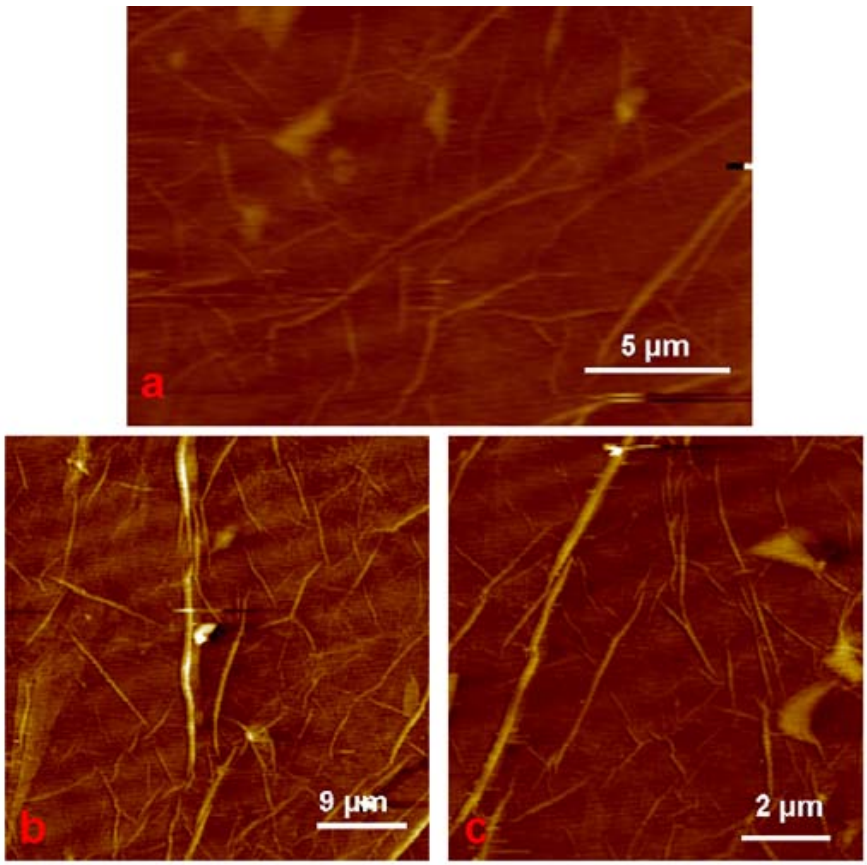

Figure D-2 (a, b, c) AFM images of the washed RGO sheets deposited onto 300 nm silica substrates via drop casting showing the wrinkles and surface features

Appendix E - Supporting information: High efficiency production of long, high-quality graphene nanoribbons with narrow width distribution

Efficiency of the nanotomy process

The overall yield of the process was a combination of the yield of the two independent sequential processes underlying GNR production viz. (a) the cleavage of the GNBs from HOPG block (*SPI Inc.*) and (b) the exfoliation of the as-cleaved GNBs into constituent GNRs.

The yield of the GNB cleaving process depends on the efficiency of cleavage and the efficiency of collection of the cleaved GNBs. After proper alignment of the nanotome, the cleavage was found to be successful in almost all cutting cycles (for each batch 50 cutting cycles was used). Assuming that we collected all the GNBs from the knife boat, the yield of the GNB cleaving process is ~ 100 %.

Thus, the overall yield of the process is efficiency limited by the second step i.e. the exfoliation process.

Superacid exfoliation process

In order to calculate the efficiency of this exfoliation process, the dried GNBs were weighed before being exfoliated. After, the chlorosulfonic acid based exfoliation into constituent GNRs, the dark black colored liquid phase was quenched in DI water (1:200) and freeze dried in a *Virtis Inc* freeze drier (Model # 10-MR-TR). The resulting solid was again weighed for calculating the efficiency of exfoliation. The efficiency for this process was found to be **~ 80 %**.

Hummer's acid exfoliation process

Using a similar strategy as described above we calculate the efficiency of the hummer's exfoliation process to be **< 10 %**.

PCA based exfoliation strategy

Using a similar strategy described above, the efficiency was found to be **< 1 %**.

Thus, the maximum over all efficiency of the production of GNRs was ~ **80 %** (for superacid exfoliation strategy)**.**

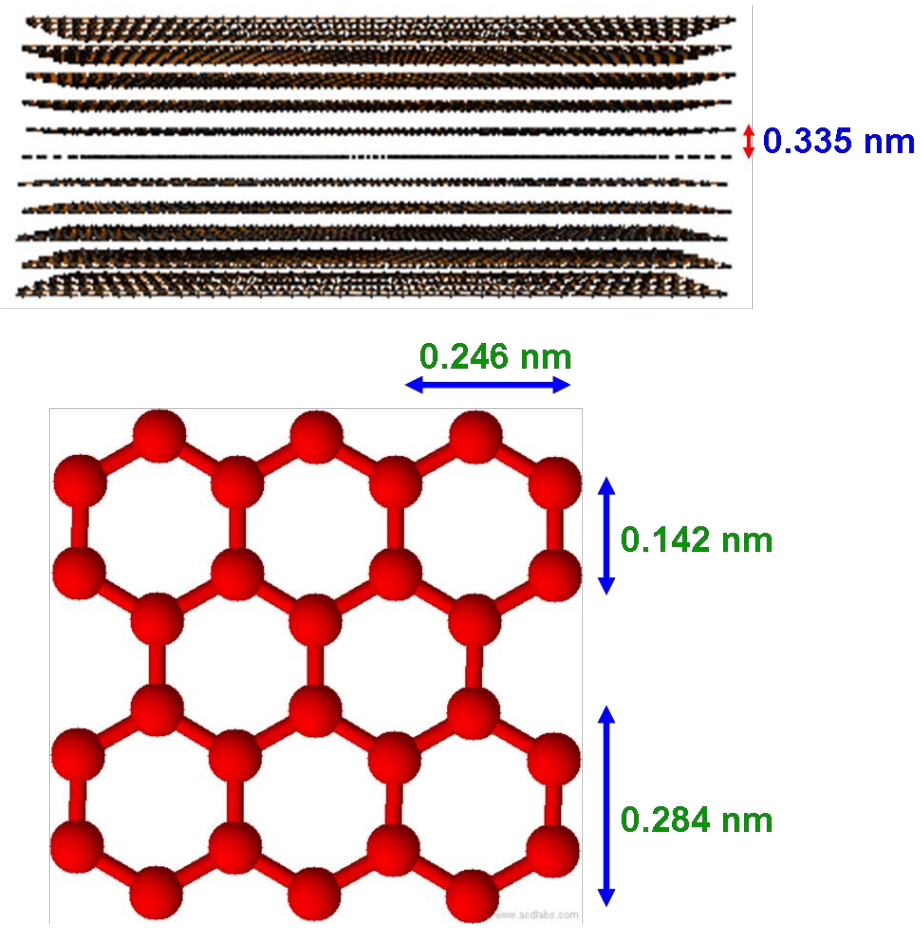

Figure E-1 Schematic diagram showing the atomic dimensions of a GNB block and a GNR. The C-C bond length is 0.142 nm and the interlayer spacing is 0.335 nm.

Considering the 7 X 7 mm areal dimensions and 1 mm thickness of the HOPG block used in our cleaving process, for every cleavage step we would produce a GNB consisting of ~ 2.9 X 10^6 GNRs (based on dimensions shown by Figure E.1). For 50 such cleavage cycles in 0.5 hour we would produce a total of ~ 1.49 X 10^8 GNRs which are in form of GNBs. Upon exfoliation of these GNBs by the superacid based exfoliation strategy, we would expect to produce ~ 2 X 10^8 GNRs per hour.

HRTEM image discussion

In order to study the effectiveness of the nanotomy process in producing long, narrow GNRs, we employed HR-TEM imaging for analyzing w ~ 15 nm GNRs. Excellent width uniformity was observed for the GNRs with the selected area electron diffraction (SAED) pattern showing hexagonal crystal lattice resembling graphene (Figure 6.8a). For several (5 samples) ribbons studied, the typical edge structure was mixed, as can be observed in the representative images (a hexagonal pattern has been superimposed as a guide to the eye) (Figure 6.8b, c). We attribute this to the combined effect of the grain boundaries of the parent HOPG, the cleavage fracture process and the superacid exfoliation strategy.

Discussion on XPS analysis of the GNRs

We used XPS to study the chemical properties of the super acid exfoliated GNRs (Figure E.2). High resolution scans for the C 1s were obtained which showed the signature peak of sp^2 bonded carbon at 284.5 eV. The absence of the sp^3 carbon associated peaks vindicates the pristine nature of the GNRs. The XPS survey scans showed the presence of trace amounts of sulfur, which were confirmed using high resolution scans for S 2p. This is consistent with the observed up-shift of the Raman G-band peak (by ~ 2 cm^{-1}) for the w ~ 15 nm GNRs, compared to the wider GNRs: a signature of charge transfer from edge functional groups (This effect is more prominent for narrow GNRs, since they have a higher percentage of edge-associated carbon atoms than basal [1]). This presence of a negligible amount of sulfur is similar to the data reported on graphene by *Behabtu et al* [2]. In view of the low penetration depth of the X-rays used in XPS (< 10 nm), we attribute the trace amounts of sulfur to the probable edge functionalization of the GNRs. Since, the edges of the GNRs, which include dangling bonds and defects, are hydrogenated [3, 4], and chlorosulfonic acid reacts with phenylic groups [5], we expect some degree of edge sulfonation. Our theoretical calculations limit the maximum incidence of sulfur at 1 atomic percentage (Based on the bottom panel of the Figure S3, we estimated the total number of edge atoms with respect to the number of basal surface atoms for a 1 micron long, 15 nm wide GNR to be 0.0073 %. Thus, in the extreme case of full sulfonation of the edges, the total theoretical amount of sulfur for unit mass of GNRs is expected to be < 1 %.). The atomic percentages of sulfur determined by the XPS scans were within the theoretical limits (C > 98 %, S ~ 0.92 %).

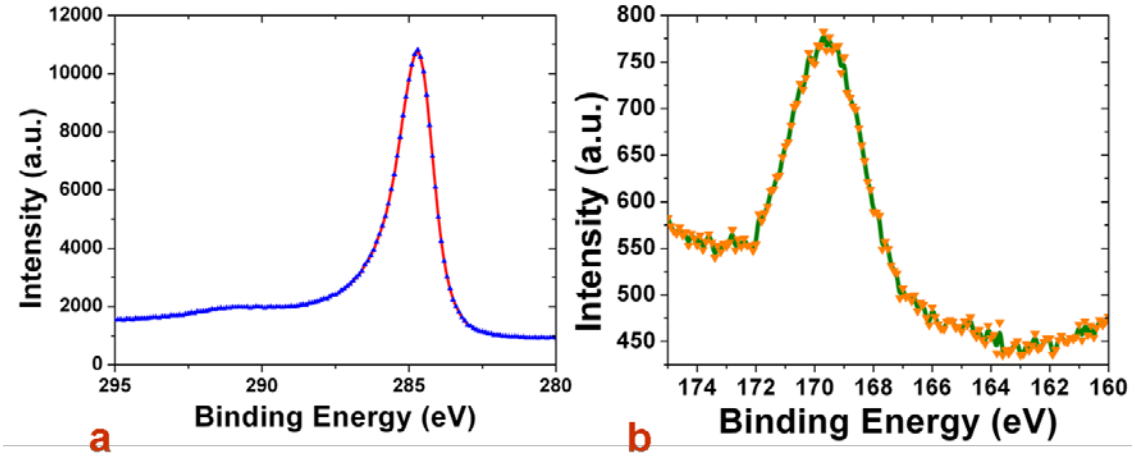

Figure E-2 High resolution XPS spectra for C-1s and S-2p levels. The scans show the sp^2-carbon peak at 284.5 eV. The low levels of sulfur were attributed to the probable edge sulfonation of GNRs by chlorosulfonic acid.

Conformal Raman spectra on a bilayer GNR (w ~ 15 nm)

Raman spectroscopy is an excellent technique for probing the quality of the graphenic structures in terms of structural (defects), chemical (doping levels) and mechanical (strain) characteristics [6, 8]. We employed Raman spectroscopy to probe the edge quality of our GNRs. We used a Renishaw inVia confocal micro-Raman spectroscope with an 100 X objective equipped with a 514.5 nm laser line to characterize our GNRs. Based on the report by *Cai et al* [7], the diameter of the Raman laser beam is given by, $d \sim 2\lambda/\pi NA$ where λ is the wavelength of the laser and NA is the numerical aperture of the objective lens employed. The diameter of the laser beam was calculated to be ~ 0.4 μm. Owing to the random edge crystallographies of the GNRs described in the current report and the diameter of the laser beam encompassing several individual GNRs in the GNR film, the Raman spectra ($I_{D/G}$ ratios) is expected to probe the average roughness of the edges including the defects and dangling bonds [4, 8]. Our GNRs were found to have low edge roughness as compared to most GNR fabrication strategies (Figure 6.9g). Further, we studied an individual w ~ 15 nm GNR, first located by scanning Raman spectroscopy for the G band and then full Raman spectra being collected at the location of maximum G-band intensity (Figure E.3). The number of layer information was extracted via

lorentzian fitting of the 2D peak [6, 8]. The $I_{D/G}$ ratios for bilayer w ~ 15 nm GNRs were ~ 0.4 – 0.5, comparable to that reported for similar dimension GNRs synthesized via the sonochemical unzipping strategy reported by the *Dai group* [4]. This reflects on the excellent quality of the as fabricated GNRs.

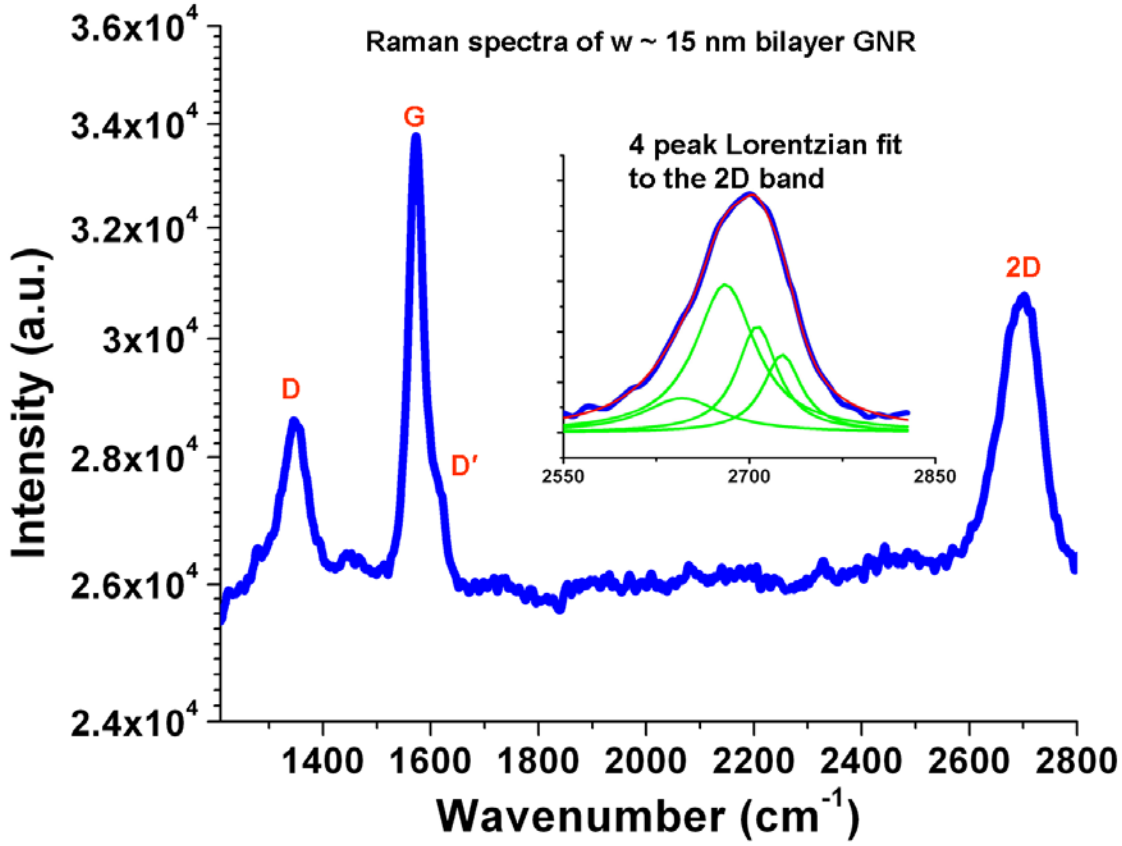

Figure E-3 A typical conformal Raman mapping of a w ~ 15 nm wide GNR immobilized on a silicon dioxide surface. Inset shows a successful 4 peak lorentzian fit of the 2D band of the GNR attributing bilayer nature. The $I_{D/G}$ was ~ 0.4-0.5

Discussion on mechanism of production of GNBs from HOPG

There has been no consensus on the mechanism of formation of nanometer thick sections in a nanotome. Two different mechanisms have been proposed for the sectioning process: (A) Direct sectioning (or True sectioning), a process similar to macroscale machining such as lathe-based cutting, in which the knife is in contact with the specimen at all times during cutting. (B) Cleavage based sectioning, in which the dull edge of a knife initiates a crack, which then

propagates in front of the knife like a wedge cleaving a piece of wood. Both of these mechanisms are known to act in concert in sectioning of heterogeneous materials and interfaces [9, 10].

In our case, we believe the predominance of the second mechanism i.e. the cleavage mechanism to be in action owing to the following observations: (a) the cutting of ~ 5 nm wide GNRs clearly rules out true sectioning since the diamond knife edge radius is known have similar dimensions. (b) the appearance of the crazes (a highly distorted and deformed volume) on the HOPG as seen in the Figure 6.10 –b is known to be a signature of cleavage process [9].

Figure 6.10 a – shows a schematic diagram of the cleavage of GNBs from the HOPG block and several cutting parameters. The regions of HOPG expected to experience high stresses are shown in red. In order to observe the cutting process in action, we partially cut a HOPG block and studied it under a FESEM. Figure 6.10 b shows the false colored FESEM images of the crack formed as a result of the initiation of the cutting process and its propagation direction aided by the formation of crazes. The red colored regions show the areas expected to be exposed to high tensile forces and compressive / shear stresses.

Discussion on fabrication of GNR films via vacuum filtration

0.1 ml of the superacid dispersed pristine-GNRs was quenched in 20 ml of DI water to produce a colloidal suspension of exfoliated pristine-GNRs in DI water (conc. ~ 0.2 mg/l). Thin, flexible pristine-GNR-films were fabricated via vacuum filtration of the DI water suspension of pristine-GNRs onto polycarbonate filters (2 inch diameter, 600 nm pore size, *SPI Inc.*) in an apparatus as shown in Figure 6.4, followed by drying in an argon atmosphere at room temperature for 2 days. Due to the use of a Büchner funnel in our filtration process, we obtained several GNR films, each having a dimension similar to the pores on the funnel (~ 0.4 mm in diameter).

Proposed mechanism of film formation

Owing to the high aspect ratio of our GNRs (w ~ 15 – 50 nm compared to the 600 nm pore size of the filter), several layers of GNRs need to come together to block a single pore. This is different from the graphene / GO film filtration where a single sheet is found to block a pore. This blockage of a pore is expected to start the deposition process by enhancing the permeation through the adjacent pore until it too is clogged by the GNRs, and hence continuing until most

pores are clogged. The average thickness of the GNR films was found to be ~ 50 nm (Figure 6.11 f). This is in contrast to the much larger GO films, where 3-5 layers (corresponding to 4-5 nm) are typical.

Sheet resistance of the films

The sheet resistance of the thin GNR film (on polycarbonate filter substrate) was measured using the standard 4 point probe technique in which 4 tungsten probes were mechanically pressed onto the samples for contact resistance-free measurements. Sheet resistance was determined from the *Van der Pauw's* formula $R_S = \frac{\pi}{\ln 2}(\frac{V}{I})$. The sheet resistance of the films was found to be 2.2 – 5.1 MΩ/□. These results are comparable to the typical values for the reduced GO films as reported by *Eda et al* (43 kΩ/□ - 0.06 T Ω/□) [11]. For surfactant stabilized graphenic films, *Lotya et al* [12] and *Hernandez et al* [13] have reported 0.022 MΩ/□ and 7.1 kΩ/□ respectively post-annealing (pre-annealing figures for *Hernandez et al* are 7.2 MΩ/□; the results reported by us are for **un-annealed samples**). In view of several randomly distributed GNR-to-GNR overlaps in the film, the contact resistance of those junctions is expected to form a major component of the sheet resistance.

Free-standing GNR-films

Several attempts in producing large freestanding GNR films by dissolving the polycarbonate filter paper substrate in chloroform failed owing to their breakage upon detachment from the substrate. However, it might be possible to achieve this by using different filters such as alumina, which is a part of on going investigation in our group. Nevertheless, the microscopic de-laminated GNR-films were immobilized onto a 400 mesh Lacey carbon TEM grid for TEM analysis. The TEM images vindicate the expected random distributions of the GNRs in the film (Figure 6.4c).

Thin-film FET fabrication with GNR-film channel

In order to study the electronic properties of our GNR films, source and drain electrodes (Au:Pd = 3:2) were sputtered onto the GNR film on polycarbonate substrate (600 nm Pore size, Polycarbonate membrane, *SPI Inc.*) using a 0.2 mm wide strip of polyethylene as channel mask (Figure 4g shows an optical image of the GNR film on polycarbonate filter substrate with source

and drain electrodes deposited. Figure 6.11e and f show FESEM and AFM images of the GNR film on the polycarbonate filter substrate.). Post-sputtering, the device is immobilized onto a gold-coated-silicon dioxide wafer via application of pressure using a PDMS stamp. The device was annealed at 60 C in an Argon atmosphere for 2 hours. Using the gold-coated-silicon wafer as the gate electrode and the polycarbonate filter substrate as the gate oxide, back-gated electrical studies were conducted (Figure 4d shows a schematic diagram of our back-gated FET device.). As a proof of concept, GNR films comprising of 3 different widths of GNRs were studies (w ~ 50 nm, 25 nm and 15 nm as determined by FESEM / TEM imaging).

Charge carrier mobilities

Carrier mobilities were calculated using the commonly used equation, $\mu = \frac{L}{W \bullet C_{OX} \bullet V_{SD}} (\frac{\Delta I_{SD}}{\Delta V_G})$, where L is the channel length; W is the channel width; C_{OX} is given by $\varepsilon_{OX}\varepsilon_0/t_{OX}$ where ε_{OX} is the permittivity of the gate oxide, ε_0 is the permittivity of free space and t_{OX} is the gate oxide thickness; V_{SD} is the source-drain voltage and $(\frac{\Delta I_{SD}}{\Delta V_G})$ is the transconductance or the slope of the transfer curve in the linear regime.

Transfer characteristics show clear semiconducting characteristics (Figure S11). When the measurements were conducted in air, a strong n-type doping character was observed for the GNR films which were attributed to the adsorbates during the fabrication process. Upon exposure to vacuum and electrical annealing as described by *Moser et al* [14], ambipolar character was restored resembling that of pristine graphene. This vindicates the good quality of the GNR films. Typical mobilities of the electrons and the holes were calculated to be 20 ± 4 $cm^2/V{\cdot}S$ for all the devices studied in this work (8 devices were studied in all, 2 for w ~ 50 nm and 3 each for w ~ 25 and 15 nm GNRs; 1 device for w ~ 50 nm GNR shorted during gating). These values are significantly higher than that reported for the wide-functionalized-reduced-GONR films reported by *Zhu et al* (~ 0.1 – 0.5 $cm^2/V{\cdot}S$) [15] attributed to the pristine nature of our GNR films. However, the mobility values reported for single GNR devices are 2 orders of magnitude higher (~ 1500 $cm^2/V{\cdot}S$ in the report by *Jiao et al* [4]). This is expected in view of the scattering at the overlap junctions of the GNRs constituting our film.

Electrical band-gaps of the GNR-films from non-linear transport regime

Further, the low temperature I_{DS} versus V_{DS} characteristics (in a *Janis ST100 cryostat*, 10^{-5} Torr base pressure, 80 K) of the GNR films at the charge neutrality point ($V_G = 0$) showed non-linearity, a characteristic of semiconductors. In order to determine the bandgaps of the respective films, we analyzed their non-linear transport characteristics as described by *Han et al* [16]. Owing to the relatively large channel lengths in our GNR film devices, the channel length dependence of the non-linear bandgap is expected to have an insignificant effect in our devices. The edges of non linear bandgap were determined from the steep increase of the absolute value of I_{DS} in the logarithmic scale (Figure 6.11a-c). A clear bandgap scaling was observed: as expected the w ~ 50 nm GNR film had a very small bandgap which could not be measured due to instrument limitations (2 devices were studied; 1 device shorted during gating), the w ~ 25 nm GNR film had a bandgap of ~ 10 meV (3 devices were studied) and the w ~ 15 nm GNR film had a bandgap of ~ 35 meV (3 devices were studied).

Temperature dependent transfer characteristics of GNR-films

In order to independently study the bandgap of the GNR films and confirm the nonlinear bandgap values determined as above, we studied the temperature dependence of the F current of the GNR film devices (w ~ 15 and w ~ 25 nm GNR film devices; w ~ 50 nm was not studied owing to the extremely small bandgap un-measurable by us due to instrumental limitations) on the lines of *Chen et al* [17]. A sequential decrease in the F current was observed as shown in the Figure 4h. We studied the thermally activated off-resonant conduction of the GNR films via Arrhenius plots of the I_F versus temperature (Figure 6.13). Two separate transport regimes were observed, one at high temperature and other at low temperatures with a crossover at a characteristic temperature T^*. At high temperatures ($T > T^*$), the transport is simply activated and the I_F follows the simple exponential dependence on temperature given by, $I_{OFF} \propto e^{\frac{-E_g}{2k_BT}}$, where E_g is the bandgap, k_B is the Boltzmann constant and T is the temperature. Plots of $\ln(I_F)$ versus 1/T were used to fit a straight line at high temperatures, to obtain average bandgaps of ~ 6 meV and ~ 30 meV for w ~ 25 nm and w ~ 15 nm GNR film devices respectively (2 devices were studied for each width). These compare well with the non linear bandgap. For the low temperature regime ($T < T^*$), stark deviation from simple activation behavior was observed for

the I_F, which was now observed to decrease more slowly. This is a signature of variable range hopping (VRH) transport model. This is expected owing to the several randomly distributed GNR overlap junctions in the films which act as scattering sites. A VRH model given by, $I_{OFF} \propto e^{-(\frac{T_0}{T})^{\gamma}}$, where T_0 is a characteristic constant and γ is the exponent, was fit to the data. For both $\gamma = 1/3$ and $\gamma = 1/4$, good fits were obtained with similar standard deviations. This is suggestive of transport in 2 and 3 dimensions including through multiple layers [18]. More studies are undergoing to characterize these transport mechanisms in detail.

References

1. Ryu, S. et al. Raman spectroscopy of lithographically patterned graphene nanoribbons. ACS Nano, **ASAP**, (2011)
2. Behabhtu, N. et al. Spontaneous high-concentration dispersions and liquid crystals of graphene. *Nat. Nano.* **5**, 406-411 (2010)
3. Wang, Z. F., Li, Q., Zheng, H., Ren, H., Shi, Q. W., Chen, J. Tuning the electronic structure of graphene nanoribbons through chemical edge modification: A theoretical study. *Phys. Rev. B* **75**, 113406-113409 (2007)
4. Jiao, L., Wang, X., Diankov, G., Wang, H., Dai, H. Facile synthesis of high-quality graphene nanoribbons. *Nat. Nano.* **5**, 321-325 (2010)
5. Cremlyn, R. J. Chlorosulfonic acid: A versatile reagent. *RSC* (2002)
6. Ferrari, A. C. Raman spectroscopy of graphene and graphite: Disorder, electron–phonon coupling, doping and nonadiabatic effects. *Solid State Communications* **143**, 47-57 (2007)
7. Cai, W. et al Thermal transport in suspended and supported monolayer graphene Grown by chemical vapor deposition. *Nano Lett.* **10**, 1645-1651 (2010)
8. Ferrari, A. C. et al. Raman spectrum of graphene and graphene layers. *Phys. Rev. Lett.* **97**, 187401-4 (2006)
9. Acetarin, J., Carlemalm, E., Kellenberger, E., Villiger, W. Correlation of some mechanical properties of embedding resins with their behaviour in microtomy. *Journal of Electron Microscopy Technique* **6**, 63-79 (1987)
10. Xu, Q., Rioux, R. M., Dickey, M. D., Whitesides, G. M. Nanoskiving: A new method to produce arrays of nanostructures. *Acc. Chem. Res.* **41**, 1566-1577 (2008)

11. Eda, G., Fanchini, G., Chhowalla, M. Large-area ultrathin films of reduced graphene oxide as a transparent and flexible electronic material. *Nat. Nano.* **3**, 270-274 (2008)
12. Lotya, M., King, P. J., Khan, U., De, S., Coleman, J. N. High-concentration, surfactant-stabilized graphene dispersions. *ACS Nano* **4**, 3155-3162 (2010)
13. Hernandez, Y. et al. High-yield production of graphene by liquid-phase exfoliation of graphite. *Nat. Nano.* **3**, 563-568 (2008)
14. Moser, J., Barreiro, A., Bachtold, A. Current-induced cleaning of graphene. *App. Phys. Lett.* **91**, 163513-3 (2007)
15. Zhu, Y., Tour, J. M. Graphene nsnoribbon thin films using layer-by-layer assembly. *Nano Lett.* **10**, 4356-4362 (2010)
16. Han, M. Y., Brant, J. C., Kim, P. Electron transport in disordered graphene nanoribbons. *Phys. Rev. Lett.* **104**, 056801-4 (2010)
17. Chen, Z., Lin, Y., Rooks, M. J., Avouris, P. Graphene nano-ribbon electronics. *Physica E: Low-dimensional Systems and Nanostructures* **40**, 228-232 (2007)
18. Jin, M., Jeong, H. K., Yu, W. J., Bae, D. J., Kang, B. R., Lee, Y. H. Graphene oxide thin film field effect transistors without reduction. *J. Phys. D: Appl. Phys.* **42**, 135109-5 (2009)

Appendix F - Supporting information: High throughput production of graphene quantum dots (GQDs) with tunable size and shape

Efficiency of the cutting process

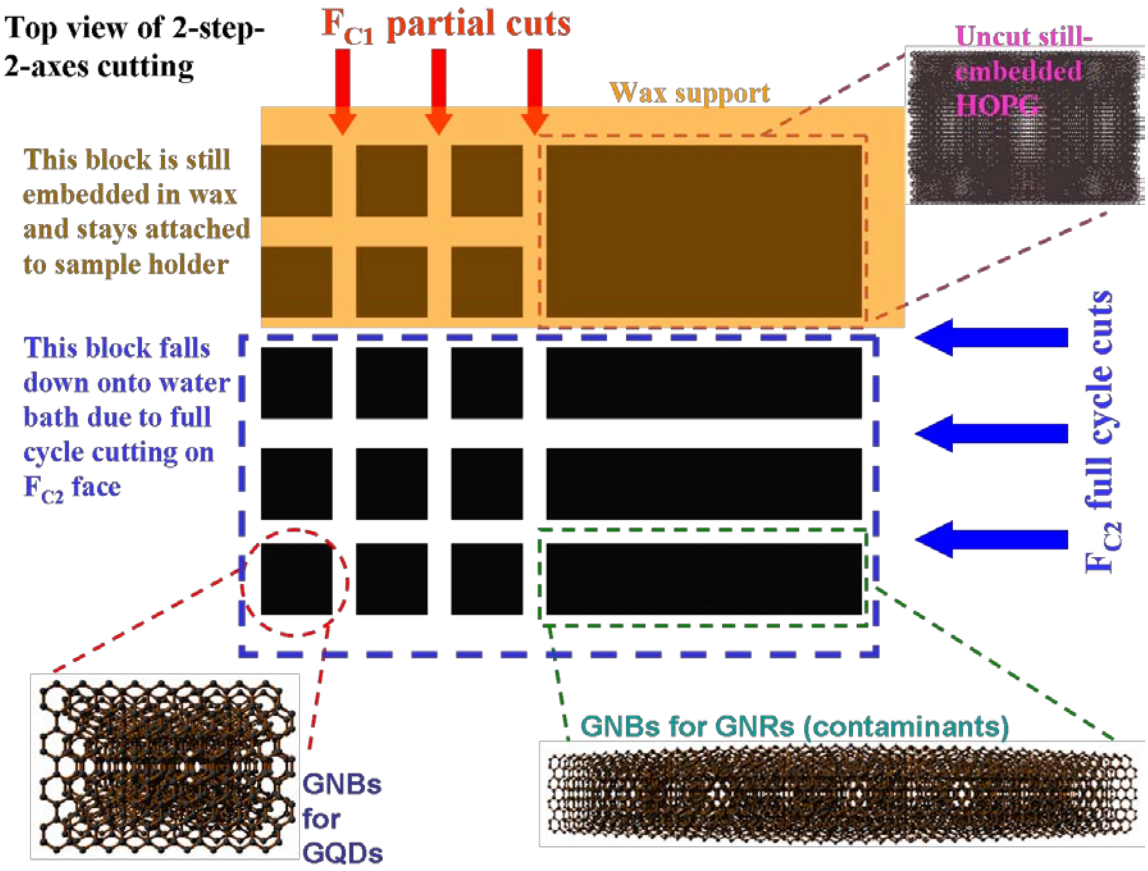

Figure F-1 Schematic diagram showing our 2-step-2-axes cutting process for synthesis of GQDs.

A typical HOPG block used for the cutting process has a length and breadth of 1 mm X 1 mm. As can be observed from the Figure F.1, since we carry out only 200 cutting cycles with d_{r1} ~ 50 – 100 nm (in order to completely cut the block about ~ 20,000 – 40,000 cutting cycles are

needed), the HOPG block is partially cut. Thus upon full cycle cutting in the second step (with d_{r2} ~ 50-100 nm) produces GQDs from the cut portions (in the first step) of the HOPG and GNRs from the uncut portions of the HOPG, as seen from the figure. Hence, for a typical cutting process of 200 cycles in each step, for production of 50 X 50 nm GQDs from a 1 X 1 mm HOPG block produces ~ 10^{10} GQDs in addition to 10^{8} GNRs, based on the graphenic dimensions given by Figure E.1 in Appendix E. This translates to an efficiency of > 99 %. It is imperative to note that upon cutting the HOPG block for the full 20,000 – 40,000 cycles in the first step, and then again in the second step, theoretically 100 % efficiency could be potentially achieved.

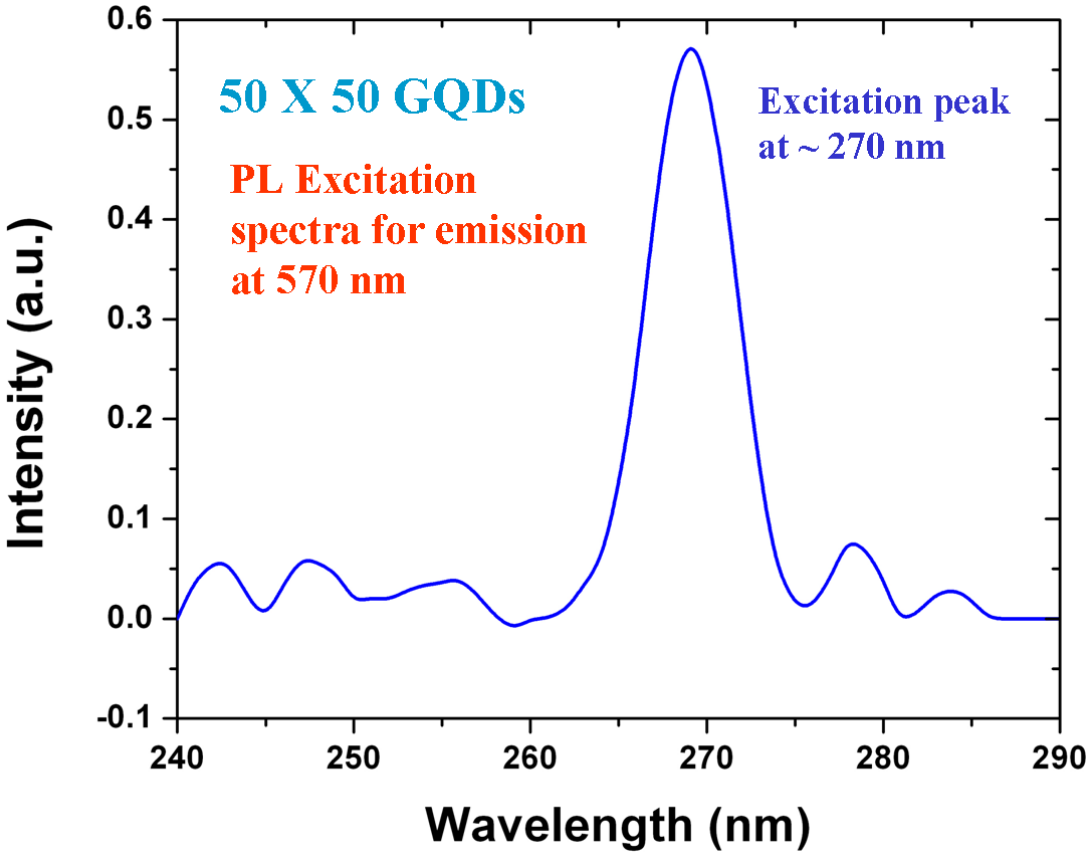

Figure F-2 PL excitation spectra of 50 X 50 nm GQDs for emission at 570 nm showing a single intense peak at ~ 270 nm which corresponds to the characteristic absorption spectra for the GQDs.